


Time-Resolved Magneto-Optical Investigations of Picosecond Magnetisation Dynamics in Arrays of Non- Ellipsoidal Ferromagnetic Nano-Elements

Submitted by **Paul Steven Keatley**, to the University of Exeter
as a thesis for the degree of Doctor of Philosophy in Physics,
June 2008.

This thesis is available for Library use on the understanding that it is copyright material and that no quotation from the thesis may be published without proper acknowledgement.

I certify that all material in this thesis which is not my own work has been identified and that no material has previously been submitted and approved for the award of a degree by this or any other University.

A handwritten signature in black ink, appearing to read 'P. Keatley', is written over a horizontal dotted line. The signature is stylized and cursive.

Abstract

In this thesis the results of magneto-optical experiments will be presented. The experiments were performed on micro-arrays of square nanomagnets in order to characterise the static and time-dependent behaviour of the nanomagnets. The static behaviour was investigated in vector-resolved scanning Kerr microscopy experiments, while the time-dependent behaviour was investigated in time-resolved scanning Kerr microscopy experiments. In the latter so-called pump-probe experiments, magnetisation dynamics were induced by exciting the sample magnetisation with a pulsed magnetic field (pump). The magnetisation dynamics were then detected using the magneto-optical polar Kerr effect (probe). The longitudinal Kerr effect was utilised in the vector-resolved scanning Kerr microscope in order to measure the in-plane components of the static magnetisation. The experimental set-up and methodology of the vector- and time-resolved scanning Kerr microscopy experiments will be discussed in detail, in particular, the detection technique that allows three components of the vector magnetisation to be measured simultaneously. Since the spatial resolution of the magneto-optical probe was insufficient to resolve the spatial character of the magnetisation dynamics within individual nanomagnets, micromagnetic simulations were used to gain insight into the character of the excited modes. Extensive testing of different micromagnetic models was carried out in order to investigate the effect of the different models on the simulated dynamics. The results of measurements carried out on the arrays of square nanomagnets revealed that the static and time-dependent behaviour of the magnetisation became more complicated as the size of the nanomagnets was reduced. In particular, similar hysteresis loops were acquired when the elements were magnetised along the uniaxial anisotropy easy and hard axes, while fast Fourier transform spectra of time-resolved signals revealed that the character of the magnetisation dynamics changed significantly as the element size and/or applied magnetic field were reduced. Interpretation of the experimental results using micromagnetic simulations revealed that the elements had a non-uniform single domain ground state magnetisation. When the field was applied along either edge of the square elements and reversed, the magnetisation was found to switch via a series of metastable non-uniform single domain states. Furthermore, the increasing non-uniformity of the single domain ground state as the element size and/or applied field were reduced lead to significant changes in the mode character excited within the elements. Comparison of

experimental spectra with simulated spectra and Fourier images of the dynamic magnetisation revealed that as the element size and/or applied field were reduced, the mode character changed from one that occupied the majority of the volume of the element, to several modes that were localised near to the edges of the element that were perpendicular to the applied field. Furthermore, deviation of the direction of the wavevector of the dynamic magnetisation from the direction of the static magnetisation was found to lead to a dynamic configurational anisotropy within nanomagnets. Following the presentation of the experimental results, the recent developments for future experimental work are presented with the aim to study precessional switching in an isolated nanomagnet. The results obtained in the experiments presented in this thesis are expected to lead to a better understanding of the non-uniform magnetisation dynamics in square nanomagnets, which have application in future magnetic data storage technologies.

To My Parents

Acknowledgements

The work presented in this thesis, and indeed this thesis itself, represents the cumulative help and support of my colleagues, friends, and family. This part of the thesis has proved to be more difficult to write than any other section in this thesis. The people that I've had the pleasure of spending time with at school, in the Air Training Corps, at sixth form, in part-time jobs, and as an undergraduate and postgraduate student, have all influenced me in one way or another. The innumerable influences, the smallest comment, compliment or criticism, have ultimately motivated me to complete my PhD and write this thesis. While it is impossible to acknowledge all of those people here, I will always remember them, and hopefully they will know their contribution to this work by making me the person I am today.

I would like to acknowledge the influence of several people in particular. To begin with I would like to thank my PhD supervisor, Prof Rob Hicken, for accommodating me on this research project at such short notice. I will always be grateful to Rob for his unwavering dedication, encouragement, and advice throughout. I would also like thank Rob for providing the opportunity to work on experiments at synchrotron facilities, and to present my work to wider audiences at several international conferences, both of which have been invaluable experiences for me. Finally, I would like to thank Rob for his time to read and critically comment on several versions of this thesis. Thank you Rob.

Past and present members of the Magnetic Materials Group have made it a stimulating group to work in. Thanks to Dr Anjan Barman and Dr Volodymyr Kruglyak for teaching me how to perform time-resolved magneto-optical microscopy experiments. A separate thanks to Volodymyr for his advice on anything physics (and more) each time I came knocking on his office door, which was pretty much a daily event. Thanks to Dr Ralph Wilks for his advice on magneto-optics and the use of electronics for the detection magneto-optical effects. Thanks to Dr Sam Ladak for helping me to settle in very quickly, and for providing the magnetic film used in experiments that led to my first paper. Thanks to Mr Shemaiah Weekes for being a superb comrade to whom I could grumble when my experiments were less than successful, and for driving for the entire time on our road trip across California. Thanks to Mr Leigh Shelford and Dr Yanwei Liu for allowing me to exercise my teaching skills by demonstrating magnetometry experiments when they first joined the group. Thanks

to Dr Andreas Neudert for bringing fresh ideas to the time-resolved experiments in Exeter, and for numerous discussions on theoretical magnetism and magneto-optics whilst I was writing this thesis. Thanks to Dr Feodor Ogrin for the opportunity to work on some of his experiments at synchrotron facilities, and for introducing me to Russian humour. Last and certainly not least, thanks to Mr Russell Edge for the excellent quality of the equipment that you created from nothing more than my scrappy sketches. The experiments presented in this thesis could not have been performed without first-rate equipment, advice and encouragement. Thank you all.

I would like to thank Prof Peter Winlove for agreeing to be my PhD mentor and internal examiner. Peter was my second year undergraduate tutor and has always kept an open door for me. I have very much enjoyed my mentor meetings with Peter during my PhD. These meetings allowed me to reflect on my work and appreciate that I was making good and steady progress throughout my PhD, which is sometimes difficult to see when your in the thick of it. Thank you Peter.

In addition to the people already mentioned, friends and colleagues outside of the Magnetic Materials Group have also made my time as a PhD student a rich and memorable one. Thanks to Dr Nathan Mayne, Dr Luke Hounsome, Dr Matthew Eames, Dr Steven Paul Hepplestone, and Dr Gemma Winter who have all been here from the outset in 1999. It's been a long slog, which seemed longer for me since most of you guys got your PhDs a whole graduation year before me. Thanks to Nathan for being there to talk sense into me when anything was getting me down, and for letting me win "The Epic" game of squash in our fourth year as undergraduates. Thanks to Luke and his wife Catherine for a great three years at 11 Old Park Road, and for inviting me to be Luke's Best Man at their wedding. I realised that I was definitely The Best Man when I caught the largest (12 lb) Pollock on the stag weekend. I would also like to thank Dr Steve Sque, Dr Eric Saunders and Dr Neil Telling for helpful advice whilst I was writing this thesis. A separate thanks to Neil for introducing me to synchrotron experiments and broadening my experimental expertise. Thanks to Dr Andrew Murray for acquiring high resolution scanning electron microscope images of the samples at short notice for the post viva corrections to this thesis. Thanks to Dr Ian Hooper and Dr Peter Vukusic for their support on the wicket despite my poor batting ability outside the nets. Thanks to Dr Matthew Lockyear for kind-of-helpful advice while writing this thesis, "Just get it done, son". Finally, separate thanks to Nathan, Leigh, Matt Eames, Steve Hepplestone, Andreas, and Volodymyr for reading and critically commenting on various chapters and sections of this thesis.

Next I would like to thank the brilliant support staff in the School of Physics for their help during my PhD. Firstly, thanks to Mr Kevyn White, Mr David Jarvis, Mr John Meakin, Mr Peter Cann and the other guys in the ground floor workshops. Thanks to Kev for the excellent quality of the optical detectors that he constructed for the experiments, and to Dave for evaporating anti-reflective coatings onto some of the samples. Thanks to John for his array of odds and ends tucked away in Stores that became necessary parts for many experiments. A separate thanks to Kev, John, and Pete for cheerleading duties at the occasional Nomads cricket match. Thanks to Mr Chris Forrest for helping to solve PC problems at short notice, and to Dr Charles Williams and Mr Tom Addison for helpful advice while I was re-designing and building the electronics for the optical detectors. Finally I would like to thank the administrative staff, in particular Mrs Natalia Ogrina, Mrs Denise Watts and Mrs Hilary Jordan, for figuring out all of my claim and order forms, which I'm just about getting the hang of. A separate thanks to Mrs Valerie Barnes, Mrs Lynda Barrell, and Mrs Victoria Brown for making sure I always had enough to eat after school open days.

Outside of the School of Physics I have an fantastic network of friends who have always encouraged and supported me. Many of my closest friendships in Exeter were made during the three years that I worked at the Imperial during my undergraduate degree. In particular, thanks to Jane and Dolly (Mr and Mrs Knott) and to Dr Lizzie Thompson for listening to me ramble on about magnets and lasers, and for always being there when anything was getting me down. I will always be grateful to Jane for introducing me to music festivals, which I adopted as an annual break from my PhD research. And thanks to Dolly for his faith. Dolly has been calling me Doctor since I started my PhD, therefore I'm glad I was successful as I think the nickname has now stuck. Thank you all for an outstanding five or six years, they seem to have gone far too quickly, but it was a great laugh.

It wasn't until I started my Physics A-Level that I began to find Physics really stimulating. Therefore, I would like to thank my excellent Physics A-level teachers at Newquay Treviglas School, Dr Jeremy Pollard and Mrs Jane Willmott, for making Physics an exciting subject to study, and for encouraging me to study Physics at University. I think it's fair to say that Dr Pollard, a former undergraduate and postgraduate student in the School of Physics at Exeter, nudged me in the direction of Exeter for which I will always be grateful.

My family have been a huge inspiration. I would like to thank my parents Sonia and Peter, and my younger sister Steph. My parents have led by example and shown my sister and I that fantastic achievements are the result of hard work and dedication, and that there are no easy routes. All Mum and Dad have ever asked of me (excluding chores and being nice to my sister) is that I do my best, and they would support me whatever I chose to do. I cannot thank you both enough for all of your love and support over the last twenty-seven years. I can honestly say that I did my best. Not bad for a “small child”. Thank you Mum, Dad and Steph.

Finally I would like to thank my partner Kelly. Not only did Kelly buy me drum lessons to take my mind off this thesis for one hour every other week, but Kelly has offered endless support, encouragement and love over the last year whilst I was writing this thesis. It's been a tough year, but we made it together. I can now play my drums guilt-free in the knowledge that this thesis is complete, and we can now have that skiing holiday. Thank you Kelly, I love you lots.

List of Contents

Title Page	1
Abstract	2
Acknowledgements	4
List of Contents	9
List of Publications	11
List of Figures	13
List of Tables	24
Declaration	25
Chapter 1 <i>Introduction</i>	28
Chapter 2 <i>Background concepts of magnetism</i>	34
2.1 Introduction	34
2.2 Classification of magnetic materials	34
2.3 Diamagnetism.....	35
2.4 Permanent atomic moments	37
2.5 Paramagnetism	41
2.6 Ferromagnetism.....	43
2.7 The exchange interaction.....	48
2.8 Band model theories of ferromagnetism	55
2.9 Ferromagnetic free energy contributions	57
2.10 The magnetisation of a ferromagnetic material.....	66
2.11 The Stoner-Wohlfarth model.....	72
2.12 Ferromagnetic resonance.....	76
2.13 The magnetic equation of motion.....	77
2.14 The Kittel formula	79
2.15 Magnetostatic spin wave modes.....	82
2.16 Spin wave modes in thin films	84
2.17 Spin waves in small non-ellipsoidal elements.....	85
2.18 Summary	89
Chapter 3 <i>Experimental techniques</i>	90
3.1 Introduction	90
3.2 Magneto-optical effects in metals	90
3.3 The magneto-optical reflection coefficients.....	96
3.4 The magneto-optical Kerr effect geometries.....	99
3.5 Detection of the magneto-optical Kerr effect.....	101
3.6 Time resolved scanning Kerr microscopy.....	109
3.7 Experimental limitations and modifications.....	121
3.8 Summary	126
Chapter 4 <i>Acquisition of vector hysteresis loops from microarrays of nanomagnets</i>	127
4.1 Introduction	127
4.2 Experimental and sample details.....	128

4.3 Results and discussion.....	139
4.4 Summary	148
Chapter 5 Use of microscale coplanar stripline with indium tin oxide windows in optical ferromagnetic resonance measurements	149
5.1 Introduction	149
5.2 Sample and experimental details	150
5.3 Results and discussion.....	153
5.4 Summary	157
Chapter 6 Time-resolved investigation of magnetisation dynamics of arrays of non-ellipsoidal nanomagnets with a non-uniform ground state	158
6.1 Introduction	158
6.2 Sample and experimental details	161
6.3 Details of numerical simulations	164
6.4 Results and discussion.....	169
6.5 Collective modes within arrays	192
6.6 Summary	194
Chapter 7 Dynamic configurational anisotropy in nanomagnets	196
7.1 Introduction	196
7.2 Sample and experimental details	198
7.3 Experimental and numerical results	200
7.4 Discussion	206
7.5 Summary	208
Chapter 8 Recent developments for future work.....	209
8.1 Introduction	209
8.2 Recent developments.....	210
8.3 Experimental set-up.....	210
8.4 Antireflective coatings	221
8.5 Vector- and time-resolved scanning Kerr microscopy	225
8.6 Summary	231
Chapter 9 Summary	232
Appendix 1 Calculation of the vector bridge longitudinal Kerr signal for the component of magnetisation perpendicular to the applied field	236
Appendix 2 Time-resolved scans acquired from arrays of nanomagnets	238
Appendix 3 The probe station assembly	240
Appendix 4 Tuning of the servomechanism loop gain	243
Appendix 5 The Mk II vector bridge detector	244
Bibliography	246

List of Publications

1. P.S. Keatley, V.V. Kruglyak, R.J. Hicken, J.R. Childress, and J.A. Katine, *Time-resolved investigation of magnetization dynamics of arrays of non-ellipsoidal nanomagnets with a non-uniform ground state*, Submitted to Physical Review B, under revision.
2. A. Neudert, P.S. Keatley, V.V. Kruglyak, J. McCord, R.J. Hicken, *Selective excitation and imaging of precessional modes in soft-magnetic squares*, Submitted to the proceedings of the IEEE Intermag Conference, Madrid 2008, for publication in the IEEE Transaction on Magnetics, accepted for publication.
3. V.V. Kruglyak, P.S. Keatley, R.J. Hicken, J.R. Childress, and J.A. Katine, *Time-resolved investigation of magnetization dynamics of arrays of non-ellipsoidal nanomagnets with a non-uniform ground state*, Submitted as a chapter in "Spin Wave Confinement" edited by S.O. Demokritov, in press.
4. V.V. Kruglyak, P.S. Keatley, A. Neudert, M. Delchini, R.J. Hicken, J.R. Childress, and J.A. Katine, *Imaging small-amplitude magnetization dynamics in a longitudinally magnetized microwire*, Physical Review B, **77**, 172407 (2008).
5. N.D. Telling, P.S. Keatley, L.R. Shelford, E. Arenholz, G. van der Laan, R.J. Hicken, Y. Sakuraba, S. Tsunegi, M. Oogane, Y. Ando, K. Takanashi, and T. Miyazaki, *Temperature dependence of the interface moments in Co₂MnSi thin films*, Applied Physics Letters, **92**, 192503 (2008).
6. Y. Sakuraba, M. Hattori, M. Oogane, H. Kubota, Y. Ando, A. Sakuma, N.D. Telling, P. Keatley, G. van der Laan, E. Arenholz, R.J. Hicken, and T. Miyazaki, *Extremely large spin-polarization in Co₂MnSi based magnetic tunnel junction*, Journal of the Magnetics Society of Japan, **31**, 338 (2007).

7. V.V Kruglyak, P.S. Keatley, R.J. Hicken, J.R. Childress, and J.A. Katine, *Dynamic configurational anisotropy in nanomagnets*, Physical Review B, **75**, 024407 (2007).
8. S.M. Weekes, F.Y. Ogrin, W.A. Murray, and P.S. Keatley, *Macroscopic arrays of magnetic nanostructures from self-assembled nanosphere templates*, Langmuir, **23**, 1057 (2007).
9. N.D. Telling, P.S. Keatley, G. van der Laan, R.J. Hicken, E. Arenholz, Y. Sakuraba, M. Oogane, Y. Ando, T. Miyazaki, *Interfacial structure and half-metallic ferromagnetism in Co₂MnSi-based magnetic tunnel junctions*, Physical Review B, **74**, 224439 (2006).
10. P.S. Keatley, V.V Kruglyak, R.J. Hicken, J.R. Childress, and J.A. Katine, *Acquisition of vector hysteresis loops from micro-arrays of nano-magnets*, Journal of Magnetism and Magnetic Materials, **306**, 298 (2006).
11. S.M. Weekes, F.Y. Ogrin, and P.S. Keatley, *Configurational anisotropy in hexagonal arrays of submicron Co elements*, Journal of Applied Physics, **99**, 08B102 (2006).
12. V.V Kruglyak, P.S. Keatley, R.J. Hicken, J.R. Childress, and J.A. Katine, *Time resolved studies of edge modes in magnetic nanoelements (invited)*, Journal of Applied Physics, **99**, 08F306 (2006).
13. P.S. Keatley, V.V. Kruglyak, A. Barman, S. Ladak, R.J. Hicken, J. Scott, M. Rahman, *Use of microscale coplanar striplines with indium tin oxide windows in optical ferromagnetic resonance measurements*, Journal of Applied Physics, **97**, 10R304 (2005).

List of Figures

Figure	Description	Page
2.3.1	The precession of a vector about an equilibrium direction is shown.	36
2.4.1	The vector model of orbital angular momentum for a d electron is shown.	38
2.4.2	The Zeeman splitting of a twofold degenerate energy level is shown.	39
2.5.1	The saturation effect in a large magnetic field and at low temperature is shown for the paramagnetic ion Fe^{3+} .	43
2.6.1	The graphical method used to determine the spontaneous magnetisation of a ferromagnetic material is shown.	46
2.6.2	The spontaneous magnetisation as a function of temperature is shown.	47
2.7.1	The variation of the exchange integral as a function of inter-atomic separation is shown for the H_2 molecule.	53
2.8.1	The density of states of the $4s$ and $3d$ bands of a ferromagnetic material is shown for temperatures above and below the Curie temperature.	56
2.9.1	The misalignment of two neighbouring atomic spins is shown.	59
2.9.2	The uniform magnetisation and demagnetising field of an ellipsoidal particle with a single magnetic domain is shown.	63
2.10.1	A typical magnetisation curve and hysteresis loop are shown for a ferromagnetic material. Hypothetical domain configurations are shown for a demagnetised single crystal and polycrystalline sample.	67

Figure	Description	Page
2.10.2	A Bloch wall between two neighbouring ferromagnetic domains of a thin film is shown.	68
2.10.3	The origin of ferromagnetic domains is shown.	69
2.10.4	Hypothetical magnetisation processes are shown.	70
2.10.5	Non-uniform, single domain magnetisation configurations (X-, leaf-, S-, and C-states) are shown for four non-ellipsoidal samples.	71
2.11.1	A single domain ellipsoid with uniform magnetisation and uniaxial shape anisotropy is shown.	72
2.11.2	Hysteresis loops derived using the Stoner-Wohlfarth model are shown.	75
2.11.3	The change in the free energy when a magnetic field is applied is shown.	76
2.13.1	The precession of the magnetisation about the effective magnetic field is shown.	78
2.15.1	A spin wave on a line of spins is shown as the successive advance in phase of the precessional motion of each spin along the line.	82
2.15.2	The Damon-Eshbach magnetostatic mode spectrum for a ferromagnetic slab is shown.	83
2.17.1	Brillouin Light Scattering spectra obtained from transversely, and longitudinally magnetised microscale stripes are shown.	86
2.17.2	Mode profiles and corresponding frequencies of a transversely magnetised microscale stripe are shown.	87

Figure	Description	Page
2.17.3	The experimental spectra obtained from an array of square nanomagnets of different size are shown. For corresponding simulated modes, the spatial distribution of the mode amplitude is shown.	88
3.3.1	The definition of linearly p- and s-polarised light is shown in addition to the Kerr rotation and ellipticity.	96
3.3.2	The geometry used in the calculation of the optical reflection coefficients at a vacuum-magnetic material interface is shown.	97
3.4.1	The polar, longitudinal, and transverse magneto-optical Kerr effect (MOKE) geometries are shown.	99
3.4.2	The calculated Kerr rotation and ellipticity angles for Fe at 800 nm for the polar and longitudinal MOKE geometry is shown.	100
3.4.3	The measured polar Kerr rotation for Ni and Fe is shown as a function of wavelength.	101
3.5.1	The geometry of the scanning Kerr microscope and the set-up of the photodiode bridge polarimeter (bridge detector) is shown.	103
3.5.2	The geometry of the probe laser beam focused upon the sample is shown.	104
3.5.3	The geometry of the Glan-Thompson polarising beam-splitter within the balanced-photodiode bridge detector is shown.	106
3.5.4	Ray tracings are shown for four rays of the probe beam that are sensitive to the out-of-plane component of the sample magnetisation.	107
3.6.1	The cavity layout of the Tsunami femtosecond laser is shown.	109
3.6.2	The experimental set-up of the time-resolved scanning Kerr microscope (TRSKM) is shown.	110

Figure	Description	Page
3.6.3	Fast photodiode signals of the Tsunami pulsed laser output are shown.	112
3.6.4	A typical time-resolved signal, obtained from a 10 μm square element of CoFe/NiFe(13.6 nm), is shown.	113
3.6.5	A typical pulsed magnetic field device is shown.	116
3.6.6	The spatial profile of the pulsed magnetic field is shown.	117
3.6.7	The profile of the current pulse within the pulsed field device is shown.	119
4.2.1	The geometry of the scanning Kerr microscope and the set-up of the quadrant-photodiode polarizing bridge detector (vector bridge) is shown.	129
4.2.2	The geometry of the laser beam focused upon the sample is shown.	131
4.2.3	Ray tracings are shown for two rays from opposite halves of the probe beam that are sensitive to the in-plane component of magnetisation that lies parallel to the applied field.	132
4.2.4	Ray tracings are shown for two rays from opposite halves of the probe beam that are sensitive to the in-plane component of magnetisation that lies perpendicular to the applied field.	133
4.2.5	Scanning electron microscopy (SEM) images of arrays of square elements of length(separation) 637(25), 428(17), 236(77), 124(30), 70(37), 637(236), and 637(688) nm are shown in (a) to (g) respectively. SEM images with higher magnification are shown for the 236, 124, and 70 nm elements in (h) to (j) respectively.	138
4.3.1	Outputs of the vector bridge detector, used to detect the in-plane components of the magnetisation vector, are shown as a function of polariser angle.	140

Figure	Description	Page
4.3.2	Hard axis vector hysteresis loops, obtained from a continuous film of CoFe/NiFe(13.6 nm), are shown.	141
4.3.3	Easy and hard axis hysteresis loops, obtained from a 10 μm square element of CoFe/NiFe(13.6 nm), are shown.	142
4.3.4	Easy and hard axis hysteresis loops obtained from individual microscale elements and arrays of nanomagnets patterned from a CoFe/NiFe(13.6 nm) film are shown.	143
4.3.5	The evolution of the coercive field is shown as the element size is reduced.	144
4.3.6	Simulated hysteresis loops and magnetisation configurations for a single 236 nm element for two directions of the magnetic field, parallel and perpendicular to the uniaxial anisotropy easy axis direction.	146
5.2.1	An optical micrograph shows the indium tin oxide (ITO) window of a hybrid Au/ITO coplanar stripline (CPS) track of a pulsed magnetic field device.	151
5.2.2	The complicated temporal profile of the current pulse in the CPS device is shown.	152
5.3.1	Typical time-resolved Kerr signals, measured by probing a continuous film of permalloy through the ITO window, are shown.	153
5.3.2	Dependence of frequency upon the bias field is shown for time-resolved signals obtained by probing the permalloy film through the ITO window, and between the ITO sections of the CPS.	154
5.3.3	The variation in phase of time-resolved signals measured at various positions across the CPS track is shown with corresponding simulations.	155

Figure	Description	Page
5.3.4	The calculated spatial profile across the CPS is shown for the in-plane and out-of-plane components of the pulsed magnetic field.	157
6.2.1	An optical micrograph of arrays of CoFe/NiFe(13.6 nm) nanomagnets between the tracks of a CPS is shown. Inset is an SEM image of an array of square elements of length(separation) 234(77) nm and a corresponding 3×3 model array used in micromagnetic simulations. The calculated spatial profile of the pulsed magnetic field across the CPS is shown.	162
6.2.2	The dependence of the uniform mode frequency on the bias field value and orientation is shown for a 10 μm square element of CoFe/NiFe(13.6 nm).	163
6.3.1	The simulated static magnetisation states of 3×3 model arrays of 236 nm square elements.	166
6.3.2	The experimental fast Fourier transform (FFT) spectra of time-resolved scans obtained from 236 nm square elements are compared with FFT spectra obtained from different micromagnetic models.	168
6.4.1	A typical raw time-resolved signal, the slowly varying background, and the signal with the background subtracted are shown, in addition to the corresponding FFT spectra, for the array of 236 nm elements at a bias field of 270 Oe.	169
6.4.2	The dependence of the mode frequency upon the element size is shown for bias field values of 1 kOe and 150 Oe. For each element size the simulated spatial distribution of the FFT amplitude of the excited modes is shown.	171
6.4.3	The simulated static magnetisation states within the centre element of 3×3 model arrays are shown.	174

Figure	Description	Page
6.4.4	The dependence of the mode spectra and the spatial character of the different modes upon the bias field is shown for the 637 nm element.	176
6.4.5	The dependence of the mode spectra and the spatial character of the different modes upon the bias field is shown for the 428 nm element.	177
6.4.6	The dependence of the mode spectra and the spatial character of the different modes upon the bias field is shown for the 236 nm element.	179
6.4.7	The dependence of the mode spectra and the spatial character of the different modes upon the bias field is shown for the 124 nm element.	180
6.4.8	The dependence of the mode spectra and the spatial character of the different modes upon the bias field is shown for the 70 nm element.	181
6.4.9	The dependence of the simulated mode spectra and the spatial character of the different modes upon the static magnetisation state of the 3×3 array is shown for the 236 nm element.	183
6.4.10	The simulated total effective field within the centre element of the 3×3 model arrays are shown.	185
6.4.11	Cross-sections of the simulated total effective field within the centre element of the 3×3 model arrays are shown for a bias field of 1 kOe.	186
6.4.12	Cross-sections are shown of the simulated total effective field and mode FFT magnitude within the centre element of the 3×3 model array of 637 nm elements for four values of the bias field.	188

Figure	Description	Page
6.4.13	Cross-sections are shown of the simulated total effective field and mode FFT magnitude within the centre element of the 3×3 model array of 236 nm elements for four values of the bias field.	189
6.4.14	Cross-sections are shown of the simulated total effective field and mode FFT magnitude within the centre element of the 3×3 model array of 70 nm elements for four values of the bias field.	191
6.5.1	Simulated images of the FFT magnitude and phase of the mode spatial character are shown for two modes with frequencies of 6.75 and 7.0 GHz excited in the centre element of a 3×3 array of 236 nm elements at a bias field of 270 Oe. The FFT magnitude is also shown for all elements in the 3×3 array, revealing collective mode excitations.	193
7.2.1	The dependence of the uniform mode frequency on the bias field value and orientation is shown for a 10 μm square element of CoFe/NiFe(2.5 nm).	199
7.3.1	Time-resolved signals and their FFT spectra obtained for different values of the bias magnetic field are shown for the field applied parallel to the edge and the diagonal of 220 nm square elements.	201
7.3.2	Time-resolved signals and their FFT spectra obtained for different orientations of the bias magnetic field are shown for the field value of 589 Oe.	202
7.3.3	Focused, vector hysteresis loops are shown for the case when the magnetic field was applied parallel to the edges of the element and along the element diagonals.	203

Figure	Description	Page
7.3.4	Simulated FFT mode spectra for the centre element in a 3×3 array and for an isolated element in response to a pulsed magnetic field are shown for four different orientations of a bias field of 589 Oe. The spatial character of the excited modes within an isolated element subject to a harmonic magnetic field of the same frequency is shown.	204
7.3.5	The dependence of the calculated mode frequencies and the total effective field averaged over different regions of the sample upon the orientation of the bias magnetic field is shown.	205
8.3.1	A schematic of the new set-up of the TRSKM and microwave probe station used in pulsed magnetic field experiments is shown.	211
8.3.2	Oscilloscope traces of the reflectivity signal are shown as the focused laser spot was placed at different positions relative to the edge of a 6 μm square element. The variation in the reflectivity signal allows the amplitude of the mechanical vibration of the probe station to be estimated.	213
8.3.3	Oscilloscope traces of the capacitive position sensor outputs of the piezoelectric stage are shown in response to an oscillatory input signal.	214
8.3.4	The non-magnetic contrast measured using the in-plane channels of the vector bridge detector as a result of scanning the microscope objective lens is shown.	216
8.3.5	A schematic of the CPS used on the probe station and calculated profile of the in-plane and out-of-plane components of the pulsed magnetic field are shown.	218
8.3.6	Traces of the current pulse profile are shown before and after the pulse is transmitted through the CPS.	219

Figure	Description	Page
8.3.7	Time-resolved scans obtained using the probe station and the previous experimental set-up are compared.	220
8.4.1	The reflectivity signal and the Kerr rotation are shown as a function of ZnS anti-reflective coating (ARC) thickness.	222
8.4.2	Vector hysteresis loops and time-resolved scans acquired from a 6 μm diameter disc patterned from a PtMn(25 nm)/CoFe(8 nm)/Al ₂ O ₃ (0.7 nm)/[CoFe/NiFe](2.5 nm) tunnel-valve stack with and without a ZnS(33 nm) ARC deposited on top of the sample are compared.	224
8.5.1	The new vector bridge longitudinal Kerr signal output, used to detect the in-plane component of the magnetisation vector, is shown as a function of polariser angle.	226
8.5.2	Vector hysteresis loops acquired using the new vector bridge are shown for a CoFe/NiFe(13.6 nm) 10 μm square element and arrays of square nanomagnets of size 234, 124, and 70 nm.	227
8.5.3	A time-resolved scan acquired using the probe station and the corresponding Fourier spectrum is shown for a 40 μm square of (Fe ₉₀ Co ₁₀) ₇₈ B ₁₂ Si ₁₀ (160 nm).	228
8.5.4	A schematic of the set-up of the TRSKM and microwave probe station used in harmonic magnetic field experiments is shown.	229
8.5.5	Vector- and time-resolved scans and images of the dynamic magnetisation are shown for two modes with frequency 8.0 GHz and 9.2 GHz that are excited in the 40 μm square of (Fe ₉₀ Co ₁₀) ₇₈ B ₁₂ Si ₁₀ (160 nm).	230
A2.1	Raw time-resolved scans obtained from an array 637 nm elements of CoFe/NiFe(13.6 nm) are shown for different bias field values.	238

Figure	Description	Page
A2.2	Raw time-resolved scans obtained from an array 428 nm elements of CoFe/NiFe(13.6 nm) are shown for different bias field values.	238
A2.3	Raw time-resolved scans obtained from an array 236 nm elements of CoFe/NiFe(13.6 nm) are shown for different bias field values.	239
A2.4	Raw time-resolved scans obtained from an array 124 nm elements of CoFe/NiFe(13.6 nm) are shown for different bias field values.	239
A2.5	Raw time-resolved scans obtained from an array 70 nm elements of CoFe/NiFe(13.6 nm) are shown for different bias field values.	239
A3.1	Detailed drawings of the probe station assembly are shown.	240
A3.2	Detailed drawings of the probe station assembly cross section are shown.	241
A3.3	Detailed drawings of the piezoelectric microscope mount are shown.	241
A3.4	Detailed drawings of the microwave probes are shown.	242
A4.4-9	A series of photographs show the procedure for tuning the capacitive position sensor servomechanism loop gain for the piezoelectric stage.	243
A5.1	The electronic circuit for the Mk II vector bridge is shown.	244
A5.2	The Mk II vector bridge output T2+T1 and P2-P1, used respectively to detect the second in-plane component and the out-of plane component of the magnetisation vector, is shown as a function of polariser angle.	245

List of Tables

Table	Description	Page
2.11.1	Solutions of the minimised free energy equations, derived using the Stoner-Wohlfarth model, are given.	73
2.11.2	The components of the magnetisation parallel to the applied field, derived using the Stoner-Wohlfarth model, are given.	74
3.7.1	Cables that may emit electromagnetic radiation at the reference frequency of the phase sensitive detection scheme for time-resolved measurements are listed.	125
4.2.1	The pad designation of the quadrant photodiode sum and difference amplifier outputs is given.	130
4.2.2	The table lists all ten outputs of the vector bridge detector and their corresponding experimental function.	136

Declaration

The work presented in this thesis is the result of the joint effort of many people. The contribution to this work by my colleagues is outlined below and will be acknowledged more specifically throughout the main text of this thesis. Particular contributions to this work by my PhD supervisor, Prof Rob Hicken, are difficult to describe as they permeate the whole of this thesis.

Chapter 1 *Introduction*

The introduction to the work presented in this thesis and the description of the motivation for conducting research in this area of physics is my own work. Details published by other authors that have been used in the discussions in Chapter 1 have been acknowledged.

Chapter 2 *Background principles of magnetism*

The background principles of magnetism relevant to this thesis have been compiled by myself in Chapter 2. The principles discussed in Chapter 2 are not the result of my own work. Throughout Chapter 2 the reference material used for each discussion has been acknowledged.

Chapter 3 *Experimental techniques*

The background principles of magneto-optics relevant to this thesis have been compiled by myself in Sections 3.2 to 3.4 of Chapter 3. However, the principles discussed in these sections are not the result of my own work. Throughout these sections the reference material used for each discussion has been acknowledged. In Sections 3.5 to 3.7 the description of the experimental techniques represents my own work. The basis for time-resolved experiments in Exeter had been set up by Prof Rob Hicken, Dr Jing Wu, Dr Ralph Wilks, Dr Anjan Barman, and Dr Volodymyr Kruglyak before I started my PhD project. The time-resolved scanning Kerr microscope (TRSKM) was set up by Dr Barman. The experiments presented in Chapter 5 were performed by myself using the TRSKM set up by Dr Barman. The experiments presented in Chapters 4, 6, 7 were performed using the TRSKM set up by myself with advice from Dr Kruglyak and Prof Hicken. Data acquisition software was written by Prof Hicken, Dr Barman, Dr Wilks and myself.

Chapter 4 Acquisition of vector hysteresis loops from microarrays of nanomagnets

The microscale elements and microarrays of nanomagnets were fabricated by Dr Jeffrey Childress and Dr Jordan Katine at Hitachi Global Storage Technologies San Jose Research Center, California. The scanning Kerr microscope was set up by myself. The vector bridge detector was designed originally by Dr Anjan Barman. The mechanics were constructed by Mr Kevyn White and the electronics were built by Dr Barman. The original vector bridge was unsuccessful in the achieving vector sensitivity. Realignment of the quadrant photodiodes and modification of the detector electronics was carried out by myself in order to achieve vector sensitivity. The characterisation of the vector sensitivity, and the acquisition of hysteresis loops from individual microscale elements and microarrays of nanomagnets was carried out by myself.

Chapter 5 Use of microscale coplanar stripline with indium tin oxide windows in optical ferromagnetic resonance measurements

The hybrid Au/indium tin oxide coplanar stripline was fabricated by Dr Jamie Scott and Dr Mahfuzur Rahman at the University of Glasgow. The permalloy film was fabricated by Dr Sam Ladak at the University of Exeter. The TRSKM was set up by Dr Anjan Barman. The sample was prepared by Dr Barman and myself, while measurements and data analysis were carried out by myself.

Chapter 6 Time-resolved investigation of magnetisation dynamics of arrays of non-ellipsoidal nanomagnets with a non-uniform ground state

The microscale elements and microarrays of nanomagnets were fabricated by Dr Jeffrey Childress and Dr Jordan Katine at Hitachi Global Storage Technologies San Jose Research Center, California. The TRSKM was set-up by myself. The measurements were carried out primarily by myself with additional help from Dr Volodymyr Kruglyak. The data analysis and micromagnetic simulations were carried out by myself, except for the macrospin fitting, which was carried out by Dr Kruglyak. The parameter files used in the micromagnetic simulations were based on those originally written by Dr Kruglyak. The analysis software for micromagnetic simulations was written by Dr Evgeny Galaktionov.

Chapter 7 *Dynamic configurational anisotropy in nanomagnets*

The microscale elements and microarrays of nanomagnets were fabricated by Dr Jeffrey Childress and Dr Jordan Katine at Hitachi Global Storage Technologies San Jose Research Center, California. The TRSKM was set-up by myself. The time-resolved measurements were carried out by myself and Dr Volodymyr Kruglyak. The vector hysteresis loop measurements were carried out by myself. The data analysis and micromagnetic simulations were carried out by Dr Kruglyak.

Chapter 8 *Recent developments for future work*

The microwave probe station was designed by myself, Prof Rob Hicken, and Mr Russell Edge. The electromagnet, sample stage, and piezoelectric stage bracket for the microscope column were built by Mr Edge. Additional supports for vibration control of the sample stage were built by Mr Kevyn White. All measurements for the characterisation of the mechanical vibration were carried out by myself. The tuning of the piezoelectric stage servomechanism loop gain was carried out by myself. The new coplanar stripline was fabricated by Dr Volodymyr Kruglyak. The current pulse profiles were measured by Dr Kruglyak and Dr Andreas Neudert. Antireflective coatings (ARC) were deposited by Mr David Jarvis. Characterisation of the enhancement of the magneto-optical effect for different ARC thicknesses was carried out by myself. The microscale elements (6 or 10 μm) and microarrays of nanomagnets were fabricated by Dr Jeffrey Childress and Dr Jordan Katine at Hitachi Global Storage Technologies San Jose Research Center, California. The 40 μm sized element sample was fabricated by Dr Michael Frommberger at the Center of Advanced European Studies and Research, Smart Materials Group, Germany. The new vector bridge detector was designed by myself. The mechanics were constructed by Mr White, while the electronics were built by myself. Advice on the construction of the electronics was given by Dr Charles Williams, Mr Tom Addison, and Mr Chris Forrest. Vector hysteresis loops were acquired by Mr Marco Delchini under my supervision during his summer research project in Exeter. Vector- and time-resolved measurement of images of the dynamic magnetisation of the 40 μm element were carried out by Dr Neudert. Testing of the synchronisation of the electronic pulse generators and microwave synthesisers with the pulsed laser was carried out by Dr Neudert and Dr Kruglyak.

“The beginning is the most important part of the work”. – Plato (428 BC-348 BC)

Chapter 1

Introduction

Over the past decade, time-resolved scanning Kerr microscopy¹ (TRSKM) has proved to be a powerful tool for the investigation of ultrafast magnetisation dynamics in novel magnetic materials. TRSKM falls within the broader classification of experiments called pump-probe techniques. Such experiments have become more common since the commercial availability of ultrafast solid state lasers² that are capable of producing pulses with a duration of less than 100 fs. In all-optical pump-probe experiments, the beam of laser pulses is split into a pump and a probe beam. The pump beam is used to excite the sample under investigation, while the probe beam passes along a variable optical time delay so that it can arrive at the sample before, simultaneously, or after the pump laser pulse. In pump-probe experiments on magnetic materials, the probe beam is usually linearly polarised. Changes in the magnetisation are then detected as changes in the polarisation of the reflected light as a result of the magneto-optical Kerr effect. The pump beam can be used to induce magnetisation dynamics within the sample in different ways. One method is to focus the pump pulse directly onto the sample. This technique can lead to the ultrafast demagnetisation³ of the sample followed by the excitation of precessional magnetisation dynamics as a result of ultrafast changes in the anisotropy field⁴. Alternatively the pump pulse can be used to trigger a pulsed magnetic field from a device⁵ that can be integrated with the sample or overlaid on top of the sample to deliver a pulsed magnetic field to the sample.

In both pumping techniques the effective field acting on the magnetisation within the sample is changed on a timescale of tens of picoseconds or less. The change in the effective field exerts a torque on the magnetisation resulting in the precessional magnetisation dynamics. More recently pump-probe experiments have been performed in which a harmonic field⁶ has been used to identify and image resonant modes. The harmonic field is synchronised with the laser pulses, while each resonant mode is excited using a harmonic field of the same frequency as the mode.

Spin wave excitations and picosecond magnetisation dynamics in thin film patterned elements are currently the subject of intense research as these ultrafast processes are expected to underpin the operation of future magnetic data storage technologies. The storage density of hard-disks has steadily increased at an annual rate of 50-60% over the past 25 years⁷. While the increase in storage density has led to a decrease in the size of the read- and write-head transducers, the transducers now require increased read- and write-rates. Data-rates of modern hard-disk read-heads⁷ are approaching 1 GHz. For a typical hard-disk storage density⁷ of 80 Gbit/in² the read-head width is 120 nm. In such nanoscale thin film elements, the dynamic eigenmodes are dipole-exchange spin waves⁸ with frequency in the microwave regime (3-30 GHz) and wavelength of 0.1-1 μm . Read-heads are magneto-resistive sensors⁷, the resistance of which depends upon the orientation of the magnetisation of a “free” layer with respect to that of a reference or “pinned” layer. Excitation of spin waves within the free layer results in a non-uniform dynamic magnetisation. As a result, the relative orientation of the magnetisation in the free and pinned layers becomes less well defined leading to a noisy magneto-resistive signal. Maintaining adequate signal-to-noise in future read-head sensors will present challenges in their design as their size becomes less than 100 nm and their operation frequency is pushed into the microwave regime.

On the hard-disk itself, each bit is written by magnetising a region of the recording medium in one of two opposite directions. The region is magnetised by applying an in-plane magnetic field using a microscale planar electromagnet⁷. The process may take a few nanoseconds as a result of magnetisation processes in the recording medium, or eddy currents within the electromagnet yolk. In contrast precessional switching^{9,10} only requires a half period of precession, corresponding to a switching time of a few hundred picoseconds. Precessional switching starts with the application of a pulsed magnetic field which induces large amplitude precessional motion of the magnetisation. If the pulsed field is turned off half-way through the precessional cycle, and the direction of the magnetisation corresponds to an equilibrium

state, then the magnetisation will remain in the new direction. The duration of the pulsed field must match a half-period of precession. However, in nano-elements the magnetisation does not precess as a single macrospin. Instead a number of eigenmodes are excited with different frequencies^{11,12}, hence the duration of the pulsed field cannot match the half-period of all modes. As a result some regions of the element will switch, while others will remain in the original orientation and would contribute to noise in a device application. Before precessional switching and faster nanoscale read-head sensors can be utilised in magnetic data storage devices, it is necessary for the spin wave spectrum of nanoscale thin film elements to be understood.

In this thesis the results of experiments that have been performed in order to characterise the static and time-dependent behaviour of the magnetisation within nanoscale thin film square elements are presented. The first step is to understand the ground state of the nanomagnets by obtaining the hysteresis loop. The second step is to understand the character of spin wave modes that are excited within the nanomagnets, and how the element size and the bias magnetic field affect their behaviour.

In Chapter 2 the principles of magnetism relevant to this thesis are introduced. The focus of the chapter is ferromagnetism and the behaviour of ferromagnetic materials. The spontaneous magnetisation of ferromagnetic materials is discussed in terms of the classical Weiss field, and the quantum mechanical exchange interaction. The contributions to the free energy of a ferromagnetic material are introduced and used to derive the hysteresis loop behaviour of an ellipsoid sample with a single magnetic domain using the Stoner-Wohlfarth model. The Landau-Lifshitz equation of motion and the Kittel formula are derived and are used respectively in simulating and fitting the magnetisation dynamics measured experimentally and presented in later chapters of this thesis. A description of magnetostatic spin wave modes is given which is followed by a brief review of important results published recently in the literature on dipole-exchange spin wave modes in patterned thin film elements. An extensive literature review is not given in this chapter, but instead the literature of most immediate relevance will be reviewed at the beginning of each chapter in which experimental results are presented.

In Chapter 3 the experimental set-up of the TRSKM is described. The chapter begins with a phenomenological description of magneto-optical effects. The role of the spin-orbit interaction in magneto-optical effects is described along with the theory developed to calculate the magneto-optical effects. The different Kerr effect geometries used to detect different components of the magnetisation vector are described in terms of the optical reflection coefficients. A description is then given of how the polar-Kerr

effect is utilised in scanning Kerr microscopy to sense the out-of-plane component of the sample magnetisation, which is followed by details of detection using a balanced photodiode polarising bridge detector. Details of the experimental set-up and methodology of TRSKM are given in addition to the interpretation of the measured signals. Finally, the actions taken to overcome the limitations of the experimental set-up are discussed.

In Chapter 4 the technique used for the acquisition of vector hysteresis loops from microarrays of nanomagnets is presented. The hysteresis loop provides the most direct means by which to quantify the magnetic parameters of the array and investigate its magnetic ground state. Knowledge obtained from the hysteresis loop can be very useful in the interpretation of time-resolved measurements performed on the same array. A review of other experimental techniques used to obtain hysteresis loops from arrays of nanomagnets is given. Since the arrays measured in time-resolved experiments presented in this thesis are microscale, measurements of hysteresis loops must be performed using a focused probe. It is shown how the longitudinal-Kerr effect can be utilised in scanning Kerr microscopy to simultaneously sense two in-plane components of the sample magnetisation, parallel and perpendicular to an applied field, in addition to the out-of-plane component. Details of detection using a balanced quadrant-photodiode polarising bridge detector are given. The detected signals are calculated in terms of the magneto-optical effects due to the in-plane components of the sample magnetisation. Hysteresis loops acquired from a continuous film are presented in order to demonstrate the vector sensitivity of the detector. Finally, hysteresis loops are presented for nanomagnets of different size that are also studied in time-resolved experiments, the results of which are presented in Chapter 6.

In Chapter 5 the use of a microscale coplanar stripline (CPS) with indium tin oxide (ITO) windows to perform time-resolved experiments is presented. The hybrid Au/ITO CPS structure can be overlaid on top of a sample grown on an opaque substrate and used to deliver a pulsed magnetic field in order to perform time-resolved measurements. Since the probe laser beam can be focused through the ITO window, a pulsed magnetic field of any desired orientation can be used to excite the sample magnetisation. The technique is demonstrated by applying it to a thin film of permalloy grown on a Si substrate. The phase of the oscillatory Kerr response was observed to vary as the probe spot was scanned across the CPS structure through the ITO window. The change in phase confirmed that the orientation of the pulsed field varied from parallel to perpendicular relative to the plane of the sample.

In Chapter 6 a comprehensive investigation of the magnetisation dynamics of arrays of square nanomagnets with a non-uniform ground state is presented. TRSKM measurements have been performed upon arrays of square ferromagnetic nano-elements of different size and for a range of bias fields. In the experimental spectra two branches of excited modes were observed to co-exist above a particular bias field. Below the so-called crossover field, the higher frequency branch was observed to vanish. The experimental results were compared to micromagnetic simulations of model arrays in order to understand the non-uniform precessional dynamics within the elements. The simulations and Fourier imaging revealed that modes from the higher frequency branch had large amplitude at the centre of the element, while modes from the lower frequency branch had large amplitude near the edges of the element perpendicular to the bias field. The simulations revealed that the spatial character of a mode was correlated with the spatial variation of the total effective field and the static magnetisation state. The simulations also revealed that the frequencies of the edge modes are strongly affected by the spatial distribution of the static magnetisation state both within an element and within its nearest neighbours. By comparing the mode frequencies within the simulated and experimental spectra the ground state of the magnetic nano-elements could be inferred.

In Chapter 7 an investigation of the dynamic configurational anisotropy in arrays of nanomagnets is presented. The angular dependence of the magnetisation dynamics in arrays of square nanomagnets was studied using TRSKM. In agreement with micromagnetic simulations, both the number of precessional modes and the values of their frequencies were observed to vary as the orientation of the external magnetic field was rotated in the element plane. It is shown that the observed behaviour cannot be explained by the angular variation of the static effective magnetic field. Instead, it is found to originate from a new type of magnetic anisotropy, a dynamic configurational anisotropy, which is due to the variation of the dynamic effective magnetic field. Some insight into the mechanisms that underlie the observed variations in frequency are obtained from the dispersion of dipolar-exchange spin waves excited within a continuous ultrathin film.

In Chapter 8 the experimental developments for future work are described. An outline of the recent developments is given, which include integration of the TRSKM with a microwave probe station to increase functionality, mechanical stability and productivity of the experiment. The new TRSKM set-up is described with particular emphasis on the mechanical stability of the microscope, impedance matching of the

CPS, and the signal-to-noise ratio of the measurements. The use of an antireflection coating to enhance the magneto-optical Kerr effect is explored and is found to increase the Kerr signal by at least a factor of three. In Section 8.5 details are given of the development of a second vector bridge detector, which features enhanced mechanical stability and electronic bandwidth. The combination of the improved design of the vector bridge and the integration of TRSKM with a microwave probe station led to the acquisition of time- and vector-resolved images of resonant spin wave modes within a microscale square element excited using a harmonic excitation field. The development of the microwave probe station will facilitate the controlled precessional switching of nanomagnets, while the improvements to the vector bridge detector will allow the trajectory of the switching to be measured. Finally, the main results of the research presented in this thesis will be summarised in Chapter 9.

“Quantum Mechanics is the key to understanding magnetism. When one enters the first room with this key there are unexpected rooms beyond, but it is always the master key that unlocks each door”. – J. H. Van Vleck (Nobel prize address, 1977)

Chapter 2

Background concepts of magnetism

2.1 Introduction

In this chapter I will introduce the background concepts of magnetism that are relevant to this thesis. In order to understand their origin, a quantum mechanical treatment is often necessary. The descriptions given in this chapter will certainly not be exhaustive. My aim is to summarise and attempt to explain the magnetic phenomena required to understand the experimental techniques and results presented in this thesis.

2.2 Classification of magnetic materials

There are two contributions to the magnetic moment of an atom, those due to the orbital angular momentum and the intrinsic spin angular momentum of the electron. The magnetisation M or magnetic moment per unit volume of a material can result from a combination of orbital and spin moments, or from just one of these contributions. The different electronic configurations of different materials result in a variety of magnetic phenomena, which include diamagnetism, paramagnetism, ferromagnetism, and anti-ferromagnetism. The experiments presented in this thesis were performed exclusively on ferromagnetic materials. However, in order to understand the underlying physics of

magnetism, it is necessary to review the origin of diamagnetism and paramagnetism for which the magnetisation is usually present only when an external magnetic field is applied. The origin of ferromagnetism and antiferromagnetism will then be reviewed with particular attention to the mechanism that gives rise to the spontaneous ordering of atomic moments, and in the case of ferromagnetic materials, a spontaneous magnetisation.

2.3 Diamagnetism

All materials exhibit diamagnetism. Its origin can be understood qualitatively by considering Lenz's law and the semi-classical model of an atom in which electrons move in orbitals about the nucleus. When an external magnetic field \mathbf{H} is applied, the electronic motion (current) within the atom is changed in such a sense that a magnetic moment is induced in the direction opposite to that of \mathbf{H} . Since the electronic motion within the atom is unimpeded, the diamagnetic moment will persist while the applied field is maintained.

The origin of diamagnetism can be understood quantitatively using a classical model¹³. We begin by considering the behaviour of a dipole moment in a uniform magnetic field. An electron with angular momentum \mathbf{G} has an associated magnetic moment $\boldsymbol{\mu}$ given by

$$\boldsymbol{\mu} = -\frac{e}{2m_e c} \mathbf{G}, \quad (2.3.1)$$

where $-e$ and m_e are the electronic charge and mass respectively, and c is the speed of light in vacuum. Since the electronic charge is negative, $\boldsymbol{\mu}$ and \mathbf{G} are anti-parallel. When a magnetic moment is placed in a uniform magnetic field, the field exerts a torque $\boldsymbol{\tau}$ upon the moment

$$\boldsymbol{\tau} = \boldsymbol{\mu} \times \mathbf{H}. \quad (2.3.2)$$

Equation 2.3.1 and 2.3.2, and Newton's Second Law for angular momentum, $\boldsymbol{\tau} = d\mathbf{G}/dt$, give

$$\frac{d\mathbf{G}}{dt} = -\frac{e}{2m_e c} \mathbf{H} \times \mathbf{G} . \quad (2.3.3)$$

Equation 2.3.3 may be written as

$$d\mathbf{G} = \boldsymbol{\omega}_H \times \mathbf{G} dt , \quad (2.3.4)$$

where $\boldsymbol{\omega}_H = -e\mathbf{H}/2m_e c$. Equation 2.3.4 represents the equation of motion of a vector \mathbf{G} that precesses with angular velocity $\boldsymbol{\omega}_H = d\theta/dt$ about $\boldsymbol{\omega}_H$, Figure 2.3.1. Therefore a

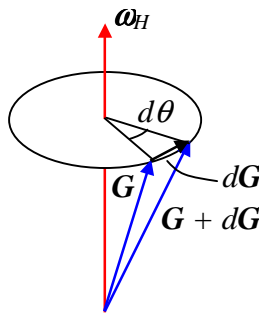


Figure 2.3.1 The physical interpretation of Equation 2.3.4 is the precessional motion of a vector \mathbf{G} about $\boldsymbol{\omega}_H$ with angular velocity $\boldsymbol{\omega}_H = d\theta/dt$.

magnetic moment in a uniform magnetic field will precess about \mathbf{H} with angular frequency $eH/2m_e c$, which is called the Larmor precession frequency.

Since angular momentum \mathbf{G} can be written as $m_e \boldsymbol{\omega}_H \overline{\rho^2}$, where $m_e \overline{\rho^2}$ is the moment of inertia of an electron in an orbital with radius ρ , Equation 2.3.1 can be written as

$$\boldsymbol{\mu} = \left(\frac{e}{2m_e c} \right) m_e \boldsymbol{\omega}_H \overline{\rho^2} = - \left(\frac{e^2}{4m_e c^2} \right) \mathbf{H} \overline{\rho^2} , \quad (2.3.5)$$

where $\overline{\rho^2} = \overline{x^2} + \overline{y^2}$ is the mean square radius of the electron orbit projected onto a plane perpendicular to \mathbf{H} . The negative sign reveals that the direction of the induced diamagnetic moment is opposite to that of the applied magnetic field. If $\overline{r^2} = \overline{x^2} + \overline{y^2} + \overline{z^2}$ is the mean square radius from the nucleus, and when averaged the

distribution is spherically symmetric so that $\overline{x^2} = \overline{y^2} = \overline{z^2}$, then $\overline{\rho^2} = \frac{2}{3}\overline{r^2}$. The diamagnetic susceptibility per cm^3 is given by

$$\chi_{dia} = -N \left(\frac{e^2}{6m_e c^2} \right) \sum_{i=1}^z \overline{r_i^2}, \quad (2.3.6)$$

which is obtained by summing over z electrons per atom, and multiplying by N atoms per cm^3 . Equation 2.3.6 is the Langevin equation for diamagnetic susceptibility.

When \mathbf{M} and \mathbf{H} are parallel the magnetic susceptibility χ is defined as

$$\mathbf{M} = \chi \mathbf{H}. \quad (2.3.7)$$

Since $\sum \overline{r_i^2} > 0$, the diamagnetic susceptibility χ_{dia} of a material is always negative and typically very small ($\sim 10^{-6}$ cgs units per mole). The dependence of χ_{dia} upon the temperature T is weak and is interpreted as a dependence of $\sum \overline{r_i^2}$ upon T .

All other magnetic phenomena, including paramagnetism, ferromagnetism and antiferromagnetism, are the result of atoms that possess a permanent magnetic moment¹³. The presence of a permanent magnetic moment is dictated by the electronic configuration of an atom. For example, atoms or ions of the transition group elements have permanent moments because of incomplete $3d$ electronic shells. Before I describe these other forms of magnetism, I will briefly review the quantum mechanical results pertinent to permanent atomic moments.

2.4 Permanent atomic moments

Orbital and spin angular momentum

Quantum mechanically, the eigenvalues L of the orbital angular momentum operator \hat{L} for an electron in a centrally symmetric potential are $[l(l+1)]^{1/2} \hbar$ in which the quantum number l takes the values $0, 1, 2, \dots, (n-1)$ and are associated with the s, p, d, f and g electrons respectively. The principle quantum number n primarily determines the energy of a particular orbit. In a magnetic field $\mathbf{H} = H_z \hat{z}$, the eigenvalues of the operator representing the Cartesian component of the orbital angular

momentum along the direction of the field \hat{L}_z are $m_l\hbar$. For a given value of l , m_l may take the $(2l + 1)$ possible values $l, (l - 1), \dots, 0, -(l - 1)$, and $-l$. For example, the eigenvalues of \hat{L}_z for a d electron are $2\hbar, \hbar, 0, -\hbar$ and $-2\hbar$. Quantisation of the orbital angular momentum leads to a spatially quantised atom since the electron orbits are restricted to particular plane orientations, Figure 2.4.1.

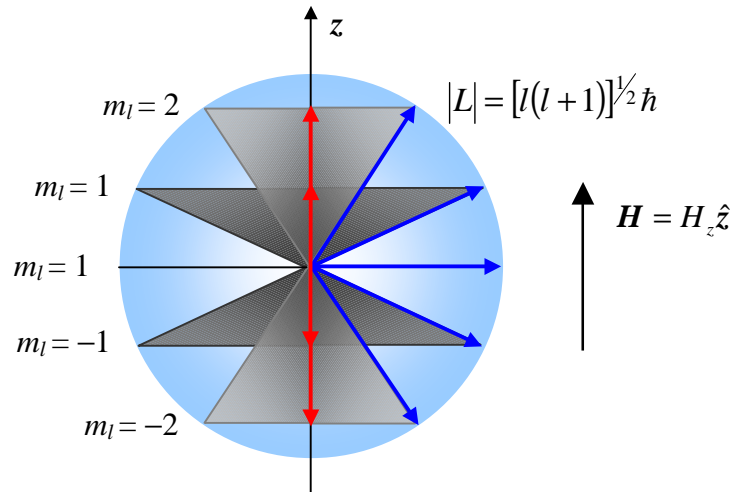


Figure 2.4.1 The vector model of orbital angular momentum for a d electron ($l = 2$). In a magnetic field \mathbf{H} , the component of the orbital angular momentum \hat{L}_z is quantised taking values $m_l\hbar$.

In accordance with Equation 2.3.1 the magnetic moment μ generated by an electron with orbital angular momentum quantum number l is given by

$$|\mu| = \frac{|e|\hbar}{2m_e c} [l(l+1)]^{1/2}, \quad (2.4.1)$$

where $e\hbar/2m_e c$ is the Bohr magneton μ_B ($= -0.927 \times 10^{-20}$ ergOe $^{-1}$). Similarly, the component of the orbital magnetic moment along the direction of the applied field is

$$\mu_z = \left(\frac{e\hbar}{2m_e c} \right) m_l. \quad (2.4.2)$$

Electrons also have an intrinsic spin angular momentum \mathbf{S} . The eigenvalues of the spin angular momentum operator \hat{S} are $m_s\hbar$. The spin quantum number m_s ($= \pm 1/2$)

determines the eigenvalue of the component of the spin angular momentum ($= \pm \hbar/2$) along the direction of the applied field. The magnetic moment due to the electron spin is not given by Equation 2.3.1, but instead is given by the product of the right hand side of Equation 2.3.1 and the spectroscopic splitting factor or g -factor. The component of the magnetic moment along the direction of the applied field μ_{sz} due to the electron spin angular momentum is then

$$\mu_{sz} = g \left(\frac{e\hbar}{2m_e c} \right) m_s. \quad (2.4.3)$$

The Zeeman effect

The state of two or more electrons with the same energy, but with different sets of quantum numbers is described as degenerate. A degenerate energy level of two electrons with $l = 0$ and $m_s = \pm 1/2$, will be split when a magnetic field is applied. The effect of spin splitting of the energy level when a magnetic field is applied is called the Zeeman effect, Figure 2.4.2. The magnetic moment of the spin $+1/2$ ($-1/2$) electron is antiparallel (parallel) to \mathbf{H} . The two electron states are separated in energy ΔE given by

$$\Delta E = 2|\mu_{sz}|H, \quad (2.4.4)$$

which is given in terms of the Bohr magneton using Equation 2.4.3 as

$$\Delta E = g|\mu_B|H, \quad (2.4.5)$$

where $g = 2.0023$ for a free electron¹³.

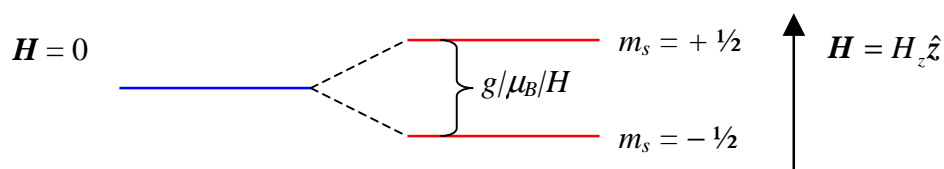


Figure 2.4.2 Zeeman splitting of a twofold degenerate energy level when an external magnetic field \mathbf{H} is applied.

Spin-orbit coupling

The addition of orbital and spin angular momentum for light atoms can be obtained using the Russell-Saunders spin-orbit coupling scheme¹³. The orbital angular momentum of all electrons within the atom are added to give a resultant vector $\mathbf{L} = \sum_i \mathbf{m}_{li}$. Similarly the spin angular momentum of all electrons are added to give a resultant vector $\mathbf{S} = \sum_i \mathbf{m}_{si}$. Finally \mathbf{L} and \mathbf{S} are combined to form a resultant atomic angular momentum $\mathbf{J} (= \mathbf{L} + \mathbf{S})$, where J can have values $(L + S), (L + S - 1), \dots, |L - S|$. The spacing between the adjacent values of J is determined by the spin-orbit coupling constant λ_{so} , which is defined so that the interaction energy is given by

$$\lambda_{so} \mathbf{L} \cdot \mathbf{S} . \quad (2.4.6)$$

The energy of the J^{th} level can be found from $\mathbf{J}^2 = \mathbf{L}^2 + \mathbf{S}^2 + 2\mathbf{L} \cdot \mathbf{S}$, where $\mathbf{J}^2 = J(J + 1)$, $\mathbf{L}^2 = L(L + 1)$ and $\mathbf{S}^2 = S(S + 1)$ and is given by

$$\frac{1}{2} \lambda_{so} [J(J + 1) - L(L + 1) - S(S + 1)] . \quad (2.4.7)$$

The total angular momentum of an atom is given by

$$|\mathbf{G}| = [J(J + 1)]^{1/2} \hbar , \quad (2.4.8)$$

and the spectroscopic splitting factor by the Landé formula

$$g = 1 + \frac{J(J + 1) + S(S + 1) - L(L + 1)}{2J(J + 1)} . \quad (2.4.9)$$

The atomic magnetic moment is then

$$\mu = g \frac{e\hbar}{2m_e c} [J(J + 1)]^{1/2} , \quad (2.4.10)$$

where the components of the atomic moment parallel to an applied field may have $2J + 1$ values of $g\mu_B m_J$, since $m_J = J, (J - 1), \dots, -(J - 1), -J$.

Quenching of the orbital angular momentum

The magnetic moment of an atom can also result from *either* orbital or spin angular momentum contributions. For example, in a crystalline material the orbital angular momentum may be quenched¹⁷. In an isolated atom, an electron experiences a centrally symmetric potential. The plane of the classical electron orbit is fixed in space such that L_x , L_y and L_z are constant. Quantum mechanically, L^2 and L_z are taken as the constants of motion in a central electric field. In a non-central electric field, *e.g.* in a crystal, the plane of the electron orbit may drift so that the angular momentum components are no longer constant and may average to zero. When L_z averages to zero the orbital angular momentum is said to be quenched and the magnetic moment is due to the spin angular momentum only, where

$$\mu_z = (L_z + gS_z)\mu_B = g\mu_B S_z. \quad (2.4.11)$$

Hence, $g \approx 2$ when $L_z \approx 0$ or quenched. It turns out that $g > 2$, due to spin-orbit coupling.

2.5 Paramagnetism

In paramagnetic materials, the interaction between permanent atomic moments is weak or zero. In the absence of a magnetic field the moments are randomly oriented and the magnetisation is zero. When an external field is applied, the moments tend to align along \mathbf{H} and the magnetisation becomes non-zero in the direction of the field. At a sufficiently high temperature T , the thermal energy of atomic moments $\sim k_B T$ becomes comparable to the potential energy of the moments within the field $\sim m_J g \mu_B H$, where k_B is the Boltzmann constant. At higher temperature, $m_J g \mu_B H / k_B T \ll 1$, and therefore the magnetisation is destroyed.

Since all materials are diamagnetic the total magnetic susceptibility χ for a paramagnetic material is

$$\chi = \chi_{para} + \chi_{dia}. \quad (2.5.1)$$

The paramagnetic susceptibility is $\sim 10^{-2}$ to 10^{-4} per mole, therefore, the small diamagnetic response is often neglected. Examples of paramagnetic materials include the iron or $3d$ transition ions (*e.g.* Fe^{3+} , Cr^{3+}) and the rare-earth or $4f$ transition ions (*e.g.* Gd^{3+}) in solutions or salts¹³.

Curie's law

In 1895 Curie¹⁴ reported that some materials possessed a temperature-dependent and field-independent susceptibility given by

$$\chi_{para} = \frac{C}{T}, \quad (2.5.2)$$

where C is Curie's constant. Curie's law (Equation 2.5.2) is the high temperature limit of paramagnetic behaviour. In large magnetic fields and at low temperatures, $m_J g \mu_B H / k_B T \ll 1$ is no longer satisfied. Instead, the number of atomic moments with a particular orientation when an external field is applied is determined by the Boltzmann factor $\exp(-E/k_B T) = \exp(m_J g \mu_B H / k_B T)$ in accordance with statistical mechanics. The magnetisation is then given by¹³

$$M = N g \mu_B J B_J(x), \quad (2.5.3)$$

where

$$B_J(x) = \frac{2J+1}{2J} \coth\left(\frac{2J+1}{2J}x\right) - \frac{1}{2J} \coth\left(\frac{x}{2J}\right), \quad (2.5.4)$$

and

$$x = \frac{J g \mu_B H}{k_B T}. \quad (2.5.5)$$

Equation 2.5.4 is called a Brillouin function and the derivation of $B_J(x)$ can be found in Reference 13. When all orientations of the magnetic moment become possible when a field is applied, *i.e.* when $J \rightarrow \infty$, $B_J(x)$ tends to the classical Langevin function

$$L(x) = \coth(x) - \frac{1}{x}. \quad (2.5.6)$$

In sufficiently large magnetic fields and low temperatures, $x \rightarrow \infty$ so that $B(x)$ and $L(x)$ approach unity. In this case, all atomic moments align with the applied field so that the magnetisation is saturated, Figure 2.5.1. In the classical Langevin model, the atomic moments align parallel to the applied field so that $M/N\mu \rightarrow 1$. Quantum mechanically, the maximum component of the moment $\mu_B g [J(J+1)]^{1/2}$ along \mathbf{H} is $Jg\mu_B$ so that $M/N\mu \rightarrow [J/(J+1)]^{1/2}$.

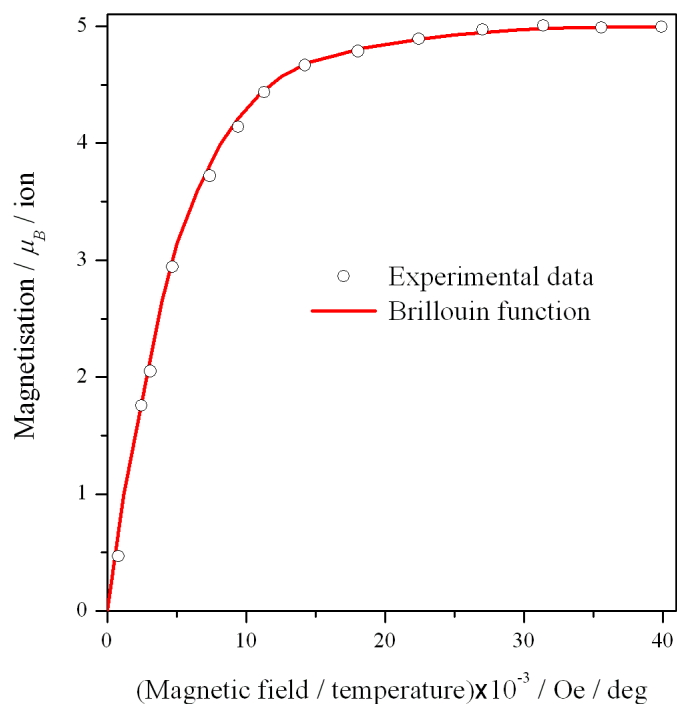


Figure 2.5.1 Saturation effect in large magnetic fields and at low temperature for the paramagnetic ion Fe^{3+} . The figure is reproduced from Reference 13.

2.6 Ferromagnetism

For some materials at sufficiently low temperatures, where $m_j g \mu_B H / k_B T \ll 1$ is no longer satisfied, the interaction between permanent atomic moments becomes important. Even in the absence of a magnetic field the thermal energy is insufficient to

cause random orientation of the moments. Instead, the moments spontaneously align with nearest neighbours in such a way that the interaction energy between neighbouring moments is minimised. The result is an ordered magnetic state. In ferromagnetic materials the moments tend to spontaneously align with the same direction. The spontaneous alignment is a result of the quantum mechanical exchange interaction, the origin of which will be described in detail in Section 2.7. Examples of room temperature ferromagnetic materials are the iron or 3d transition group elements, Fe, Co, Ni, and their alloys.

It is useful to separate the discussion of ferromagnetic materials into two parts. The first part will describe the paramagnetic behaviour of ferromagnetic materials, which occurs at sufficiently high temperatures where $m_J g \mu_B H / k_B T \ll 1$. The second part will describe the spontaneous magnetisation behaviour of ferromagnetic materials, where $m_J g \mu_B H / k_B T \ll 1$ is no longer satisfied.

The Curie-Weiss law – paramagnetic behaviour

To describe the spontaneous alignment of the magnetic moments in a ferromagnetic material, Weiss introduced an internal field¹⁵ (Weiss field) proportional to the magnetisation $\sim \lambda_W M$, where λ_W is a constant. Using Equation 2.5.2 and writing the total magnetic field as $H + \lambda_W M$, Equation 2.3.7 becomes

$$M = \frac{C}{T} (H + \lambda_W M). \quad (2.6.1)$$

Then solving for M

$$M \left(1 - \frac{C \lambda_W}{T} \right) = \frac{CH}{T}, \quad (2.6.2)$$

and recovering the form of Equation 2.3.7

$$M = \frac{CH}{(T - C \lambda_W)} = \frac{CH}{(T - T_C)}, \quad (2.6.3)$$

where the magnetic susceptibility is given by

$$\chi_{para} = \frac{C}{(T - T_C)}. \quad (2.6.4)$$

The Curie-Weiss law (Equation 2.6.4) describes the susceptibility of ferromagnetic materials for $T > T_C$, in which case the material exhibits paramagnetic behaviour. For $T < T_C$ the material is ferromagnetic and exhibits a spontaneous magnetisation.

The spontaneous magnetisation – the Weiss field theory

To describe the spontaneous magnetisation of a ferromagnetic material we can begin by using Equations 2.5.3 to 2.5.5. In the case of a ferromagnetic material the Weiss field can be included in Equation 2.5.5 so that

$$x = \frac{Jg\mu_B}{k_B T} (H + \lambda_w M). \quad (2.6.5)$$

The external magnetic field H is set to zero so that the spontaneous magnetisation can be studied. Equation 2.5.3 and 2.6.5 can be rewritten in the form

$$\frac{M(T)}{M(0)} = B_J(x), \quad (2.6.6)$$

and

$$\frac{M(T)}{M(0)} = \frac{k_B T}{N\lambda_w J^2 g^2 \mu_B^2} x, \quad (2.6.7)$$

respectively, where

$$M(0) = NJg\mu_B, \quad (2.6.8)$$

and $M(T)$ is the temperature dependent magnetisation. The magnetisation defined in Equation 2.6.8 is the maximum possible magnetisation and results from Equation 2.5.3 since $B_J(x) \rightarrow 1$ when $x \rightarrow \infty$, *i.e.* when $T \rightarrow 0$.

Equations 2.6.6 and 2.6.7 can be solved graphically by finding the intersection of the two equations when plotted as a function of x . Figure 2.6.1 shows schematically three cases for different values of T . The tangent of the Brillouin function at $x=0$ corresponds to a critical temperature T_f . For $T < T_f$ a non-vanishing solution exists at point P , which represents a spontaneous magnetisation in this temperature regime. For $T > T_f$ the two curves intersect at $x=0$ only, for which $M(T)/M(0)=0$, *i.e.* the spontaneous magnetisation vanishes. Therefore, T_f is the ferromagnetic Curie temperature, below which a spontaneous magnetisation exists.

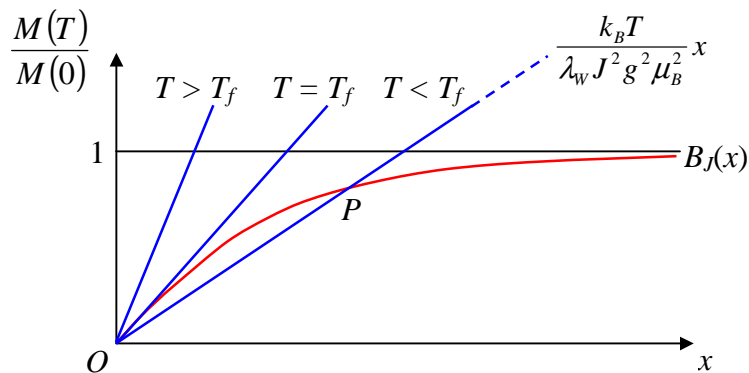


Figure 2.6.1 Schematic of the graphical method used to determine the spontaneous magnetisation at a particular temperature T . For $T < T_f$, the ferromagnetic Curie temperature, non-vanishing solutions exist, corresponding to the spontaneous magnetisation.

Experimental observations reveal that the inverse susceptibility $1/\chi$ just above T_f is not linear, but instead, slightly upward concave. The intercept on the temperature axis of the extrapolation of the linear regime of $1/\chi$ is T_C , where $T_C > T_f$. The non-linearity of $1/\chi$ just above T_f is due to structural phase changes of the ferromagnetic material, *e.g.* in Fe, from a body-centred to a face-centred cubic structure as T increases.

For small $x \ll 1$, the Brillouin function (Equation 2.5.4) can be written as

$$B_J(x) = \frac{J+1}{3J}x - \frac{J+1}{3J} \frac{2J^2 + 2J + 1}{30J^2} x^3. \quad (2.6.9)$$

Therefore, for $x \rightarrow 0$, the gradient of the tangent is $(J+1)/3J$, which is equal to the gradient of the straight line for $T = T_f$ so that

$$T_f = \frac{Ng^2\mu_B^2J(J+1)}{3k_B}\lambda_w. \quad (2.6.10)$$

Substituting λ_w obtained from Equation 2.6.10 into Equation 2.6.7 gives

$$\frac{M(T)}{M(0)} = \frac{J+1}{3J} \left(\frac{T}{T_f} \right) x, \quad (2.6.11)$$

where the value of $M(T)/M(0)$ as a function of T/T_f can be determined using the graphical method outlined above or by making suitable algebraic substitutions¹³. The best fit of the experimental data for $M(T)/M(0)$ can be obtained using the expression

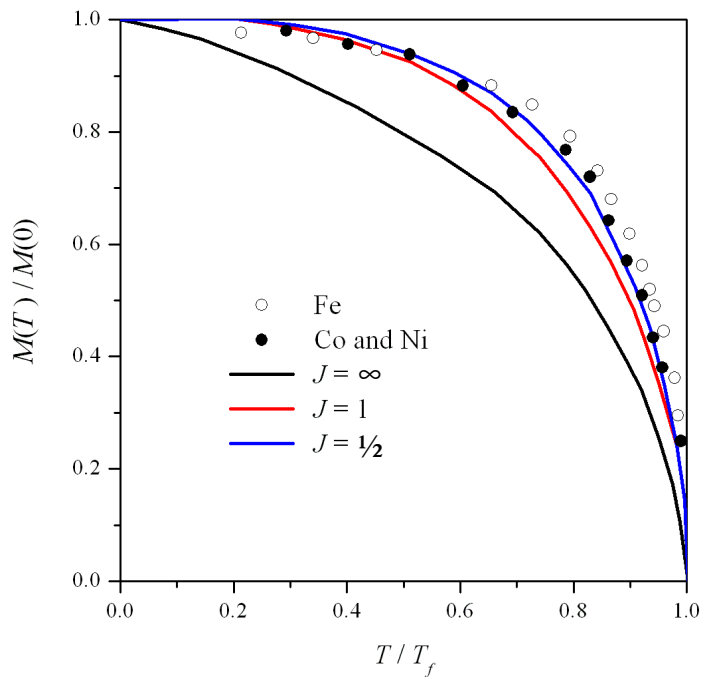


Figure 2.6.2 The spontaneous magnetisation as a function of temperature reproduced from Reference 13. The curves are obtained from the Weiss field theory of the spontaneous magnetisation, while the data points are obtained experimentally. The curve for which $J = \infty$ corresponds to the classical case.

$$\frac{M(T)}{M(0)} = 1 - \beta T^{\frac{3}{2}}, \quad (2.6.12)$$

where β is a fitting parameter. Figure 2.6.2 reveals that the Weiss field theory is in good agreement with the experimental data. However, at low temperatures the experimental data reveals that the magnetisation falls off more rapidly with increasing temperature than the theoretical curves for $J = 1$ and $\frac{1}{2}$. In a more rigorous approach, Equation 2.6.12 can be derived quantum mechanically in terms of the exchange interaction and spin-wave theory.

2.7 The exchange interaction

In the previous section, the alignment of the magnetic moments in a ferromagnetic material was described by an internal field introduced by Weiss that was proportional to the magnetisation, $H_W \sim \lambda_W M$. For $T > T_C$, the thermal energy $\sim k_B T$ of atomic moments becomes greater than the interaction energy $\sim \mu_B H_W$ and ferromagnetic order is destroyed. Thus, the strength of the Weiss field can be estimated from $\mu_B H_W \approx k_B T_C$. For Fe with $T_C = 1043$ K, $H_W \sim 10^7$ Oe. The magnetic field produced by the dipole-dipole interaction is $\sim \mu_B/a^3 \sim 10^3$ Oe, where a is the lattice parameter of the material. Therefore, an alternative explanation is required for the interaction between permanent atomic moments that gives rise to their spontaneous alignment.

The nature of the interaction between magnetic moments was not understood until quantum mechanics was well established. In 1928 Heisenberg¹⁶ developed a theory based on the Heitler-London model of the H_2 molecule to introduce the concept of the exchange interaction. Heisenberg showed that the Weiss field is a manifestation of the exchange interaction for which there is no classical analogue. The exchange interaction is electrostatic in origin and is a result of the Pauli exclusion principle. The charge distribution of a system of two spins depends upon whether the spins are parallel or antiparallel¹⁷. In accordance with the Pauli exclusion principle, two electrons (fermions) with the same spin cannot exist in the same spatial state at the same time, while two electrons with opposite spin can. Thus, the electrostatic energy of the two electron system will then depend upon the relative orientation of the electron spins. Furthermore, when two identical electrons exchange spatial co-ordinates, the symmetry requirement that the complete wavefunction describing the many-particle state remains

antisymmetric must be obeyed. The exchange energy is the difference in the energy between parallel and antiparallel configurations of the electron spins. In order to illustrate the origin of the exchange interaction, the main features of Heisenberg's model described in Reference 13 will now be outlined.

Consider a system of two non-interacting electrons at co-ordinates r_1 and r_2 that move in similar potential fields $V(r_1)$ and $V(r_2)$. The system is described by the Schrödinger equation

$$\left[-\frac{\hbar^2}{2m} (\nabla_1^2 + \nabla_2^2) + V(r_1) + V(r_2) \right] \Psi = E \Psi . \quad (2.7.1)$$

The solutions that describe the two electron systems are

$$\Psi^{(1,2)}(r_1, r_2) = \Psi_{\{n\}}(r_1) \Psi_{\{n'\}}(r_2) \quad (2.7.2)$$

and

$$\Psi^{(2,1)}(r_1, r_2) = \Psi_{\{n\}}(r_2) \Psi_{\{n'\}}(r_1) \quad (2.7.3)$$

with energy $E = E_{\{n\}} + E_{\{n'\}}$ in both cases. $\Psi_{\{n\}}(r_1)$ is the single electron solution to the Schrödinger equation when electron 1 is in a state described by the set of quantum numbers $\{n\}$, and $\Psi_{\{n'\}}(r_2)$ is the solution when electron 2 is in the state $\{n'\}$. $\Psi_{\{n\}}(r_2)$ and $\Psi_{\{n'\}}(r_1)$ are the obtained solutions when the electrons exchange their co-ordinates r_1 and r_2 . However, since electrons are indistinguishable it is necessary that

$$|\Psi^{(1,2)}(r_1, r_2)|^2 dr_1 dr_2 = |\Psi^{(2,1)}(r_1, r_2)|^2 dr_1 dr_2 . \quad (2.7.4)$$

It follows from Equation 2.7.4 that under the exchange of the electron co-ordinates the two-electron wavefunction can yield symmetrical wavefunctions

$$\Psi^{(1,2)}(r_1, r_2) = +\Psi^{(2,1)}(r_1, r_2), \quad (2.7.5)$$

or antisymmetrical wavefunctions

$$\Psi^{(1,2)}(r_1, r_2) = -\Psi^{(2,1)}(r_1, r_2). \quad (2.7.6)$$

Since Equations 2.7.2 and 2.7.3 do not possess any symmetry properties, the only possible wavefunction solutions that satisfy Equation 2.7.4 are linear combinations of the two-electron wavefunction

$$\Psi_{sym}^{(1,2)}(r_1, r_2) = \frac{1}{\sqrt{2}} [\Psi_{\{n\}}(r_1)\Psi_{\{n'\}}(r_2) + \Psi_{\{n\}}(r_2)\Psi_{\{n'\}}(r_1)], \quad (2.7.7)$$

and

$$\Psi_{anti}^{(1,2)}(r_1, r_2) = \frac{1}{\sqrt{2}} [\Psi_{\{n\}}(r_1)\Psi_{\{n'\}}(r_2) - \Psi_{\{n\}}(r_2)\Psi_{\{n'\}}(r_1)]. \quad (2.7.8)$$

The factor $1/\sqrt{2}$ is a normalising factor assuming that $\Psi_{\{n\}}(r_1)$ and $\Psi_{\{n'\}}(r_2)$ have already been normalised. Here we see from the antisymmetric many particle wavefunction (Equation 2.7.8) that the Pauli exclusion principle is also obeyed. If the two electrons occupied the same quantum state with identical sets of quantum numbers $\{n\} \equiv \{n'\}$, we see that $\Psi^{(1,2)}(r_1, r_2) \equiv \Psi^{(2,1)}(r_1, r_2)$ from Equations 2.7.2 and 2.7.3. Then from Equation 2.7.8 the probability of two electrons in the same system occupying the same quantum state is zero. The single-electron wavefunctions are functions of spatial and spin co-ordinates and may be written as

$$\Psi^{(\pm)}(r_1, r_2) = \Phi_{space}(r_1, r_2)\chi_{spin}, \quad (2.7.9)$$

where $\Psi^{(-)}(r_1, r_2)$ indicates that for an antisymmetric single-electron wavefunction, the spatial Φ and spinor χ parts must be of opposite symmetry. The spatial wavefunction is a solution to the Schrödinger equation for an electron without spin and the spinor is a function of spin co-ordinates only. There are two combinations that give an antisymmetric two-electron wavefunction,

$$\Psi_I^{(-)}(r_1, r_2) = \Phi_{space}^{(+)}(r_1, r_2)\chi_{spin}^{(-)} \quad (2.7.10)$$

and

$$\Psi_{II}^{(-)}(r_1, r_2) = \Phi_{space}^{(-)}(r_1, r_2)\chi_{spin}^{(+)} \quad (2.7.11)$$

In Equations 2.7.10 and 2.7.11 the two-electron spinors are linear combinations of the single-electron spinors in a state described by the spin quantum numbers S and m_s ,

$$\chi_{spin}^{(\pm)} = \sqrt{\frac{1}{2}} (\chi_{sm_s}^{(1)} \chi_{sm_s'}^{(2)} \pm \chi_{sm_s}^{(2)} \chi_{sm_s'}^{(1)}). \quad (2.7.12)$$

The two combinations of the spatial and spinor wavefunctions give rise to the singlet state with total spin $S = 0$ when the two electron spins are antiparallel

$$\Psi_I^{(-)}(r_1, r_2) = A [\Phi_{\{n\}}(r_1) \Phi_{\{n'\}}(r_2) + \Phi_{\{n\}}(r_2) \Phi_{\{n'\}}(r_1)] \cdot [\chi_{+1/2}^1 \chi_{-1/2}^2 - \chi_{+1/2}^2 \chi_{-1/2}^1], \quad (2.7.13)$$

and the triplet state with total spin $S = 1$ ($m_s = 1, 0, -1$) when the spins are parallel

$$\Psi_{II}^{(-)}(r_1, r_2) = B [\Phi_{\{n\}}(r_1) \Phi_{\{n'\}}(r_2) - \Phi_{\{n\}}(r_2) \Phi_{\{n'\}}(r_1)] \cdot \begin{bmatrix} \chi_{+1/2}^1 \chi_{+1/2}^2 \\ \chi_{+1/2}^1 \chi_{-1/2}^2 + \chi_{+1/2}^2 \chi_{-1/2}^1 \\ \chi_{-1/2}^1 \chi_{-1/2}^2 \end{bmatrix}, \quad m_s = \begin{cases} 1 \\ 0 \\ -1 \end{cases} \quad (2.7.14)$$

where constants A and B are normalising factors.

The electrostatic interaction Hamiltonian \hat{H}_{12} for the two H atoms a and b within the H_2 molecule is given by

$$\hat{H}_{12} = \frac{e^2}{r_{ab}} + \frac{e^2}{r_{12}} - \frac{e^2}{r_{1b}} - \frac{e^2}{r_{2a}}, \quad (2.7.15)$$

where r_{ab} is the distance between the nuclei, r_{12} is the distance between the electrons and r_{1b} and r_{2a} are the distances between a given nucleus and the electron of the other atom. The energy E_I and E_{II} of the singlet and triplets states can be calculated by considering \hat{H}_{12} as an electrostatic perturbation of the two-electron system, where the energy correction to the unperturbed system is $E = \int \Psi^* \hat{H}_{12} \Psi d\tau$. Thus the energy of the singlet and triplet states are

$$E_I = A^2 (K_{12} + J_{12}), \quad (2.7.16)$$

and

$$E_{II} = B^2(K_{12} - J_{12}), \quad (2.7.17)$$

respectively, where K_{12} is the average Coulombic interaction energy given by

$$K_{12} = \int \Phi_{\{n\}}^*(r_1) \Phi_{\{n'\}}^*(r_2) H_{12} \Phi_{\{n\}}(r_1) \Phi_{\{n'\}}(r_2) d\tau_1 d\tau_2, \quad (2.7.18)$$

and J_{12} is the exchange integral given by

$$J_{12} = J_{ex} = \int \Phi_{\{n\}}^*(r_1) \Phi_{\{n'\}}^*(r_2) H_{12} \Phi_{\{n\}}(r_2) \Phi_{\{n'\}}(r_1) d\tau_1 d\tau_2. \quad (2.7.19)$$

The exchange integral (Equation 2.7.19) is a direct result of the requirement that the electrons are indistinguishable.

As demonstrated here, the Heisenberg model can be used to illustrate the origin of the exchange interaction. For the H_2 molecule, J_{ex} is negative, therefore in its ground state the spins are antiparallel. It is by no means a straightforward step from the H_2 molecule to ferromagnetism in Fe, Co and Ni transition metals. For a material to exhibit ferromagnetism, the exchange integral J_{ex} must be positive. The conditions that favour a positive J_{ex} may be understood using the following qualitative arguments¹⁸.

In Equation 2.7.19, $\Phi_{\{n\}}^*(r_1) \Phi_{\{n'\}}^*(r_2) \Phi_{\{n\}}(r_2) \Phi_{\{n'\}}(r_1)$ will be positive if the wavefunctions $\Phi_{\{n\}}$ and $\Phi_{\{n'\}}$ have no nodes in the regions of significant overlap. J_{ex} will then be positive if the positive contributions of the Hamiltonian (Equation 2.7.15) exceed those from the negative terms. These conditions are met if the r_{ab} is large compared to the orbital radii. J_{ex} is then likely to be positive for d and f wavefunctions for the atoms of some iron and rare earth metals, for example Fe, Co, Ni, and Gd. The schematic variation of the exchange integral with inter-atomic separation r_{ab} is shown in Figure 2.7.1.

Spin waves

Consider a ferromagnetic material at absolute zero temperature. At absolute zero, the ground state of the spin system is completely ordered in accordance with the third law of thermodynamics. Furthermore, the magnetisation will be saturated since the spin quantum number m_s will have its maximum possible value ($m_s = 1/2$) so that from Equation 2.6.8, $M = N/\mu_B$, where $g = 2$, and N is the number of atomic moments

per unit volume. If the temperature is raised so that a single spin is reversed, the spin system can then occupy its first excited state. In the first excited state, the exchange interaction will act to realign the reversed spin with its nearest neighbours. However, the return of the spin system to its ground state is improbable at the slightly elevated temperature, while the probability of a spin being reversed is the same for each atom. Thus, the exchange interaction causes a reversal of a neighbouring spin while the previous spin returns to its ground state. As a result, the reversed spin does not remain localised to a particular atom, but instead propagates via the exchange interaction between nearest neighbour moments. The resulting propagation of the reversed spin through the crystal is called a spin wave.

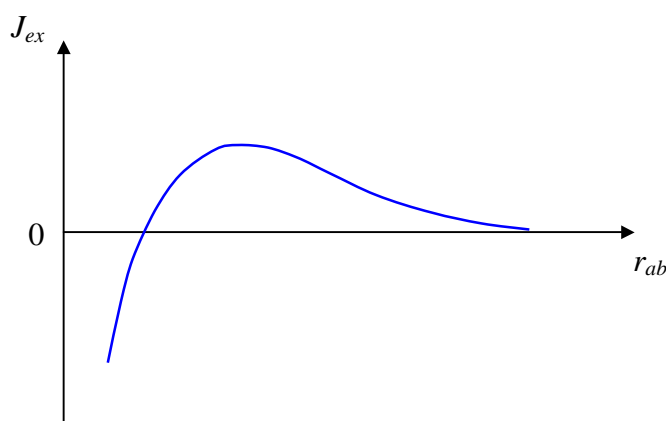


Figure 2.7.1 The schematic variation of the exchange integral as a function of inter-atomic separation r_{ab} is shown for the H_2 molecule.

The spontaneous magnetisation – the Bloch spin wave model

In the spin wave theory one can consider the change in the spontaneous magnetisation by the excitation of a spin wave. Since the exchange of any two reversed spins in the first excited state of the spin system represents the same state of the system, spin waves obey Bose-Einstein statistics¹³. Furthermore, more than one spin wave can be excited with the same energy since the spin wave “gas” is degenerate. Therefore, the average number \bar{n}_k of spin waves for a given wave number k corresponds to an average number of \bar{n}_k reversed spins at a temperature T , which is described by the Planck distribution law

$$\bar{n}_k = \frac{1}{e^{E_k/k_B T} - 1}, \quad (2.7.20)$$

where E_k is the energy of a spin wave with associated wave number k . The total number of spin waves \bar{n} is then given by

$$\bar{n} = \sum_k \bar{n}_k. \quad (2.7.21)$$

The number of states between k and $k + dk$ is

$$D(k)dk = \frac{4\pi k^2 dk}{(2\pi/L)^3}, \quad (2.7.22)$$

where $D(k)$ is the density of states, $(2\pi/L)^3$ is the volume of a single state, and $4\pi k^2 dk$ is the volume of a spherical shell in k -space. The dispersion relationship for an exchange spin wave¹³ in a cubic crystal with lattice parameter a is given by

$$E_k = J_{ex} k^2 a^2, \quad (2.7.23)$$

where J_{ex} is called the exchange constant. Equation 2.7.22 then becomes

$$D(E)dE = \frac{V}{4\pi^2} \left(\frac{1}{a^2 J_{ex}} \right)^{3/2} E^{1/2} dE. \quad (2.7.24)$$

Using Equations 2.7.20, 2.7.21, and 2.7.24 the total number of spin waves is

$$\bar{n} = \frac{V}{4\pi^2} \left(\frac{1}{a^2 J_{ex}} \right)^{3/2} \int_0^\infty \frac{E^{1/2} dE}{e^{E/k_B T} - 1}. \quad (2.7.25)$$

By making the substitution $x = E/k_B T$, the integration can be performed using a series expansion, for which the result¹³ is

$$\bar{n} = 0.1174 V \left(\frac{k_B T}{a^2 J_{ex}} \right)^{3/2}. \quad (2.7.26)$$

Now the change in the spontaneous magnetisation due to the excitation of spin waves can be written as

$$\frac{\Delta M}{M(0)} = \frac{M(0) - M(T)}{M(0)} = \frac{\bar{n}}{N}. \quad (2.7.27)$$

The volume V of a simple cubic, body-centred cubic and face-centred cubic lattice is Na^3 , $Na^3/2$, and $Na^3/4$ respectively, so that

$$\frac{\Delta M}{M(0)} = \frac{0.1174}{\eta} \left(\frac{k_B T}{J_{ex}} \right)^{3/2}, \quad (2.7.28)$$

where $\eta = 1, 2,$ and 4 respectively. Equation 2.7.28 is called the Bloch $T^{3/2}$ law and is identical to Equation 2.6.12 when

$$\beta = \frac{0.1174}{\eta} \left(\frac{k_B}{J_{ex}} \right)^{3/2}. \quad (2.7.29)$$

2.8 Band model theories of ferromagnetism

Theories of ferromagnetism based on the Heisenberg model assume that the electrons are localised at the atoms. For metals and their alloys this assumption is incorrect, and so band model theories of ferromagnetism were developed. Here I will briefly outline two band model theories;¹³ that of Stoner¹⁹, followed by that of Vonsovski²⁰ and Zener²¹.

The Stoner band theory of ferromagnetism

Stoner's model, is now known as a collective electron theory of ferromagnetism in which interactions between conduction electrons are considered. Bloch-type wavefunctions were used to account for interaction between conduction electrons and ion cores. Since ferromagnetic metals belong to the iron group, the calculations were made for electrons and holes of the $3d$ band, while the carriers of the $4s$ band were assumed not to contribute to ferromagnetism. Stoner's theory is based on three main

assumptions. Firstly, the $3d$ band is parabolic in the vicinity of the Fermi level so that the density of states is $\propto E^{1/2}$. Secondly, the exchange interaction between electrons is described by the Weiss field $H_W = \lambda_W M(T)$ so that the energy of an electron with spin parallel or antiparallel to the magnetisation is $\pm \mu_B \lambda_W M(T)$. Third, the electrons and holes obey Fermi-Dirac statistics.

Stoner's calculation of M as a function of T was performed numerically and included a dependence of M upon the magnitude of the exchange forces compared to the Fermi energy. It followed that the theory could then predict non-integral numbers of effective magnetic carriers. The results showed improvements over the molecular field theory for both the spontaneous magnetisation for $T < T_C$, and the susceptibility for $T > T_C$. Comparison of experimentally measured susceptibilities with Stoner's results revealed consistent agreement of the effective magnetic carrier numbers with those deduced from experiments. The non-integral effective magnetic carrier numbers are due to an energy overlap of the $3d$ band with the much wider $4s$ band, Figure 2.8.1. Both bands are filled to the same (Fermi) energy level. For example, for Ni with a total of 10 electrons in the $3d$ and $4s$ bands, there are 9.4 electrons in the $3d$ band and 0.6 electrons in the $4s$ band (0.6 holes in the $3d$ band)¹³.

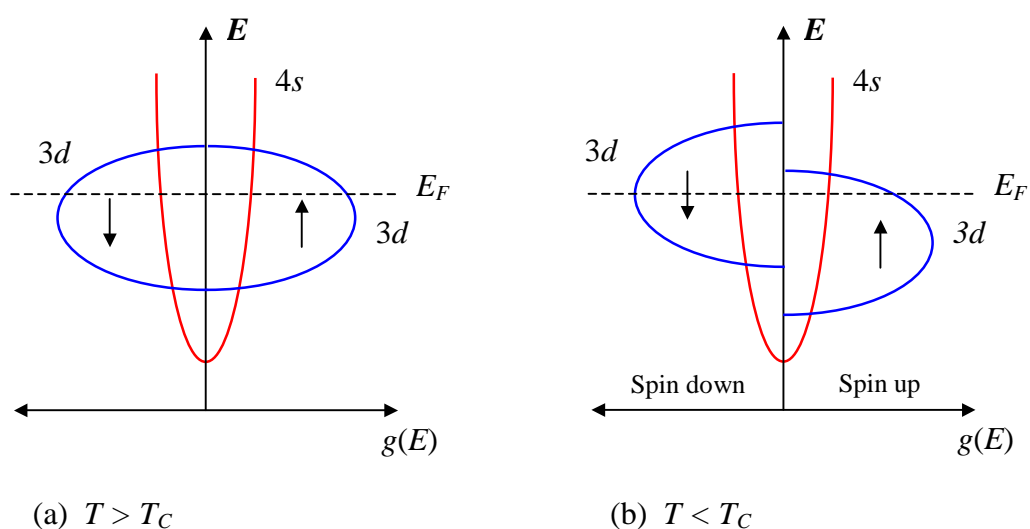


Figure 2.8.1 A schematic representation of the density of states $g(E)$ of the $4s$ and $3d$ bands of a ferromagnetic material at (a) $T > T_C$ and (b) $T < T_C$. In (a) the material is paramagnetic with equal electron spin populations at the Fermi energy level E_F . In (b) the material is ferromagnetic. Spin-splitting of the d band due to the exchange interaction results in an imbalance of electron spin populations at the Fermi level.

The Vonsovsky and Zener band theory of ferromagnetism

The band model theory of Vonsovsky and Zener is more refined than Stoner's model since it includes the Heisenberg exchange interaction between electrons. Firstly, it is assumed that $3d$ electrons are localised at atomic sites and that the exchange interaction between the shells of $3d$ electrons align the $3d$ electron spins. Secondly, $4s$ conduction electrons are non-localised and interact with localised $3d$ electrons via the exchange interaction. The parallel $3d$ spins are considered to be equivalent to an internal magnetic field that interacts with the $4s$ electrons. The result is the spin polarisation of the $4s$ electrons as their spin will tend to align with the spin of the $3d$ electrons in order to minimise the exchange energy.

For ferromagnetism to be realised it is not necessary for neighbouring $3d$ shells to interact. The exchange interaction between a $4s$ conduction electron and an unfilled $3d$ shell will promote the spin polarisation of the $4s$ electron. In turn the exchange interaction between that $4s$ electron and a different $3d$ shell will promote the spin polarisation of the $3d$ shell. This mechanism is called indirect- or superexchange¹³.

The theory of Vonsovsky and Zener can be thought of as an intermediate model between the localised model of Heisenberg and the collective electron theory of Stoner. The Stoner model led to improved agreement with experimental data compared with the classical Weiss field model (Section 2.6). However, in the Stoner model the exchange interaction is represented by the classical Weiss field. In more refined theories, *e.g.* the Bloch spin wave model (Section 2.7), the Heisenberg exchange Hamiltonian is used to model the exchange interaction in order to obtain the dispersion relation of exchange spin waves. Detailed comparison of the models with experimental data has shown that for Ni the collective electron model is favoured, while for Fe and Gd the Heisenberg model is better¹³.

2.9 The ferromagnetic free energy contributions

The ground state and dynamic magnetisation of a ferromagnetic sample are dictated by the interplay between the different contributions to its total free energy. The static magnetisation can be described by Brown's differential equation²²

$$\mathbf{M} \times \mathbf{H}_{eff} = 0, \quad (2.9.1)$$

where \mathbf{H}_{eff} is the total effective magnetic field. Equation 2.9.1 means that in equilibrium the torque acting on the magnetisation is zero throughout the sample, and that the magnetisation is parallel to the effective field. The total effective field is defined as the functional derivative of the free energy density W with respect to the magnetisation²²

$$\mathbf{H}_{eff} = -\frac{\delta W}{\delta \mathbf{M}}, \quad (2.9.2)$$

where the total free energy density may be written as

$$W = w_{ex} + w_Z + w_{ms} + w_{ani} + w_o, \quad (2.9.3)$$

where w_{ex} , w_Z , w_{ms} , w_{ani} represent the exchange, Zeeman, magnetostatic, and anisotropic energy contributions. The final term w_o represents any other contributions to the total energy, for example, magnetostriction. The total free energy F is then the integral of the free energy density over the volume V of the ferromagnetic sample

$$F = \int_V W dV. \quad (2.9.4)$$

The exchange energy

The tendency for atomic magnetic moments to align with the same direction in ferromagnetic materials has already been described in terms of the classical Weiss field and the quantum mechanical exchange interaction. In Section 2.7 the exchange integral (Equation 2.7.19) was shown to be analogous to the difference in energy of the singlet and triplet states for which the electronic spins in the H_2 molecule are anti-parallel and parallel respectively. In order to discuss the magnetic properties of a ferromagnetic material it is sufficient to replace the exchange integral with the so called exchange (or Heisenberg) Hamiltonian^{13,22}

$$\hat{H}_{ex} = -2J_{ex} \sum_j \mathbf{S}_i \cdot \mathbf{S}_j, \quad (2.9.5)$$

where \mathbf{S}_i and \mathbf{S}_j are the total spins of atoms i and j respectively. It is assumed that the electron wavefunctions of atom i only overlap with those of nearest neighbour atoms j ,

i.e. the exchange interaction is a short range interaction. Therefore, the sum is taken over j nearest neighbour atoms only. It is also assumed that the orbital angular momentum is quenched and that the exchange energy between electrons in the same atom is constant and can be omitted¹³.

Consider two neighbouring atomic spins in a ferromagnetic material. For the exchange energy to be minimised there is a tendency for neighbouring atomic moments to align in the same direction. When the moments deviate from this equilibrium state, an angle θ_{ij} is formed between the neighbouring moments. The misalignment results in an energy penalty, and the exchange energy is no longer minimised.

If the angle between the atomic moments is small it is convenient to replace the spin operators in the exchange Hamiltonian with classical spin angular momentum vectors. Figure 2.9.1 shows the unit vectors \mathbf{u}_i and \mathbf{u}_j of two neighbouring atomic spins i and j that are misaligned by an angle θ_{ij} . The exchange Hamiltonian (Equation 2.9.5)

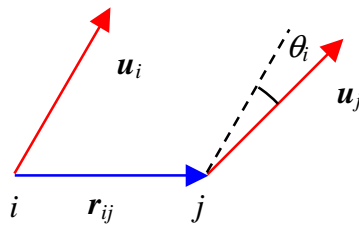


Figure 2.9.1 The unit vectors \mathbf{u}_i and \mathbf{u}_j of two neighbouring atomic spins i and j that are misaligned by a small angle θ_{ij} and separated by \mathbf{r}_{ij} .

may then be rewritten as

$$\hat{H}_{ex} = w_{ex} = -2J_{ex}S^2 \sum_j \cos \theta_{ij} \cong J_{ex}S^2 \sum_j \theta_{ij}^2, \quad (2.9.6)$$

when the angle between the adjacent spins is small. A more general form of the exchange energy per unit volume is²²

$$w_{ex} = A_{ex} \left[(\nabla u_x)^2 + (\nabla u_y)^2 + (\nabla u_z)^2 \right], \quad (2.9.7)$$

where

$$A_{ex} = \frac{J_{ex} S^2}{a} \eta, \quad (2.9.8)$$

is the exchange constant, a is the lattice parameter, and $\eta = 1, 2$ and 4 for a simple cubic, body-centred cubic, and face-centred cubic structure respectively. For a hexagonal close-packed structure, *e.g.* Co, $\eta = 2\sqrt{2}$.

The Zeeman energy

The Zeeman energy is the potential energy of the atomic moments of a ferromagnetic sample when an external magnetic field is applied. When an external field is applied, the magnetisation will tend to align with the field in order to minimise the potential energy. If the magnetisation deviates from this equilibrium orientation an increase in the potential energy results. The energy penalty is proportional to the angle between the magnetisation and the field, thus the Zeeman energy per unit volume is

$$w_z = -\mathbf{M} \cdot \mathbf{H}. \quad (2.9.9)$$

The external field in Equation 2.9.9 may not necessarily be a steady bias field between the poles of an electromagnet, for example. The field may be a time varying pulsed⁹ or harmonic field⁶. The field may also originate from atomic moments at a ferromagnetic/antiferromagnetic multilayer interface, which is called an exchange bias field²³. In the latter, interfacial atomic moments of the antiferromagnetic layer interact with those of the ferromagnetic layer. The exchange interaction acts to align the ferromagnetic moments with the same direction as the interfacial moments of the antiferromagnetic layer. The exchange bias field is used to describe the interfacial exchange in terms of an external field, in a similar way that the Weiss field was used to describe the exchange interaction between atomic moments of a ferromagnetic material. The strength of the exchange bias field is inversely proportional to the thickness of the antiferromagnetic layer.

The magnetostatic energy

The magnetostatic energy is concerned with long range magnetostatic interactions of atomic moments with the magnetostatic fields of other atomic moments within a ferromagnetic sample. The magnetostatic energy per unit volume has the form

$$w_{ms} = -\frac{1}{2} \mathbf{H}_d \cdot \mathbf{M} , \quad (2.9.10)$$

where $\mathbf{H}_d = -\nabla U$ is the demagnetising field and U is the magnetostatic potential given by²²

$$U(\mathbf{r}) = -\int \frac{\nabla' \cdot \mathbf{M}(\mathbf{r}')}{|\mathbf{r} - \mathbf{r}'|} d\mathbf{r}' + \int \frac{\mathbf{n} \cdot \mathbf{M}(\mathbf{r}')}{|\mathbf{r} - \mathbf{r}'|} dS' , \quad (2.9.11)$$

where ∇' contains derivatives with respect to the components of \mathbf{r}' . The factor of $\frac{1}{2}$ in Equation 2.9.10 ensures that the interaction between any two moments does not contribute to the magnetostatic energy twice. Mathematical comparison with electrostatics allows Equation 2.9.11 to be interpreted in terms of bound magnetic charges. The first term can be interpreted as a contribution to the potential due to a volume charge density $-\nabla \cdot \mathbf{M}$, while the second term is a contribution due to a surface charge density $\mathbf{n} \cdot \mathbf{M}$ where \mathbf{n} is a surface normal vector.

In a sufficiently large external magnetic field, the magnetisation is uniform and the volume term in Equation 2.9.11 vanishes since $\nabla \cdot \mathbf{M} = 0$. The demagnetising field is then

$$\mathbf{H}_d = -\nabla U(\mathbf{r}) = -\mathbf{M} \nabla \int \frac{\mathbf{n}}{|\mathbf{r} - \mathbf{r}'|} dS' , \quad (2.9.12)$$

which is linear in the components of \mathbf{M} . Furthermore, from Equations 2.9.10 and 2.9.12 it can be seen that the magnetostatic energy of a uniformly magnetised material is quadratic in the components of \mathbf{M} . The demagnetising field is often written as

$$\mathbf{H}_d = -\tilde{\mathbf{N}}(\mathbf{r})\mathbf{M} , \quad (2.9.13)$$

where $\tilde{N}(\mathbf{r})$ is the demagnetising tensor. By inspection of Equations 2.9.12 and 2.9.13, it can be seen that the components of the demagnetising tensor can be evaluated using

$$\tilde{N}(\mathbf{r}) = \nabla \int \frac{\mathbf{n}}{|\mathbf{r} - \mathbf{r}'|} dS', \quad (2.9.14)$$

so that the demagnetising factors of a ferromagnetic sample depend only on the shape of the sample. The magnetic field within a ferromagnetic sample (internal field) \mathbf{H}_{int} is different to the applied external field due to the demagnetising field. The internal field is given by

$$\mathbf{H}_{int} = \mathbf{H} - \tilde{N}(\mathbf{r})\mathbf{M}, \quad (2.9.15)$$

where the internal field is representative of the material parameters since shape effects are accounted for by the demagnetising factors.

The strength of the magnetostatic interaction is several orders of magnitude weaker than that of the exchange interaction (Section 2.7). However, the exchange interaction is short range and isotropic^{13,22}, while the magnetostatic interaction is long range and sensitive to the shape of a sample. Therefore, the magnetostatic energy is an important contribution to the total free energy. Minimising the magnetostatic energy gives rise to anisotropic effects in which the magnetisation prefers to align along a particular axis of a ferromagnetic sample. Ferromagnetic domains may also develop in order to minimise the magnetostatic energy further.

Magnetic anisotropy

In the context of ferromagnetism, anisotropy is described as the work required to magnetise a sample along a particular direction relative to an easy axis of magnetisation¹³. There are several different types of magnetic anisotropy that may contribute to w_{ani} in Equation 2.9.3 which include magnetostatic shape anisotropy, magnetocrystalline anisotropy, and surface anisotropy. Here I will outline the form of magnetic anisotropies that are relevant to this thesis.

Shape anisotropy energy

The preference for the magnetisation to be oriented along a particular axis of a sample so that the magnetostatic energy can be minimised is called shape anisotropy. An ellipsoid shaped sample (Figure 2.9.2) is a special case since it is the only geometry for which both the magnetisation and the demagnetising field are uniform^{13,22}. The demagnetising factors of an ellipsoid are constants that depend upon its dimensions^{13,24}, where $N_x \neq N_y = N_z$. The demagnetising field is therefore different for different orientations of the magnetisation. As a result, the magnetostatic (or shape anisotropy) energy is only minimised when the magnetisation lies along the major axis of the ellipsoid. Therefore, the ellipsoid is said to have uniaxial shape anisotropy and the major axis of the ellipsoid is called the easy-axis of magnetisation.

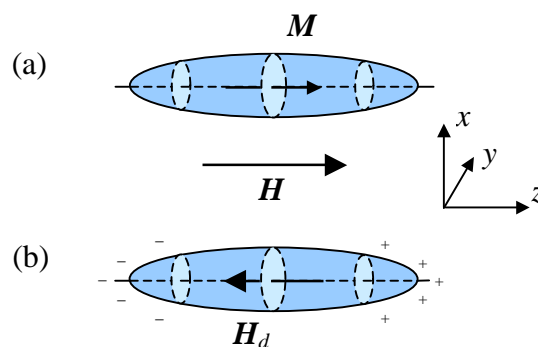


Figure 2.9.2 An ellipsoidal particle with uniform magnetisation \mathbf{M} in an external magnetic field \mathbf{H} is shown in (a). The picture of magnetic surface charge that arises from the comparison of equations for the magnetostatic and electrostatic potentials is shown in (b). The ellipsoid is a special case since it is the only geometry for which the magnetisation and the demagnetising field \mathbf{H}_d are both uniform.

Experimental samples are rarely ellipsoids. A thin film can be considered as a limiting case of an ellipsoid where the z - and y -dimensions are a few orders of magnitude greater than the x -dimension or thickness. The out-of-plane demagnetising factor N_x is then 4π and the two in-plane demagnetising factors N_y and N_z are effectively zero. In that case, using Equation 2.9.10 the shape anisotropy energy per unit volume is

$$w_{ms} = 2\pi M_s^2 (\mathbf{u} \cdot \mathbf{n})^2, \quad (2.9.16)$$

and is minimised when the magnetisation $\mathbf{M} = M_s \mathbf{u}$ lies in the plane of the film. Such a plane is often called an easy-plane of magnetisation, while the out-of-plane direction is referred to as a hard-axis.

The experiments presented in this thesis were performed on non-ellipsoidal ferromagnetic elements. In non-ellipsoidal samples the demagnetising field and magnetisation are non-uniform. While magnetostatic shape anisotropy effects exist for these samples, it is much more complicated than in the case of the thin film for which the demagnetising field and magnetisation are uniform.

Magnetocrystalline anisotropy

The preference for the magnetisation to be oriented along particular crystallographic axes of a sample is called magnetocrystalline anisotropy. The origin of magnetocrystalline anisotropy is the spin-orbit interaction²⁵. In the absence of the spin-orbit interaction the energy of the electron spin system is $\propto \mathbf{S}_i \cdot \mathbf{S}_j$ (Equation 2.9.5) and independent of the direction of the magnetisation. When the spin-orbit interaction is present, a small orbital moment is induced which couples the total (spin + orbital) moment to the crystal axes. As a result, the energy depends on the direction of the magnetisation relative to the crystal axes, and the energy reflects the symmetry of the crystal structure.

For hexagonal crystals, *e.g.* Co at room temperature, the magnetocrystalline anisotropy energy per unit volume w_{mc} may be written as²²

$$w_{mc} = -K_1 \cos^2 \theta + K_2 \cos^4 \theta = -K_1 u_z^2 + K_2 u_z^4, \quad (2.9.17)$$

where z is parallel to the c -axis of the hexagonal crystal lattice and θ is the angle between the magnetisation and the c -axis. The anisotropy constants K_1 and K_2 are temperature dependent and are determined experimentally. It is often found that $|K_2| \ll |K_1|$ so that the higher order term in Equation 2.9.17 may be neglected. The magnetocrystalline anisotropy energy for hexagonal crystals depends only on θ , so that for materials with $K_1 > 0$, the c -axis is the easy axis and the anisotropy is described as uniaxial.

For cubic crystals, *e.g.* Fe and Ni the magnetocrystalline anisotropy energy per unit volume w_{mc} may be written as²²

$$w_{mc} = K_1(u_x^2 u_y^2 + u_y^2 u_z^2 + u_z^2 u_x^2) + K_2 u_x^2 u_y^2 u_z^2, \quad (2.9.18)$$

where u_i ($i = x, y, z$) are the components of the unit vector of the magnetisation along the x , y , and z -directions which are defined along the crystallographic axes. Again, the anisotropy constants K_1 and K_2 are temperature dependent and are determined experimentally. For materials with $K_1 > 0$, *e.g.* Fe, the easy axes are along crystallographic axes²² [100], [010] and [001], while the body diagonals, *e.g.* [111], are hard axes²⁶. For materials with $K_1 < 0$, *e.g.* Ni, the easy axes are along the body diagonals²².

Surface anisotropy

At the surface of a ferromagnetic sample the symmetry of the material is reduced. A magnetic moment of the surface layer of atoms has nearest neighbour moments within the layer and within the next layer of the material. However, outside the material, the moment does not have any nearest neighbours. Therefore, the exchange energy of the interaction between the moment and its nearest neighbours cannot be the same as in the bulk of the material. The surface anisotropy energy should then represent the tendency for surface moments to align either parallel or perpendicular to the surface of the material. The surface anisotropy energy per unit area may then be written as²²

$$w_s = \frac{1}{2} K_s (\mathbf{u} \cdot \mathbf{n})^2, \quad (2.9.19)$$

where K_s is the surface anisotropy constant and is determined experimentally. The total surface anisotropy energy is then obtained by integrating over the surface of the ferromagnetic sample. The uniaxial shape anisotropy and the surface anisotropy can often be difficult to distinguish²⁷. Since the form of these anisotropy energy contributions are the same, we can define an effective shape anisotropy for thin films that accounts for the surface anisotropy²⁷

$$w_{eff} = 2\pi M_{eff}^2 (\mathbf{u} \cdot \mathbf{n})^2. \quad (2.9.20)$$

2.10 The magnetisation of a ferromagnetic material

Ferromagnetic domains

A suitably prepared ferromagnetic sample may exhibit a magnetisation ranging from zero (in the absence of an external magnetic field) to a saturation value of $\sim 10^3 \text{ emu}\cdot\text{cm}^{-3}$ when an external magnetic field of $\sim 10 \text{ Oe}$ is applied²⁶. Such behaviour is fundamentally different to that of paramagnetic materials, for which an external field of $\sim 10 \text{ Oe}$ has a negligible effect on the magnetisation of a system of non-interacting atomic moments. Figure 2.10.1(a) shows a typical magnetisation curve OA and hysteresis loop $ABCDEFA$ for a ferromagnetic material. At point O on the magnetisation curve in Figure 2.10.1(a) the sample is described as demagnetised in which case the ferromagnetic domains are configured so that the net magnetisation is zero. Figure 2.10.1(b) and (c) show hypothetical domain configurations of a demagnetised single crystal and polycrystalline material respectively. When a sufficiently large magnetic field is applied, saturation of the magnetisation occurs for which all atomic moments align in the same direction as the applied field (point A on curve OA in Figure 2.10.1). When the field is reduced the variation of the magnetisation may not follow the reverse of curve OA due to irreversible magnetisation processes. Instead the magnetisation typically follows curve AB . At point B the external field is zero and the sample possesses a non-zero, or remanent magnetisation M_r . When the field is reversed and increased in the opposite direction, the magnetisation decreases and becomes zero at point C . The external field at point C is called the coercive field H_c . As the field is increased further the sample becomes magnetised again with a net magnetisation in the opposite direction to that at point A . At point D the field is sufficiently large to saturate the magnetisation. The demagnetising/magnetising processes along the curve $ABCD$ are repeated for curve $DEFA$. At point O on the magnetisation curve in Figure 2.10.1(a) the domains are configured so that the net magnetisation is zero and the sample may be described as demagnetised. Figure 2.10.1(b) and (c) show hypothetical domain configurations of a demagnetised single crystal and polycrystalline material respectively. The domain configuration shown for a single crystal in Figure 2.10.1(b) can also be achieved in

polycrystalline thin film square elements of $\text{Ni}_{81}\text{Fe}_{19}$ (Permalloy) with microscale lateral dimensions^{28,29}. Such a domain configuration is called a Landau flux closure state, which is stabilised as a result of the minimised magnetostatic energy. The Landau state is achieved by applying an alternating external field with an amplitude that slowly decreases to zero.

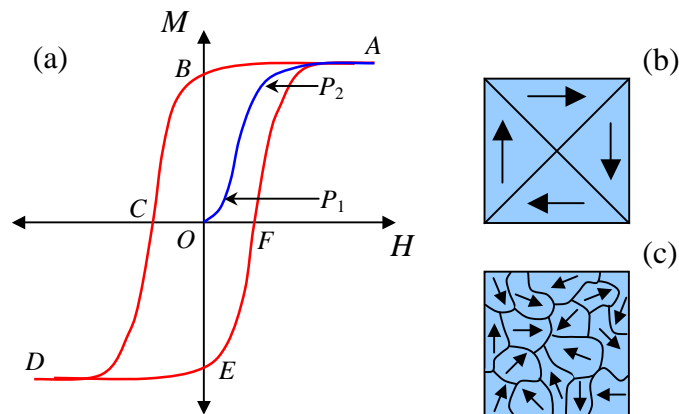


Figure 2.10.1 A typical magnetisation curve OA and hysteresis loop $ABCDEF$ for a ferromagnetic material is shown in (a) where P_1 and P_2 on curve OA represent points at which transitions in the magnetisation processes occur. At point O ferromagnetic domains in a single crystal (b) and a polycrystalline material (c) are configured so that the net magnetisation is zero. For clarity in (c) each crystallite has been drawn as a single domain. However, in general each crystallite will have a multi-domain structure.

In 1907 Weiss¹⁵ introduced the concept of ferromagnetic domains in order to describe the behaviour of the magnetisation when the external field was swept. Within each domain the local magnetisation is saturated, while the magnetisation of neighbouring domains is not necessarily aligned. Between neighbouring domains are narrow boundaries called domain walls. Across the width of the domain wall the atomic moments gradually rotate from the orientation of the magnetisation in one domain to that of the adjacent domain. Figure 2.10.2 shows a Bloch wall in a thin film as an example. Within the Bloch wall the atomic moments rotate out of the xy -plane which results in the accumulation of magnetic surface charge. In bulk material the surface charge has little effect on the magnetostatic energy¹³. However, in thin films the magnetostatic energy may no longer be minimised due to the strong demagnetising field resulting from the close proximity of opposite surface charge on either side of the film.

Therefore, in thin films a Néel wall may form in which the atomic moments remain in the xy -plane as they rotate within the wall. As a result there is no accumulation of surface charge and the magnetostatic energy may be minimised further.

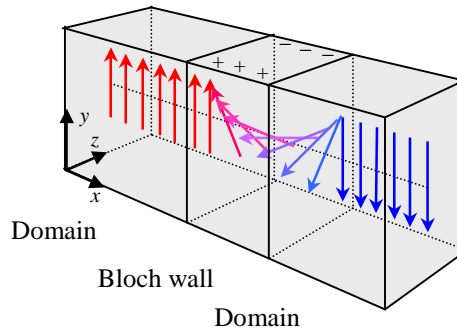


Figure 2.10.2 A Bloch wall between two neighbouring ferromagnetic domains of a thin film. The film plane is in the xy -plane. Across the width of the wall the atomic moments gradually rotate from the orientation of the magnetisation in one domain to that of the adjacent domain. Within the Bloch wall the magnetisation rotates out-of-plane which results in the accumulation of magnetic charge on the surface of the sample.

If domain walls were not present the angle between interfacial atomic moments of adjacent domains would be 180° and the exchange energy would not be minimised. Domain walls act to allow the rotation of the magnetisation between two adjacent domains without a significant exchange energy penalty. This process can be understood in terms of the exchange energy density (Equation 2.9.6) for a chain of $N + 1$ atomic moments

$$w_{ex} = J_{ex} S^2 \left(\frac{\pi}{N} \right)^2, \quad (2.10.1)$$

where the small angle between adjacent atomic moments is π/N . The exchange energy of the chain of atomic moments is then

$$w_{ex} = \frac{1}{N} J_{ex} S^2 \pi^2, \quad (2.10.2)$$

which is inversely proportional to N , or equivalently, to the width of the wall. It appears that the exchange energy can be minimised by increasing the width of a domain wall.

However, the width Δ of the domain wall is dictated by the competition between the exchange and anisotropy energies of the wall, where

$$\Delta \sim \sqrt{A_{ex}/K_u}, \quad (2.10.3)$$

for the case of uniaxial anisotropy. In Reference 30 an estimate of these energy coefficients yields a Bloch wall width in Fe of ~ 10 nm.

The origin of ferromagnetic domains

The origin of ferromagnetic domains can be understood qualitatively by considering the magnetostatic, exchange, and anisotropy energy contributions to the total free energy. In Figure 2.10.3 cross sections of a single crystal sample are shown for four different hypothetical domain configurations. In Figure 2.10.3(a) the magnetisation is saturated and the sample possesses a single domain. In this configuration the exchange energy is minimised since all atomic moments are aligned with the same direction. However, the magnetostatic energy is large as a result of the

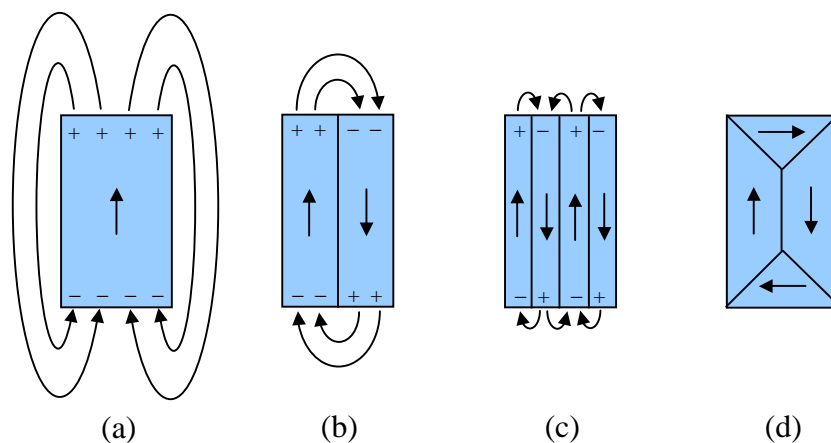


Figure 2.10.3 The origin of ferromagnetic domains, reproduced from Reference 26. In (a) the magnetisation is saturated so the exchange energy is minimised, while the magnetostatic energy is large due to magnetic surface charge. The formation of domains in (b) and (c) to reduce the magnetostatic energy is limited by the increase in the exchange energy to form additional domain walls. Closure domains in (d) act to minimise the magnetostatic energy by eliminating magnetic surface charge.

magnetic charge present on the surface of the sample. The magnetostatic energy is reduced in Figure 2.10.3(b) by the formation of two domains with opposite magnetisation. However the exchange energy is elevated since the magnetisation is non-uniform within the domain wall. To reduce the magnetostatic energy further more domains may form, as in Figure 2.10.3(c). The subsequent formation of domains to reduce the magnetostatic energy is limited by the increase in the exchange energy to form additional domain walls. The process may continue until the increase in the exchange (or domain wall) energy exceeds the reduction of the magnetostatic energy. It is possible to reduce the magnetostatic energy further by the formation of closure domains, as shown in Figure 2.10.3(d), in which case the magnetic surface charge is eliminated.

Magnetisation processes

When an external magnetic field is applied the domain configuration will change so that there is a net magnetisation parallel to the applied field. Figure 2.10.4 shows hypothetical magnetisation processes for the demagnetised sample shown in Figure 2.10.1(b). In Figure 2.10.4(b) the domains with energetically favourable orientation of the magnetisation grow at the expense of those with unfavourable orientations of the magnetisation. In Figure 2.10.4(c) the magnetisation of individual domains rotate to align with the applied field. In both cases the component of the net magnetisation parallel to the applied field increases, which reduces the Zeeman energy

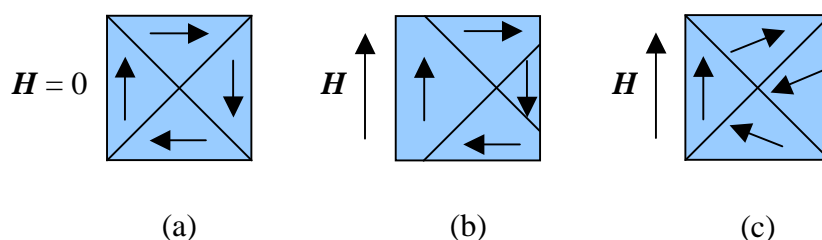


Figure 2.10.4 Hypothetical magnetisation processes, reproduced from Reference 26. In (a) the sample is demagnetised in the absence of the external field. In (b) the sample is magnetised by growth of domains with \mathbf{M} parallel to \mathbf{H} corresponding to movement of the domain walls. In (c) the sample is magnetised by a rotation of the magnetisation of individual domains.

contribution to the total free energy. When the external field is weak the magnetisation process is dominated by reversible domain wall motion, while in strong fields the process is dominated by magnetisation rotation²⁶. For intermediate field strengths (between points P_1 and P_2 on curve OA in Figure 2.10.1) irreversible domain wall motion occurs.

Non-uniform single domains

The transition of a sample from a multi-domain to a single domain configuration was first established by Kittel³¹. The transition was calculated by comparing the magnetostatic energy of a uniformly magnetised, single domain sample to the domain wall energy of a multi-domain configuration. Below critical dimensions, the atomic moments align in the same direction so that the exchange energy is minimised. The result is a stable single domain state. In Section 2.9 it was shown that the ellipsoid was the only sample geometry for which the magnetisation and demagnetising field are both uniform. In general the magnetisation of a single domain sample is non-uniform³². In non-ellipsoidal samples, the magnetisation tends to become non-uniform so that the magnetostatic energy can be reduced with only a minimum increase in the exchange energy. Figure 2.10.5 shows the most common single domain states of non-ellipsoidal samples.

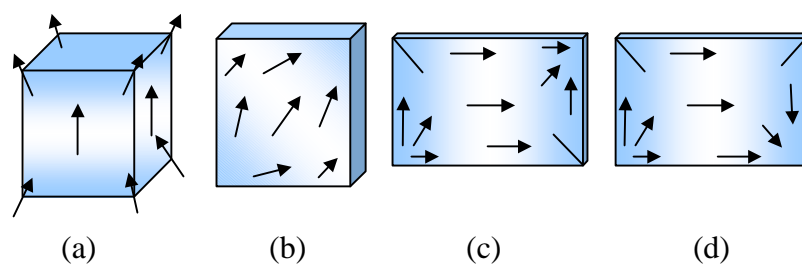


Figure 2.10.5 Non-uniform, single domain magnetisation configurations are shown for four non-ellipsoidal samples. The magnetisation configurations are described as (a) the X- or flower-state, (b) the leaf-state, (c) the S-state, and (d) the C-state. Reproduced from Reference 32.

2.11 The Stoner-Wohlfarth model

The Stoner-Wohlfarth model³³ can be used to calculate the hysteresis loops expected from a single domain ellipsoid by minimising the total free energy of the system. In the model the ellipsoid is assumed to have uniform magnetisation and uniaxial shape anisotropy with an easy axis along the major axis of the ellipsoid. Furthermore, the exchange energy is assumed to be constant and can therefore be omitted. The total free energy density is then given by

$$W = -\mathbf{M} \cdot \mathbf{H} - K_u (\mathbf{u} \cdot \hat{\mathbf{k}})^2, \quad (2.11.1)$$

where $\mathbf{u} = \mathbf{M}/M_s$ and $\hat{\mathbf{k}}$ is a unit vector along the direction of the easy axis of magnetisation, Figure 2.11.1.

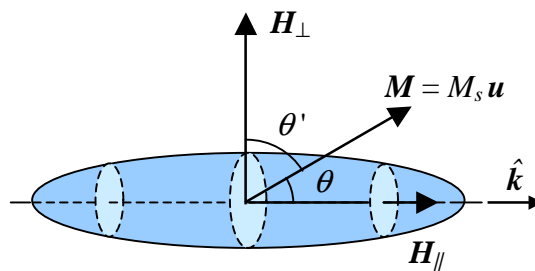


Figure 2.11.1 A single domain ellipsoid with uniform magnetisation \mathbf{M} and uniaxial shape anisotropy. The easy axis of magnetisation is along the direction of the unit vector $\hat{\mathbf{k}}$.

Stable magnetisation states can be calculated by minimising the free energy density with respect to the orientation of the magnetisation relative to the applied field. Calculating the stable states when the field is applied parallel and perpendicular to the easy axis allows the easy and hard axis hysteresis loops to be obtained respectively. In the first case where \mathbf{H} is parallel to $\hat{\mathbf{k}}$ an angle θ is defined between \mathbf{u} and \mathbf{H} (Figure 2.11.1). The total energy density is then written as

$$W = -M_s H \cos \theta - K_u \cos^2 \theta, \quad (2.11.1)$$

where stable magnetisation states can be found by minimising the energy density with respect to θ where

$$\frac{\partial W}{\partial \theta} = M_s H \sin \theta + 2K_u \sin \theta \cos \theta = 0, \quad (2.11.2)$$

and

$$\frac{\partial^2 W}{\partial \theta^2} > 0. \quad (2.11.3)$$

In the Stoner-Wohlfarth model it is assumed that the atomic moments rotate coherently as a single spin or macrospin. It is also assumed that the macrospin rotates in a plane containing the easy axis.

In the second case when \mathbf{H} is perpendicular to \mathbf{k} an angle θ' is defined between \mathbf{u} and \mathbf{H} (Figure 2.11.1). Similarly, the total energy density is then written as

$$W = -M_s H \cos \theta' - K_u \sin^2 \theta', \quad (2.11.4)$$

for which

$$\frac{\partial W}{\partial \theta'} = M_s H \sin \theta' - 2K_u \sin \theta' \cos \theta' = 0, \quad (2.11.5)$$

and

$$\frac{\partial^2 W}{\partial \theta'^2} > 0. \quad (2.11.6)$$

The solutions to Equations 2.11.2 and 2.11.5 are summarised in Table 2.11.1.

$\mathbf{H} \parallel \hat{\mathbf{k}}$	$\mathbf{H} \perp \hat{\mathbf{k}}$
$\sin \theta = 0 \Rightarrow \theta = n\pi$	$\sin \theta' = 0 \Rightarrow \theta' = n\pi$
$\cos \theta = -\frac{M_s H}{2K_u}$	$\cos \theta' = \frac{M_s H}{2K_u}$

Table 2.11.1 Solutions to Equations 2.11.2, and 2.11.5, where n is an integer.

From Figure 2.11.1 the component of the magnetisation along the direction of the applied field when \mathbf{H} is parallel to $\hat{\mathbf{k}}$ is

$$M = M_s \cos \theta, \quad (2.11.7)$$

and

$$M = M_s \cos \theta', \quad (2.11.8)$$

when \mathbf{H} is perpendicular to $\hat{\mathbf{k}}$. By using the solutions in Table 2.11.1, Equations 2.11.7 and 2.11.8, and observing the conditions in Equations 2.11.3 and 2.11.6, the component of the magnetisation parallel to the applied field can be determined. The components of the magnetisation parallel to the applied field are summarised in Table 2.11.2 along with the corresponding field ranges for which the direction of the magnetisation minimises the free energy. The corresponding hysteresis loops are shown in Figure 2.11.2.

When the angle between the magnetisation and the applied field is 90° , the magnetisation state is unstable. In the case when \mathbf{H} is parallel to $\hat{\mathbf{k}}$, experimental hysteresis loops do not follow the predicted behaviour of $M \propto -H$ (shown by the dashed line in Figure 2.11.2(a)) for $-2K_u/M_s < H < 2K_u/M_s$. Instead a system with a

$\mathbf{H} \parallel \hat{\mathbf{k}}$		$\mathbf{H} \perp \hat{\mathbf{k}}$	
M	H	M	H
$+M_s$	$H > \frac{2K_u}{M_s}$	$+M_s$	$H > \frac{2K_u}{M_s}$
$-M_s$	$H < \frac{2K_u}{M_s}$	$-M_s$	$H < -\frac{2K_u}{M_s}$
$-\frac{M_s^2 H}{2K_u} \propto -H$	$-\frac{2K_u}{M_s} < H < \frac{2K_u}{M_s}$	$\frac{M_s^2 H}{2K_u} \propto H$	$-\frac{2K_u}{M_s} < H < \frac{2K_u}{M_s}$

Table 2.11.2 Components of the magnetisation parallel to the applied field \mathbf{H} for the cases when \mathbf{H} is applied parallel ($\mathbf{H} \parallel \hat{\mathbf{k}}$) and perpendicular ($\mathbf{H} \perp \hat{\mathbf{k}}$) to the direction of the easy axis $\hat{\mathbf{k}}$. For each case the component of the magnetisation parallel to \mathbf{H} is shown along with the corresponding field ranges for which the direction of the magnetisation minimises the free energy.

magnetisation $+M$ at $H = -2K_u/M_s$ (corresponding to $\theta = 0$) decays into the stable magnetisation state $-M$ at $H = -2K_u/M_s$ (corresponding to $\theta = \pi$). That is, when the applied field is reversed, the original direction of the magnetisation $+M$ no longer minimises the free energy, Figure 2.11.3. The energy of the magnetisation state $+M$ increases and no longer represents a local energy minimum. Experimentally, statistical fluctuations due to thermal agitation of atomic moments may initiate rotation of the magnetisation from the original state $+M$ to the new state $-M$ allowing the free energy to be minimised.

It is clear from the previous discussion and Figure 2.11.2(a) that when $H = 0$ the magnetisation can be in one of two stable remanent states parallel to the easy axis, for which the magnetostatic energy is minimised. In the case when \mathbf{H} is perpendicular to $\hat{\mathbf{k}}$ the component of the remanent magnetisation parallel to the field direction is initially zero. When the field is increased the magnetisation is rotated out of the stable remanent state and $M \propto H$. At a sufficiently high field the magnetisation saturates ($M = M_s$) in accordance with $\sin\theta' = 0$ so that the magnetisation is parallel to the applied field and the Zeeman energy is minimised.

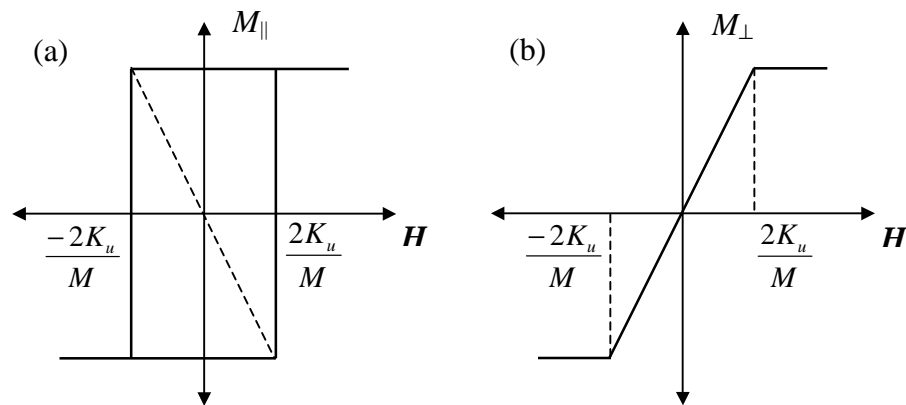


Figure 2.11.2 Hysteresis loops derived using the Stoner-Wohlfarth model. When the field \mathbf{H} is applied along the easy axis direction $\hat{\mathbf{k}}$, the component of magnetisation parallel to \mathbf{H} follows the square loop shape shown in (a) and is typical of an easy axis. When \mathbf{H} is applied perpendicular to $\hat{\mathbf{k}}$, the component of the magnetisation parallel to \mathbf{H} follows the S-loop shape shown in (b) and is typical of a hard axis.

Hysteresis loops obtained experimentally from continuous thin films can be approximately modelled using the Stoner-Wohlfarth model. However, for small non-ellipsoidal samples, such as those measured in experiments presented in this thesis, the demagnetising field and magnetisation are non-uniform. As a result the magnetisation does not rotate coherently as a macrospin when the applied magnetic field is reversed. Instead, the magnetisation may occupy a series of non-uniform single domain states, similar to those shown in Figure 2.10.5 as the field is reversed. This leads to significant deviation of the hysteresis loop shape from those predicted by the Stoner-Wohlfarth model, and those obtained in measurements on the continuous film of the same material. Hysteresis loops measured from arrays of square nanomagnets will be presented and discussed in Chapter 4.

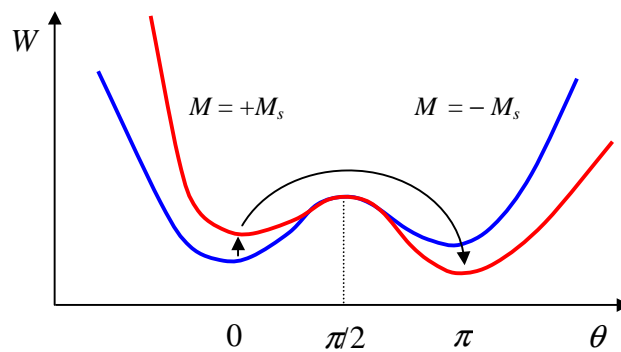


Figure 2.11.3 When the magnetic field is reversed, the energy of the initial magnetisation state $+M_s$ at $\theta = 0$ is raised in energy. The magnetisation rotates from the original state $+M$ to the new state $-M_s$ at $\theta = \pi$ which allows the free energy to be minimised.

2.12 Ferromagnetic resonance

In the remaining sections of this chapter the precessional magnetisation dynamics of ferromagnetic materials will be introduced and discussed. For simplicity it will be assumed that the sample is magnetised to saturation by a sufficiently large static magnetic field so that the sample possesses a single domain. Equilibrium is achieved when all magnetic moments align with the static field. However, as shown in Section 2.3, atomic moments in an external field are not rigidly aligned along the field direction, but instead precess about the equilibrium orientation with frequency ω_H . In

fact the equilibrium orientation is the direction of an effective field \mathbf{H}_{eff} , which includes the static field \mathbf{H} , demagnetising field \mathbf{H}_D , and anisotropy field \mathbf{H}_K contributions. In ferromagnetic materials the atomic moments tend to precess coherently as a result of the exchange interaction between neighbouring moments. Therefore, in some cases, *e.g.* in continuous thin films, it is sufficient to consider the dynamics of a single macrospin. Resonance of the magnetisation precession can be achieved by applying a microwave field of frequency ω_H in a direction perpendicular to the static field. The phenomenon is known as ferromagnetic resonance (FMR) and is commonly used to investigate the dynamic properties of ferromagnetic materials. Measurement of the microwave power absorbed as a function of either microwave frequency or static field allows the resonant magnetic modes of the material to be identified.

FMR can also be considered in terms of the quantisation of the total spin angular momentum. The reversal of a single electron spin corresponds to the smallest possible change in angular momentum. The energy difference between the two states is $g|\mu_B|H_{eff}$ (Figure 2.4.2). Energy will then be absorbed at a frequency ω_H described by

$$\hbar\omega_H = g|\mu_B|H_{eff}. \quad (2.12.1)$$

2.13 The magnetic equation of motion

The precessional magnetisation dynamics in a ferromagnetic crystal can be described by the Landau-Lifshitz equation of motion³⁴. When the magnetisation is in equilibrium, the variation δ of the free energy with the magnetisation must be zero

$$\delta \int_V W(\mathbf{M}, \mathbf{M}') dV = 0, \quad (2.13.1)$$

where W is the free energy of the system per unit volume, and $\mathbf{M}' = \partial\mathbf{M}/\partial x$. The calculus of variations leads to the expression

$$\int_V \mathbf{H}_{eff}(\mathbf{M}) \delta\mathbf{M} dV = 0, \quad (2.13.2)$$

where any variation in the magnetisation $\delta\mathbf{M}$ is perpendicular to the magnetisation \mathbf{M} such that the absolute value of \mathbf{M} is constant. Therefore $\mathbf{H}_{eff}(\mathbf{M})$ is parallel to \mathbf{M} , and is

the effective magnetic field. For the magnitude of \mathbf{M} to remain constant, any change in the magnetisation with time should be of the form

$$\frac{d\mathbf{M}}{dt} = -\gamma [\mathbf{M} \times \mathbf{H}_{eff}] + \mathbf{R}, \quad (2.13.3)$$

where $\gamma = e/mc$ is the magneto-mechanical ratio, and \mathbf{R} is a phenomenological relaxation term directed from \mathbf{M} to \mathbf{H}_{eff} , Figure 2.13.1. Equation 2.13.3 is known as the Landau-Lifshitz equation of motion and is used to describe the precessional dynamics of the magnetisation in a ferromagnetic material. Many of the magnetic properties of the material enter the equation of motion via the effective field.

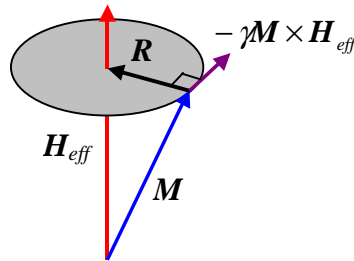


Figure 2.13.1. A schematic representation of the precession of the magnetisation \mathbf{M} about the effective magnetic field \mathbf{H}_{eff} . A phenomenological restoring force \mathbf{R} acts to align \mathbf{M} with \mathbf{H}_{eff} and return the system to equilibrium.

The influence of a restoring force \mathbf{R} (Figure 2.13.1) acts to align \mathbf{M} with \mathbf{H}_{eff} and return the system to equilibrium. When the magnitude of the magnetisation is conserved, two phenomenological relaxation terms may be employed, the Landau-Lifshitz relaxation term³⁴

$$\mathbf{R}_{LL} = -\frac{\lambda}{M^2} [\mathbf{M} \times [\mathbf{M} \times \mathbf{H}_{eff}]], \quad (2.13.4)$$

or the Gilbert relaxation term³⁵

$$\mathbf{R}_G = -\frac{\alpha}{M} \left[\mathbf{M} \times \frac{\partial \mathbf{M}}{\partial t} \right], \quad (2.13.5)$$

where λ and α are the Landau-Lifshitz and Gilbert damping constants respectively.

Macroscopic equations of motion for the magnetisation can also be derived quantum mechanically. The equations of motion are derived from the commutator of the spin angular momentum and the spin Hamiltonian¹³, which includes Zeeman, magnetostatic, anisotropy and exchange energy contributions. From a postulate of quantum mechanics, the commutation of the angular momentum \mathbf{G} (where $\boldsymbol{\mu} = -(g|e|/2m_e c) \mathbf{G} = -|\gamma| \mathbf{G}$) with the spin-Hamiltonian \hat{H} in $[\hat{H}, \mathbf{G}]$, is given by¹³

$$\hat{H}\mathbf{G} - \mathbf{G}\hat{H} = -i\hbar \frac{d\mathbf{G}}{dt}, \quad (2.13.6)$$

where $\hat{H} = -\boldsymbol{\mu} \cdot \mathbf{H} = |\gamma| \mathbf{G} \cdot \mathbf{H}$ which gives

$$(\mathbf{G} \cdot \mathbf{H}) \mathbf{G} - \mathbf{G}(\mathbf{G} \cdot \mathbf{H}) = -\frac{i\hbar}{|\gamma|} \frac{d\mathbf{G}}{dt}. \quad (2.13.7)$$

For the x -component only,

$$(G_y H_z - G_z H_y) = -\frac{1}{|\gamma|} \frac{dG_x}{dt} \quad (2.13.8)$$

is obtained from Equation 2.13.7, since the commutation relationships for G_x , G_y , and G_z are $[G_x, G_x] = 0$, $[G_z, G_x] = i\hbar G_y$ and $[G_x, G_y] = i\hbar G_z$. Similar results are obtained for the y - and z -components, hence from Equation 2.13.8 the classical equation of motion for a single spin is

$$\frac{d\mathbf{G}}{dt} = -|\gamma| \mathbf{G} \times \mathbf{H}. \quad (2.13.9)$$

2.14 The Kittel formula

The Kittel formula is used to calculate the frequency of the uniform mode of magnetisation precession accounting for the various contributions to the effective field. When the static magnetisation is saturated and uniform, the calculation of the resonant (uniform) mode is straightforward. When the magnetisation is not saturated the static

magnetisation will become non-uniform and the effective field will contain a contribution from the exchange interaction. In this case the resonant magnetic modes are more difficult to calculate since the phase of the magnetisation precession is different in different regions of the material. The non-uniform resonant modes are made up of different Fourier components or spin-waves, which will be discussed in the next section of this chapter.

For a uniformly magnetised (single domain) ellipsoid (Figure 2.9.2), the effective field can be written as

$$\mathbf{H}_{eff} = \mathbf{H} + \mathbf{H}_1(t) - \tilde{\mathbf{N}} \cdot \mathbf{M} + \mathbf{H}_K, \quad (2.14.1)$$

where \mathbf{H} is the external-static field applied along the z -axis ($\mathbf{H} = H_z \mathbf{z}$), $\mathbf{H}_1(t)$ is an external-alternating field, $\tilde{\mathbf{N}} \cdot \mathbf{M}$ is the demagnetising field, and \mathbf{H}_K represents any anisotropy fields. In order to obtain a general expression for the resonance frequency the anisotropy field can be represented in terms of an effective demagnetising tensor³⁶ $\tilde{\mathbf{N}}_K$ so that

$$\mathbf{H}_K = -\tilde{\mathbf{N}}_K \cdot \mathbf{M}. \quad (2.14.2)$$

For simplicity the principle axes of the ellipsoid are chosen to coincide with the coordinate axes so that both $\tilde{\mathbf{N}}$ and $\tilde{\mathbf{N}}_K$ are diagonal. In FMR experiments the alternating field is usually applied in the xy -plane perpendicular to the static field. However, we will assume that the alternating field can be written as

$$\mathbf{H}_1(t) = H_{1x}(t)\mathbf{x} + H_{1y}(t)\mathbf{y} + H_{1z}(t)\mathbf{z}, \quad (2.14.2)$$

where $|\mathbf{H}_1(t)| \ll |\mathbf{H}|$ and that $\mathbf{H}_1(t) = \mathbf{H}_1 e^{i\omega t}$.

The magnetisation can be expressed as the sum of a static part \mathbf{M}_s and small alternating part $\mathbf{M}_1(t)$ where $|\mathbf{M}_1(t)| \ll |\mathbf{M}_s|$ and $\mathbf{M}_1(t) = \mathbf{M}_1 e^{i\omega t}$. The static component is assumed to lie parallel to \mathbf{H} with magnitude equal to the saturation magnetisation M_s so that $d\mathbf{M}_s/dt = -\gamma \mathbf{M}_s \times \mathbf{H} = 0$ if $H_1 \ll H$. The approximation that \mathbf{M}_s and \mathbf{H} are parallel is commonly assumed in FMR calculations and is justified if either (i) the shape and magneto-crystalline anisotropies are negligible ($H_K \ll H$), (ii) the easy axes of

these anisotropies are parallel to \mathbf{H} , or (iii) that \mathbf{H} is parallel to intermediate or hard axes, where $H \geq H_K$. We may then write the magnetisation as

$$\mathbf{M} = M_{1x}(t)\mathbf{x} + M_{1y}(t)\mathbf{y} + [M_s + M_{1z}(t)]\mathbf{z}. \quad (2.14.4)$$

Substitution of \mathbf{M} and \mathbf{H}_{eff} into Equation 2.13.3 and ignoring second order terms yields

$$\begin{aligned} \frac{d\mathbf{M}_1(t)}{dt} = -|\gamma| \left[\mathbf{M}_s \times \mathbf{H}_1(t) + \mathbf{M}_1(t) \times \mathbf{H} + M_s M_{1y}(t) (N_y + N_{Ky} - N_z - N_{Kz}) \mathbf{i} \right. \\ \left. - M_s M_{1x}(t) (N_x + N_{Kx} - N_z - N_{Kz}) \mathbf{j} \right]. \end{aligned} \quad (2.14.5)$$

The components of Equation 2.14.5 are then

$$\frac{i\omega M_{1x}(t)}{|\gamma|} = -M_{1y} [H + M_s (N_y + N_{Ky} - N_z - N_{Kz})] + M_s H_{1y}, \quad (2.14.6)$$

and

$$\frac{i\omega M_{1y}(t)}{|\gamma|} = M_{1x} [H + M_s (N_x + N_{Kx} - N_z - N_{Kz})] - M_s H_{1x}. \quad (2.14.7)$$

The component $dM_{1z}/dt = 0$ since $|\mathbf{M}_s|$ is constant. When $H_{1x} = H_{1y} = 0$, the solutions of M_{1x} and M_{1y} are non-trivial, which allows the resonant frequency to be calculated from the condition

$$\begin{vmatrix} \frac{i\omega_r}{|\gamma|} & -[H_r + M_s (N_y + N_{Ky} - N_z - N_{Kz})] \\ H_r + M_s (N_x + N_{Kx} - N_z - N_{Kz}) & \frac{i\omega_r}{|\gamma|} \end{vmatrix} = 0, \quad (2.14.8)$$

where ω_r is the resonance frequency and H_r is the corresponding resonance field. Solving for ω_r yields the Kittel formula,

$$\omega_r^2 = \gamma^2 [H_r + M_s (N_x + N_{Kx} - N_z - N_{Kz})] [H_r + M_s (N_y + N_{Ky} - N_z - N_{Kz})]. \quad (2.14.9)$$

As previously discussed, the ellipsoid can be used to model a thin film with demagnetising factors $N_x = 4\pi$, and $N_y = N_z = 0$. The effective anisotropy factors³⁶ are

$N_{Kx} = N_{Ky} = 2K_u/M_s^2$, and $N_{Kz} = 0$. The Kittel formula for a thin film with in-plane uniaxial anisotropy is then

$$\omega_r^2 = \gamma^2 \left(H_r + \frac{2K_u}{M_s} \right) \left(H_r + 4\pi M_s + \frac{2K_u}{M_s} \right), \quad (2.14.10)$$

when \mathbf{H} is applied parallel to the easy axis.

2.15 Magnetostatic spin wave modes

Long wavelength magnetostatic spin waves

The static magnetisation of small non-ellipsoidal samples is non-uniform. The corresponding non-uniform demagnetising field leads to a non-uniform total effective field within the sample. Therefore, atomic moments in different parts of the sample precess with different phase resulting in non-uniform dynamics of the magnetisation even if the applied excitation field is uniform throughout the sample. The variation of the phase of the precessional motion of atomic moments is illustrated in Figure 2.15.1 for a line of spins. A spin wave on a line of spins is formed from the successive advance in phase of the precessional motion of each spin along the line. When the

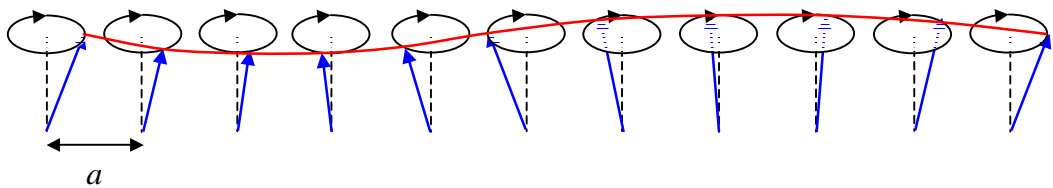


Figure 2.15.1 A spin wave on a line of spins is formed from the successive advance in phase of the precessional motion of each spin along the line. The advance in phase between each nearest neighbour is constant. Here the wavelength of the spin wave is $10a$, where a is the lattice parameter.

wavelength of the spin wave is much larger than the lattice parameter, and the advance in phase between each spin is constant, the exchange energy is negligible compared to the magnetostatic interaction. Since the spin wave is a result of the non-uniform demagnetising field, the wavelength of the spin wave is comparable to the dimensions of the sample. The spin waves also exhibit little or no propagation and are often called magnetostatic or Walker modes³⁷.

Backward volume and Damon-Eshbach magnetostatic modes

Damon and Eshbach were the first to study magnetostatic spin wave modes in a ferromagnetic slab³⁸. The sample magnetisation was assumed to consist of a static part along the z -direction and a small dynamic part, Equation 2.14.4. The total effective field was then the sum of the static field and a small dynamic demagnetising field resulting from the dynamic part of the magnetisation. The dispersion relations for the magnetostatic modes were obtained by solving the Landau-Lifshitz equation of motion (Equation 2.13.3) and the Maxwell equations applying appropriate boundary conditions. The dispersion relations are shown graphically in Figure 2.15.2.

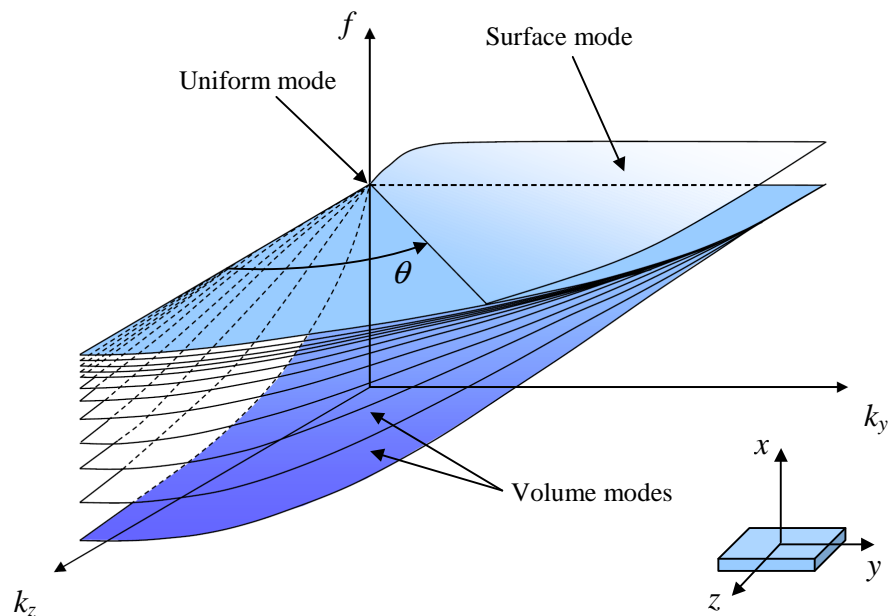


Figure 2.15.2 The Damon-Eshbach magnetostatic mode spectrum for a ferromagnetic slab magnetised along the z -direction, reproduced from Reference 38. Inset is the co-ordinate system used in the calculations.

The spectrum consists of a surface mode and a manifold of volume modes, all of which converge to the uniform mode when the wavevector is zero. The frequency of the magnetostatic modes varies continuously as the angle between the in-plane wavevector and the static magnetisation changes. When the wavevector is parallel to the magnetisation, only volume modes are excited with frequencies lower than that of the uniform mode. As the wavevector rotates through a critical angle θ from the magnetisation, a surface mode with frequency greater than that of the uniform mode appears. When the wavevector is perpendicular to the magnetisation, the volume modes become degenerate with the uniform mode.

The volume modes are often called backward volume (BV) magnetostatic modes. The modes are described as “backward” since they possess negative group velocity ($d\omega/dk_z < 0$). The spectrum of magnetostatic modes in an unbounded ferromagnetic medium is given by the Herring-Kittel formula³⁹

$$\left(\frac{\omega}{\gamma}\right)^2 = H_{eff} \left(H_{eff} + 4\pi M_s \sin^2 \theta_k \right), \quad (2.15.1)$$

where θ_k is the angle between the wavevector and the magnetisation and H_{eff} may contain the usual contributions, including exchange.

2.16 Spin wave modes in thin films

In a thin film of thickness d , the spin wave spectrum is modified since the translational symmetry is broken in the vicinity of the surfaces. The boundary conditions, *i.e.* two film surfaces in close proximity, lead to a quantised out-of-plane wave vector so that exchange spin wave modes become confined across the film thickness. Such modes are often called perpendicularly standing spin wave (PSSW) modes³⁹. The exchange interaction can be represented by an effective exchange field¹³

$$\mathbf{H}_{ex} = \frac{2A_{ex}}{M_s^2} \nabla^2 \mathbf{M}. \quad (2.16.1)$$

In the long wavelength limit $kd \ll 1$ and the spectrum of dipole-exchange spin waves in a thin film is then³⁹

$$\left(\frac{\omega}{\gamma}\right)^2 = \left(H + \frac{2A_{ex}}{M_s} k^2\right) \left(H + \frac{2A_{ex}}{M_s} k^2 + 4\pi M_s F_{pp}(k_{yz}d)\right), \quad (2.16.2)$$

where F_{pp} is the matrix element of the magnetostatic interaction, and

$$k^2 = k_y^2 + k_z^2 + \left(\frac{p\pi}{d}\right)^2 = K^2 + \left(\frac{p\pi}{d}\right)^2, \quad (2.16.3)$$

where p ($= 0, 1, 2, \dots$) is the number of half wavelengths of the PSSW mode within the film thickness d . When the exchange interaction is neglected the mode for which $p = 0$ has a dispersion relation similar to that of the magnetostatic Damon-Eshbach (DE) mode³⁹,

$$\left(\frac{\omega}{\gamma}\right)^2 = H(H + 4\pi M_s) + (2\pi M_s)^2 (1 - \exp(2Kd)). \quad (2.16.4)$$

The spin wave modes can then be categorised as two types of mode. For modes with $p = 0$ the mode is a magnetostatic DE mode, while for $p > 0$ the modes are PSSW modes.

2.17 Spin waves in small non-ellipsoidal elements

Recently attempts have been made to calculate the spin wave spectra of thin film non-ellipsoidal elements^{8,40}. Typically the elements have micrometer in-plane dimensions and a film thickness between 10 and 50 nm. At small element sizes the exchange interaction competes with the magnetostatic interaction, which leads to a non-uniform internal magnetic field within the elements. As a result the calculation of the spectra becomes a more difficult task. The problem can be simplified slightly by considering a wire element.

In Reference 40 the spin wave spectra of stripes (width $w = 1 \mu\text{m}$, length $l = 90 \mu\text{m}$, and thickness $d = 35 \text{ nm}$) were investigated experimentally using Brillouin Light Scattering³⁹ (BLS). The experiment was set up so that the external field, and hence the magnetisation, was either parallel or perpendicular to the long edge of the

wire (y -direction). In both cases the wavevector parallel to the short edge of the wire (z -direction) was detected. The measurement configurations were therefore described as the DE ($\mathbf{M} \perp \mathbf{k}$) and BV ($\mathbf{M} \parallel \mathbf{k}$) geometry respectively. Typical BLS spectra are shown in Figure 2.17.1(a). In the DE geometry, DE and PSSW modes were observed.

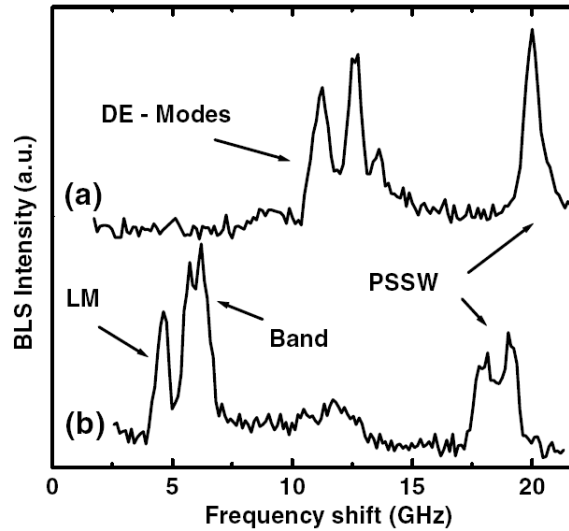


Figure 2.17.1 Taken from Reference 40. BLS spectra obtained on the stripe array for $K = 1 \times 10^5 \text{ cm}^{-1}$ at $H_e = 500 \text{ Oe}$ for (a) the DE geometry and (b) the BV geometry. LM indicates the localised mode.

In the BV geometry a dispersionless or localised mode (LM) was observed in addition to a band of unresolved modes and PSSW modes. To calculate the spin wave modes Equation 2.16.2 was used where the wavevector was given by

$$\mathbf{k} = \frac{p\pi}{d} \mathbf{x} + \mathbf{K} = k_x \mathbf{x} + k_y \mathbf{y} + k_z \mathbf{z}. \quad (2.17.1)$$

In the DE geometry the magnetisation and internal field within the wire are uniform. Therefore, the quantisation condition $K = m\pi/w$ was applied. The frequencies of the laterally quantised modes were calculated with $p = 0$ and $m = 1, 2, 3, 4, 5$, while the frequency of the PSSW mode was calculated with $p = 1$ and $m = 0$. However, in the BV geometry, the calculation is more difficult because the internal field is non-uniform. The edge region (with zero internal field and non-uniform magnetisation) was assumed to reflect spin-waves propagating from the center of the stripe towards these regions.

Furthermore, a second turning point in the effective field was identified, above which only modes with an imaginary effective wavevector could exist. The region between these two boundaries was identified as a potential well for propagating spin waves which gave rise to the LM mode observed in the BLS data.

In Reference 8 the mode profiles of dipolar-exchange spin wave modes were calculated for rectangular elements (width $w = 1 \mu\text{m}$, length $l = 1.75 \mu\text{m}$, and thickness $d = 35 \text{ nm}$). It is assumed that the non-uniform dynamic magnetisation within the element can be represented as the product of the eigenfunctions of a longitudinally magnetised wire and a transversely magnetised wire. The assumption is justified since the internal field is non-uniform along the long edge of the element parallel to the external field, while along the short edge of the element the internal field is approximately constant. The mode profiles and corresponding frequencies of a transversely magnetised wire in an external field of 2 kOe were calculated by numerically solving the derived analytical integro-differential equations and are shown in Figure 2.17.2. At 2 kOe exchange-type and magnetostatic-type modes are spatially

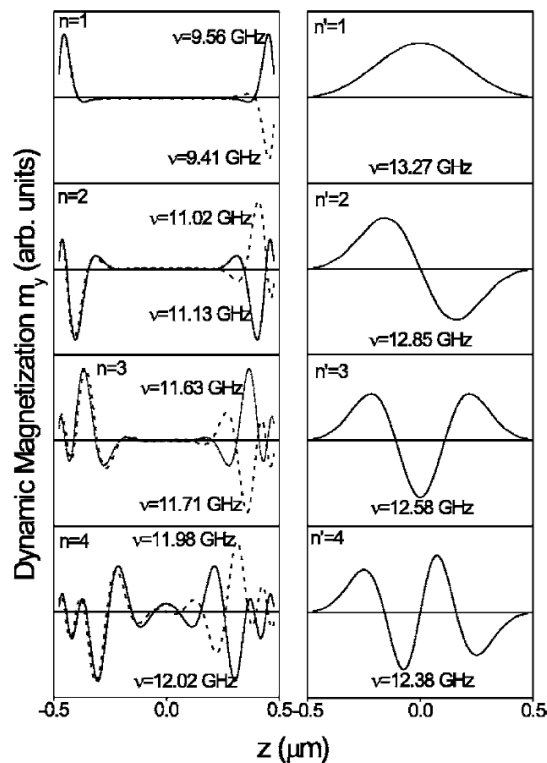


Figure 2.17.2 Taken from Reference 8. Mode profiles and corresponding frequencies of a $1 \mu\text{m}$ wide and 33 nm thick wire in a transverse external field of 2 kOe. The index n denotes the exchange-dominated modes while n' denotes the dipole-dominated modes.

separated. The exchange-dominated modes (labelled n) have large amplitude near to the edges of the element perpendicular to the external field, while the dipole-dominated modes (labelled n') are localised near the centre of the stripe. However, when the external field is less than 1 kOe the distinction is less clear and regions of zero internal field near the edges perpendicular to the external field migrate towards the centre of the element.

In Reference 11 the spin wave spectra of square elements (width $w = l = 630$ nm to 64 nm, and $d = 2.5$ nm) were investigated experimentally using time-resolved scanning Kerr microscopy. The spectra are shown in Figure 2.17.3(a). The frequency of the excited modes was observed to increase as the element size was reduced. However, a shift in the frequency from about 7 GHz to 5 GHz was seen as the element size was reduced below 220 nm, Figure 2.17.3(a).

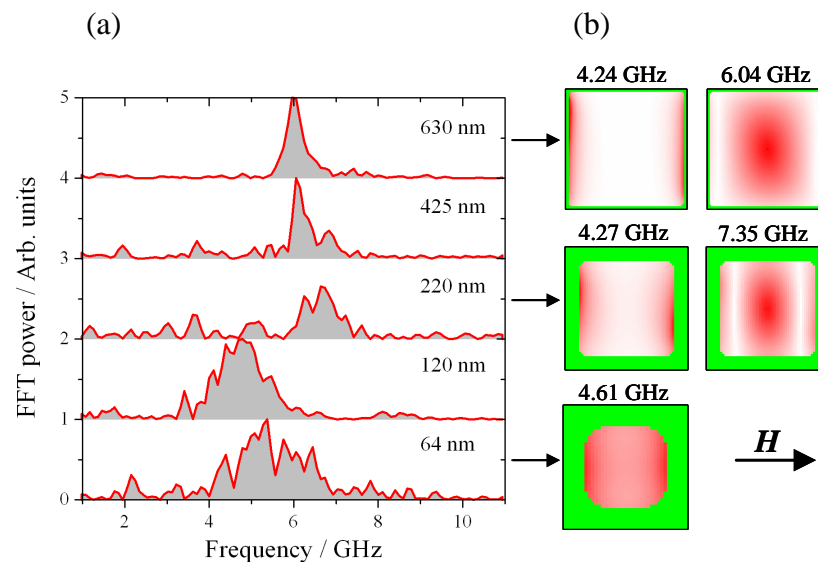


Figure 2.17.3 Reproduced from Reference 11. In (a) the experimental spectra obtained from an array of square nanomagnets of different size patterned from a CoFe/NiFe(2.5 nm) film show the dependence of the mode frequency upon the element size at a bias field H of 405 Oe. For element sizes 630, 220, and 64 nm the simulated spatial distribution of the out-of-plane component of the magnetisation is shown in (b). The green background in the images in (b) are non-magnetic regions.

As shown in Reference 8 the long range magneto-dipole interaction makes the analytical description of modes excited in small non-ellipsoidal element difficult. Furthermore, in nanoscale non-ellipsoidal elements the static magnetisation becomes

non-uniform (Figure 2.10.5) in addition to the total effective field within the element. This has led to the development and successful use of numerical algorithms to simulate the spatial dependence and temporal evolution of the magnetisation dynamics in thin film ferromagnetic elements. In particular, in Reference 11 and in this thesis, the Object Oriented Micromagnetic Framework⁴¹ (OOMMF) was used to understand the spatial character of modes excited in non-ellipsoidal nanomagnets with non-uniform ground state. In Reference 12 the effect of the strength of the exchange interaction, dipolar interactions with nearest neighbour elements, and rounding of the corners of the elements were investigated. Such investigations have led to the development of reliable micromagnetic models for the interpretation of the magnetisation dynamics in non-ellipsoidal elements.

In Reference 11 the results of micromagnetic simulations revealed that the shift in frequency was due to a change in the mode character from a mode with large out-of-plane component of the dynamic magnetisation at the center of the element, to a mode with large out-of-plane component along the edges of the element perpendicular to the bias magnetic field, Figure 2.17.3(b). Furthermore, for the simulated element size of 220 nm the center- and edge-type modes were found to coexist. In Chapter 6 the results of experiments performed on elements of similar size and composition, but thickness of 13.6 nm are presented. Details of the OOMMF model use to understand the experimentally observed magnetisation dynamics will be given in Section 6.3. The richer mode spectrum of thicker elements allows the interplay between the center- and edge-type modes to be investigated in addition to the evolution of their spatial character at reduced bias fields, a regime in which the assumptions made in the analytical theories are no longer satisfied.

2.18 Summary

In summary the background principles of magnetism relevant to this thesis have been introduced. The subject of the chapter converged towards the non-uniform magnetisation dynamics in finite-sized non-ellipsoidal ferromagnetic elements, which is the focus of this thesis. In the next chapter the experimental techniques used to investigate the precessional magnetisation dynamics in novel magnetic materials will be introduced in detail.

“Measure what is measurable, and make measurable what is not so”. – Galileo Galilei
(1564 – 1642)

Chapter 3

Experimental techniques

3.1 Introduction

In this chapter I will begin by reviewing the origin of magneto-optical effects in metals. I will then give a phenomenological description of the magneto-optical Kerr effect, and describe how the effect is used in the experiments presented in this thesis. Finally, I will describe the experimental techniques used for static and time-resolved magneto-optical measurements. A description of the measured samples will not be presented in this chapter, but instead will be reserved for chapters in which corresponding results are presented and discussed. Some experimental data will be shown in this chapter for the purpose of illustration, in which case details of the sample will be given.

3.2 Magneto-optical effects in metals

In 1845 Faraday⁴² discovered that the polarisation of light was changed after transmission through a glass sample subjected to a magnetic field. Furthermore, he found that the change was related to the magnetic field. In fact, the glass was diamagnetic and the change in polarisation was proportional to the magnetisation

induced when the magnetic field was applied. The effect is now known as the magneto-optical Faraday effect and was shown by Kundt⁴³ in 1884 to be exhibited by ferromagnetic thin films that were thin enough for incident light to be transmitted. In 1877, following advances in the surface preparation of metals, Kerr⁴⁴ discovered changes in the polarisation of light reflected from the surface of a ferromagnetic material. The magneto-optical Faraday effect and magneto-optical Kerr* effect (MOKE) are proportional to the temperature dependent magnetisation $\mathbf{M}(T)$ of a ferromagnetic material, and appear to vanish at $T > T_C$. Seemingly then, the Faraday and Kerr effects may be used to investigate the properties of ferromagnetic materials. However, the type of magneto-optical effect chosen for an experiment often depends upon the type of sample to be measured. The majority of samples studied in experiments presented in this thesis were opaque. Therefore, it was necessary to use the Kerr effect to measure the magneto-optical response of the sample. To build an appropriate experiment for such investigations and then to correctly interpret the measured magneto-optical signals, it is necessary for the origin of the Kerr effect to be understood.

Phenomenological description

A phenomenological description of magneto-optical effects in ferromagnetic materials can be achieved by considering the response of the material to an electromagnetic field in terms of the dielectric (or permittivity) tensor^{45,47}. For isotropic materials, or materials with high crystal symmetry (*e.g.* cubic), a single dielectric constant ϵ is sufficient to describe the response of the material. The dielectric constant relates the displacement vector \mathbf{D} to the electric field \mathbf{E} according to $\mathbf{D} = \epsilon \mathbf{E}$. In ferromagnetic materials the symmetry is broken by the spontaneous magnetisation \mathbf{M} . When the symmetry is lowered the optical response must instead be described by a dielectric tensor of the form

$$\tilde{\epsilon} = \begin{pmatrix} \epsilon_{xx} & \epsilon_{xy} & \epsilon_{xz} \\ -\epsilon_{xy} & \epsilon_{xx} & \epsilon_{yz} \\ -\epsilon_{xz} & -\epsilon_{yz} & \epsilon_{xx} \end{pmatrix}. \quad (3.2.1)$$

* Note that the *magneto*-optical Kerr effect is different to the similarly named *electro*-optical Kerr effect, discovered by Kerr in 1875, which is an example of electrical birefringence. In this thesis “the Kerr effect” refers to the *magneto*-optical Kerr effect.

Equation 3.2.1 is the dielectric tensor for cubic ferromagnetic materials, where symmetry considerations reduce the number of free variables. Furthermore, Onsager's relations require the diagonal elements to be even ($\epsilon_{ii}(M) = \epsilon_{ii}(-M)$) and the off-diagonal elements to be odd ($\epsilon_{ij}(M) = -\epsilon_{ij}(-M)$) in the magnetisation^{45,46,47}. To first-order in the magnetisation the diagonal elements are independent of \mathbf{M} , while the off-diagonal elements are proportional to \mathbf{M} and zero in the absence of \mathbf{M} . In the case when the magnetisation is parallel to the z -axis, the dielectric tensor has the form

$$\tilde{\boldsymbol{\epsilon}} = \begin{pmatrix} \epsilon_{xx} & \epsilon_{xy} & 0 \\ -\epsilon_{xy} & \epsilon_{xx} & 0 \\ 0 & 0 & \epsilon_{xx} \end{pmatrix}, \quad (3.2.2)$$

where ϵ_{xy} is proportional to the component of the magnetisation along the z -axis⁴⁸. One consequence of the off-diagonal tensor elements $\pm\epsilon_{xy}$ in Equation 3.2.2 is that linearly polarised light with the electric field along the x -axis will induce an electric displacement along the y -axis. Magneto-optical effects are readily illustrated by considering the response of the material to left- and right-circularly polarised light, where $E_y = iE_x$ and $E_y = -iE_x$ respectively⁴⁵. Using Equation 3.2.2 it can be shown that the different dielectric constants for left- (ϵ_+) and right- (ϵ_-) circularly polarised light are

$$\epsilon_{\pm} = \epsilon_{xx} \pm i\epsilon_{xy}. \quad (3.2.3)$$

The resulting difference in the complex refractive indices for the two circular polarisation states gives rise to the magneto-optical Faraday and Kerr effects.

Microscopic origin

Similarly to ferromagnetism, the microscopic origin of magneto-optical effects was not understood until quantum mechanics was well established. Until then, ferromagnetic materials were assumed to possess a large internal field that gave rise to the observed properties. Voigt found that the magnetic field required to give rise to the observed magneto-optical effects was⁴⁸ $\sim 10^7$ Oe, the same order of magnitude as the Weiss field, Section 2.6. Weiss introduced the molecular field to account for the spontaneous alignment of magnetic moments in a ferromagnetic material. After the advent of quantum mechanics, Heisenberg showed that the exchange interaction was

responsible for the alignment of the moments, Section 2.7. However, magneto-optical effects cannot be described in terms of the exchange interaction between the moments. An interaction between the moments cannot induce motion of electrons in the same way that an external field can. The motion of electrons (current) is necessary in order to describe the optical response of a material to an electromagnetic field. Electronic motion is related to the optical properties (dielectric tensor $\tilde{\epsilon}$) of a material via the conductivity tensor $\tilde{\sigma}$, where

$$\tilde{\epsilon} = 1 + i \frac{4\pi}{\omega} \tilde{\sigma}, \quad (3.2.4)$$

and ω is the angular frequency of the electromagnetic field⁴⁵. Hulme⁴⁹ realised that the spin-orbit interaction could explain the connection between the optical and ferromagnetic properties of a material. In accordance with Equations 3.2.3 and 3.2.4, a theory of magneto-optical effects only requires the calculation of the elements of the conductivity tensor. For completeness, I will briefly describe the influence of the spin-orbit interaction.

The spin-orbit interaction

The spin-orbit interaction couples the spin components of the electron wavefunctions to the spatial components, which govern the electric dipole matrix elements and optical selection rules⁵⁰. The property of spin, which emerges from relativistic quantum mechanics and the Pauli exclusion principle, can be included into a non-relativistic theory by assigning a spin quantum number and requiring that the wave function remains antisymmetric when electrons are interchanged²⁵. In this non-relativistic model (Section 2.7) the electrostatic interaction between electrons does not depend upon the electron spin. One consequence is that the exchange Hamiltonian is isotropic and therefore cannot describe magneto-optical effects or magneto-crystalline anisotropy in ferromagnetic materials. In order to describe these phenomena, relativistic electron dynamics must be considered.

The Dirac equation for a relativistic electron in an electromagnetic field is invariant under Lorentz transformation. When the Dirac equation for an electron in a weak electrostatic potential is solved²⁵, the spin-orbit energy emerges as a relativistic

correction to the Hamiltonian of the Schrödinger equation for an electron with spin. The spin-orbit energy term has the form

$$\hat{H}_{so} = -\frac{e\hbar}{4m_e^2c^2} \mathbf{s} \cdot (\nabla\phi \times \mathbf{p}), \quad (3.2.5)$$

where \mathbf{s} is the magnetic moment (or spin) of the electron, and \mathbf{p} is the momentum of the electron as it moves through the crystal electric field $-\nabla\phi$ of the material⁴⁸. For the simplest case of an isolated atom, ϕ is spherically symmetric, $\nabla\phi \propto \mathbf{r}$ and $\mathbf{r} \times \mathbf{p} = \mathbf{L}$. Thus, the form of the spin-orbit coupling of Equation 2.4.6 is recovered. As a relativistic electron moves through an electric field, it experiences a magnetic field⁵¹. Using the vector triple product identity $\mathbf{a} \cdot (\mathbf{b} \times \mathbf{c}) = \mathbf{c} \cdot (\mathbf{a} \times \mathbf{b})$, Equation 3.2.5 can be written in the form $\mathbf{p} \cdot (\mathbf{s} \times \nabla\phi)$. The interaction energy of an electron with momentum \mathbf{p} with a magnetic field of vector potential \mathbf{A} is of the form⁴⁸ $\mathbf{p} \cdot \mathbf{A}$. Therefore, $\mathbf{s} \times \nabla\phi$ can be considered as the magnetic vector potential \mathbf{A} of an effective magnetic field that affects the orbital motion of electrons⁴⁸. The effective magnetic field can then be used to illustrate the origin of magneto-optical effects in ferromagnetic materials. In non-ferromagnetic materials (including ferromagnetic materials at $T > T_C$) there are equal spin-up and spin-down electron populations at the Fermi level, Figure 2.8.1(a). For ferromagnetic materials at $T < T_C$ there is an imbalance of electron spin populations at the Fermi level due to exchange splitting of the spin-up and spin-down energy bands, Figure 2.8.1(b). The imbalance leads to a net spin-orbit induced motion of electrons, which manifests itself as a magneto-optical property of the material. In non-ferromagnetic materials the induced motion of spin-up and spin-down electrons is equal and opposite and therefore does not yield a net magneto-optical effect.

In the remaining part of this section I will outline two methods used to calculate the conductivity tensor; that of Argyres⁴⁸, followed by that of Bennett and Stern⁵². For more details the reader should refer to the cited references, in which the authors go on to calculate the magneto-optical Faraday and polar-Kerr effects in ferromagnetic materials.

The method used by Argyres to calculate magneto-optical effects

The method used by Argyres to calculate the magneto-optical Faraday and polar-Kerr effect in ferromagnetic materials starts with the calculation of the wavefunction of an electron in an electromagnetic field⁴⁸. Firstly, the eigenfunctions of

the single electron Hamiltonian in the absence of the external electromagnetic field were obtained. The potential energy of the single electron within a material includes contributions from atomic nuclei and all other electrons. Secondly, the spin-orbit interaction (Equation 3.2.5) was treated as a perturbation to the single electron Hamiltonian in order to account for the relativistic nature of the electron. Third, the electromagnetic field was treated as a time-dependent perturbation acting on the electron.

Once the electron wavefunctions were obtained, the conductivity tensor elements were derived using the current density operator for an electron in the presence of an electromagnetic field⁴⁸. As mentioned in the phenomenological description of magneto-optical effects, the off-diagonal elements of the conductivity tensor are antisymmetric, proportional to the magnetisation, and give rise to magneto-optical effects. Using the conductivity tensor and Maxwell's equations with appropriate boundary conditions, the magneto-optical constants were calculated for left- and right circularly polarised light. The superposition of two circular polarisation states results in linearly polarised light. Linearly polarised light reflected from the surface of the ferromagnetic material becomes elliptically polarised as a result of the different reflection coefficients for the different circular components. Finally, Argyres showed that the magneto-optical rotation and ellipticity are proportional to the magnetisation of the material.

The method used by Bennett and Stern to calculate magneto-optical effects

The method used by Bennett and Stern⁵² relates the elements of the conductivity tensor to optical transition rates. Macroscopically, the average power absorbed can be written in terms of the incident electric field and the conductivity tensor elements. Microscopically, the absorption is due to electronic transitions between different quantum states, which are governed by the dipole selection rules. The transition probability rate can be calculated from Fermi's golden rule, and is proportional to the transition matrix elements of the kinetic momentum. The kinetic momentum is invariant under a Lorentz transformation and includes the term $s \times \nabla \phi$ which represents the effective magnetic vector potential that results from the spin-orbit interaction. Summing over all known transitions yields the power absorbed. The elements of the conductivity tensor can then be calculated by relating the power absorbed in terms of

transition rates to the power absorbed in terms of the elements of the conductivity tensor.

3.3 The magneto-optical reflection coefficients

As stated in the previous section, the Kerr rotation Φ_K and ellipticity ε_K are proportional to the magnetisation of the reflecting ferromagnetic metal to first order. Therefore, by measuring changes in the polarisation of light reflected from the material, changes in the magnetisation can be detected. The polarisation of incident linearly polarised light can be described by the orientation of the electric field with respect to the plane of incidence. Linearly polarised light with the electric field \mathbf{E} parallel (perpendicular) to the plane of incidence is described as p- (s-) polarised light, Figure 3.3.1.

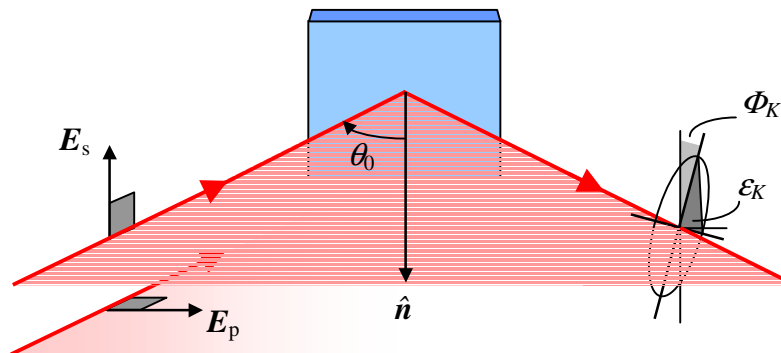


Figure 3.3.1 When the electric field of linearly polarised light is parallel (perpendicular) to the plane of incidence, the polarisation of the light is described as p- (s-) polarised. Incident s- and p-polarised (inset) light reflected from a ferromagnetic material become elliptically polarised as a result of the Kerr effect. The rotation of the major axis of the ellipse Φ_K is the Kerr rotation and ε_K is the Kerr ellipticity.

Argyres⁴⁸ showed that the effect of the spin-orbit interaction can be described by an effective magnetic field (Section 3.2). The field mimics a Lorentz force $\propto \mathbf{u} \times \mathbf{E}$, where $\mathbf{u} = \mathbf{M}/M_s$, which acts on electron currents induced by the incident light³⁰. The Lorentz deflection of the electrons results in the rotation of the electric polarisation. In

turn this leads to an \mathbf{M} -dependent rotation of the electric field (or polarisation) of the reflected light.

The reflected electric field components $E_p^{(r)}$ and $E_s^{(r)}$ of the elliptically polarised light can be described in terms of the incident electric field components E_p and E_s by using the Jones matrix formalism

$$\begin{pmatrix} E_s^{(r)} \\ E_p^{(r)} \end{pmatrix} = \begin{pmatrix} r_{ss} & r_{sp} \\ r_{ps} & r_{pp} \end{pmatrix} \begin{pmatrix} E_s \\ E_p \end{pmatrix}, \quad (3.3.1)$$

where r_{ij} are the optical reflection coefficients. Expressions for the magneto-optical reflection coefficients at the interface between a vacuum and the surface of a magnetic material have been given in Reference 53 to second order in the magneto-optical coupling strength (or Voigt) parameter⁴⁵ Q . The geometry used in the calculation of the optical reflection coefficients is shown in Figure 3.3.2.

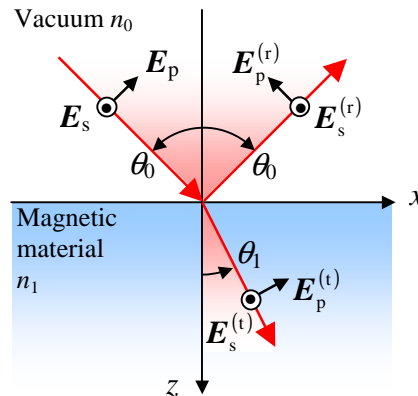


Figure 3.3.2 The geometry used in the calculation of the optical reflection coefficients at a vacuum-magnetic material interface.

Retaining terms to first order in Q , the reflection coefficients are given in Reference 54 as

$$r_{ss} = \frac{n_0 \cos \theta_0 - n_1 \cos \theta_1}{n_0 \cos \theta_0 + n_1 \cos \theta_1}, \quad (3.3.2)$$

$$r_{pp} = \frac{n_1 \cos \theta_0 - n_0 \cos \theta_1}{n_1 \cos \theta_0 + n_0 \cos \theta_1} + \frac{2iQn_0n_1 \cos \theta_0 \sin \theta_1 u_y}{(n_1 \cos \theta_0 + n_0 \cos \theta_1)^2}, \quad (3.3.3)$$

$$r_{ps} = -\frac{iQn_0n_1 \cos \theta_0 (\sin \theta_1 u_x + \cos \theta_1 u_z)}{\cos \theta_1 (n_0 \cos \theta_0 + n_1 \cos \theta_1) (n_1 \cos \theta_0 + n_0 \cos \theta_1)}, \quad (3.3.4)$$

$$r_{sp} = \frac{iQn_0n_1 \cos \theta_0 (\sin \theta_1 u_x - \cos \theta_1 u_z)}{\cos \theta_1 (n_0 \cos \theta_0 + n_1 \cos \theta_1) (n_1 \cos \theta_0 + n_0 \cos \theta_1)}, \quad (3.3.5)$$

where $\mathbf{u} = \mathbf{M}/M_s$. The angles θ_0 and θ_1 are the angles defined in Figure 3.3.2 and are related by Snell's law

$$n_0 \sin \theta_0 = n_1 \sin \theta_1, \quad (3.3.6)$$

where n_0 and n_1 are the refractive indices of the vacuum and the magnetic material respectively. In terms of the optical reflection coefficients the complex Kerr rotation and ellipticity are defined as

$$\Phi_K = -\text{Re} \left\{ \frac{r_{sp}}{r_{pp}} \right\} \quad (3.3.7)$$

and

$$\varepsilon_K = \text{Im} \left\{ \frac{r_{sp}}{r_{pp}} \right\} \quad (3.3.8)$$

respectively, for incident p-polarised light, and

$$\Phi_K = \text{Re} \left\{ \frac{r_{ps}}{r_{ss}} \right\} \quad (3.3.9)$$

and

$$\varepsilon_K = \text{Im} \left\{ \frac{r_{ps}}{r_{ss}} \right\} \quad (3.3.10)$$

respectively, for incident s-polarised light.

For a non-magnetic metal r_{ps} and r_{sp} are zero, and r_{ss} and r_{pp} are non-zero and complex. Therefore, the polarisation of incident p- or s-polarised light reflected from a non-magnetic metal remains unchanged. However, for a ferromagnetic metal r_{ps} and r_{sp} are also non-zero and complex. The result is that incident p- (s-) polarised light will induce an s- (p-) electric field component in the reflected light. In general $r_{pp} \neq r_{ss}$ and $E_p^{(r)}/E_p \neq E_s^{(r)}/E_s$ which can yield a rotation of the polarisation plane if the incident light is not purely p- or s-polarised, even when $\mathbf{M} = 0$. In order to detect changes in the magnetisation the measured rotation of the polarisation should be a result of the Kerr effect only. Therefore, in magneto-optical experiments it is desirable to use either p- or s- polarised light.

3.4 The magneto-optical Kerr effect geometries

There are three principle geometries in which the MOKE can be used to detect the magnetisation of a ferromagnetic material. The polar, longitudinal, and transverse MOKE geometries are shown in Figure 3.4.1. The geometries are defined by the orientation of the magnetisation \mathbf{M} with respect to both the plane of incidence and the

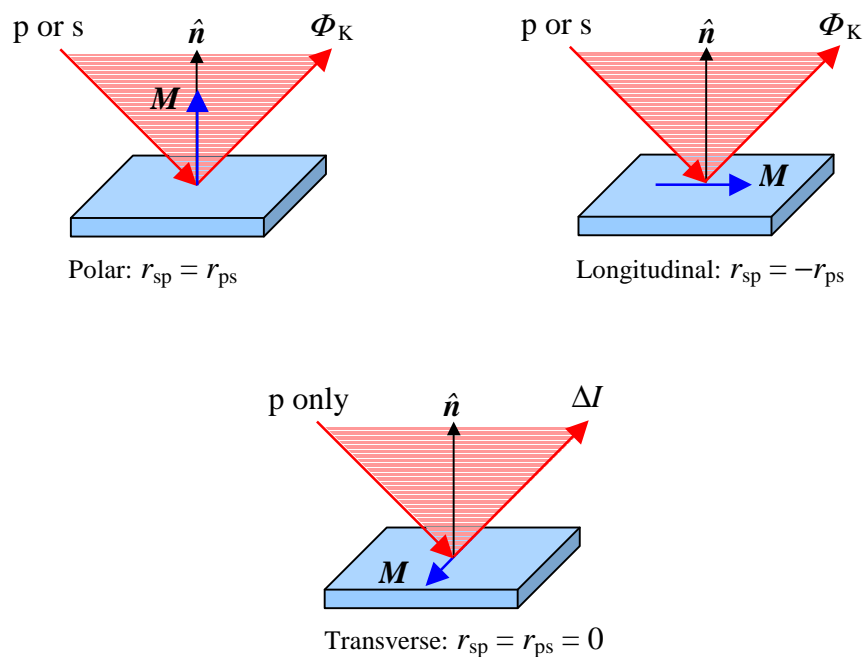


Figure 3.4.1 The three principle MOKE geometries; polar, longitudinal, and transverse.

reflecting interface. In the polar and longitudinal geometry \mathbf{M} lies parallel to the plane of incidence. In the polar geometry \mathbf{M} is perpendicular to the reflecting interface (out-of-plane), while in the longitudinal geometry \mathbf{M} is parallel to the interface (in-plane). In both cases incident p- or s-polarised light may be used, however $r_{sp} = r_{ps}$ and $r_{sp} = -r_{ps}$ for the polar and longitudinal geometry respectively. In both cases the Kerr effect leads to a magnetisation-dependent rotation Φ_K of the major axis of the elliptically polarised reflected light. At normal incidence ($\theta_0 = 0$) Equations 3.3.2-8 reveal that the Kerr effect is largest in the polar geometry ($u_z = 1, u_x = u_y = 0$), while the Kerr effect vanishes in the longitudinal geometry ($u_x = 1, u_y = u_z = 0$).

In Figure 3.4.2 the calculated Kerr rotation and Kerr ellipticity angles are shown for light of wavelength $\lambda = 800$ nm reflected from a vacuum/Fe interface at angles of incidence between 0° and 90° . The results are reproduced from Reference 55. The Kerr angles are shown for the polar and longitudinal geometries and for p-polarised (blue curves) and s-polarised (red curves) incident light. The results show, for example, that in the longitudinal geometry using s-polarised light, Φ_K (ϵ_K) is largest for $\theta_0 \approx 45^\circ$ (60°).

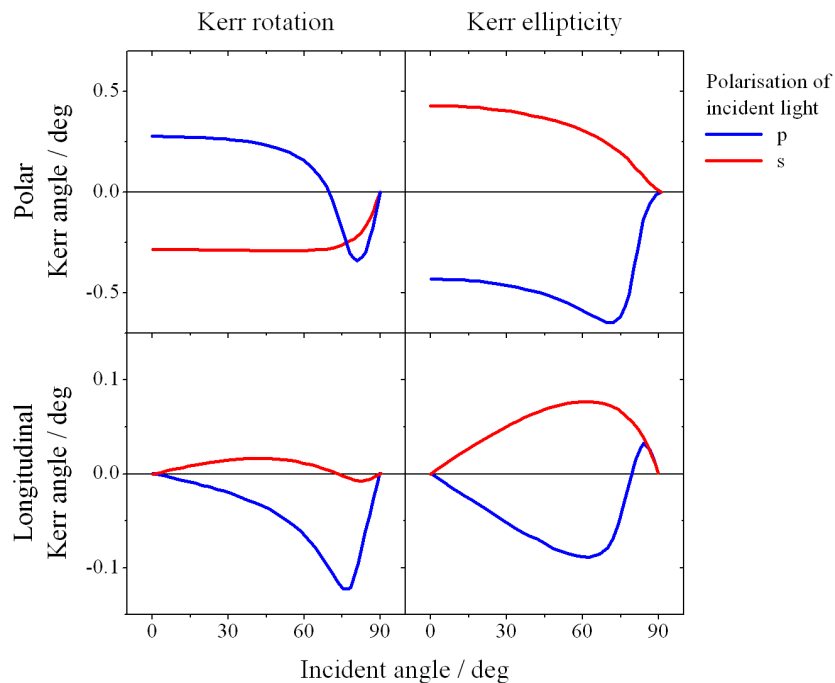


Figure 3.4.2 Calculated Kerr rotation and ellipticity angles for Fe at 800 nm for the polar and longitudinal geometry. Reproduced from Reference 55.

The strength of the Kerr effect also depends upon the wavelength of the incident light and the reflecting material via the conductivity tensor. The conductivity tensor depends upon the refractive index of the reflecting material, which in turn depends upon the frequency of the incident light. Figure 3.4.3 shows the measured polar Kerr rotation for Ni and Fe as a function of wavelength. The results are reproduced from Reference 56.

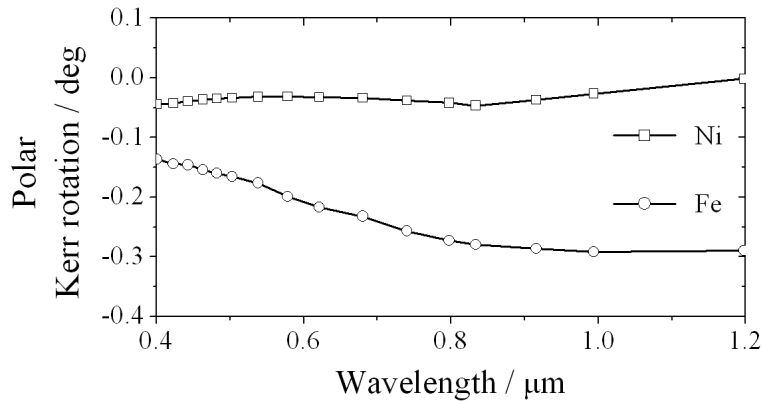


Figure 3.4.3 The measured polar Kerr rotation for Ni and Fe are shown as a function of wavelength. The results are reproduced from Reference 56.

In the transverse geometry ($u_y = 1, u_x = u_z = 0$) \mathbf{M} is perpendicular to the plane of incidence and lies in the plane of the sample. Since only r_{pp} has a dependence upon u_y (Equation 3.3.3) p-polarised light must be used to detect \mathbf{M} . For s-polarised light \mathbf{E} is parallel to \mathbf{M} , which does not yield a magneto-optical effect. Using the simple Lorentz deflection model it is clear that there is no deflection of electrons in the transverse geometry for s-polarised light ($\mathbf{u} \times \mathbf{E} = 0$). Even p-polarised light does not result in a polarisation rotation since \mathbf{M} is perpendicular to the plane of incidence and \mathbf{E} . Instead the Lorentz deflection gives rise to a rotation of \mathbf{D} in the plane of incidence, which leads to an \mathbf{M} -dependent change in reflectivity ΔI .

3.5 Detection of the magneto-optical Kerr effect

In the previous section it was shown that there are three MOKE geometries that can be used to detect the magnetisation of the sample. The particular geometry chosen for an experiment depends upon the sample, the behaviour of the magnetisation, and the

detection technique. For example, in the experiments on microscale samples reported in this thesis, a microscope objective lens was required to focus the probe laser beam onto the sample. Conveniently, by performing this measurement at normal incidence the same objective lens could be used to collect and re-collimate the beam before it entered the detector. However, at normal incidence only the polar Kerr effect can be sensed, which is sensitive to the out of plane component of the sample magnetisation only. If the sample magnetisation remained in-plane, the polar Kerr geometry would not yield any information about behaviour of the sample magnetisation. In the time-resolved experiments presented in this thesis the precessional behaviour of the magnetisation generates a small out-of-plane component M_z , which can be detected using the polar Kerr effect. When a beam is focused by the objective lens, the focused rays form a cone. The cone is formed of planes of incidence at all azimuth angles with a range of angle of incidence. Figure 3.4.2 shows that the polar Kerr effect can be measured using p- or s-polarised light and at angles of incidence away from the normal. Therefore, sensitivity to M_z is maintained while using the objective lens. In order to measure the in-plane components in the same experimental geometry, modification of the detection technique is necessary. It will be shown in Chapter 4 that quadrant photodiode detectors can be used to measure both the polar and longitudinal Kerr effects so that all three components of the magnetisation can be detected simultaneously.

Figure 3.5.1 shows the experimental geometry of the scanning Kerr microscope used in the time-resolved experiments. The optical axis of the probe laser beam $a-a'$ was normal to the sample plane. Before the beam entered the microscope it was expanded by a factor of ten in order to reduce the beam divergence and enhance the spatial resolution of the microscope. An aperture was placed in the expanded beam to define the desired beam diameter. The transmitted beam was then passed through a linear polariser so that the direction of the electric field was well defined as it entered the microscope. The polarisation of the beam was set so that the electric field was either vertical or horizontal with respect to the plane defined by $a-a'$ and $b-b'$. The beam was focused to a spot with a diffraction limited diameter using a microscope objective lens. The reflected beam was then collected and re-collimated using the same objective lens.

The magnification of the microscope objective lens chosen for a particular experiment was often dependent upon the sample geometry. For instance, in Chapter 5 a continuous film of permalloy was probed through the substrate of the pulsed magnetic field device used to excite the sample magnetisation. Since the substrate thickness was

~ 0.5 mm it was necessary to use a $\times 10$ objective lens with a long working distance of ~ 4 mm. Since the sample was a continuous film, the spatial resolution was sufficient to locate the regions of the film that were of interest. In contrast, for experiments presented in Chapters 6 and 7, microscale samples were fabricated on the same substrate as the pulsed field device. Therefore, an objective lens with a short working distance of < 1 mm could be used. This objective lens had a magnification of $\times 40$ which provided sufficient spatial resolution to locate and image the microscale samples, Figure 3.5.1(inset).

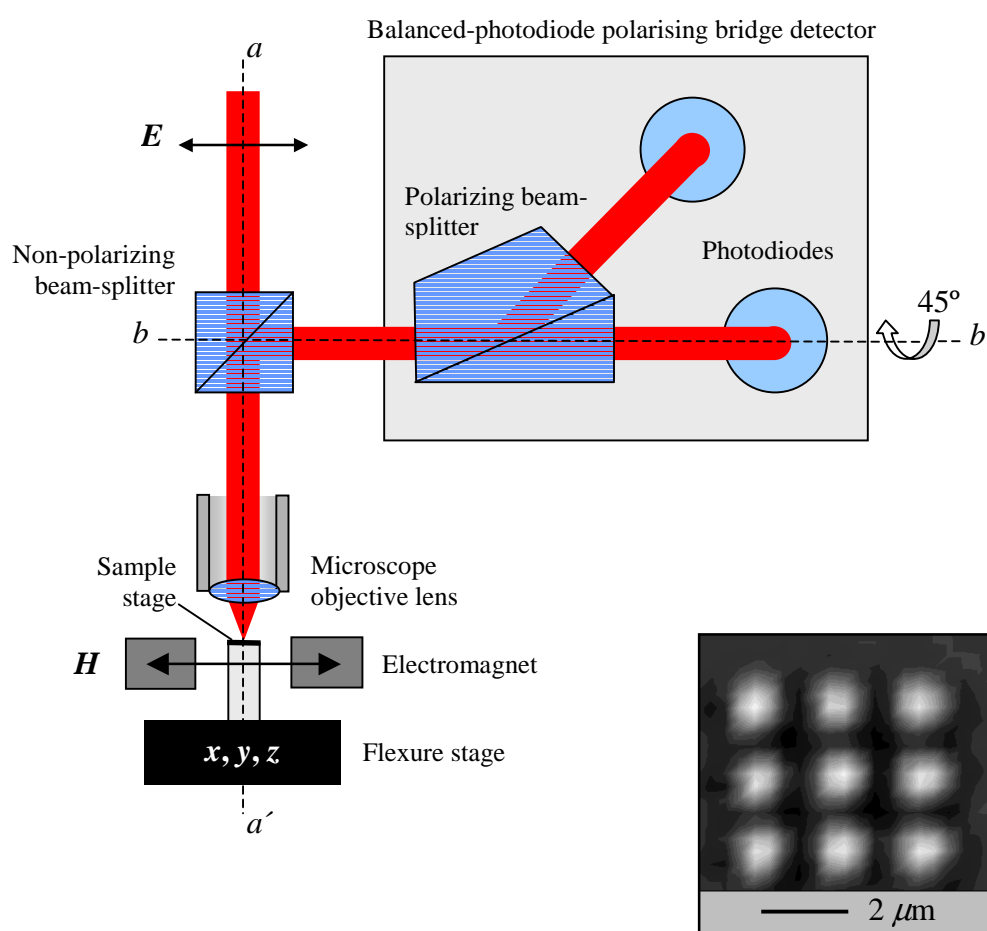


Figure 3.5.1 The geometry of the scanning Kerr microscope and the set-up of the photodiode bridge polarimeter (bridge detector) are shown. The bridge detector is set at an angle of 45° about optical axis $b-b'$ with respect to optical axis $a-a'$. Inset is an optical micrograph of a nine element array of 637 nm square elements obtained using a $\times 40$ microscope objective lens.

The geometry of the focused probe beneath the $\times 40$ objective lens is shown in Figure 3.5.2. The ray tracings show that rays propagating in the plane of incidence parallel to the transmission axis of the polariser are p-polarised, while rays in the orthogonal plane are s-polarised. The reflection coefficients r_{ps} and r_{sp} (Equations 3.3.4 and 3.3.5) are equal for the polar Kerr effect ($u_z = 1$, $u_x = u_y = 0$), which yields a Kerr rotation of the same magnitude for p- and s-polarised rays. Since M_z is parallel to the

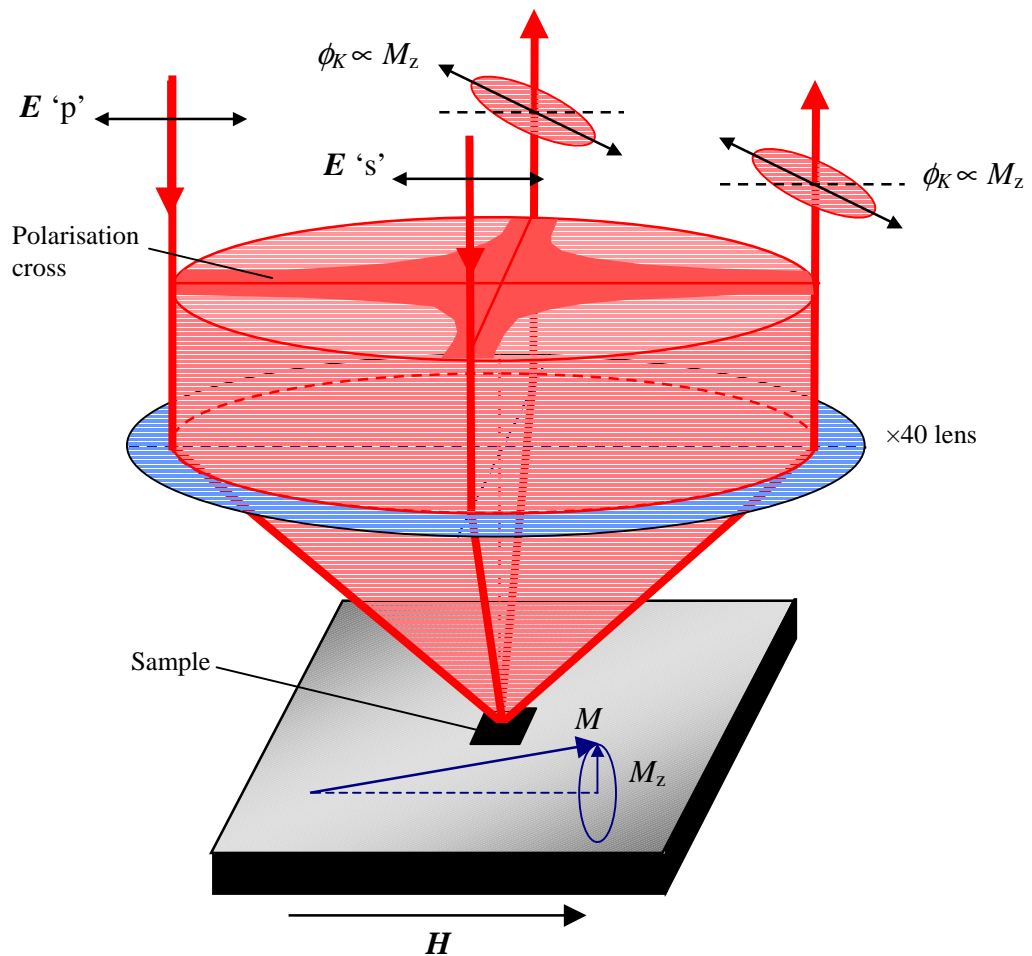


Figure 3.5.2 The geometry of the probe laser beam focused upon the sample is shown. The cone is formed by planes of incidence at all azimuth angles with a range of incident angles. The highlighted ray paths show planes of incidence where the incident light is p- and s-polarised.

optical axis $a-a'$, rays propagating in the opposite direction to those shown in Figure 3.5.2 “see” the M_z in the same sense, which yields a polar Kerr rotation of the same sign. The magnitude and sign of the polar Kerr rotation is equal for p- and s-polarised rays, and for rays propagating in the opposite direction in the same plane of

incidence. Therefore, the sensitivity to M_z was maintained when all of the reflected beam was sampled. In contrast, it will be shown in Chapter 4 that it is necessary to sample individual halves of the reflected beam in order to detect the in-plane components of the magnetisation using the longitudinal Kerr effect.

An objective lens can give rise to unintentional polarisation of off-axis rays passing near to the edges of the lens^{30,57}. The off-axis rays are generated by the oblique angles of incidence near to the edges of the lens. The plane of incidence the off-axis rays are neither parallel or perpendicular to the original polarisation direction of the beam. As a result, each ray becomes slightly p-polarised with respect to its plane of incidence, which leads to a rotation of the polarisation plane. The cross-shaped shaded region across the beam profile in Figure 3.5.2 is often referred to as the Airy⁵⁷ or depolarisation cross³⁰ since rays outside the cross do not have a well defined polarisation. Since the reflection coefficients for r_{pp} and r_{ss} (Section 3.3) are different, the light becomes elliptically polarised when reflected from the sample. The rotation and ellipticity of the off-axis rays is a non-magnetic effect, *i.e.* it is not a result of the Kerr effect. Furthermore, the elliptically polarised rays are not fully extinguished by a crossed analysing polariser^{30,57}. To block the elliptically polarised parts of the beam from entering the detector, a cross shaped aperture can be used³⁰. However, in experiments presented in this thesis, balanced-photodiode polarising bridge detectors were used to measure the Kerr rotation. The depolarised regions give rise to a common offset of the signal generated by the photodiodes. Later in this section it will be shown that the Kerr rotation is measured by taking the difference of the two photodiode outputs, in which case the depolarisation offset vanishes.

The reflected beam was sampled using a non-polarising beam-splitter. The polar Kerr rotation was measured using a photodiode bridge polarimeter (bridge detector) containing a Glan-Thompson polarising beam-splitter and two photodiodes. The detectors used were built previously by Dr Jing Wu⁵⁸ and Dr Ralph Wilks*. The Glan-Thompson polarising beam-splitter is made of two birefringent prisms of calcite. The prisms are cut and cemented together so that the optical axes of the calcite crystals are parallel, Figure 3.5.3. In a calcite crystal the value of the refractive index is different along the directions parallel and perpendicular to the optical axis. Therefore, a ray with E -field perpendicular to the optical axis will propagate with velocity v_{\perp} , while a ray with a parallel E -field will propagate with velocity v_{\parallel} , where $v_{\perp} < v_{\parallel}$. Since the refractive index $n = c/v$, where c is the speed of light in a vacuum and n is the

* School of Physics, University of Exeter, Stocker Road, Exeter, EX4 4QL

refractive index of the material, it is clear that $n_{\parallel} < n_{\perp}$. This is a result of anisotropic electronic interactions with the \mathbf{E} -fields⁵⁹. The Glan-Thompson polarising beam-splitter is designed to transmit two beams of orthogonal polarisation separated by an angle of 45° . The \mathbf{E} -field of the (un)deviated ray is (parallel) perpendicular to the optical axis and therefore experiences the refractive index (n_{\parallel}) n_{\perp} . Since $n_{\parallel} < n_{\perp}$ the critical angle for total internal reflection of the ray with parallel \mathbf{E} -field is larger than that for the ray with a perpendicular \mathbf{E} -field. The Glan-Thompson polarising beam-splitter is designed so that the angle of incidence of rays of the two polarisation components are such that one is transmitted, while the other is totally internally reflected.

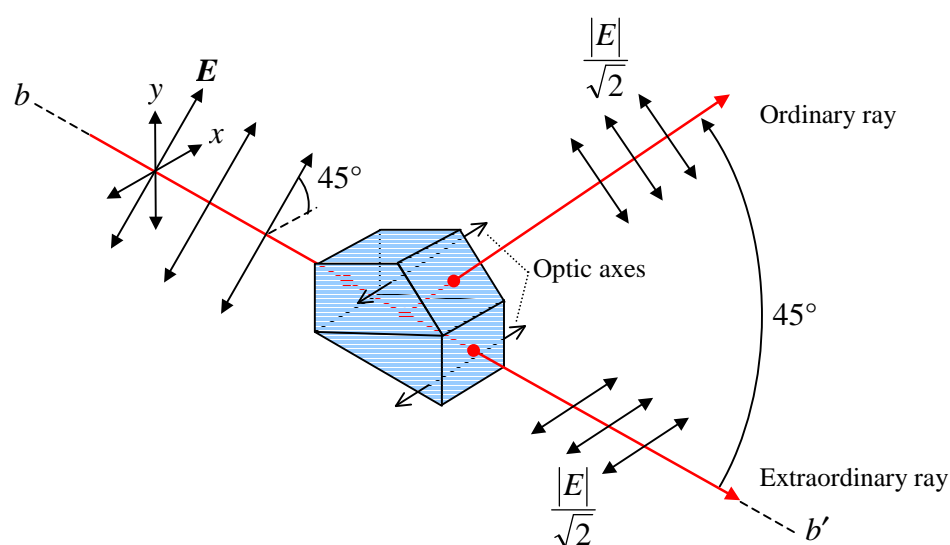


Figure 3.5.3 The geometry of the Glan-Thompson polarising beam-splitter within the balanced-photodiode bridge detector is shown. Before a magnetic field is applied to the sample, the orientation of the detector and, hence, the beam-splitter are set so that the intensity of the two transmitted beams are equal.

Two large area silicon photodiodes were used in the bridge detector. The photodiodes had a responsivity of 0.55 A/W at a wavelength of 800 nm. A positive lens was used to focus each incident beam onto the respective photodiode. The focused spot was well within the perimeter of the active region of the photodiode, and therefore the sensitivity of the detector to any misalignment was reduced. The current generated by each photodiode was converted into a voltage signal using trans-impedance amplifiers with a gain of $10^6 \Omega$. The reflectivity of the sample was proportional to the sum of the

amplified photodiode outputs. It will be shown here that the difference of the photodiode outputs yields a signal proportional to M_z .

The bridge detector was set to an angle of 45° about optical axis $b-b'$ with respect to optical axis $a-a'$. Therefore, the polarizing beam-splitter was oriented so that prior to excitation of the magnetisation the two transmitted beams are of equal intensity, Figure 3.5.3. The intensity of the electric field of the two transmitted beams prior to applying a magnetic field was then $\propto \cos^2(\pi/4) = 1/2$.

Now consider what happens when the magnetisation is excited. During the precessional cycle the magnetisation cants out-of-plane, Figure 3.5.2. The small out-of-plane component of the magnetisation gives rise to the polar Kerr effect. The Kerr rotation of the principle axis of the elliptically polarised reflected light can then be detected using the bridge detector. Figure 3.5.4 shows a ray tracing of the polar Kerr microscope. The ray tracing shows that the Kerr rotation is of the same magnitude and

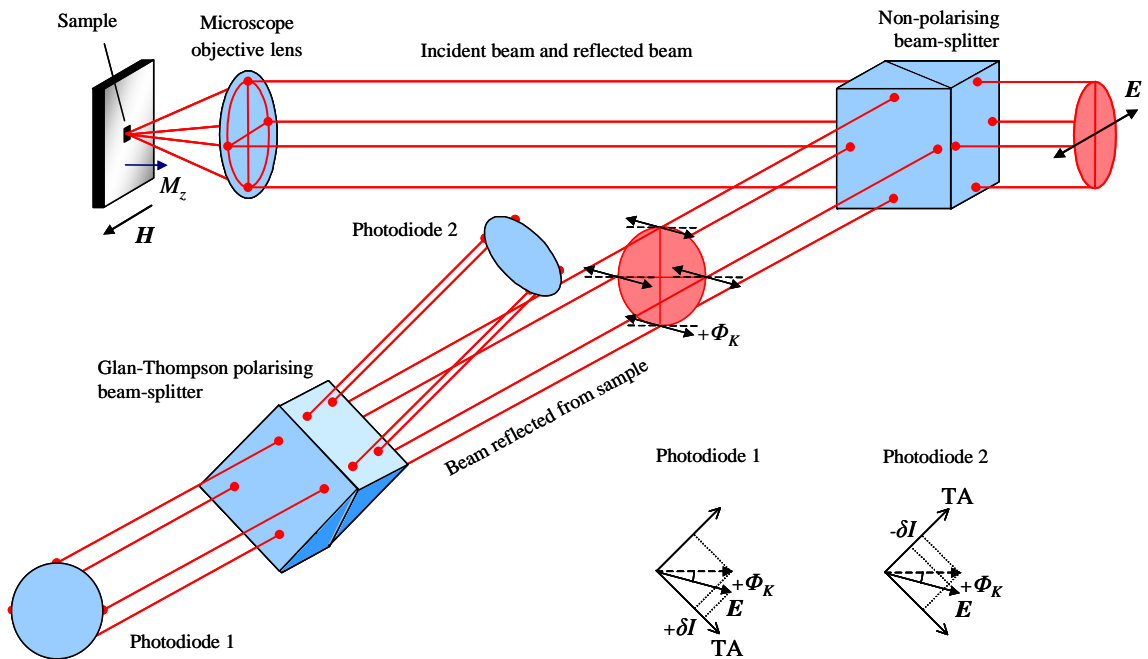


Figure 3.5.4 Ray tracings are shown for four rays of the probe beam that are sensitive to M_z . Inset are schematic illustrations of the operation of the Glan-Thompson polarising beam splitter. The intensity shift δI of the electric field component parallel to the transmission axis (TA) for each transmitted beam is shown for photodiode 1 and 2.

sign for the four rays shown. The rays correspond to the orthogonal planes of incidence shown in Figure 3.5.2. The Kerr rotation will be discussed from the perspective of the bridge detector, *i.e.* looking upstream, opposite to the direction of beam propagation. The two beams transmitted from the polarising beam-splitter have orthogonal polarisation states, Figure 3.5.3. Therefore, we may assign two orthogonal transmission axes (TA) to the polarising beam-splitter. Only components of \mathbf{E} -fields parallel to the transmission axes are transmitted. The inset schematics in Figure 3.5.4 show how the intensity falling upon each photodiode is changed as a result of the Kerr rotation. The intensity of the electric field that falls upon photodiode (PD) 1 and 2 is

$$I_{PD1} \propto \cos^2\left(\frac{\pi}{4} + \Phi_K\right) \quad (3.5.1)$$

and

$$I_{PD2} \propto \cos^2\left(\frac{\pi}{4} - \Phi_K\right). \quad (3.5.2)$$

Using a trigonometric identity for $\cos(\alpha \pm \beta)$, Equation 3.5.1 may be written as

$$I_{PD1} \propto \left[\cos\left(\frac{\pi}{4}\right) \cdot \cos(\Phi_K) - \sin\left(\frac{\pi}{4}\right) \cdot \sin(\Phi_K) \right]^2, \quad (3.5.3)$$

where Φ_K is typically small so that Equation 3.5.3 may be written as

$$I_{PD1} \propto \left[\frac{1}{\sqrt{2}} - \frac{1}{\sqrt{2}} \cdot \Phi_K \right]^2. \quad (3.5.4)$$

Expanding the square and neglecting second order terms in Φ_K gives

$$I_{PD1} \propto \frac{1 - 2\Phi_K}{2}. \quad (3.5.5)$$

Similarly for Equation 3.5.2, we obtain

$$I_{PD2} \propto \frac{1 + 2\Phi_K}{2}. \quad (3.5.6)$$

The difference of intensity signals generated at photodiodes 1 and 2 yields

$$I_{PD2} - I_{PD1} \propto \frac{1 + 2\Phi_K}{2} - \frac{1 - 2\Phi_K}{2} = 2\Phi_K, \quad (3.5.7)$$

where Φ_K is proportional to M_z .

The bridge detection scheme has two advantages. Firstly, the difference of the photodiode amplifier outputs yields a signal that is proportional to twice the polar Kerr rotation, Equation 3.5.7. Secondly, any non-magnetic intensity background or noise of the laser beam can be rejected by the difference operation, which is often referred to as common mode rejection⁶⁰. Common mode rejection was used to remove the non-magnetic background generated by depolarisation effects in the microscope objective lens.

3.6 Time-resolved scanning Kerr microscopy

The pulsed light source used in the pump-probe experiments was a mode-locked Ti:sapphire laser (Spectra-Physics Tsunami). The Tsunami femtosecond cavity layout* is shown in Figure 3.6.1. The Ti:sapphire crystal was pumped using the 5 W output of a diode pumped Nd:YVO₄ continuous-wave visible (532 nm) laser (Spectra-Physics Millennia V). Regenerative mode-locking² of the Tsunami with an acousto-optic modulator within the laser cavity ensured that an 80 MHz repetition rate was achieved and maintained⁶¹. The Tsunami could also be self mode-locked by Kerr lensing in the Ti:sapphire rod². However, regenerative mode-locking was used since it ensured that the laser remained mode-locked for extended periods of time, *i.e.* during experiments.

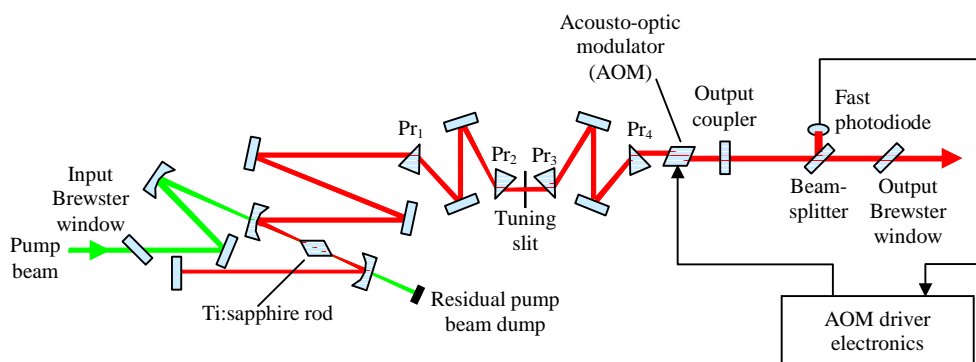


Figure 3.6.1 The Tsunami femtosecond cavity layout is shown. Reproduced from Reference 61.

* The Tsunami is also available with a picosecond cavity layout.

The Tsunami was tuned using prisms Pr_2 and Pr_3 and the tuning slit to produce an output beam of sub 100 fs optical pulses at a wavelength of 785 nm (unless stated otherwise). The stated wavelength is that at which the pulse width and average power output of the Tsunami were optimised. The average power output from the Tsunami at 785 nm was typically 0.6 W, where each pulse had energy of ~ 8 nJ. The beam had a diameter of ~ 2 mm and a beam divergence of ~ 1 mrad. The polarisation of the beam was vertical.

The set-up of the time-resolved scanning Kerr microscope (TRSKM) apparatus is shown in Figure 3.6.2. All mirrors outside the laser cavity were broadband dielectric mirrors suitable for use with wavelengths in the range 700-950 nm with reflectivity $> 98\%$ for angles of incidence in the range 0-45°. Mirrors M_1 and M_2 were used to change the height (Δh) of the Tsunami output beam from 14 cm to 17 cm in order to accommodate the electromagnet. The polarisation of the beam was also changed by mirrors M_1 and M_2 from vertical (s-polarisation) to horizontal (p-polarisation). Two apertures A_1 and A_2 , set to a height of 17 cm above the surface of the table, were used concurrently with mirrors M_1 and M_2 to realign the beam after any drift of the beam alignment within the laser cavity.

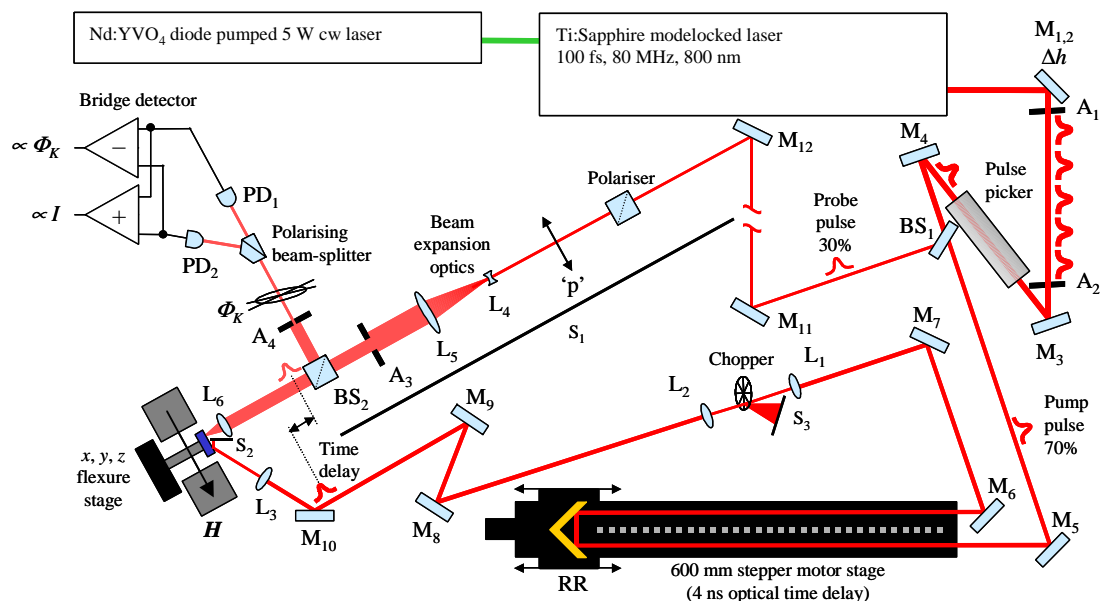


Figure 3.6.2 The experimental set-up of the TRSKM is shown. The meanings of the symbols are given in the text along with the details of the experimental methodology.

Between mirrors M_3 and M_4 the beam was passed through an electro-optic modulator (ConOptics 350-160) that was used as a “pulse picker”. The electro-optic modulator was controlled using a modulator driver (ConOptics 25D) and synchronisation electronics (ConOptics 305). The electro-optic modulator contains a potassium dideuterium phosphate crystal and a polarising beam splitter (polariser). The principle of operation of the pulse picker is based on the Pockels effect⁵⁹. The pulse picker was aligned so that the fast and slow axes of the crystal were at 45° with respect to the electric field of the incident p-polarised beam. The transmission axis of the polariser, fixed at 45° with respect to the fast and slow axes of the crystal, was then parallel to the electric field. The electric field of the incident beam propagates through the crystal with equal amplitude components along the fast and slow axes of the crystal. When a bias voltage (dc electric field) is applied, birefringence is induced in the crystal and the refractive index is reduced (increased) along the fast (slow) axis of the crystal. The two electric field components propagate through the crystal with different velocity and exit the crystal with different phase. This allowed the polarisation of the transmitted beam to be changed by changing the bias voltage.

The applied voltage and time delay were set while monitoring the intensity of transmitted pulses using a fast photodiode and a 500 MHz bandwidth oscilloscope (LeCroy LT322 Waverunner). The bias voltage of the modulator driver was set to change the polarisation of the optical pulses from p- to s-polarisation. The polarising beam splitter allows one polarisation state to be transmitted (p) while the orthogonal polarisation state (s) is rejected. The principle is similar to that of the Glan-Thompson polarising beam-splitter described in Section 3.5. Therefore, each s-polarised optical pulse was ‘picked’ out by the polariser, while p-polarised pulses were transmitted. The temporal alignment of the modulator driver with the optical pulses was achieved by triggering the pulse picker electronics using an 80 MHz signal generated by the fast-photodiode within the laser cavity (Figure 3.6.1). The temporal alignment was optimised using a 16 ns digital time delay. The pulse picker was used to reduce the pulse repetition rate of the beam (where stated). Setting the pulse picker counter value to n allows every $(n + 1)^{\text{th}}$ optical pulse to be transmitted. Figure 3.6.3 shows a fast photodiode signal of an unpicked beam and a picked beam with $n = 4$.

The emerging p-polarised beam was split into two beams using a broadband (700-950 nm) dielectric beamsplitter BS_1 . The reflection/transmission ratio for p-polarised light was 30/70. Optical pulses from the more intense transmitted beam were used as pump pulses, while pulses of the less intense reflected beam were used as the

probe pulses. The greater intensity of the pump beam was desirable since it was used to trigger the pulsed magnetic field device. The intensity of the pump beam was related to the magnitude of the pulsed field via the triggering mechanism, which will be described later in this section.

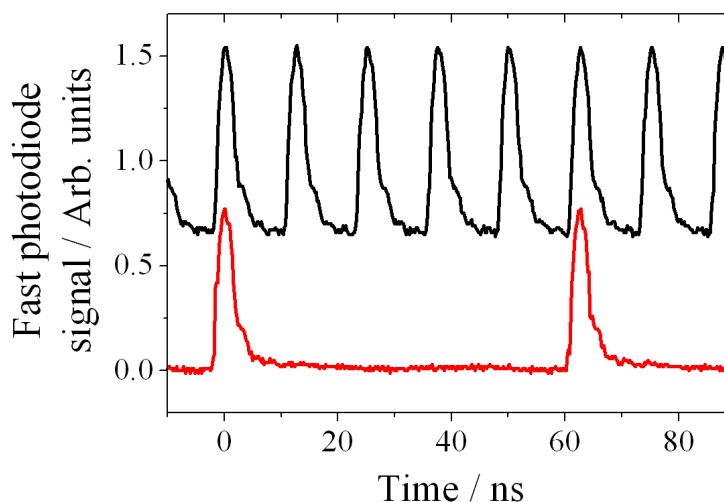


Figure 3.6.3 The fast photodiode signals of an unpicked (black curve) and a picked beam with $n = 4$ (red curve) are shown. Setting the counter value $n = 4$ allows every $(n + 1)^{\text{th}}$ optical pulse to be transmitted.

To perform a time-resolved experiment the relative time delay between the pump and probe pulses must be varied. There are three particular parts of a time-resolved scan that are useful to recognise when setting up a time-resolved experiment. A typical time resolved signal is shown in Figure 3.6.4. The first region of the scan is negative time delay ($t < 0$) where the probe pulse arrives prior to the pump-pulse and the polar Kerr signal is zero. The second region is positive time delay ($t > 0$) where the pump pulse arrives prior to the probe pulse and a finite polar Kerr signal may be detected. The third region is zero time delay where the initial excitation of the magnetisation is observed as an increase in the polar Kerr signal from zero ($t = 0$). At zero time delay the pump and probe pulses have similar optical path lengths and overlap in the time domain. There are two methods of varying the relative time delay between the pump and probe pulses. The first method is to vary the optical path length of the probe beam, and the second is to vary that of the pump beam. The time delay is varied by using a hollow Au retro-reflector mounted on a 600 mm stepper motor stage. The

optical time delay is shown in Figure 3.6.2 between mirrors M_5 and M_6 . The corresponding total time delay was 4 ns. Typically, the magnetisation dynamics measured in the time-resolved experiments were observed over a few nanoseconds. In previous experiments^{62,63} a 2 ns time delay was used. However, the length of the time-resolved scan is related to the frequency resolution of the corresponding Fourier spectrum. By using a 4 ns time delay the resolution of spectra was improved.

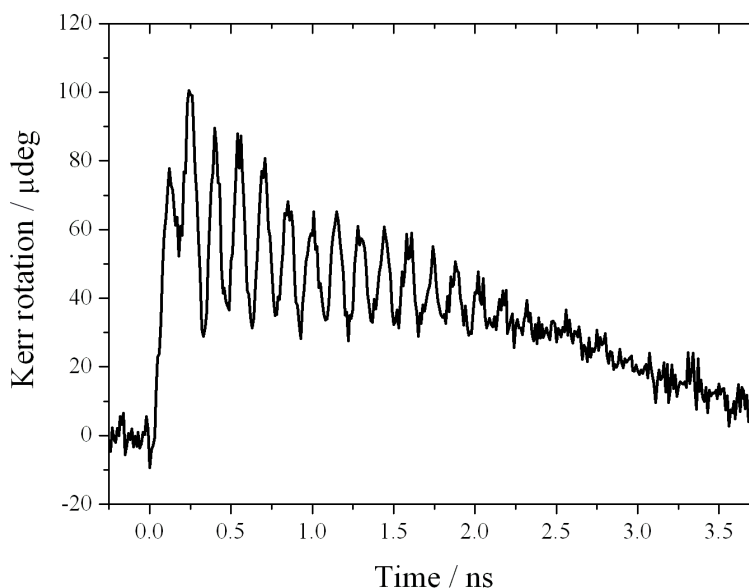


Figure 3.6.4 A typical time-resolved signal obtained from a $10\ \mu\text{m}$ square patterned from a CoFe/NiFe(13.6 nm) film is shown. The time-resolved signal was obtained in the TRSKM configuration described in this chapter. The measured out-of-plane Kerr rotation is typically a few tens of microdegrees. The background is a result of the transient pulsed magnetic field.

In experiments performed upon microscale elements and arrays it is necessary to maintain the highest possible degree of mechanical stability during time-resolved scans. Mechanical vibration and drift are intrinsic to time-resolved experiments due to the mechanical method of varying the time delay. Between mirror M_5 and the retro-reflector it was necessary for the beam to propagate parallel to the direction of travel of the stepper motor stage, both in the horizontal and vertical plane. Any misalignment would yield a translation of the beam on mirror M_6 as the retro-reflector moves along the stage. In order to achieve the best alignment stability of the probe beam in the polar

Kerr microscope, it was advantageous to vary the optical path length of the pump beam rather than the probe beam. In this case the region of negative time delay is observed for the greatest optical path lengths of the pump pulse, while positive time delay is observed for the shortest path lengths.

To detect the small out-of-plane component of the magnetisation, a phase-sensitive detection (PSD) scheme was required. A lock-in amplifier (EG&G Instruments Model 7256) was used to measure the polar Kerr signal output from the bridge detector. To do this a mechanical chopper was used to modulate the pump beam at a frequency of ~ 2 kHz. As a result, the pulsed field device was effectively switched on and off at the modulation frequency. Ultimately the polar Kerr signal associated with the reflected probe pulses is modulated at the same frequency. A square waveform signal of amplitude 2.5 V was generated by the chopper driver electronics and was used as the reference signal for the lock-in amplifier.

During the set-up of the experiment, the intensity of the chopped pump beam was monitored using a photodiode and a 500 MHz oscilloscope. After propagating along the time delay line, the spot diameter beam of the pump beam was greater than the window width of the chopper as a result of the beam divergence. Therefore, the modulated intensity of the pump beam was observed to be sinusoidal rather than square shaped. Therefore, the intensity of the pump beam was not constant while the chopper was open. Therefore, it was possible that the magnitude of the pulse field could vary during the time that the chopper was open. To achieve a square shaped intensity modulation, the pump beam was focused and re-collimated using lenses L_1 and L_2 of focal length $f \sim 8$ cm separated by $2f$. The chopper was positioned near the focal point between the lenses where the spot diameter of the beam was smaller than the window width of the chopper. By using a square wave modulation of the pump beam intensity, the magnitude of the pulsed field was expected to be consistent for all transmitted pump pulses.

After setting up a time-resolved experiment it is often necessary to adjust the position of zero time delay. Usually it is desirable for zero time delay to be near the start of the scan so that only a minimal amount of negative time delay is measured (Figure 3.6.4). Mirrors M_8 and M_9 were used to add or remove a few centimetres of optical path. Finally the pump beam was directed towards the pulsed field device using mirror M_{10} .

The pulsed field device and samples were mounted together on a sample stage with manual x , y , z position control to locate microscale samples and arrays under the

focused probe beam. The sample stage was positioned between the pole pieces of an electromagnet capable of applying magnetic fields of ~ 2 kOe. The coils of the electromagnet were water cooled to prevent overheating while producing large magnetic fields. The magnetic field was applied in-plane and could be applied along any azimuth direction about the optical axis of the probe beam.

To acquire images of the sample, a three axis piezoelectric flexure stage (Physik Instrumente P-509) was mounted between the manual x , y , z stages and the sample stage. The scanning range(resolution) of the flexure stage was $100\ \mu\text{m}$ (1 nm) in the x - and y -directions orthogonal to the optical axis a - a' of the probe beam, and $20\ \mu\text{m}$ (0.1 nm) in the z -direction, parallel to the optical axis. The spatial resolution of the microscope was not limited by the resolution of the flexure stage, but instead by the diffraction limited spot size of the focused probe beam. For example, using a $\times 40$ microscope objective lens, a spot size of ~ 800 nm could be achieved. Such a spot size allowed individual 637 nm square elements to be resolved by scanning the sample below the focused probe beam using the flexure stage, Figure 3.5.1(inset).

The pulsed magnetic field device

A schematic of a typical pulsed field device is shown in Figure 3.6.5. The main components of the device were the photoconductive switch and coplanar stripline (CPS). The photoconductive switch consists of two bond pads separated by a “switch region” of inter-locking Au strips of width and separation of $10\ \mu\text{m}$. A lens L_3 (Figure 3.6.2) of focal length ~ 17 cm was used to focus the pump beam onto the photoconductive switch. The focused pump spot was incident upon the switch region and covered several Au strips. A CCD camera was used to observe the focused pump spot while mirror M_{10} and lens L_3 (Figure 3.6.2) were used to position the spot on the switch region. To acquire images of reflectivity and the dynamic magnetisation, the sample (including the pulsed field device) was scanned beneath the focused probe beam using the flexure stage. In order to acquire images of the dynamic magnetisation, it was necessary for the triggering of the photoconductive switch to be maintained. Since the spot area of the pump beam was much smaller than the switch region, the focused pump beam remained within the switch region during the scan.

The switch was fabricated on an intrinsic GaAs semiconducting substrate using the following method⁵⁸. Firstly, photoresist was spun onto the substrate and exposed to ultra-violet (UV) light through a mask. Secondly, the exposed photoresist was

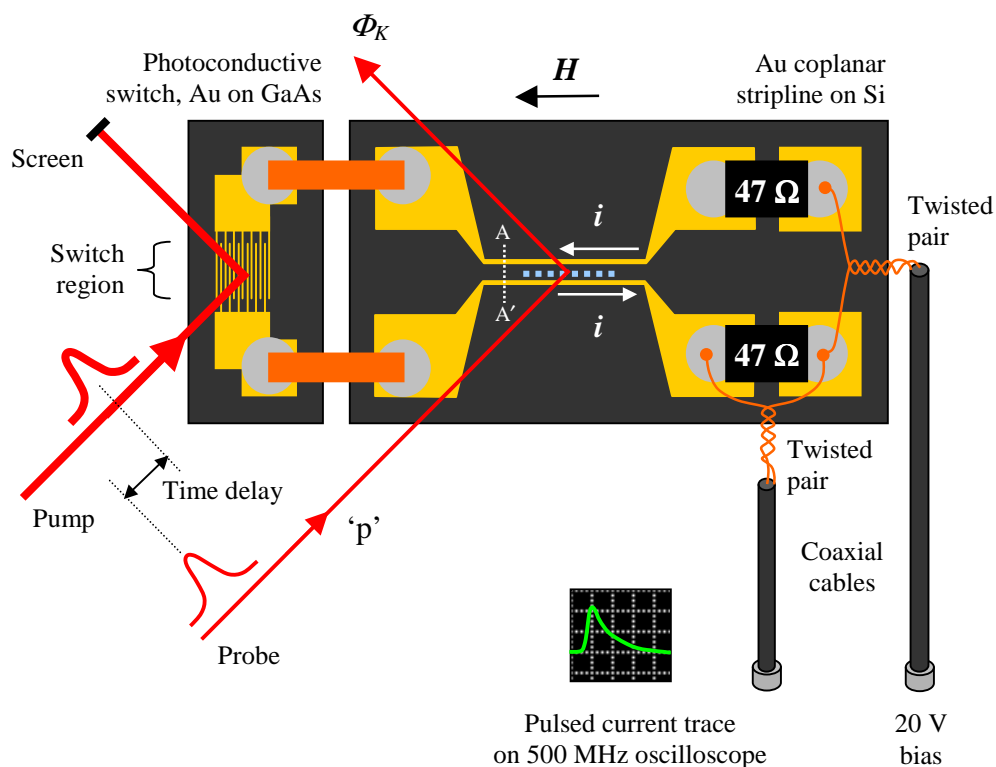


Figure 3.6.5 A typical pulsed magnetic field device is shown. The device consists of a photoconductive switch and a coplanar stripline (CPS). The pump pulse gates the biased switch allowing a current pulse to propagate along the CPS. The associated pulsed magnetic field around the CPS tracks was used to excite the sample magnetisation. The response of the sample magnetisation to the pulsed field was measured using the polar Kerr effect at each time delay so that the response could be mapped over time.

developed. Third, the Au pattern was formed by deposition in an evaporation chamber followed by lift-off of unwanted Au and photoresist. The switch was connected to a Au CPS using Cu interconnects and Ag paint. The CPS was fabricated on an insulating substrate of typically quartz or oxidised Si using similar methods as described for the switch. To minimise impedance mismatches, the CPS structure was designed to have a constant width/separation ratio for all cross-sections along its length. The width and separation at the centre of the structure in the region of the samples was $30 \mu\text{m}$. At the opposite end of the CPS to the switch, a bias voltage of typically 20 V was applied to the switch-CPS circuit via a coaxial cable and a twisted Cu pair.

The photon energy of pump pulses incident upon the switch region was sufficient to excite electrons from the valance band to the conduction band of the GaAs. Once the switch was gated, a pulsed current was able to propagate along the CPS. The

pulsed current induced a pulsed magnetic field around the CPS tracks, which was then used to excite the sample magnetisation. Figure 3.6.6(a) shows a schematic of the spatial profile of the pulsed field corresponding to the CPS cross-section AA' in Figure 3.6.5. Between the tracks of the CPS the pulsed field is out-of-plane, while above the tracks the pulsed field is in-plane. Figure 3.6.6(b) shows the calculated in-plane and out-of-plane components of the pulsed field. The peak current was assumed to be 64 mA and of uniform density within the CPS tracks. Between the CPS tracks at the sample location, the out-of-plane component of the pulsed field was calculated to be ~ 10 Oe. It should be noted that the assumption of uniform current density within the CPS is an approximation, and that within the CPS device the current propagates near to the surface of the CPS material. However, for the purpose of the work presented in this thesis, the uniform current density approximation is sufficient for the calculation of the pulsed field components.

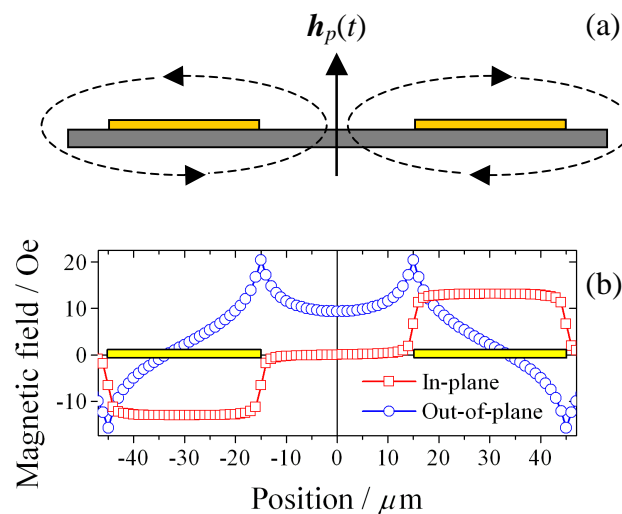


Figure 3.6.6 The spatial profile of the magnetic field is shown in (a) corresponding to the coplanar stripline cross-section AA' in Figure 3.6.5. In (b) the calculated profiles of the in-plane and out-of-plane components of the pulsed field are shown.

Previously, experiments have been performed to determine the rise time and decay time of the pulsed field using an electro-optic sampling measurement of an LiNbO₃ crystal⁶⁴ that was overlaid on the CPS. Typically, the rise time was estimated to be 40 ps, while the decay time was estimated to be 2 ns. However, it should be noted

that when the crystal was present, the permittivity of the region above the CPS was modified, which can then modify the pulsed field profile. The decay time is associated with the recombination time of carriers in the GaAs.

Two $47\ \Omega$ surface mount resistors were mounted at the end of each track to attenuate each current pulse and prevent reflections of the pulse at the impedance mismatch at the end of the CPS. The narrow section of the CPS was estimated from Reference 65 to have a characteristic impedance of $\sim 95\ \Omega$. In order to prevent reflections, it was necessary for the impedance of different sections of the CPS structure to be matched. Therefore, the width-to-separation ratio was maintained throughout the CPS structure. However, measurements of the potential difference across a surface mount resistor at the end of a CPS track (Figure 3.6.5) revealed that the temporal profile of the current pulse was often complicated. The complicated profile was a result of reflections in the CPS structure and the connecting circuitry. The potential difference was measured on a 500 MHz oscilloscope, which had insufficient bandwidth to resolve all features of the current pulse. However, observing the bandwidth limited trace in real-time allowed the current pulse to be optimised. For example, Figure 3.6.7 shows a large reflection about 25 ns after the main pulse. Assuming that the speed of propagation of the current pulse in a coaxial cable is equal one-third of the speed of light⁶⁵, then the reflection corresponds to an impedance mismatch in a coaxial cable 1.25 m from the device. This reflection was caused by the impedance mismatch at the power supply for the voltage bias or the oscilloscope. It was necessary to be aware of these reflections as they can give rise to coherent suppression⁶⁶ of the magnetisation dynamics. The profile of the current pulse could be improved by changing the temporal position of the reflection. This was achieved by changing the length of the cable between the pulsed field device and the power supply and/or oscilloscope. Sometimes, the temporal position of a reflection could not be changed, in which case the reflection was likely to have been caused by an impedance mismatch at the connections to the bond pads (Figures 3.6.5). Generally, the profile of the current pulse could be improved sufficiently so that experiments could be performed successfully.

In addition to the current pulse profile, the amplitude and duration of the current pulse were also difficult to control. Initially the amplitude of the current pulse was optimised by adjusting the position and focus of the pump beam on the photoconductive switch. The current pulse amplitude could also be increased by increasing the bias voltage. Typically, a bias voltage of 20 V was used, however 25-30 V was used in some experiments. However, large bias voltages can result in permanent damage to the

photoconductive switch resulting from dielectric breakdown. The performance of each photoconductive switch was tested prior to use in the pulsed field device. The dc resistance was measured in darkness, and then under a desk lamp. Typically, the resistance of a good switch was $> 10 \text{ M}\Omega$ in darkness, which reduced to about $10 \text{ k}\Omega$ under the desk lamp. The difference in resistance in darkness and when illuminated was generally a good indication of the current pulse amplitude, where a larger difference in the resistance resulted in a larger pulse amplitude. The pulse amplitude measured using a 500 MHz bandwidth oscilloscope was observed to vary between $\sim 1.5 \text{ V}$ and $\sim 0.5 \text{ V}$ for a good and a poor switch respectively.

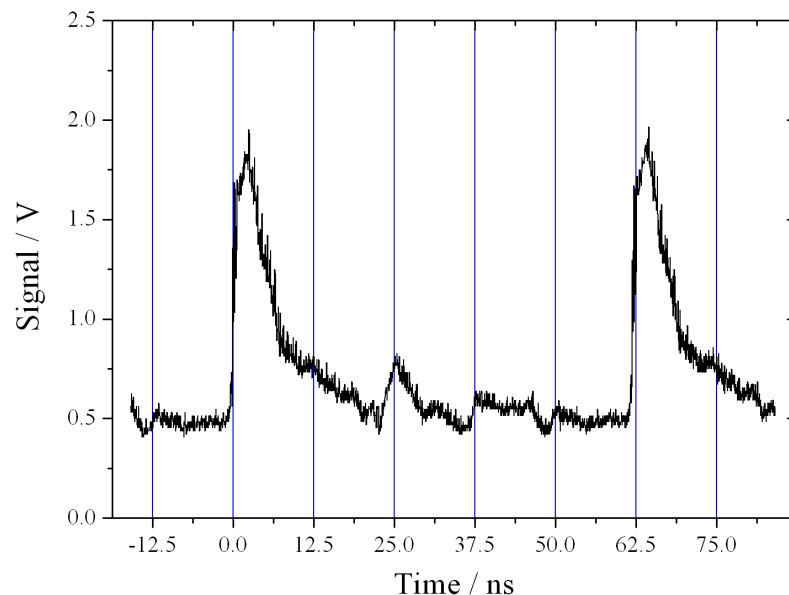


Figure 3.6.7 The current pulse profile of the CPS device used in experiments presented in Chapter 5. The signal was measured using a 500 MHz bandwidth oscilloscope.

The duration of the current pulse was limited by the carrier recombination time in the photoconductive switch⁵ in addition to reflections. The rise time was also limited by dispersion of different Fourier components of the current pulse within the CPS structure. If the rise time is too slow, the pulsed field may not couple to high frequency modes. Despite the lack of control of the current pulse duration, most of the modes of interest could be excited for the range of bias fields available since the short rise time of the pulsed field provided sufficient bandwidth.

The current pulse profile could also be optimised by using the pulse picker to reduce the repetition rate of the laser beam. For example, if a reflection of the current pulse due to an impedance mismatch is present in the pulsed field device, it may interfere with the subsequent current pulse and result in coherent suppression⁶⁶ of the pulsed magnetic field. Therefore, by reducing the repetition rate of the laser beam the time between subsequent pump pulses can be increased, which allows sufficient time for any reflections of the current pulse to be attenuated. For example, in Figure 3.6.7, four out of every five laser pulses are picked (also see Figure 3.6.3), where the temporal position of the laser pulses are shown as vertical blue gridlines. Reducing the repetition rate of the laser beam reduces the average power of the pump and probe beam. While the energy of each pump pulse incident upon the photoconductive switch remains approximately the same, the Kerr signal output from the bridge detector is reduced since it is an average of fewer probe pulses.

For the pump and probe pulses to arrive at the sample at the same time during the time-resolved scan, *i.e.* to observe zero time delay, the two pulses must have the same optical path length during the scan. The probe beam was passed along a fixed delay (not shown) between mirrors M_{11} and M_{12} to compensate for the additional optical path length of the pump beam. After the probe beam was reflected from mirror M_{12} it was passed through a polariser so that the direction of the electric field was well defined. The probe beam was then expanded using planar-concave lens L_4 and planar-convex lens L_5 . The beam diameter was then selected using aperture A_3 prior to entering the polar Kerr microscope. The polar Kerr microscope has previously been described in detail in Section 3.5. The microscope was focused manually using two rack and pinion stages. Coarse focusing was performed using a stage of 30 mm travel while finer focusing was performed with a stage of 2 mm travel. To optimise the focus of the microscope the z -axis of the flexure stage was used, but was limited to 20 μm of travel.

At a laser repetition rate of 80 MHz and chopper frequency of 2 kHz, each cycle of modulation of the pump beam corresponds to 40×10^3 pump and probe pulses. In the first half of the cycle, 20×10^3 pump pulses were transmitted through the chopper window and used to trigger the pulsed field device. In the second half of the cycle, the remaining 20×10^3 were blocked, and the magnetisation was not excited. All 40×10^3 corresponding probe pulses entered the bridge detector. However, only the first 20×10^3 probe pulses carried information of the out-of-plane component of the dynamic magnetisation. There was no polar Kerr rotation of the 20×10^3 probe pulses of the

second half of the cycle since the pulsed field device was not triggered when the pump beam was blocked. The 10 kHz bandwidth of the bridge detector electronics was insufficient to measure the Kerr rotation of individual probe pulses, but instead the average Kerr rotation of many pulses was measured. The Kerr signal output from the bridge detector oscillated at the modulation frequency between a finite Kerr voltage and zero. The lock-in amplifier was used to detect the change in the Kerr signal using phase sensitive detection (PSD) with the monitor output from the chopper electronics as the reference frequency. The measured polar Kerr signal at each time delay was the average over a few hundred to a few thousand modulation cycles. That is, the integration time constant of the lock-in amplifier was typically $\sim 0.5\text{-}2$ s. The time constant (τ_c) was strongly sample dependent. Continuous films and microscale elements required $\tau_c = 0.5\text{-}1$ s, while microscale arrays required $\tau_c = 1\text{-}2$ s or greater.

3.7 Experimental limitations and modifications

In order to enhance the signal-to-noise ratio of the experiment, some improvements were made to the set-up and the experimental procedures. In TRSKM measurements, the sources of noise were typically mechanical, optical, or electrical. In this section I will describe some particular sources of noise and outline the action taken to eliminate their effect on the measurements. To monitor the noise, a negative time delay was set for which the Kerr signal was expected to be zero (Figure 3.6.4). The front panel of the lock-in amplifier was then used to monitor the “background” Kerr signal from the bridge detector. Action was then taken to reduce the background signal (noise) observed on the front panel. Typically τ_c was set to 0.5 s so that the effect of any action could be readily seen.

Mechanical drift

The performance of the TRSKM was continuously hindered by mechanical drift and vibration. While it was not possible to completely eliminate these mechanical effects, the extent to which they affected the experiment could be minimised. Immediately after mounting a sample, the mechanical stages used for coarse positioning of the sample and focusing of the microscope would exhibit several micrometers of drift as they relaxed. Non-influencing locks were used on the x , y and z stages to reduce the

initial drift of the sample. A similar home made lock was added to the coarse rack and pinion stage to reduce the initial drift of the focus. The piezoelectric stage was used to track the sample and adjust the focus until the mechanical stages had relaxed. Typically, the initial drift was about 5-10 μm in the hour following the mounting of a sample, after which time the drift usually settled. Tracking the position of the sample, *e.g.* an array of area of $\sim 4 \times 4 \mu\text{m}^2$, was not difficult since the scan range of the x - and y -axis of the piezoelectric stage was 100 μm . However, the z -axis was limited to 20 μm of travel, and therefore it was necessary for the drift of the focus to remain within the limits of the z -axis of the piezoelectric stage. If the drift exceeded the range of the z -axis, it was necessary to recover the focus by carefully adjusting the fine rack and pinion stage and the flexure stage concurrently. The initial drift could not be avoided, but it was possible to become familiar with the direction, magnitude, and duration of the drift. The co-ordinates of the piezoelectric stage could then be set prior to mounting the sample so that the drift was anticipated and compensated for. Familiarisation with the initial drift allowed experiments to begin with minimum loss of time while correcting for the initial drift.

Mechanical drift also occurred as a result of thermal expansion of the microscope and the sample stage throughout the day. Air conditioning was used in an attempt to stabilise the room temperature. The magnitude of the drift was about a few micrometers over a period of one day. Again, familiarisation with the drift allowed it to be anticipated and compensated for by setting the appropriate co-ordinates of the piezoelectric stage.

The sample was also susceptible to drift as a result of the current pulse propagating along the CPS and connecting circuitry. While the pump beam was continuously chopped, the sample remained in mechanical equilibrium. This can be understood if the mechanical relaxation time was longer than the chopping period (~ 0.5 ms). If the pump beam was continuously blocked the sample would drift out of focus to a new position of mechanical equilibrium. This may be understood in terms of a Lorentz force acting on the current pulse electrons as they propagate through the CPS circuitry in the magnetic field of the electromagnet. When the pump beam was blocked the current pulse was not triggered. Therefore, the Lorentz force acting on the electrons was turned off and the sample would drift out of focus. Unblocking the pump beam would trigger the current pulse again so that the Lorentz force was exerted on the electrons and the sample returned to focus.

Mechanical vibration

Mechanical vibration of the sample stage resulted in a reduced signal-to-noise ratio. Several sources of mechanical vibration were identified. Exeternal sources, *e.g.* the chiller for the laser coolant, were isolated by building the experiment on a pneumatically isolated optical table.

As described in the previous section, the pump beam was chopped using a mechanical chopper, the frequency of which was used for PSD. Any mechanical vibration of the chopper that resulted in vibration of the sample significantly reduced the signal-to-noise ratio since the frequency of the vibration was the same as the reference frequency for the PSD. To minimise the mechanical vibration of the chopper, the chopper was isolated from the optical table. The chopper was mounted on a clamp-stand that was set on the floor of the lab, while the optical table was isolated from the ground using pneumatic isolators.

The stepper motor stage used for the optical time delay also caused mechanical vibration as it moved. To minimise the influence of the vibration on the measurements, a sufficiently long settle time was implemented prior to acquiring data at a particular time-delay. Typically, τ_c was set to 1 s, while the data acquisition software observed a settle time of 4 s. For a 4 ns time-resolved scan with 400 data points, the acquisition time was 27 minutes.

When measuring patterned samples, *e.g.* arrays of sub-micrometer elements, vibration of the sample became more important than for a continuous film. This is because the amount of magnetic (elements) and non-magnetic (substrate) material beneath the focused probe spot continuously changes. The instantaneous Kerr signal therefore continuously changes. Therefore, an average Kerr signal must be recorded by setting an appropriate value for τ_c . Typically, $\tau_c = 2$ s was used in time-resolved measurements on arrays, which corresponds to an acquisition time of 53 minutes for a 400 data point scan. The mechanical vibration of the sample stage was minimised by clamping it securely to the optical table. In addition to clamping the base of the sample stage support, a frame was used to clamp the top of the sample stage support to the optical table.

Scattered pump light

As described in the previous section, the intensity of the pump laser beam was modulated at a frequency of ~ 2 kHz using a mechanical chopper. Therefore, it was

essential that scattered light from the pump beam did not enter the detector. Since the modulation frequency of the pump beam intensity and the Kerr rotation are the same, scattered pump light can significantly reduce the signal-to-noise ratio of the experiment if the modulated pump light enters the detector. A lock-in amplifier cannot differentiate between the modulated polar Kerr signal and the modulated signal due to scattered pump light. The technique used to identify sources of scattered pump light was to block the probe beam immediately after BS₁ (Figure 3.6.2) and monitor the front panel of the lock-in amplifier. Each optical component of the pump beam, starting with the photoconductive switch, was then systematically blocked using a beam dump. When the beam was blocked up-stream of the component causing the scatter, the background signal displayed on the front panel of the lock-in was reduced. Most of the scatter was usually from the chopper. Therefore, a screen S₁ (Figure 3.6.2) was placed along the pump-side of the microscope and detector optics. Also the chopper was aligned so that the scattered light was directed away from the microscope and the detector and dumped at screen S₃. Screen S₂ was placed beside the microscope objective to prevent scattered pump light from the photoconductive switch entering the microscope objective.

Other optical sources of noise

In static measurements, *e.g.* hysteresis loops measurements, no PSD scheme was used. Instead the dc Kerr signal from the bridge detector was measured. In that case stray light from fluorescence tubes and computer monitors that are modulated at low frequencies, *e.g.* 50 Hz, were isolated by turning off the lights and setting any monitors to standby. Furthermore, the experimental set-up was optically isolated from the user equipment by a labyrinth wall.

Electrical noise

A conductor carrying alternating current can transmit electromagnetic radiation, while an electromagnetic field can induce an alternating current in a conductor. Therefore, in the time-resolved experiments it was necessary to shield signal carrying conductors. Therefore, coaxial cables were used in which the central conductor was shielded by a conducting sheath connected to ground. Electromagnetic radiation emitted from a cable carrying a signal at the modulation frequency could induce electrical noise at another part of the experiment, particularly the detector electronics.

This type of electrical noise significantly reduced the signal-to-noise ratio of the experiment since the noise was at the reference frequency used for PSD. It was particularly important for coaxial cables that carried modulated signals at 2 kHz to be isolated from other electronic components. Table 3.7.1 lists the cables that may emit electromagnetic radiation at the reference frequency of the PSD. The technique used to identify the sources of electrical noise was similar to that for identifying the sources of scattered pump light. Firstly, the probe beam is blocked immediately before the detector so that only electrical signals are detected and displayed on the front panel of the lock-in. It was noted, that the main contribution to the electrical noise was the pulsed field device. It was likely that the electrical noise from the pulsed field device originated from Cable 6, the unshielded open loop parts of the twisted pair at the CPS bond pads (Figure 3.6.5). However, the electrical noise could be minimised, while the bias voltage was on. The bias voltage and bridge detector power supplies were carefully positioned at locations in the laboratory where the electrical noise was a minimum. The bridge detector power supply was placed underneath the optical table and at the opposite end to the detector, while the bias voltage power supply was positioned about 5 m away from the detector on the opposite side of the labyrinth wall to the experiment. The cables identified in Table 3.7.1 were also wrapped in Al foil in an attempt to isolate the cables further. For some cables, *e.g.* Cable 1, the additional shielding reduced the background signal, while shielding of other cables, *e.g.* Cable 3 resulted in an increase in the background signal. Therefore, a trial and error approach to the additional shielding was adopted.

Cable	Description
1	Bias voltage supply to the pulsed field device
2	Pulsed field device to the oscilloscope
3	Detector power supply to the detector
4	Detector to the lock-in amplifiers
5	Chopper control unit to the lock-in amplifier
6	Open loop of the twisted pair at CPS bond pads

Table 3.7.1 Cables that may emit electromagnetic radiation at the reference frequency of the phase sensitive detection scheme for time-resolved measurements.

3.8 Summary

In summary I have reviewed the origin and different geometries of the magneto-optical Kerr effect relevant to the experimental techniques used in the experiments presented in this thesis. I have described in detail how a balanced-photodiode, polarising bridge detector can be used to measure the polar Kerr effect and detect the out-of-plane component of the sample magnetisation. The TRSKM was then described in detail with an outline of the experimental techniques employed. Finally the limitations of the TRSKM were discussed in addition to the various actions taken to improve the signal-to-noise ratio.

“When there are two quantities, \mathbf{M} and \mathbf{H} , such that cyclic variations of \mathbf{H} cause cyclic variations of \mathbf{M} , then if the changes of \mathbf{M} lag behind those of \mathbf{H} , we may say that there is Hysteresis in the relation of \mathbf{M} to \mathbf{H} ”. – James Alfred Ewing⁶⁷

Chapter 4

Acquisition of vector hysteresis loops from microarrays of nanomagnets

4.1 Introduction

Magnetometry measurements provide the most direct means by which to quantify the magnetic parameters of ferromagnetic nano-elements and investigate their micromagnetic state. Knowledge of the magnetic ground state is a prerequisite for understanding the spectra of the magnetisation dynamics¹¹, and hence, dynamic properties such as precessional switching⁹. Magnetometry studies of nanoscale elements have previously been performed with a super-conducting quantum interference device⁶⁸ and an alternating gradient magnetometer⁶⁹. However, arrays of size $\sim 1 \text{ cm}^2$, consisting of $\sim 10^6$ elements of length $\sim 100 \text{ nm}$ and film thickness $\sim 50 \text{ nm}$, were required to produce adequate signal. The magneto-optical Kerr effect (MOKE) has been used to investigate the effect of configurational anisotropy⁷⁰⁻⁷³, inter-element separation⁷², and exchange bias²³ within arrays of nanoscale elements that are typically tens of microns in size. However, isolated microscale samples fabricated by electron beam lithography and samples integrated with microscale waveguides require a microscale probe. Such samples are used in time-resolved Kerr microscopy experiments in which a sub-micrometer optical probe and the polar Kerr effect are used to detect the out-of-plane component of the magnetisation precession, Chapter 3.

Details and results of such experiments will be given in Chapters 5, 6, and 7. In this chapter I will present static Kerr magnetometry experiments using the scanning Kerr microscope described in Chapter 3. The bridge detector described in Chapter 3 was replaced with a quadrant-photodiode polarising bridge detector (vector bridge detector) that allows hysteresis loops for the two in-plane components of the sample magnetisation (parallel and perpendicular to the applied field) to be measured simultaneously using a focused, sub-micrometer optical probe. The measurements have been successfully performed upon micro-arrays of nanomagnets, which require high sensitivity due to the low packing fraction of the nanomagnets within the arrays. Excellent mechanical stability is also necessary so that the spot remains focused at the centre of the array as the magnetic field is ramped up and down. While detectors with vector sensitivity have been used previously to image domain structures⁷⁴ and study precessional switching within microscale elements⁹, measurements of in-plane vector hysteresis loops were not reported.

4.2 Experimental and sample details

Experimental details

MOKE measurements were performed with a mode-locked Ti:sapphire laser of 785 nm wavelength. A microscope objective of numerical aperture 0.65 was used to focus the beam to a diffraction limited spot of ~ 800 nm diameter. The measured Kerr signal yields the average response of the material within the area of the spot. A three axis piezoelectric stage was used, firstly, to position the sample array beneath the focused laser spot, and secondly, to optimise the focus of the probe beam upon the sample. The reflected beam was collected and re-collimated by the microscope objective, and sampled using a non-polarising beam-splitting cube.

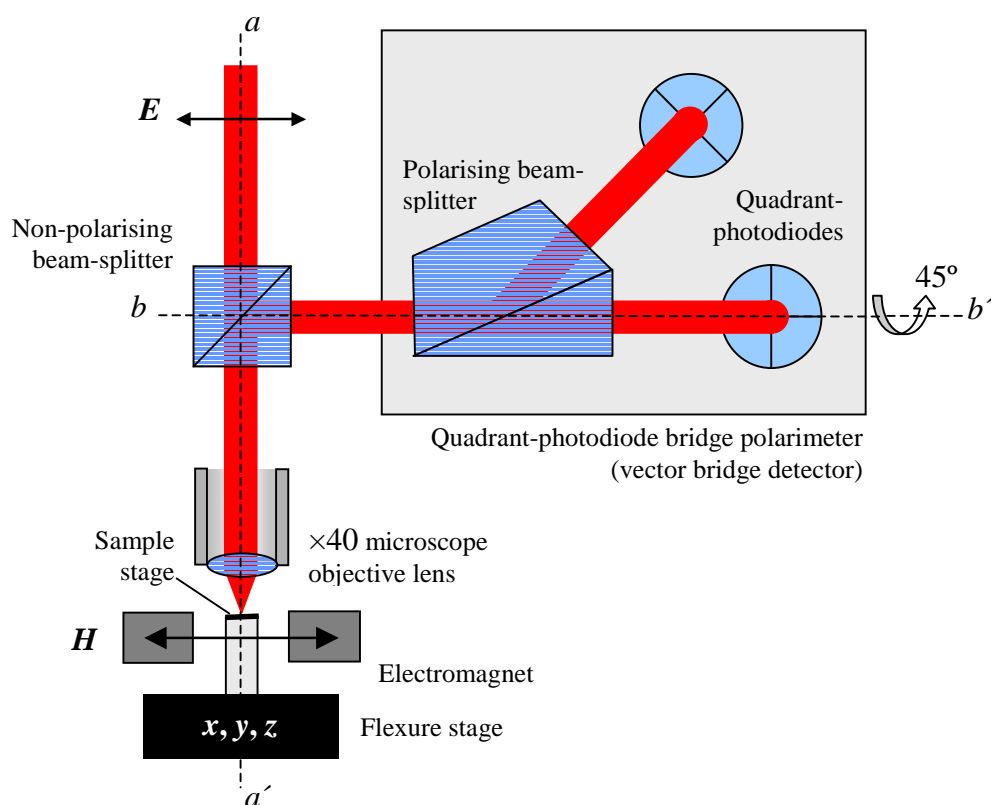


Figure 4.2.1 The geometry of the scanning Kerr microscope and the set-up of the quadrant-photodiode polarising bridge detector (vector bridge) is shown. The vector bridge is set at an angle of 45° about optical axis $b-b'$ with respect to optical axis $a-a'$.

A vector bridge detector containing a Glan-Thompson polarising beam-splitter and two quadrant-photodiode detectors (quad-detectors) was used to measure the vector magnetisation, Figure 4.2.1. Two Pacific Silicon Sensor (PSS) quadrant-photodiodes (QP) with integrated sum and difference (SD) amplifiers (model PSS-QP50-6SD) were used in the vector bridge detector. Each quadrant-photodiode had a total area of 50 mm^2 (50) and a responsivity of 0.55 A/W at a wavelength of 800 nm . It was important to ensure that the spot size falling upon the quadrant-photodiodes was large compared to the width of the inactive “gap” between quadrants. A minimum and maximum spot diameter of 1 mm and 7.8 mm respectively is recommended by the manufacturer. Typically, a spot diameter of $\sim 6 \text{ mm}$ was used since the rear aperture of the microscope objective was 6.5 mm . The integrated sum and difference amplifiers were designed and built by Pacific Silicon Sensor. Firstly, the current generated by each photodiode quadrant Q_i was converted to a voltage signal V_i using trans-impedance amplifiers with a gain of $10^4 \Omega$. The output signals corresponding to the bond pads

(Pad i) are shown in Table 4.2.1 and were generated by unity-gain sum and difference amplifiers.

Pad 1	Photodiode bias
Pad 2	$(V_3+V_4)-(V_1+V_2)$
Pad 3	$(V_2+V_3)-(V_1+V_4)$
Pad 4	$V_1+V_2+V_3+V_4$
Pad 5	+15 V
Pad 6	Ground
Pad 7	-15 V

Table 4.2.1 The table lists the pad designation for the PSS-QP50-6SD quadrant photodiode sum and difference amplifier outputs. The voltage signal V_i is the output of the integrated trans-impedance amplifier for the i^{th} quadrant. In the vector bridge detector Pads 2 and 3 are used to measure two orthogonal in-plane components of the vector magnetisation using the longitudinal MOKE. Pad 4 is used to measure the out-of-plane component using the polar MOKE. Pad 4 is also used to measure reflectivity. Pads 5, 6, and 7 supply power and a ground reference to the device. Pad 1 was not connected, but can be used to apply a bias voltage to the quadrant-photodiode.

The vector bridge detector can be used to measure three orthogonal components of the vector magnetisation simultaneously, two in-plane components, parallel (M_{\parallel}) and perpendicular (M_{\perp}) to the applied in-plane field \mathbf{H} , and an out-of-plane component (M_z). The detector was mounted on a rotary mount, which allowed the detector to be rotated about optical axis $b-b'$. The detector was set at an angle of 45° about optical axis $b-b'$ with respect to optical axis $a-a'$. As described in Chapter 3, the polarising beam-splitter was oriented so that prior to applying a magnetic field the two transmitted beams were of equal intensity, Figure 3.5.3. A change in M_z then yields a polar Kerr rotation and leads to a difference in intensity of the two transmitted beams. The sum of the four signals generated by each quadrant is output at Pad 4 of each quad-detector (Table 4.2.1) and is referred to as the intensity signal of each quad-detector. Subtracting the intensity signals from the two quad-detectors yields a difference signal that is proportional to the polar Kerr rotation and the polar component of the vector

magnetisation*. Before the magnetic field H was applied, the detector was rotated about optical axis $b-b'$ until the polar difference signal was zero (nulled). Once nulled the intensity of light falling upon the two quad-detectors was equal. However, in the geometry shown in Figure 4.2.1 the applied field is in-plane. When the field was reversed, it was assumed that the magnetisation remained in-plane. Therefore, no change in the out-of-plane component of the magnetisation was expected.

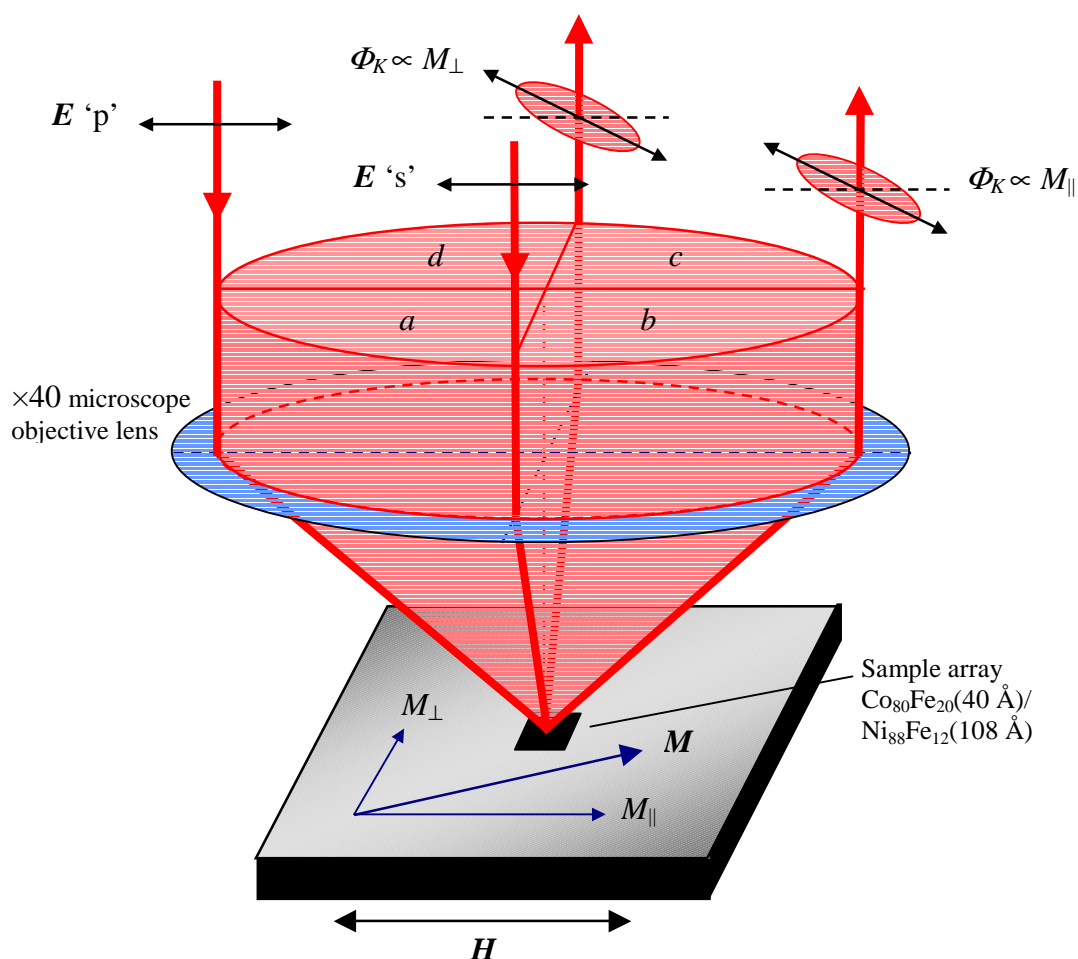


Figure 4.2.2 The geometry of the laser beam focused upon the sample is shown. When focused, the linearly polarised beam has infinite planes and angles of incidence. The highlighted ray paths show planes of incidence where the incident light is p- and s-polarised.

Typically, the longitudinal Kerr rotation is similar for p- and s-polarised light at an angle of incidence of $\sim 45^\circ$, while at normal incidence the Kerr rotation vanishes, Figure 3.4.2. Therefore, an objective lens with a high numerical aperture was chosen since a large cone angle was necessary for sensitivity to the longitudinal Kerr effect.

* The principle of detection of the polar MOKE using the vector bridge is the same as that described in Chapter 3.

The cone of rays focused onto the sample was divided into four parts, which enabled the longitudinal Kerr rotation from the two in-plane components of the vector magnetisation to be measured as shown in Figure 4.2.2. In order to sense M_{\parallel} , beam halves $(a + d) \rightarrow (b + c)$ and $(b + c) \rightarrow (a + d)$ are used, while M_{\perp} is sensed using beam halves $(a + b) \rightarrow (c + d)$ and $(c + d) \rightarrow (a + b)$. For a particular magnetisation component, the Kerr rotation induced on opposite halves of the reflected beam are equal in magnitude and opposite in sign. After transmission through the polarising beam-splitter, the changes in the intensity of the different halves of the beam must be separately sampled and combined since they would cancel if the full beam was sampled. Therefore, the quad-detectors with integrated amplifiers were required, firstly to isolate and amplify the signals from the different quadrants of the beam, and secondly, to perform particular sum and difference operations on the signals in order to recover the in-plane components of the vector magnetisation.

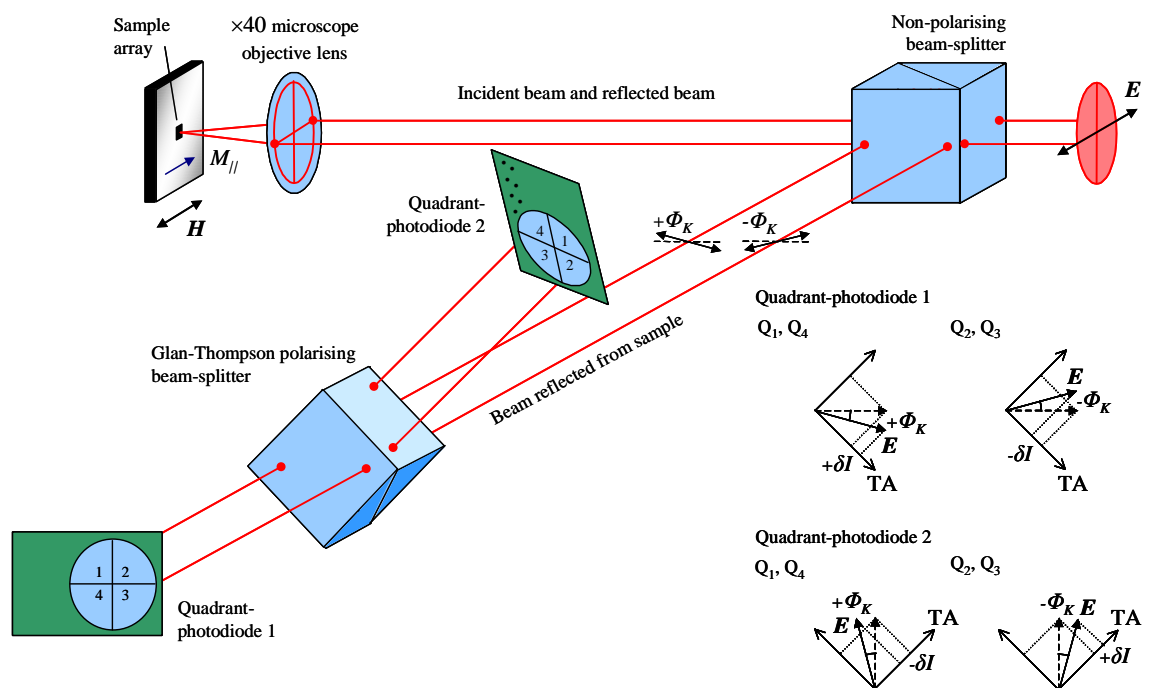


Figure 4.2.3 Ray tracings are shown for two rays from opposite halves of the probe beam that are sensitive to M_{\parallel} . Inset are schematic illustrations of the operation of the Glan-Thompson polarising beam splitter. The intensity shift δI of the electric field component parallel to the transmission axis (TA) for each transmitted beam is shown for each half of quadrant-photodiode 1 and 2.

In Figures 4.2.3 and 4.2.4 ray tracings of the vector-resolved Kerr microscope are shown. In Figure 4.2.3, two rays of opposite sides of the laser beam propagate in the horizontal plane of incidence of the microscope objective lens. As shown in Figure 4.2.2, the plane of incidence of each ray forms the longitudinal Kerr geometry in which each ray is sensitive to M_{\parallel} . Similarly, in Figure 4.2.4, two rays propagate in the vertical plane of incidence forming the longitudinal Kerr geometry in which each ray is sensitive to M_{\perp} . The important feature of Figures 4.2.3 and 4.2.4 is the projection of the halves of the beam sensitive to M_{\parallel} and M_{\perp} (as identified in Figure 4.2.2) onto the two quadrant-photodiode detectors. The quad-detector outputs at Pad 2 and 3 are shown in Table 4.2.1. It is clear from the quadrant combinations that the outputs are the differences of signals generated from opposite halves of the quad-detector. Therefore, it is important that the quad-detectors are aligned so that the division between opposite halves of the quadrant-photodiode are parallel or perpendicular to the applied field \mathbf{H} . In that way the Kerr rotation of opposite halves of the beam shown in Figure 4.2.2 can be measured.

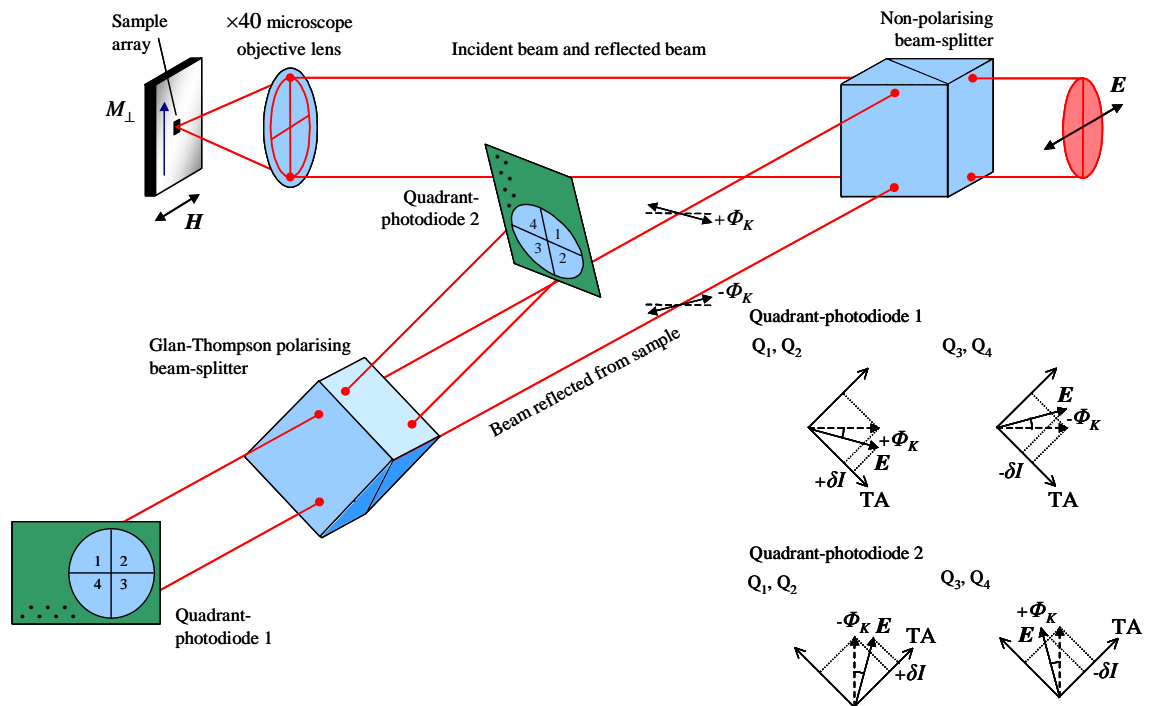


Figure 4.2.4 Ray tracings are shown for two rays from opposite halves of the probe beam that are sensitive to M_{\perp} . Inset are schematic illustrations of the operation of the Glan-Thompson polarising beam splitter. The intensity shift δI of the electric field component parallel to the transmission axis (TA) for each transmitted beam is shown for each half of quadrant-photodiode 1 and 2.

In order to sense M_{\parallel} and M_{\perp} , the correct combination of signal outputs at Pad 2 and 3 of each quad-detector must be calculated. Figures 4.2.3 and 4.2.4 show arbitrary Kerr rotations due to M_{\parallel} and M_{\perp} for two rays of the beam reflected from the sample. As in Chapter 3, the Kerr rotation will be discussed from the perspective of the detector, *i.e.* looking upstream, opposite to the direction of beam propagation. Figure 4.2.3 and 4.2.4 reveal the particular halves of the quadrant-photodiodes that the rays sensitive to M_{\parallel} and M_{\perp} fall upon. Inset are schematics of the operation of the polarising beam-splitter. The polarising beam-splitter allows a selected polarisation state (*e.g.* p-polarised) to be transmitted and continue along the original beam direction, while the orthogonal polarisation state (*e.g.* s-polarised) is reflected and exits the prism along an optical axis that is oriented 45° from the original beam direction. As described in Section 3.5, the beam-splitting polariser is rotated 45° about optical axis $b-b'$ with respect to optical axis $a-a'$ so that the two transmitted beams are of equal intensity before applying a magnetic field. The intensity of the electric field of the two transmitted beams prior to applying a magnetic field is then $\propto \cos^2(\pi/4) = 1/2$.

Now consider what happens when a magnetic field is applied. In Figure 4.2.3 for the two rays shown, the Kerr rotation Φ_K is proportional to M_{\parallel} , but is equal and opposite in opposite halves of the beam. The intensity of the electric field that falls upon the opposite halves Q_1+Q_4 and Q_2+Q_3 of quadrant-photodiode 1 is

$$I_{Q_1+Q_4} \propto \cos^2(\pi/4 - \Phi_K) \quad (4.2.1)$$

and

$$I_{Q_2+Q_3} \propto \cos^2(\pi/4 + \Phi_K) \quad (4.2.2)$$

respectively, where Q_i ($i = 1,2,3,4$) are the quadrant labels according to the specifications supplied by the manufacturer. Similarly, the intensity that falls upon opposite halves of quadrant-photodiode 2 is

$$I_{Q_1+Q_4} \propto \cos^2(\pi/4 + \Phi_K), \quad (4.2.3)$$

and

$$I_{Q_2+Q_3} \propto \cos^2(\pi/4 - \Phi_K) \quad (4.2.4)$$

respectively. Using a trigonometric identity for $\cos(\alpha \pm \beta)$, Equation 4.2.1 may be written as

$$I_{Q_1+Q_4} \propto [\cos(\pi/4) \cdot \cos(\Phi_K) + \sin(\pi/4) \cdot \sin(\Phi_K)]^2, \quad (4.2.5)$$

where Φ_K is typically small so that Equation 4.2.5 may be written as

$$I_{Q_1+Q_4} \propto \left[\frac{1}{\sqrt{2}} + \frac{1}{\sqrt{2}} \cdot \Phi_K \right]^2. \quad (4.2.6)$$

Expanding the square and neglecting second order terms in Φ_K gives

$$I_{Q_1+Q_4} \propto \frac{1+2\Phi_K}{2}. \quad (4.2.7)$$

Similarly for Equation 4.2.2, we obtain

$$I_{Q_2+Q_3} \propto \frac{1-2\Phi_K}{2}. \quad (4.2.8)$$

Table 4.2.1 shows that the quad-detector signal output at Pad 3 is proportional to the difference signal $(V_2+V_3)-(V_1+V_4)$. For quad-detector 1 (QD1), such an operation yields

$$[(V_2 + V_3) - (V_1 + V_4)]_{\text{QD1}} \propto \frac{1-2\Phi_K}{2} - \frac{1+2\Phi_K}{2} = -2\Phi_K, \quad (4.2.9)$$

where Φ_K is proportional to M_{\parallel} . A similar analysis of quad-detector 2 yields

$$[(V_2 + V_3) - (V_1 + V_4)]_{\text{QD2}} \propto \frac{1+2\Phi_K}{2} - \frac{1-2\Phi_K}{2} = 2\Phi_K, \quad (4.2.10)$$

which has opposite sign to Equation 4.2.9. The output signal at Pad 2 of each quad-detector has a magnitude proportional to $|2\Phi_K|$ since the Kerr rotation is measured using two rays on opposite sides of the beam. In contrast, a conventional longitudinal MOKE geometry uses a single ray (or equivalently, beam), Figure 3.4.1.

The outputs of the vector bridge detector are listed in Table 4.2.2. Outputs 1-7 are used for the alignment of the detector. In particular, Pad 2 and 3 of each quad-detector are used to align (centre) the quadrant-photodiodes with the transmitted beams from the polarising beam-splitter. Pad 4 of each quad-detector and their difference are then used to align the polarising beam-splitter at 45° so that the intensity of light falling

upon quadrant-photodiodes 1 and 2 is equal. Measurements of reflectivity are made by summing outputs at Pad 4 of both quad-detectors. For measurements of the vector magnetisation components (M_{\parallel} , M_{\perp} , and M_z) the listed combinations of Pads 2, 3 and 4 at outputs 7-9 are used.

1	(Pad 2) _{QD1}	Alignment of quadrant-photodiode 1
2	(Pad 2) _{QD2}	Alignment of quadrant-photodiode 2
3	(Pad 3) _{QD1}	Alignment of quadrant-photodiode 1
4	(Pad 3) _{QD2}	Alignment of quadrant-photodiode 2
5	(Pad 4) _{QD1}	Alignment of the polarising beam-splitter
6	(Pad 4) _{QD2}	Alignment of the polarising beam-splitter
7	(Pad 4) _{QD2} – (Pad 4) _{QD1}	Alignment of the polarising beam-splitter Polar MOKE (M_z) measurements
8	(Pad 3) _{QD2} – (Pad 3) _{QD1}	Longitudinal MOKE (M_{\parallel}) measurements
9	(Pad 2) _{QD2} + (Pad 2) _{QD1}	Longitudinal MOKE (M_{\perp}) measurements
10	(Pad 4) _{QD2} + (Pad 4) _{QD1}	Reflectivity measurements

Table 4.2.2 The table lists all ten outputs of the vector bridge detector and their corresponding experimental function.

The pad combinations listed in Table 4.2.2 for outputs 7-9 are advantageous for two reasons. Firstly, the Kerr rotation signal will be a factor of two larger⁶⁰ than if a single quad-detector was used. Secondly, any intensity noise of the laser beam can be rejected by the difference operation, which is often referred to as common mode rejection⁶⁰. In the case of detecting M_{\parallel} (as shown in Figure 4.2.3) a difference amplifier was used to perform the following operation

$$\left(\text{Pad } 3\right)_{\text{QD2}} - \left(\text{Pad } 3\right)_{\text{QD1}} \propto 4\Phi_K . \quad (4.2.11)$$

where the output signal is a factor of two larger than the individual output signals from Pad 3 of quad-detectors 1 and 2.

A similar analysis for the rays shown in Figure 4.2.4, which form a plane of incidence parallel to M_{\perp} , is shown in Appendix 1. The only subtle difference in the analysis is due to the configuration of quad-detector 2 within the vector bridge detector. For the convenience of making electrical connections to the bond pads, quad-detector 2 is rotated 180° with respect to quad-detector 1 (or upside-down), which can be seen in Figure 4.2.4 (and 4.2.3). Consider quadrant-photodiode half Q_1+Q_2 of quad-detector 1 and 2. It is clear from Figure 4.2.4(inset) that the change in intensity δI is of the same sign for each quad-detector. Subtracting the signals from Pad 2 of each quad-detector would yield no magneto-optical signal. The correct combination of the quad-detector outputs at Pad 2 is in fact their sum.

Sample details

Measurements were made upon single microscale elements and arrays of nanoscale elements. The samples (wafer reference number A87) were fabricated by Dr Jeffrey Childress* and Dr Jordan Katine*. The arrays were square, with length $\sim 4 \mu\text{m}$, and consisted of square elements of length(separation) 124(30), 236(77), 428(17) and 637(25) nm, while the single square elements had lengths of 2, 4, 6 and $10 \mu\text{m}$. The elements and arrays were formed from a Ta(50 Å)/Al₂O₃(10 Å)/Co₈₀Fe₂₀(40 Å)/Ni₈₈Fe₁₂(108 Å)/Ta(100 Å) film sputtered onto a Si wafer and patterned by electron beam lithography and ion milling. The sample had a similar composition to the free layer of a hard-disk read-head sensor⁷. A continuous film coupon reference sample (coupon reference number SA0522D) was co-deposited onto a 1" diameter glass substrate. The Al layer was oxidised in O₂ at 500 mTorr for 15 minutes. A uniaxial anisotropy was induced in the sheet material by field annealing prior to fabrication of the elements.

Scanning electron microscopy (SEM) images of the arrays were acquired by Dr Andrew Murray**. The SEM images are shown in Figure 4.2.5. Figures 4.2.5(h) to (j) clearly show that element edge roughness and rounding of element corners become more significant as the element size is reduced. From the SEM images the radius of rounding was found to be ~ 15 nm for all element sizes.

* Hitachi Global Storage Technologies, San Jose Research Center, 3403 Yerba Buena Road, San Jose, California 95135

** School of Physics, University of Exeter, Stocker Road, Exeter, EX4 4QL

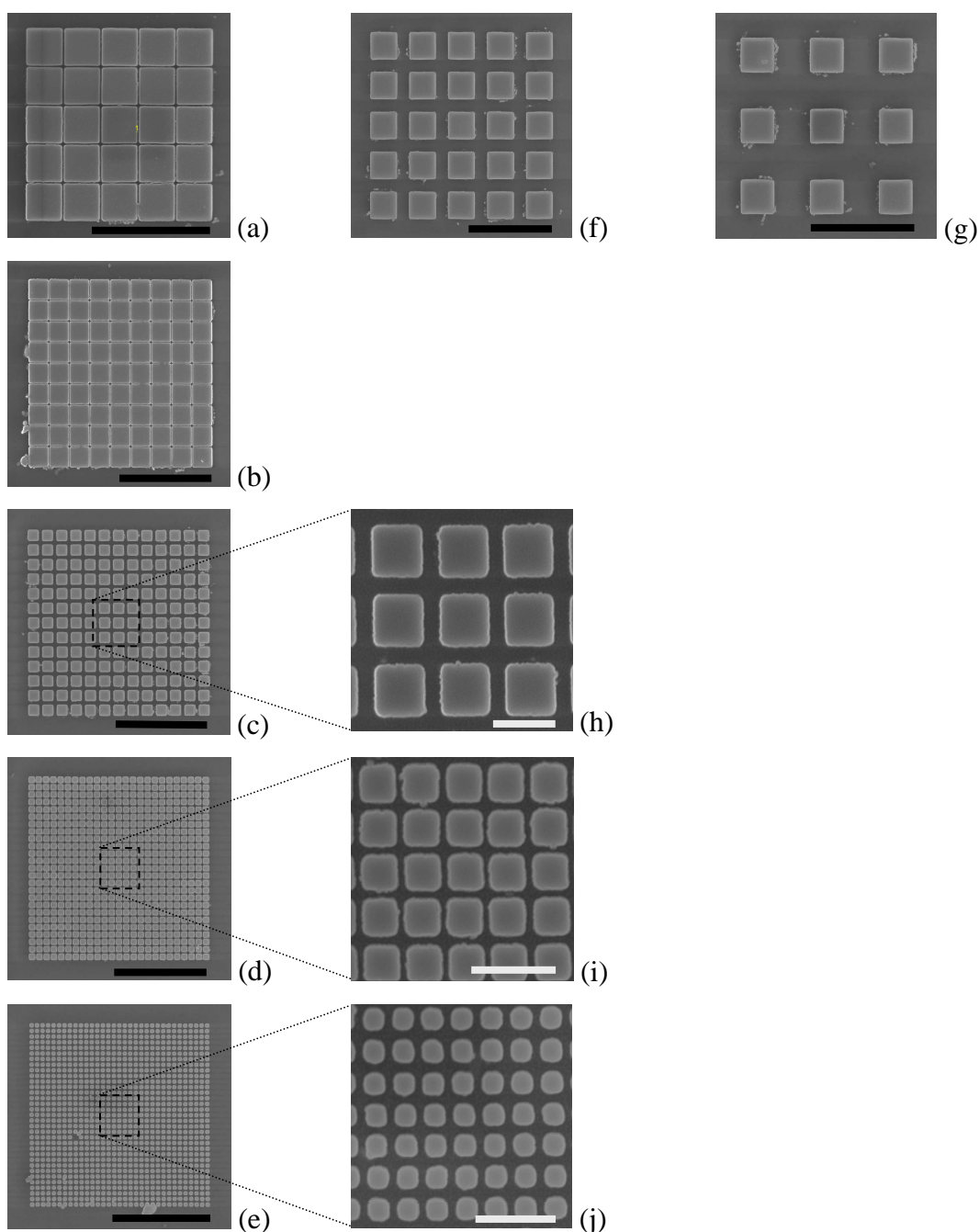


Figure 4.2.5 Scanning electron microscopy (SEM) images of arrays of square elements of length(separation) 637(25), 428(17), 236(77), 124(30) and 70(37) nm are shown in (a) to (e) respectively. SEM images of arrays of 637 nm elements with separation 236 nm and 688 nm are shown in (f) and (g) respectively. The length of the black bar in each image is $2\ \mu\text{m}$. SEM images with higher magnification are shown for the 236, 124, and 70 nm elements in (h) to (j) respectively. The length of the white bar in each image is 300 nm. The higher magnification images clearly show that the element edge roughness and rounding of element corners became more significant as the element size was reduced. Measurements of vector hysteresis loops from the array of 70 nm elements were unsuccessful.

4.3 Results and Discussion

Prior to the magnetometry experiments it was necessary to ensure that the measured signals output from the vector bridge detector were proportional to the Kerr rotation, and hence, the in-plane components of the vector magnetisation. To do this both in-plane magnetic signals were measured as a function of the polarisation of the incident laser beam. A quarter waveplate was inserted into the probe laser beam upstream of the non-polarising beam-splitting cube and the linear polariser. The quarter waveplate was set so that the beam was approximately circularly polarised so that the intensity of the beam transmitted by the polariser was approximately constant. For the M_{\parallel} signal, half of the beam was blocked vertically so that only one of the two rays shown in Figure 4.2.3 entered the detector. Similarly for the M_{\perp} signal, half of the beam was blocked horizontally. Blocking half of the beam resulted in the longitudinal Kerr geometry shown in Figure 3.4.1 to be set up beneath the microscope objective. By rotating the polariser the linearity of each in-plane signal to a polarisation rotation, and hence M_{\parallel} and M_{\perp} , could be established.

In Figure 4.3.1 the in-plane signals are shown as a function of the polariser angle. The important features are the linear regions near to the angles of 176° and 356° for which the electric field E (or polarisation) of the probe beam is respectively parallel and perpendicular to the applied magnetic field. These are also the polariser angles at which the two transmitted beams from the polarising beam-splitter in the vector bridge detector are of equal intensity. The Kerr rotation Φ_K is typically small (~ 10 millidegrees). Therefore, in the region about the polariser angle of 176° or 356° , the in-plane signals can be assumed to be linearly proportional to Φ_K , and hence M_{\parallel} and M_{\perp} .

In the following, the labelling convention of Figure 4.2.2 is used to describe the halves of the beam beneath the microscope objective that are sensitive to M_{\parallel} and M_{\perp} and that produce the presented hysteresis loops. This is more straightforward than tracing the rays back to particular halves of the quadrant-photodiodes in the vector bridge detector in Figures 4.2.3 and 4.2.4.

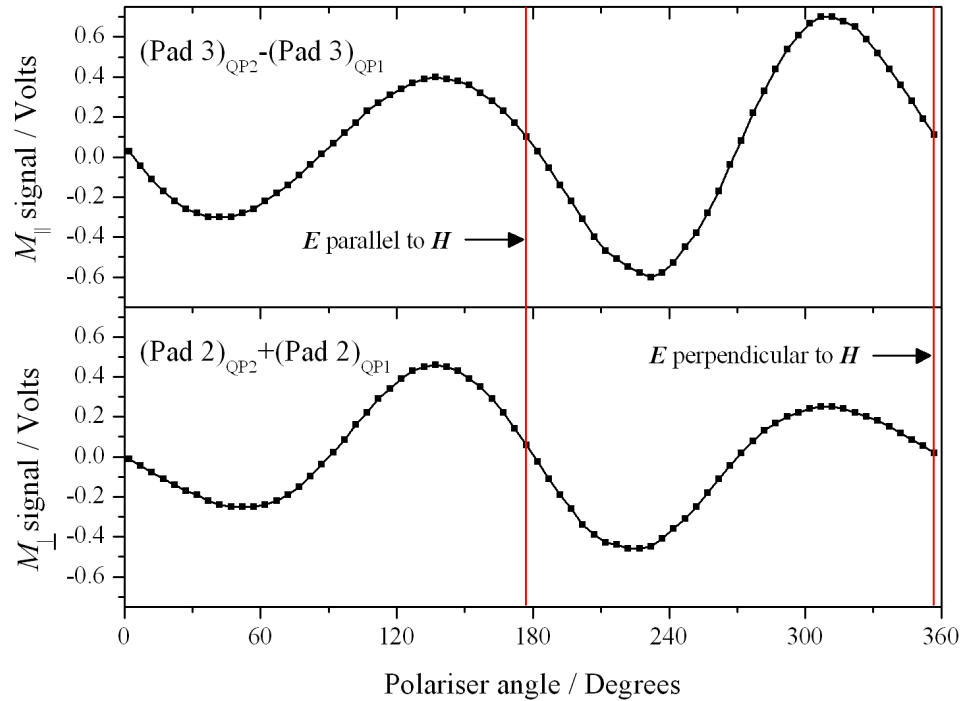


Figure 4.3.1 Outputs of the vector bridge detector, used to detect the in-plane components of the vector magnetisation, are shown as a function of polariser angle. A quarter waveplate was used upstream of the polariser so that the intensity of the probe laser beam was almost constant as the polariser was rotated.

Figure 4.3.2 shows M_{\parallel} and M_{\perp} hysteresis loops acquired simultaneously from the continuous film reference coupon. The loops demonstrate the successful detection of the components of the vector magnetisation parallel and perpendicular to the applied field. The magnetic field was applied parallel to the hard axis for which the sample magnetisation is expected to exhibit a coherent rotation when the field is reversed. The M_{\parallel} loop (Figure 4.3.2(a)), sensed with the halves of the beam $(a + b) \rightarrow (c + d)$ and $(c + d) \rightarrow (a + b)$, and the M_{\perp} loop (Figure 4.3.2(b)), sensed with the halves of the beam $(a + d) \rightarrow (b + c)$ and $(b + c) \rightarrow (a + d)$, have the form predicted by the Stoner-Wohlfarth model³³. When the sample and applied field are rotated through 90° , M_{\parallel} is instead sensed by $(a + d) \rightarrow (b + c)$, while M_{\perp} is sensed by $(a + b) \rightarrow (c + d)$. Figures 4.3.2(c) and (d) show that the M_{\parallel} and M_{\perp} loops obtained with the orthogonal halves of the beam are now swapped over, conclusively demonstrating that two orthogonal in-plane components of the vector magnetisation are detected. The slight differences in the loop shape for M_{\parallel} in Figures 4.3.2(a) and (c), and M_{\perp} in

Figures 4.3.2(b) and (d), are attributed to a slight change in the alignment of the reflected probe beam on the quadrant-photodiodes when the sample and applied field are rotated through 90° . The M_{\parallel} loops were found to be in good agreement with those obtained from inductive loop measurements made upon the reference coupon (not shown).

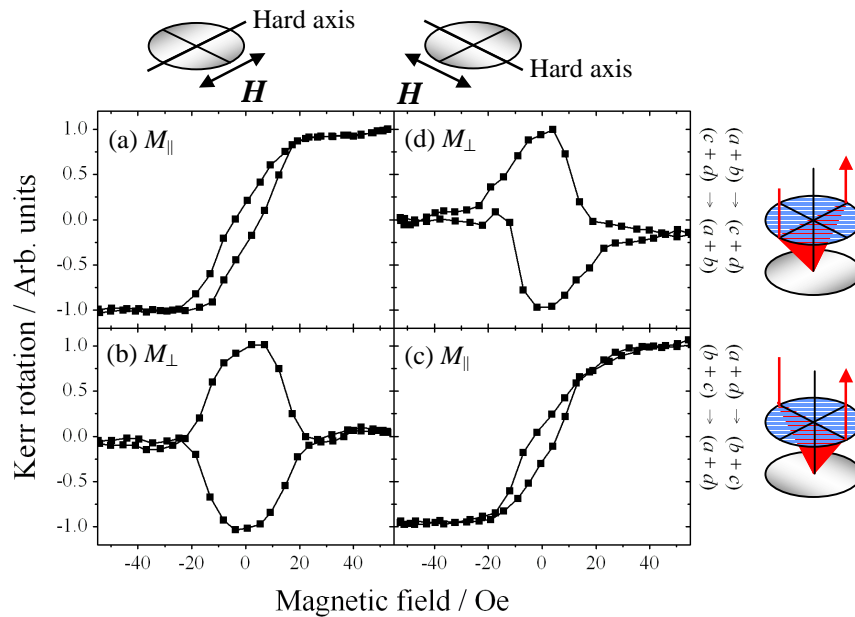


Figure 4.3.2 Hard axis M_{\parallel} (a) and M_{\perp} (b) hysteresis loops are shown for the continuous film. The M_{\parallel} (c) and M_{\perp} (d) loops are sensed by orthogonal halves of the focused laser beam (cartoon inset right) when the sample and H are rotated through 90° (cartoon inset top). While the loops are normalised here, the height of the M_{\perp} loops was found to be $\sim 80\%$ of the height of the M_{\parallel} loops.

While the hysteresis loops in Figure 4.3.2 are normalised, the height (or Kerr rotation) of the M_{\perp} loops was found to be $\sim 80\%$ of the height of the M_{\parallel} loops. In the case of coherent rotation the height of the M_{\perp} loop is expected to be the same as the M_{\parallel} loop as the magnetisation rotates through 90° with respect to the applied field. This suggests that in the continuous film reference coupon, the magnetisation is almost coherent as it switches when the applied field is reversed.

Figure 4.3.3 shows M_{\parallel} and M_{\perp} hysteresis loops acquired simultaneously from the $10\ \mu\text{m}$ element with the magnetic field applied parallel to the easy and hard axis directions. The easy axis M_{\parallel} loop is sensed by beam half $(a + d) \rightarrow (b + c)$ and has a

square shape typical of an easy axis loop (Figure 4.3.3(b)). The easy axis M_{\perp} loop sensed by beam half $(a + b) \rightarrow (c + d)$ reveal spikes that are correlated with the switching field in the M_{\parallel} loop (Figure 4.3.3(a)). When the field is applied parallel to the hard axis (Figure 4.3.3(c) and (d)), M_{\parallel} and M_{\perp} loops with shape similar to those in Figure 4.3.2(c) and (d) are obtained respectively. However, the hard axis loops for the $10 \mu\text{m}$ element have larger saturation and coercive fields. This may be attributed to dipolar fields and pinning sites associated with the edge roughness of the element.

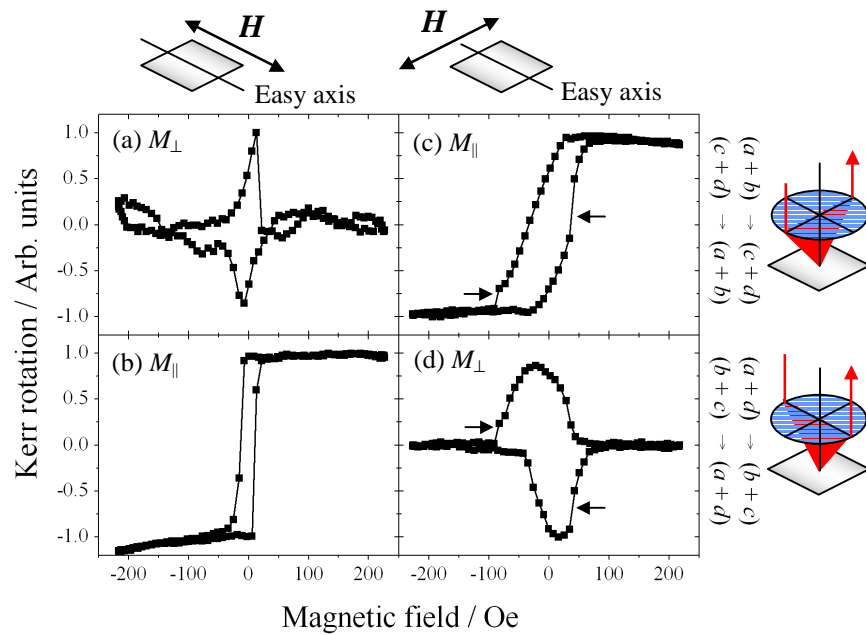


Figure 4.3.3 Easy and hard axis M_{\parallel} and M_{\perp} hysteresis loops are shown for a $10 \mu\text{m}$ single square element. Easy and hard axis M_{\parallel} loops are sensed by orthogonal halves of the focused laser beam (cartoon inset right) when \mathbf{H} is rotated through 90° (cartoon inset top). While the loops are normalised here, the height of the M_{\perp} loops was found to be $\sim 40\%$ of the height of the M_{\parallel} loops.

While the hysteresis loops in Figure 4.3.3 are normalised, the height of the M_{\perp} loops was found to be $\sim 40\%$ of the height of the M_{\parallel} loops. This suggests that the magnetisation is not switching by coherent rotation, for which the height of the M_{\parallel} and M_{\perp} loops are expected to be the same. Instead, narrow magnetic domains, with length parallel to the easy axis and perpendicular to the applied field, may exist when the field is applied along the hard axis³⁰. Within adjacent domains, the magnetisation can rotate in opposite directions as the applied field is reversed, thus reducing the net M_{\perp} signal if

more than one domain is present in the region of the focused probe beam. Dipolar fields and pinning sites associated with element edge roughness may lead to pinning of the domain walls and an increase in the saturation and coercive fields. Discrete jumps (indicated by arrows) are well correlated between the M_{\parallel} and M_{\perp} loops and may suggest the occurrence of the de-pinning and propagation of a domain wall through the sub-micron region of the focused probe beam.

Figure 4.3.4 shows easy and hard axis M_{\parallel} hysteresis loops acquired from the single elements and element arrays. Measurable M_{\perp} signals were obtained from the four largest single elements only (shown only for the 10 μm element in Figure 4.3.3). For the arrays of smaller elements, M_{\perp} signals were not clearly observed. This may be attributed to opposite magnetisation reversal within different elements so that the net M_{\perp} signal vanishes in the region of the focused probe beam. The loops in Figure 4.3.4 were obtained in the same manner as the M_{\parallel} loops of the 10 μm element. The loops shown in

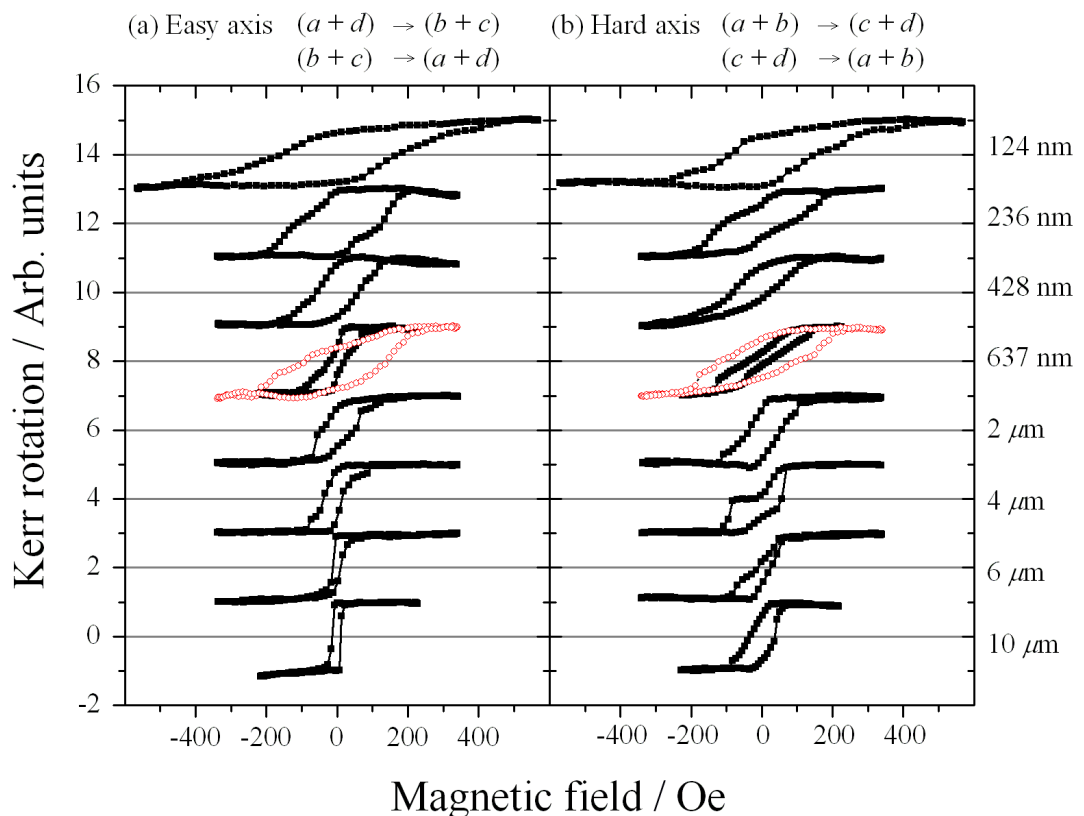


Figure 4.3.4 M_{\parallel} easy (a) and hard (b) axis hysteresis loops for all elements. For the 637 nm element, loops were acquired from two arrays with element separation of 25 nm (black filled squares) and 234 nm (red open circles). SEM images of the arrays are shown in Figures 4.2.5(a) and (f) respectively.

Figure 4.3.4(a) reveal a non-monotonic increase in coercive field from 11 Oe in the $10\ \mu\text{m}$ single element to 170 Oe in the 124 nm element array. A change from a higher coercive field in the $2\ \mu\text{m}$ single element to a lower coercive field in the 637 nm element array is observed, as shown for the easy axis loops in Figure 4.3.5. A similar change is observed for the hard axis loops (Figure 4.3.4(b)). One striking feature of the loops obtained from the nanoscale elements in arrays is that the shapes of the easy and hard axis loops are very similar, while for the single elements there remain significant differences between the loop shapes. For example, the easy and hard axis remanent magnetisation for the $10\ \mu\text{m}$ element is $\sim 100\%$ and $\sim 60\%$ respectively, while the remanence for the 124 nm element is $\sim 60\%$ for both anisotropy axes. Furthermore, asymmetric switching events are seen for the hard axis loops obtained from the three largest elements, while the five smallest elements exhibit a symmetric hysteresis loop shape. In addition, the loops obtained for the easy axis are symmetric for all elements measured, further demonstrating a greater similarity between easy and hard axis loop shapes for the smaller elements than for the larger elements.

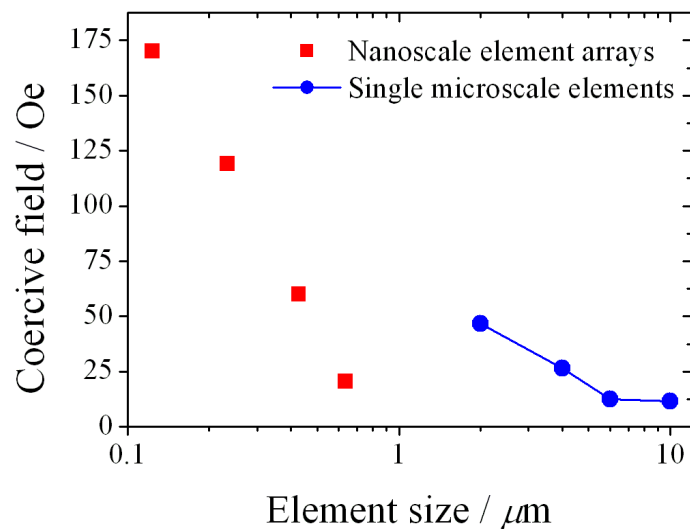


Figure 4.3.5 Evolution of the measured coercive field of easy axis M_{\parallel} loops as the element size is reduced.

As previously discussed, the similarity in the height of the M_{\parallel} and M_{\perp} hard axis loops acquired from the continuous film (Figure 4.3.2) indicate coherent rotation of the magnetisation as the applied field is swept. For the single microscale elements, the

asymmetric switching events seen for the hard axis loops (Figure 4.3.4), in addition to the reduced M_{\perp} signal, suggest that the magnetisation reverses via the nucleation, depinning, and propagation of domain walls. As described in Section 2.10, minimising the dipolar (magnetostatic) and domain wall (exchange) energy reduces the potential for the nucleation of domain walls in smaller elements. Therefore, the sudden reduction in coercive field between $2\ \mu\text{m}$ and $637\ \text{nm}$, and the similarity of the easy and hard axis loop shapes, may indicate a transition from domain wall motion to incoherent rotation of a non-uniform single domain state (Figure 2.10.5). Alternatively, the reduction in coercive field may be an effect of inter-element dipolar interactions within the arrays.

There are many factors that can affect the hysteresis loop shape. As just mentioned, inter-element dipolar interactions within arrays can significantly modify the loop shape with respect to the single element, for example by reducing the coercive field. Figure 4.2.5(a) and (f) show SEM images of two arrays of $637\ \text{nm}$ elements with an element edge-to-edge separation of $25\ \text{nm}$ and $234\ \text{nm}$ respectively. In Figure 4.3.4 for the $637\ \text{nm}$ element, the loop shown by filled black squares was acquired from the array with smaller element separation, while the loop shown by red open circles was obtained from the array with larger element separation. The loops reveal that the coercive field increases with increased element separation. Therefore, the sudden reduction in coercive field between $2\ \mu\text{m}$ and $637\ \text{nm}$ in Figure 4.3.5 may be attributed to inter-element dipolar interactions.

The similarity of the easy and hard axis hysteresis loop shape for nanoscale elements in arrays may be attributed to similar non-uniform single domain states when the magnetic field is applied along orthogonal edges of the element⁷¹. In Figure 4.3.6 simulated hysteresis loops and magnetisation configurations are shown for a single $236\ \text{nm}$ element. In Figures 4.3.6(a) and (b) the magnetic field is applied parallel and perpendicular to the uniaxial anisotropy easy axis direction respectively. In each case the magnetic field was applied 4° from the edge of the element in order to stabilise the S-state before the applied field was reversed. One striking feature of the simulated loops in Figures 4.3.6(a) and (b) is the similarity of the loop shape, which was also observed experimentally (Figure 4.3.4). While the nearest-neighbour dipolar interactions are not modeled for the single element, some insight into the switching of the nanoscale elements by incoherent rotation can be gained. As shown experimentally for the $637\ \text{nm}$ element, the dipolar interactions significantly affect the coercive and switching fields. Therefore, the agreement of the coercive and switching fields between the simulated and experimental loops was expected to be poor. In addition, edge

roughness was omitted from the model, while rounding of the element corners (with radius ~ 15 nm) was included.

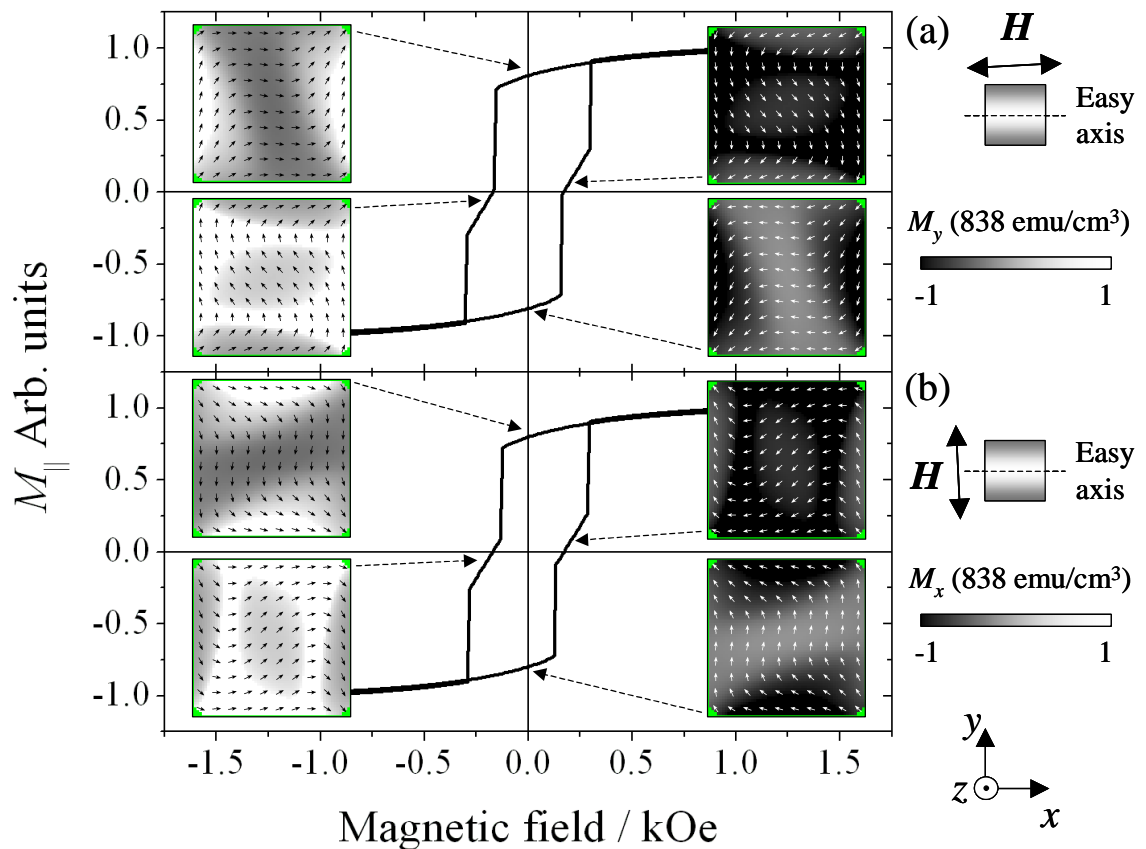


Figure 4.3.6 Simulated hysteresis loops and magnetisation configurations for a single 236 nm element. In (a) and (b) the magnetic field is applied parallel and perpendicular to the uniaxial anisotropy easy axis direction respectively. The images of the magnetisation configurations (inset) reveal that the magnetisation switches via a series of non-uniform single domain states as the applied field is reversed. In (a) and (b) the grayscale represents M_y and M_x normalised to $M_s = 838$ emu/cm³ respectively. In (a) and (b), white(black) represent $+M_y$ and $+M_x(-M_y$ and $-M_x)$ respectively. In each case the magnetic field was applied 4° from the edge of the element in order to stabilise the S-state before the applied field was reversed.

While the agreement of the coercive and switching fields is poor, the shape of the experimental and simulated loops is similar. In Figure 4.3.4, for the 236 nm element easy axis loop from $-H$ direction, the magnetisation begins to switch at ~ 0 Oe, but then enters a metastable state at ~ 50 Oe before switching to the reversed stable state at ~ 125 Oe where it saturates in the $+H$ direction at ~ 200 Oe. In Figure 4.3.6 for the easy axis loop from $-H$ saturation, the magnetisation switches to a metastable state at

~ 150 Oe before switching again to a stable state at ~ 300 Oe. As already discussed, the switching fields of the simulated loop are in poor agreement with the experimental loop. However, the general features of the experimental loops are reproduced in the simulations, which was also found for the 637, 428, and 124 nm elements.

In order to understand the similarity of the loop shape for the two directions of the applied field, magnetisation configurations of the element are shown for four different points on the loops in Figures 4.3.6(a) and (b). The magnetisation configuration at remanence, following saturation at $+1.5$ kOe parallel and perpendicular to the easy axis direction, is shown in the top-left image of Figure 4.3.6(a) and (b) respectively. In the images in Figure 4.3.6(a) and (b) the grayscale represents M_y and M_x normalised to $M_s = 838$ emu/cm³ respectively (white(black) represent $+M_y$ and $+M_x(-M_y$ and $-M_x)$ respectively). It is clear that the magnetisation configuration in each case is the non-uniform single domain S-state (Figure 2.10.5(c)). However, the S-state configurations are different when the field is applied parallel and perpendicular to the easy axis direction. In each case the magnetisation is parallel to the applied field except in the narrow regions along the edges of the element perpendicular to the applied field. As the field is reversed the magnetisation switches into a metastable S-state (Figures 4.3.6(a) and (b), bottom-left image). As the field is reversed, the magnetisation along the edges of the element rotates slightly, while the magnetisation at the center of the element rotates significantly. As the field is increased further in the reversed direction, the magnetisation switches along all edges of the element resulting in a stabilised S-state. The reversed S-state is shown at remanence (Figures 4.3.6(a) and (b), bottom-right image). As the field is reversed to the original direction, similar non-uniform switching of the magnetisation can be seen (Figures 4.3.6(a) and (b), top-right image).

The difference between the easy and hard axis behavior may be reduced further by pinning of the magnetisation at edge defects, which occurs irrespective of the applied field direction. This effect is more significant in the smallest elements. The random occurrence of the defects may also lead to the observed slanting of the experimental hysteresis loops. The slanting may result from a distribution of switching fields present in the ensemble of elements in the region of the focused probe beam. However, switching field distributions have also been attributed to a distribution of intrinsic anisotropy within arrays of nanoscale elements rather than fabrication related effects such as element edge roughness⁷⁵. Further measurements are required to isolate the effects of these different mechanisms, but are beyond the scope of this thesis.

4.4 Summary

In summary, hysteresis loops of the vector magnetisation have been obtained from continuous sheet material, individual microscale square elements, and $4\ \mu\text{m}$ arrays of nanoscale square elements using a scanning Kerr microscope of sub-micrometer spatial resolution equipped with a vector bridge detector. The measurements on sheet material have demonstrated that two orthogonal in-plane components of the vector magnetisation are sensed, and that the corresponding hysteresis loops can be measured simultaneously. A comparison of experimental loops obtained from different element sizes has revealed an increase in the coercive field as the element size was reduced in addition to a greater similarity between the easy and hard axis loop shape. However, loops for two arrays of $637\ \text{nm}$ elements with different element separation have revealed that the coercive and switching fields are sensitive to inter-element dipolar interactions. Micromagnetic simulations of hysteresis loops and magnetisation configurations within a single $236\ \text{nm}$ element have revealed that the magnetisation switches via a series of non-uniform single domain states. When the magnetic field was applied along different edges of the element, the simulated magnetisation configurations revealed that the incoherent switching mechanisms were similar, which lead to a similar hysteresis loop shape for each field direction. Since the simulations were performed for single nanoscale elements, the trends in coercive field seen for the experimental loops obtained from arrays of nanoscale elements could not be fully interpreted. Indeed the acquisition of the hysteresis loop is often a prerequisite for understanding the high frequency response of micro- and nanoscale magnetic elements. This work demonstrates that a scanning Kerr microscope equipped with a vector bridge detector is a powerful tool for the characterisation of nanomagnet arrays of very small area.

“*Simple it may be, but not ineffectual; rude, but not crude*”. – Rev. John Kerr’s response to the claim that his apparatus was comparatively simple and ineffectual when he was presented with the Royal Medal⁴⁵

Chapter 5

Use of microscale coplanar striplines with indium tin oxide windows in optical ferromagnetic resonance measurements

5.1 Introduction

Techniques such as optical ferromagnetic resonance (FMR)^{63,76,77} and pulsed inductive microwave magnetometry⁷⁸ have been developed to study the magnetisation dynamics of thin films and micrometer scale magnetic elements. A microscale coplanar stripline (CPS) or waveguide structure is used to deliver a pulsed magnetic field to the sample. In optical FMR the local magnetisation dynamics are sensed with a delayed optical probe pulse via the magneto-optical Kerr effect (MOKE). In order to experience a significant pulsed magnetic field, the sample must be brought into close contact with the CPS, which can be achieved by depositing the sample directly onto the CPS. However, this is only feasible if the sample growth is insensitive to the substrate conditions. Wider application of the technique requires that measurements be made on samples deposited on arbitrary substrates. In Reference 79, optical FMR measurements were made on spin valve structures fabricated on opaque substrates using a CPS fabricated on a transparent substrate. Because of the restricted optical access, measurements could only be made between the tracks of the CPS, *i.e.* with an out-of-plane pulsed magnetic field. However, measurements with an in-plane pulsed field are advantageous in some cases because of the stronger response of the sample

magnetisation, and are essential if precessional switching is to be observed^{9,10}. In this chapter I will present results of experiments performed using a hybrid Au/indium tin oxide (ITO, $\text{In}_2\text{O}_3/\text{SnO}_2$) CPS device fabricated on a transparent substrate. The device allows optical FMR measurements to be performed on magnetic samples grown on arbitrary substrates with both out-of-plane and in-plane pulsed magnetic fields. The use of the hybrid CPS is demonstrated in the magnetic characterisation of a 25 nm thick permalloy film grown upon a Si substrate. The response of this simple sample is also used to characterise the spatial profile of the pulsed magnetic field above the plane of the CPS.

5.2 Sample and experimental details

Sample details

The sample was fabricated by Dr. Sam Ladak*. A permalloy ($\text{Ni}_{81}\text{Fe}_{19}$) film was deposited onto a thermally oxidised Si [100] / SiO_2 (100 nm) wafer by dc magnetron sputtering from a base pressure of 5×10^{-7} Torr. A protective 20 nm thick layer of Al_2O_3 was deposited by rf sputtering. A bias magnetic field of 150 Oe was applied during the growth to induce a uniaxial magnetic anisotropy. For a preliminary characterisation of the sample, hysteresis loops were acquired in the longitudinal MOKE geometry (Figure 3.4.1) using a HeNe continuous wave laser. It was found that the permalloy film had a uniaxial anisotropy field of 6 Oe.

The hybrid Au/ITO CPS device was fabricated by Dr. Jamie Scott**. A quartz plate was pre-coated with a thin film of ITO (150 nm) of ~95% transparency and measured sheet resistance of ~30 Ω /square. Photoresist was spun onto the plate and patterned so as to form an etch mask with a track width and separation of 30 μm . The unwanted ITO was removed by dry etching in a methane/hydrogen plasma for 13 minutes at a pressure of 11 mTorr. After removal of the remaining resist, a layer of fresh resist was spun onto the plate. The new resist was exposed and developed so as to leave the full length of the CPS structure exposed apart from a $30 \times 30 \mu\text{m}^2$ region half way along each track. Next a Ti (30 nm)/Au (150 nm) bilayer was deposited and the remaining resist lifted off. Each track was 3 mm long with a DC resistance of about

* School of Physics, University of Exeter, Stocker Road, Exeter, EX4 4QL

** Department of Physics and Astronomy, University of Glasgow, Glasgow, G12 8QQ

70 Ω and had a Au-free window of 30 μm width at its center. Using Reference 65 the characteristic impedance was estimated to be about 200 Ω . Figure 5.2.1 shows an intensity image of an ITO window obtained by scanning the sample beneath the focused laser beam. The ITO window sections can be clearly seen for both tracks. The bias field \mathbf{H} was applied parallel to the CPS, while the pulsed field $\mathbf{h}_p(t)$ varied from out of plane either side of the CPS track, to in-plane above the tracks.

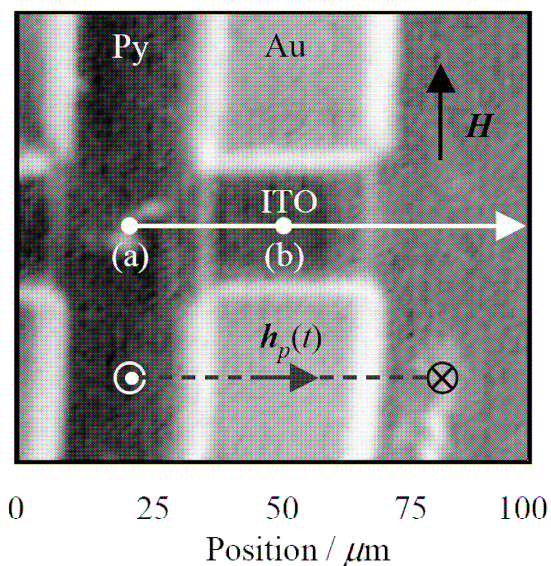


Figure 5.2.1 An optical micrograph showing a hybrid Au/ITO coplanar stripline (CPS) track. The dark grey background seen between the tracks and through the ITO window is the continuous permalloy (Py) film. Time-resolved measurements were obtained with the probe focused between the CPS tracks (a), through the ITO window (b), and at 5 μm intervals along the white arrow. The inset schematics show the orientation of the bias field \mathbf{H} and the pulsed field $\mathbf{h}_p(t)$.

Experimental details

The CPS structure was placed face down onto the sample, and the pump-probe measurements were performed at a wavelength of 790 nm using the time-resolved scanning Kerr microscope described in Chapter 3. An optically gated current pulse generated a pulsed magnetic field around the tracks of the CPS structure, after which it was absorbed in two 47 Ω surface mount resistors placed at the end of the tracks. Figure 5.2.2 shows the temporal current profile. In order to avoid overlap of the current

pulse with weaker delayed reflections from the preceding pulse, the pulse-picker (Section 3.6) was used to attenuate four out of every five laser pulses. The vertical gridlines indicate temporal separation of pump laser pulses. The complicated shape is ascribed to multiple reflections of the current pulse from impedance mismatches within the CPS and connecting circuitry.

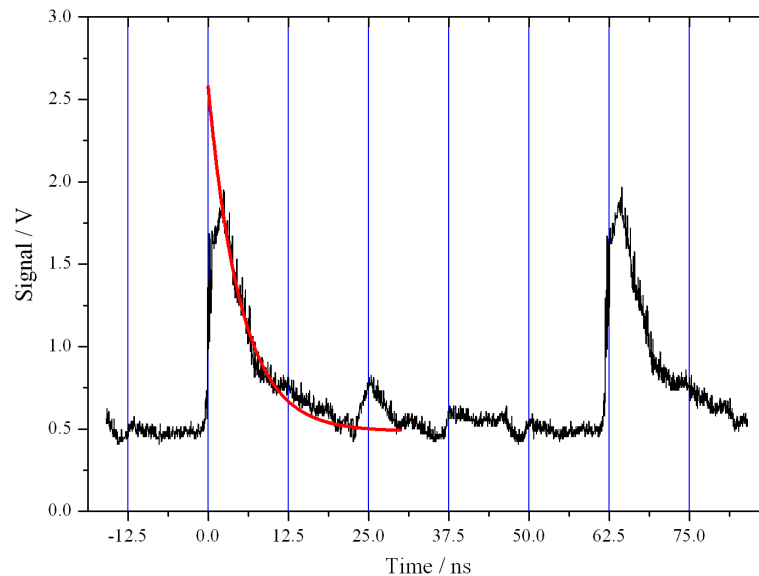


Figure 5.2.2 The complicated temporal profile of the current pulse in the CPS device. Vertical gridlines indicate temporal separation of pump laser pulses. A commercially available pulse picker was used to attenuate four of every five laser pulses. An exponential fit (red curve) of the falling edge of the current pulse is used to estimate the pulse amplitude, correcting for the limited bandwidth (500 MHz) of the oscilloscope.

The probe beam was expanded by a factor of ten, and a microscope objective of numerical aperture of 0.25 was used to focus the probe through the CPS substrate (and ITO windows) to a diffraction limited spot of about $3\ \mu\text{m}$ diameter on the sample surface. A scanning translation stage was used to position the spot at different positions upon the surface of the sample. The out-of-plane component of the magnetisation M_z was probed by means of the polar Kerr effect, using a polarising bridge detector. The measured Kerr signal was typically about 0.1-0.5 mdeg. An in-plane bias magnetic field H of variable amplitude was applied parallel to the tracks during the measurements.

5.3 Results and discussion

Figure 5.3.1(a) shows typical time-resolved Kerr signals obtained from the regions of the sample that were subject to an in-plane pulsed field, by probing through the ITO window. Figure 5.3.1(b) shows the fast Fourier transform (FFT) power spectra calculated from the time-resolved signals. The mode frequencies were extracted by fitting the spectra to a Lorentzian function, and are plotted in Figure 5.3.2 as a function of the bias field strength. The figure also shows the mode frequencies calculated in a similar manner from time-resolved signals measured between the tracks of the CPS structure where the pulsed field lies perpendicular to the plane. In each case the pulsed field was perpendicular to the bias field, and so was not expected to affect the frequency of the uniform mode precession. The frequencies measured in these two configurations are seen to agree very well.

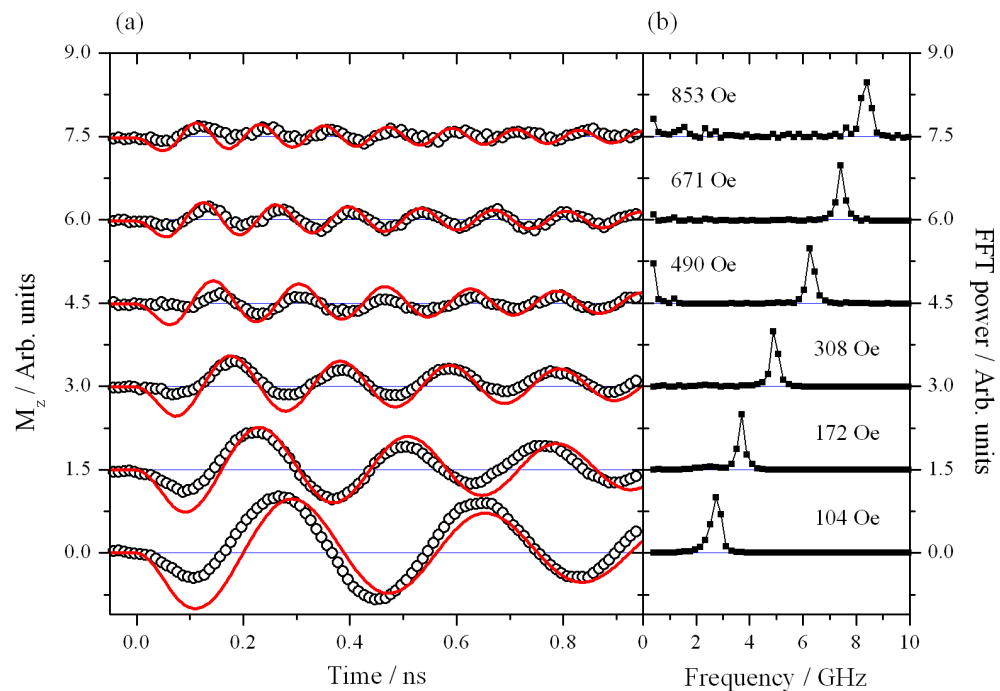


Figure 5.3.1 Typical time-resolved Kerr signals (open circles) and corresponding simulations (red line) obtained by probing through the ITO window for six different bias fields are shown in (a). A linear background has been subtracted from the signals. Fast Fourier transforms of the experimental signals in (a) are shown in (b).

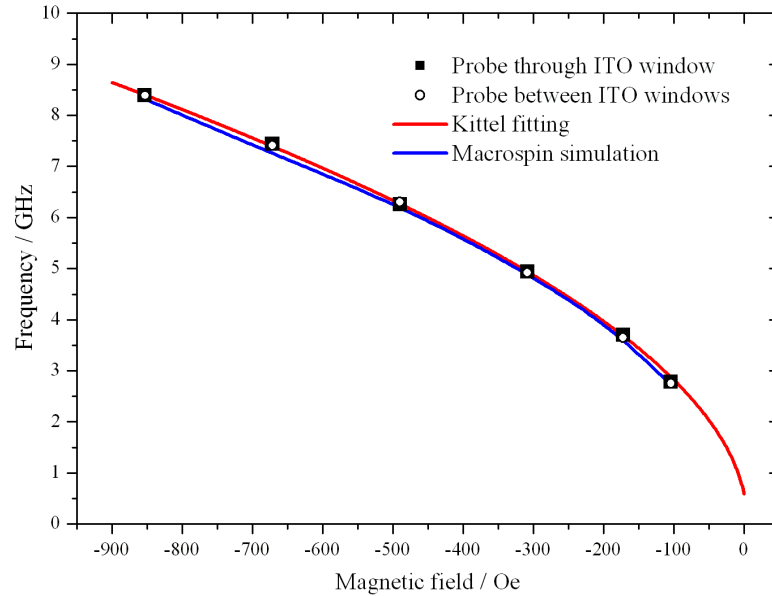


Figure 5.3.2 Dependence of frequency upon the applied magnetic field for time-resolved signals obtained by probing through the ITO window (filled squares) and between the ITO sections of the CPS (open circles).

Although the signals acquired at different positions appear similar in the frequency domain, they differ in the time domain. Figure 5.3.3 shows time-resolved Kerr signals obtained at $5 \mu\text{m}$ intervals across the CPS structure, as shown by the white arrow in Figure 5.2.1. Between the ITO sections of the tracks the pulsed field lies out-of-plane, whereas above the ITO window the pulsed field lies in the plane. Outside the tracks the pulsed field cants out-of-plane in the opposite direction to that between the tracks. Between these three configurations there is a gradual variation of the pulsed field orientation. The change of pulsed field orientation results in a variation of the initial torque exerted on the sample across the CPS. This leads to a variation in the phase of the time-resolved signals measured at different positions. The phase shift is illustrated in Figure 5.3.3 by the green symbols drawn through the first positive peak of each signal.

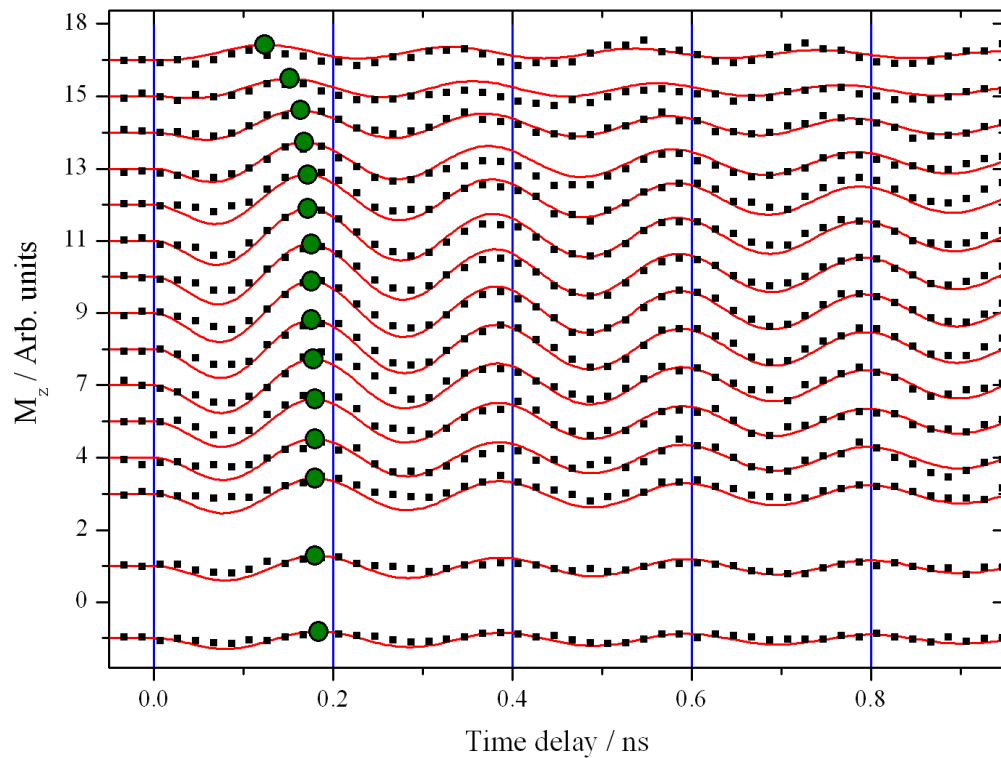


Figure 5.3.3 Time-resolved Kerr signals measured at various positions across the CPS track (symbols) with corresponding simulations (red curves). The signals from top to bottom correspond to positions at $5 \mu\text{m}$ intervals along the arrow shown in Figure 5.2.1. The green symbols illustrate the change in phase between the different signals.

In order to confirm our interpretation of the experimental results, macrospin simulations⁶² of the magnetisation dynamics of the sample at different positions under the CPS were performed. The Landau-Lifshitz equation³⁴ was solved in the small angle approximation⁷⁹ to obtain the following expression for the frequency ω of the uniform mode

$$\omega^2 = \gamma^2 \left[H \cos \phi + \frac{2K_u}{M_s} \cos(2(\phi - \phi_K)) \right] \times \left[H \cos \phi + \frac{2K_u}{M_s} \cos^2(\phi - \phi_K) + 4\pi M_s \right], \quad (5.3.1)$$

where γ , K_u and M_s are the gyromagnetic ratio, uniaxial anisotropy constant and magnetisation, respectively. The angles ϕ and ϕ_K are the angles subtended by the static magnetisation and uniaxial anisotropy axis with the applied field. The dependence of the frequency upon the bias field strength was first fitted to Equation 5.3.1 in the quasi-

alignment approximation, which assumes that the static magnetisation of the sample lies parallel to the bias field. The fitting is shown by the red curve in Figure 5.3.2. Assuming a value of 2 for the g -factor and using the measured value of the anisotropy field, a value of 770 emu/cm^2 was extracted for the magnetisation, which lies close to the bulk value⁸⁰ of 800 emu/cm^2 for permalloy ($\text{Ni}_{80}\text{Fe}_{20}$). The blue curve shows a macrospin simulation of the field dependence of the frequency in which the static orientation of the sample magnetisation was calculated using the steepest descent method. The curves are in good agreement, justifying the assumption of quasi-alignment made in the fitting. The extracted magnetic parameters were used to simulate the shape of the time-resolved signals for different values of the bias magnetic field and for different positions of the probe spot on the sample surface, as shown in Figures 5.3.1(a) and 5.3.3, respectively. The simulated dynamics of M_z shown by the curves in Figure 5.3.1(a) reproduce the reduction of frequency and the increased amplitude of the uniform mode as the applied field strength is decreased. The pulsed field was assumed to rise to its peak value after 60 ps. The in-plane and out-of-plane components of the pulsed field were calculated by integration of the Biot-Savart law over two strips of uniform current density with dimensions equal to those of the CPS tracks.

As mentioned in Section 3.6 the assumption of uniform current density within the CPS tracks is an approximation, but does allow a reasonable estimate of the components of the pulsed magnetic field across the CPS to be calculated. Since the magnetisation dynamics investigated in this thesis are in the limit of small amplitude precession, pulsed fields of only a few Oersted are sufficient for the excitation of the sample magnetisation. In the limit that $\mathbf{h}_p(t) \ll \mathbf{H}$, an estimate of the pulsed field components is sufficient. Therefore, knowledge of the particular current density within the CPS is not essential in order to successfully simulate the experimentally acquired time-resolved signals in Figures 5.3.1 and 5.3.3.

In order to estimate the peak value of the current pulse propagating along the CPS tracks, the voltage drop across one of the surface mount resistors was measured with a 500 MHz bandwidth oscilloscope (Figure 3.6.5). To account for the finite bandwidth of the instrument the decay of the pulse profile in Figure 5.2.2 was fitted to an exponential function, which yields a relaxation time of 5.1 ns. The peak voltage was taken to be the value of this exponential function at the time that the measured signal initially rose to 50% of its maximum value. An estimated peak current value of 31.4 mA was obtained using this method. The magnetic field was calculated for

heights above the CPS in the range of 0.5 to 50 μm . The best agreement between the phase and amplitude of the measured and simulated signals at different positions across the CPS structure was obtained for an assumed separation of 30 μm between the sample and CPS. At this separation the magnitude of the in-plane and out-of-plane pulsed field at the sample position was estimated to be 1.5 and 2.0 Oe, respectively. The good agreement between experiment and simulation confirmed that the orientation of the pulsed field varied between parallel and perpendicular with respect to the plane of the sample, as shown in Figure 5.3.4. Since the orientation of the pulsed field varies across the CPS track the initial torque on the sample magnetisation will vary. This causes the magnetisation to be deflected in different directions at different positions across the track. Therefore, the measured M_z will appear delayed when the magnetisation initially moves in-plane prior to canting out-of-plane.

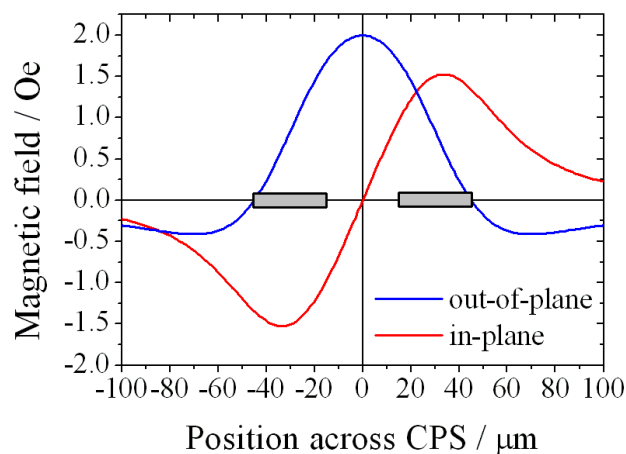


Figure 5.3.4 The calculated spatial profile of the in-plane and out-of-plane components of the pulsed magnetic field across the CPS are shown for a track-sample separation of 30 μm .

5.4 Summary

In summary, it was demonstrated that a hybrid Au/ITO CPS allows magnetisation dynamics to be studied in a sample fabricated on an opaque substrate, following excitation by either an in-plane or an out-of-plane pulsed magnetic field. It was shown that a phase shift exists in the time-resolved Kerr signals obtained at different positions across the ITO window. Macrospin simulations confirm the variation of the pulsed field between the out-of-plane and in-plane configurations.

“...thus magnetic force and light were proved to have relations to each other. This fact will most likely prove exceedingly fertile, and of great value in the investigation of conditions of nature force”. – Faraday’s laboratory notebook ⁴⁵

Chapter 6

Time-resolved investigation of magnetisation dynamics of arrays of non-ellipsoidal nanomagnets with a non-uniform ground state

6.1 Introduction

In this chapter a comprehensive study of the magnetisation dynamics of arrays of non-ellipsoidal nanomagnets will be presented. It was described in Section 2.10 how it becomes energetically favourable for small samples to possess only a single magnetic domain, and that the magnetisation and demagnetising field within the single domain is generally non-uniform. As shown in Section 2.17 the internal magnetic field in finite sized non-ellipsoidal magnetic elements is non-uniform, which introduces additional complexity into the character of the observed magnetisation dynamics. For example, the non-uniform demagnetising field may lead to the spatial confinement and quantisation of spin wave modes on the nanoscale^{11,12,39,40,81-90}. For thin film elements where the magnetisation lies in-plane, the magnitude of the static in-plane demagnetising field and the non-uniformity of the total effective field acting upon the magnetisation increases when the element aspect ratio (size/thickness) is reduced⁶³. This results in a richer mode spectrum and hence in a less uniform magnetic response to a pulsed magnetic field, which can be directly imaged in the case of micrometer sized magnetic elements⁹¹⁻⁹⁵. The dominant role of the long range magneto-dipole interaction

in the phenomena observed so far makes their analytical description complicated, and generally requires numerical solution of integro-differential equations. However, the interpretation of the magnetisation dynamics in non-ellipsoidal elements at finite bias field values becomes even more involved and challenging since it is not only the effective internal magnetic field, but also the static magnetisation that is non-uniform. This has led to the development and successful use of numerical algorithms to simulate the spatial dependence and temporal evolution of the magnetisation dynamics in thin film magnetic elements⁹⁶.

In References 11 and 85, ~ 2.5 nm thick square nanomagnets of length less than 200 nm were studied. A novel dynamical regime was observed in which the response to a uniform pulsed magnetic field was dominated by non-uniform precessional modes localised near the edges of the elements perpendicular to the direction of the bias field^{11,85} (Figure 2.17.3). Micromagnetic simulations of magnetisation dynamics in thicker elements revealed the possible existence of a greater number of modes of a more complicated character¹², and also suggested that the exact ground state of the magnetisation in the nano-elements might be the key factor in determining their dynamical properties.

In order to explore the effect of the magnetic ground state upon the mode spectrum of nano-elements in more detail, measurements (presented in this chapter) were performed on a set of samples that are similar in composition, shape and lateral size to those in References 11 and 85, but have about five times greater total thickness. Hence, the elements are characterised by a greater non-uniformity of the static magnetisation and the total effective field within the element. It was found that the precessional mode spectra vary in a discontinuous and complicated fashion as the bias magnetic field is reduced. Good agreement may be obtained between the experimental spectra and those obtained from micromagnetic simulations when the following features are included in the simulations. Firstly, imperfections of element shape are included in the simulations. Secondly, model arrays of 3×3 elements are studied so that the magnetic environment of the centre element is correctly modelled. Third, the static magnetisation state of all elements in the model array is carefully prepared by applying a similar bias field history to the model arrays as in the experiment. All three factors are found to be important in correctly reproducing the experimental spectra and ultimately understanding the evolution of the spatial character of modes excited in elements of different size and at different values of the bias field.

Despite the agreement between the experimental and simulated spectra, the assignment of the mode character becomes far less clear than in the case of the thinner elements in Reference 11. In particular, it was found that the widely adopted concept of the spin wave potential well⁴⁰ (Section 2.17) does not always correctly describe the observed behaviour. A general feature of the results presented in this chapter is the occurrence of a crossover from a quasi-uniform excitation that occupies the majority of the element volume to a regime that is dominated by several modes weakly localised near the element edges that lie perpendicular to the bias field. The transition is found to be mediated by the increasingly non-uniform static magnetisation at low bias field values, and by the associated non-uniformity of the total effective field throughout the element. This new feature of the magnetisation dynamics in non-ellipsoidal nano-elements is exhibited for all elements sizes as the bias field is reduced and has not previously been reported. Furthermore, it was found that the frequencies of modes belonging to the lower frequency branch are very sensitive to the non-uniform ground state. Indeed, from our measurements, it was possible to infer that the elements studied here occupy the S-state. The experimental spectra also reveal that the lower frequency branch exhibits significant broadening of the linewidth, particularly at low bias fields and/or small element sizes.

The increased thickness, the associated enhanced stray dipolar field, and more non-uniform magnetisation are also known to result in a stronger interaction of magnetic elements within arrays^{39,87}. The interaction has manifested itself before as extrinsic configurational anisotropy^{39,72} and as correlated switching of individual nano-elements within arrays⁹⁷. It has also been shown to lead to the splitting of normal modes of individual circular elements of 200 nm diameter within an array with 50 nm inter-element edge-to-edge separation⁸⁷. The splitting has been interpreted as the formation of collective spin wave modes within the arrays⁹⁸. The simulations presented in this chapter suggest that the increased linewidth of the lower frequency modes observed in the experiments may be associated with the presence of these collective modes.

6.2 Sample and experimental details

The samples (wafer reference number A87) were fabricated by Dr Jeffrey Childress* and Dr Jordan Katine*. The arrays were square, with length $\sim 4 \mu\text{m}$, and consisted of square elements of length (separation) 637 (25), 428 (17), 236 (77), 124 (30), and 70 (37) nm. Vector hysteresis loops acquired from these arrays have already been presented in Chapter 4. The arrays were formed from a Ta(50 Å)/Al₂O₃(10 Å)/Co₈₀Fe₂₀(40 Å)/Ni₈₈Fe₁₂(108 Å)/Ta(100 Å) film sputtered onto a Si wafer and patterned by electron beam lithography and ion milling. The sample had a similar composition to the free layer of a hard disk read head sensor⁷. The Al layer was oxidised in O₂ at 500 mTorr for 15 minutes. Uniaxial anisotropy was induced in the sheet material by field annealing prior to the post-deposition array fabrication. In order to perform pump-probe measurements, a coplanar stripline (CPS), consisting of two 300 nm thick Au transmission lines with width and separation of 30 μm , was fabricated either side of the arrays parallel to the field annealing direction. As described in Section 3.6 a pulsed magnetic field was optically triggered in the CPS device by connecting a GaAs(substrate)/Au(300 nm) photoconductive switch to one end of the CPS, while applying a bias voltage of ~ 20 V to the other end. A microscope objective of numerical aperture 0.65 ($\times 40$) was used to focus the probe beam to a diffraction limited spot with a sub-micrometer diameter. The out-of-plane component of the dynamic magnetisation was detected by measuring the polar Kerr rotation using the polarising bridge detector described in Section 3.5. The measured signal was an average response from an ensemble of elements at the centre of the array within the probed region. The amplitude of the measured Kerr rotation was typically a few tens of microdegrees. A static bias magnetic field was applied in the plane of the sample parallel to the field annealing direction and the tracks of the stripline structure. The bias field was set by reducing the field from a value of 1.5 kOe that far exceeded the saturation field observed in the in-plane hysteresis loops shown in Figure 4.3.4 that were acquired from these arrays using vector Kerr magnetometry⁹⁹ (Chapter 4).

An optical micrograph obtained by scanning the sample beneath the focused laser beam is shown in Figure 6.2.1(a). The arrays are seen between the two (white) tracks of the CPS device. The different greyscale intensity of the different arrays corresponds to different packing fractions. Figure 6.2.1(b) shows the calculated profile

* Hitachi Global Storage Technologies, San Jose Research Center, 3403 Yerba Buena Road, San Jose, California 95135

of the in-plane and out-of-plane components of the pulsed magnetic field. Details of the calculation are given in Chapter 5 and Reference 100. Assuming a current of 64 mA of uniform density in the cross-section of the striplines, the calculation revealed that the out-of-plane pulsed magnetic field was uniform to within 0.4% over the area of the array. Figure 6.2.1(c) shows a scanning electron microscope (SEM) image of the array of 236 nm square elements with a packing fraction of $\sim 56\%$. From the image, one can see that the elements have slightly rounded corners. The SEM images of the studied elements were used to determine the radius of rounding of their corners and the inter-element separations. Figure 6.2.1(d) shows a 3×3 model array that corresponds to the SEM image in Figure 6.2.1(c) and represents one of those used in the micromagnetic simulations. The inset in Figure 6.2.1(a) shows the coordinate system used in the analysis and the direction of the bias field H .

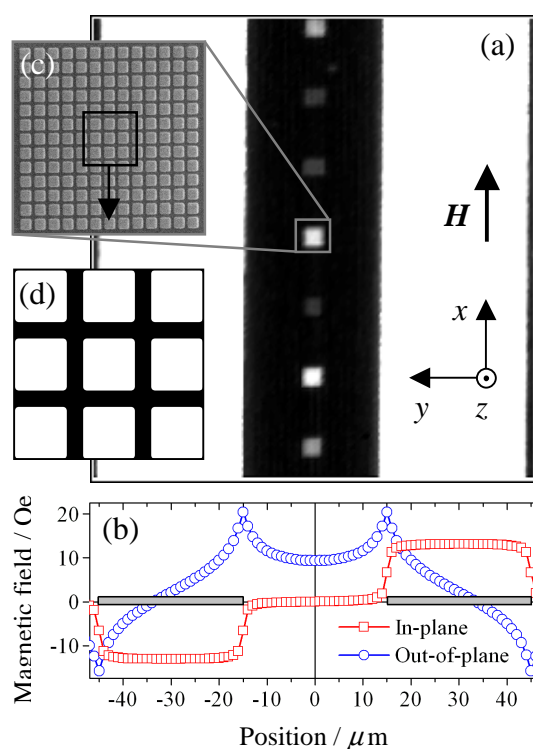


Figure 6.2.1 An optical micrograph of the sample is shown in (a). In (b) the calculated profile of the in-plane (open-squares) and out-of-plane (open-circles) components of the pulsed magnetic field is shown. In (c) an SEM image the array of 236 nm square elements is shown (a higher magnification image is shown in Figure 4.2.5(h)). In (d) a 3×3 model array used in micromagnetic simulations is shown, corresponding to the SEM image in (c). The inset in (a) shows the coordinate system used in this chapter.

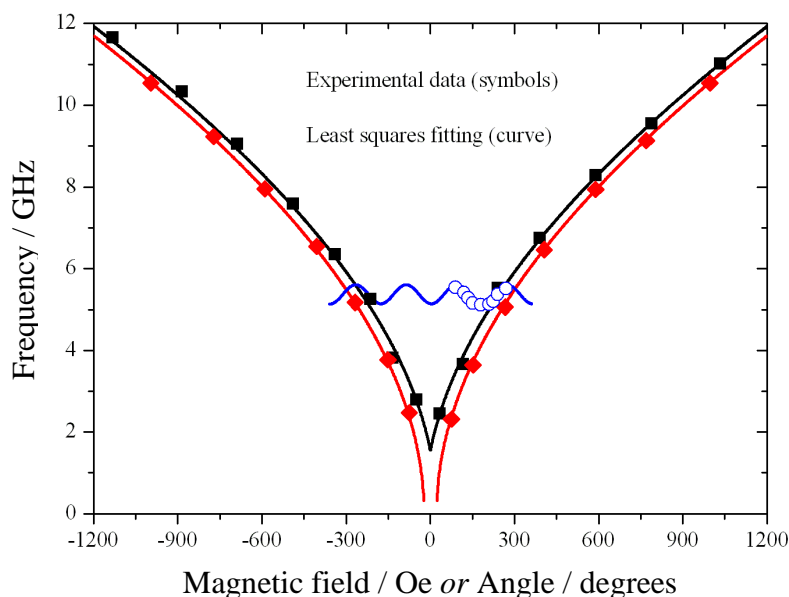


Figure 6.2.2 The dependence of the uniform mode frequency on the bias field magnitude (red and black symbols and curves), and on the bias field orientation (blue symbols and curves) for a $10 \mu\text{m}$ square element. Black squares and red diamonds show the experimental frequencies when the bias field was applied along the easy and hard axes respectively. Blue open circles show experimental frequencies as a function of the bias field orientation when the bias field magnitude was 270 Oe. The corresponding curves are least squares fits to the macrospin model in the quasi-alignment approximation.

A continuous film reference sample was co-deposited onto a 1" diameter glass substrate (coupon reference number SA0522D). Vibrating sample magnetometry (VSM) measurements made upon reference samples with different bilayer thickness revealed that 12.1 \AA of the $\text{Ni}_{88}\text{Fe}_{12}$ layer was lost due to inter-diffusion with the Ta capping layer¹¹. From the VSM measurements the saturation magnetisations of the $\text{Co}_{80}\text{Fe}_{20}$ and $\text{Ni}_{88}\text{Fe}_{12}$ were deduced to be 1445 and 585 emu/cm^3 , respectively. The layers were strongly exchanged coupled, therefore the bilayer was considered to be a single layer with thickness of 13.6 nm, which is equal to the sum of the thickness of the constituent layers after accounting for the effect of the interdiffusion. The magnetisation of the bilayer was taken to be 838 emu/cm^3 , the volume-weighted average of the individual layer saturation magnetisations. Similarly to References 11 and 85, time-resolved measurements were made upon a co-deposited $10 \mu\text{m}$ square. The precessional frequency of the uniform mode for each bias field was obtained by calculating the fast Fourier transform (FFT) power spectrum of each time-resolved

signal. Figure 6.2.2 shows the frequency data as a function of the bias field value, and bias field orientation. The uniaxial anisotropy ($9450 \pm 677 \text{ erg/cm}^3$) and surface anisotropy ($-0.491 \pm 0.018 \text{ erg/cm}^2$) parameters of the patterned material were extracted by fitting the frequency versus bias field data to a macrospin model in the quasi-alignment approximation. The value of the g -factor was assumed to be 2.1. The easy axis was found to be canted by about 4° from the direction of the striplines. The material parameters deduced here were used in micromagnetic simulations, which are described later. The validity of the assumption of quasi-alignment was verified by performing dynamical macrospin simulations in which the ground state or static orientation of the magnetisation was determined using the steepest descent method.

6.3 Details of numerical simulations

The size of an individual element within the arrays was smaller than the spatial resolution of the experiment. Therefore, micromagnetic simulations have been performed for all samples studied experimentally using the Object Oriented Micromagnetic Framework⁴¹ (OOMMF). Particular attention has been given to imperfections in the shape, magnetic environment and ground state of the elements. Magnetostatic dipolar interactions with the nearest neighbouring elements are more significant in the thicker (13.6 nm) elements than for the previously studied^{11,85} thinner (2.5 nm) elements due to the increased magnetic charge on the element edges perpendicular to the bias field. To account for any modifications to the element ground state and splitting of the excited modes due to interelement interactions, 3×3 model arrays of square elements were generated. Details of element size, edge-to-edge separation, element imperfection, and specifically the radius of rounding of element corners were determined from the SEM images and used to construct the model array used in the simulations. The radius of rounding of element corners was found to be 15 nm for all elements sizes.

For each bias field two stages of numerical simulation were performed. In the first stage the ground state of the magnetisation was calculated for which the energy of the magnetic system was minimised. The magnetisation was relaxed quickly by setting the damping constant of the simulated material to 0.5. The exchange constant A_{ex} was set to $13 \times 10^{-7} \text{ erg/cm}$. To acquire the static state of the magnetisation two methods were investigated. In the first method the static state at each bias field was prepared by

allowing the magnetisation to relax from the uniform state. In this method the bias field was applied along the x -direction. In the second method, for the bias field of 1 kOe only, the static state was also prepared by relaxing the magnetisation from the uniform state. However, subsequent static states at bias field values less than 1 kOe were then prepared by relaxing the magnetisation from the static state obtained at the previous bias field value. In the second method the bias field was applied 4° from the x -direction, parallel to the uniaxial easy axis, so that all elements within the model array would have the same static magnetisation state.

It is known that OOMMF favors the flower³² or X-state due to the assumption of zero temperature⁸. However, the S-state³² can be stabilised at finite temperatures⁸. We have also found that rounding of the element corners can promote the C-state³² in some elements (Figure 6.3.1(a)). Schematic representations of these non-uniform single domain states are shown in Figure 2.10.5. Canting the bias field by 4° in the static simulation stabilised the S-state in the majority of elements (Figure 6.3.1(b)). When a bias field of 1 kOe was canted from the x -direction by an angle of less than 4° , it was found that different elements within the array could acquire different static magnetisation states. In Figure 6.3.1 the results of the simulated static state of the 3×3 model arrays are shown for bias field values of 1 kOe and 770 Oe for the two methods previously outlined. Figure 6.3.1(a) shows the results of the first method, relaxing from the uniform state, while Figure 6.3.1(b) shows results of the second method, relaxing from the static state obtained at the previous bias field value. It is clear from the images that the static states obtained using the two methods are different. In particular in Figure 6.3.1(a), for a bias field of 1 kOe, five elements are in the C-state (including the centre element) and four elements are in the S-state. At 770 Oe the ground states of the elements surrounding the centre element are unchanged, while the centre element is now in the S-state. Furthermore, as the bias field was reduced from 770 to 590 Oe (not shown) the static state of a corner element was found to change from an S- to a C-state. Such irregular changes in the static state were seen for all element sizes and make the interpretation of the mode spectra and spatial character very difficult. In Figure 6.3.1(b) at bias fields of 1 kOe and 770 Oe, canting the bias field 4° from the x -direction has led to all elements occupying the S-state. It was expected that if all elements occupied the same static state, then the interpretation of the mode spectra and spatial character would be more readily understood. Hence, the second method was used to simulate the static state for all element sizes. In the experiments, the bias field was not intentionally canted

with respect to the x -direction, although one should expect some misalignment of a few degrees to occur.

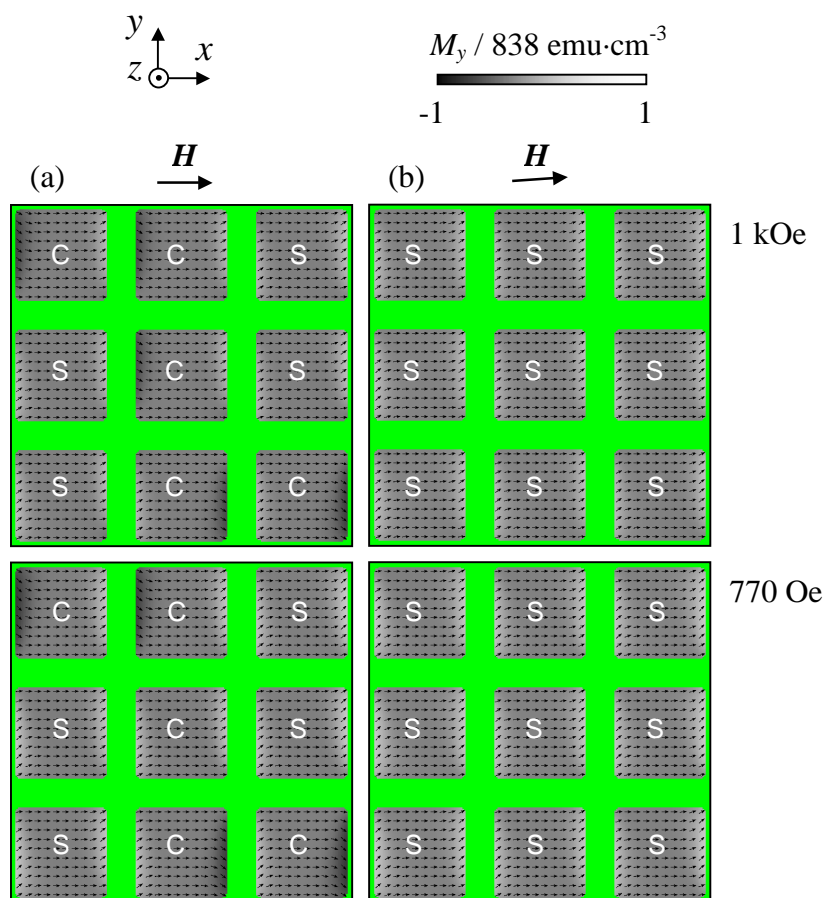


Figure 6.3.1 The static magnetisation states of 3×3 model arrays of 236 nm elements simulated for bias field values of 1 kOe and 770 Oe. The gray scale represents the component of magnetisation that is parallel to the y -direction (M_y) normalised to the saturation magnetisation 838 emu/cm^3 . The white and black shades represent $+M_y$ and $-M_y$, respectively. The green background represents non-magnetic regions. In (a) the static state at each bias field (applied parallel to the x -axis) was prepared by allowing the magnetisation to relax from the uniform state. In (b) the static state at a bias field of 1 kOe (applied 4° from the x -axis) was prepared by relaxing the magnetisation from the uniform state. Subsequently, the static state at 770 Oe was prepared by relaxing the magnetisation from the state at 1 kOe.

The second stage of the micromagnetic simulations was to calculate the dynamic response of the magnetisation of the model arrays to a uniform out-of-plane pulsed magnetic field. As in Reference 11, the pulsed magnetic field used in the simulations was assumed to have a rise time of 40 ps, a decay time constant of 2 ns, and a magnitude of 15 Oe. The damping parameter and g -factor were assumed to have values

of 0.01 and 2.1 respectively. Again, the exchange constant A_{ex} was set to 13×10^{-7} erg/cm. For the centre element within the model array, the nearest neighbour environment was expected to be a good approximation to that of elements in the interior of the real arrays. Therefore, the average time-resolved response of only the centre element was compared with that obtained experimentally.

To determine the spatial character of the excited modes, images of the modes were generated from the simulated time-resolved data as in Reference 94. The magnetisation at each time delay was recorded as a vector field map. For each pixel, a time-resolved trace was generated from the out-of-plane component of the magnetisation. Calculating the FFT of the time-resolved trace for each pixel revealed the Fourier components that were excited in a particular pixel. The calculated FFT were then used to reconstruct images of the magnitude and phase of the dynamical magnetisation. Thus for each mode previously identified from the FFT spectra obtained from the average response of the centre element, a corresponding “Fourier image” was calculated showing the spatial profile of the magnitude and phase of the dynamical magnetisation. For clarity, the images of the FFT magnitude are normalised to 75% of the maximum value of the magnitude in the centre element. The green background of the Fourier images represents non-magnetic material.

Prior to performing an extensive series of micromagnetic simulations, the model to be used to simulate the experimental spectra was investigated. Figure 6.3.2 shows the experimental (a), and simulated spectra of (b) the centre element of the 3×3 model array of elements with rounded element corners (shown in Figure 6.2.1(d)), (c) a single element from that array, (d) the centre element of a 3×3 array of perfect squares, and (e) a single perfect square are compared. The simulations were performed for an element size of 236 nm at a bias field of 590 Oe applied 4° from the x -direction. The static magnetisation of all of the simulated elements was found to be the S-state. The spectrum for the single perfect square element (Figure 6.3.2(e)) reveals poor agreement with the experimental spectrum with a lower frequency peak almost 2 GHz below the experimental peak. While the spectrum of the single element with rounded corners (Figure 6.3.2(c)) was in better agreement with experiment, there was no splitting of the simulated peak to support the large linewidth observed experimentally. The spectrum of the rounded square array (Figure 6.3.2(b)) was found to agree reasonably well with the experimental spectra. In addition, reasonable agreement was found between the experimental spectrum and the spectrum of the perfect square array (Figure 6.3.2(d)).

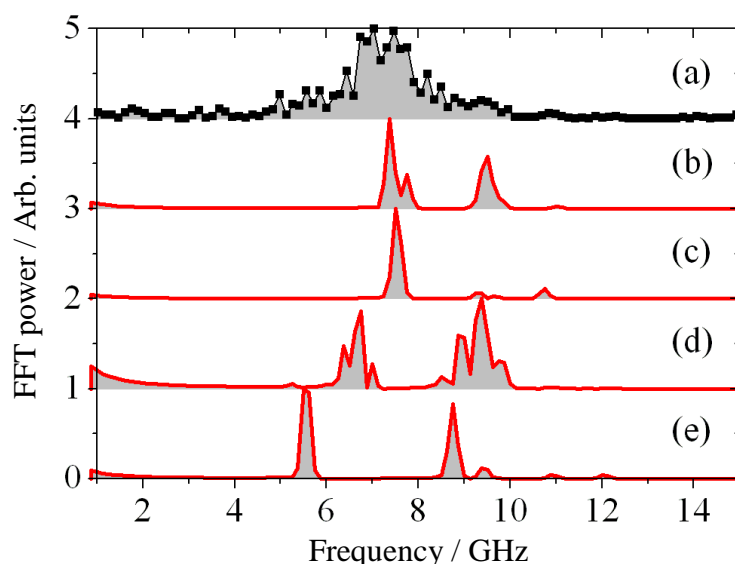


Figure 6.3.2 The experimental (a) and simulated spectra of (b) the centre element of the 3×3 model array of elements with rounded element corners (shown in Figure 6.2.1(d)), (c) a single element from that array, (d) the centre element of a 3×3 array of perfect squares, and (e) a single perfect square are shown. The simulations were performed for a 236 nm element with a bias field of 590 Oe applied 4° from the x -direction. The static magnetisation of all the simulated elements was found to be in the S-state. It is clear from the simulated spectra that both imperfections in element shape and different magnetic environments give rise to very different spectra.

Therefore, we conclude that simulations using 3×3 model arrays are required to reproduce the experimental spectrum. Additional splitting of the higher and lower frequency modes was observed in the spectrum for the perfect square array, but was not observed in the array of elements with rounded corners. Also the relative weight of different modes within the spectrum of the rounded square array was found to match that of the experimental spectrum better than the spectrum of the perfect square array. Therefore, the array of elements with rounded corners was favoured for simulations of the experimental spectra. The simulations in Figure 6.3.2 also revealed that the frequencies of the higher frequency modes were less sensitive than those of the lower frequency modes to the edge conditions of the model *i.e.* rounding of element corners and nearest neighbour magnetostatic interactions. This was evident from a ~ 2 GHz variation in frequency of the lower frequency modes between the different models, while the variation in frequency of the higher frequency mode was only ~ 1 GHz. Indeed, Fourier images (to be presented and discussed later) reveal that the lower frequency modes are associated with edge regions of the element, while the higher

frequency modes are associated with the centre region of the element, in agreement with the conclusions of Reference 12.

6.4 Results and discussion

Time-resolved signals

Figure 6.4.1(a) shows a typical time-resolved signal measured from the 236 nm element array at a bias field of 270 Oe. Time-resolved data for all element sizes and bias fields can be seen in Appendix 2. The oscillations due to the magnetisation precession are superimposed on a slowly varying background due to a transient out-of-plane canting of the magnetisation which follows the temporal profile of the pulsed

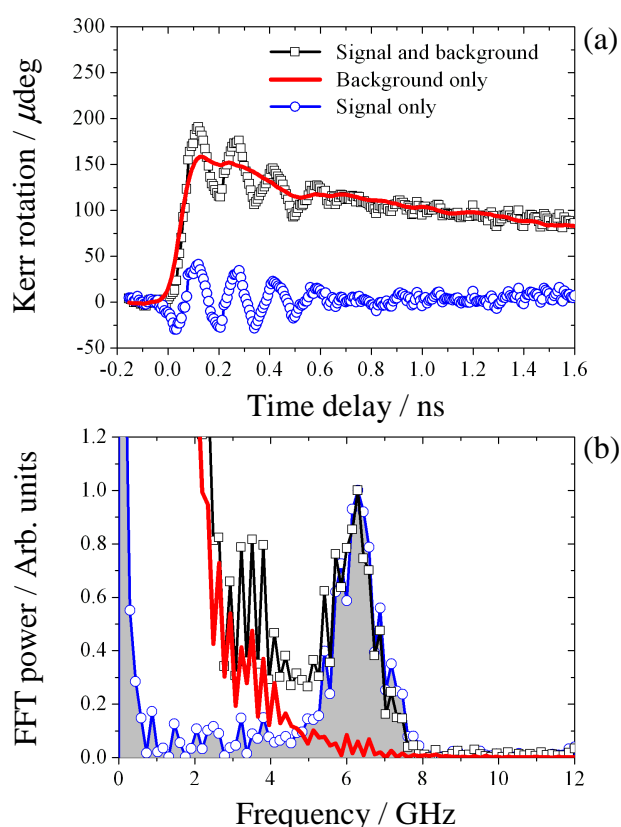


Figure 6.4.1 A typical raw time-resolved signal (line with squares), the slowly varying background (solid line), and the signal with the background subtracted (line with circles) are shown in (a) for the array of 236 nm elements at a bias field of 270 Oe. In (b) the FFT power spectra of the traces in (a) are shown.

magnetic field. This temporal profile was determined from signals measured at a bias field of ~ 1.5 kOe, at which no significant oscillatory response was observed. To isolate the oscillatory part of the signal, this background was subtracted from the time-resolved signals measured at lower field values¹⁰¹. Figure 6.4.1(b) shows the FFT spectra calculated from the time-resolved signals in Figure 6.4.1(a). The peaks in the spectra calculated from firstly the raw signal, and secondly the raw signal with the background subtracted, agree well for frequencies greater than about 5.5 GHz. The background subtraction extends the range of observable frequencies down to about 1 GHz.

Size dependence

First the dependence of the mode character upon the element size¹¹ was considered. FFT spectra calculated from the measured and simulated time-resolved signals are shown in Figure 6.4.2 for two values of the bias field (a) 1 kOe, and (b) 150 Oe. At the bias field value of 1 kOe, the dependence of the experimental FFT spectra upon the size of the elements closely resembles that observed in Reference 11. As the element size is reduced from 637 to 236 nm, the frequency of the dominant mode initially increases. At an element size of 124 nm, two modes are clearly seen in both the experimental and simulated data. The “higher frequency mode” continues the trend of increasing frequency as the element size is reduced, however in the 124 nm element its spectral power is reduced. The “lower frequency mode” is separated from the higher frequency mode by about 5 GHz in the experimental spectra and has slightly higher spectral power. The frequency of the lower frequency mode then increases as the element size is reduced further. The behaviour is qualitatively reproduced by the simulated spectra. The spectra show a crossover in mode intensity for an element size of about 124 nm, while for thinner elements (2.5 nm) in Reference 11 the crossover was observed to occur at the larger element size of about 220 nm. In Reference 11, the crossover was interpreted in terms of the relative size of the demagnetised regions within elements with quasi-uniform static magnetisation. The size of the demagnetised regions is expected to increase as the thickness of the elements is increased and the aspect ratio reduced. Therefore, one would expect the crossover to occur at a greater rather than smaller element size for the thicker elements in this study when compared to those of Reference 11. However exactly the opposite trend is observed in Figure 6.4.2(a) with the crossover occurring at a smaller element size for the thicker elements. This suggests that the spatial distribution of the demagnetising field is not the

dominant factor that determines the character of the excited modes. The assumption of uniform static magnetisation may also be incorrect. Indeed, the magnetisation is expected to be less uniform in the thicker elements. Alternatively, the discrepancy may provide evidence for an increased magneto-dipole interaction between elements as the elements become thicker.

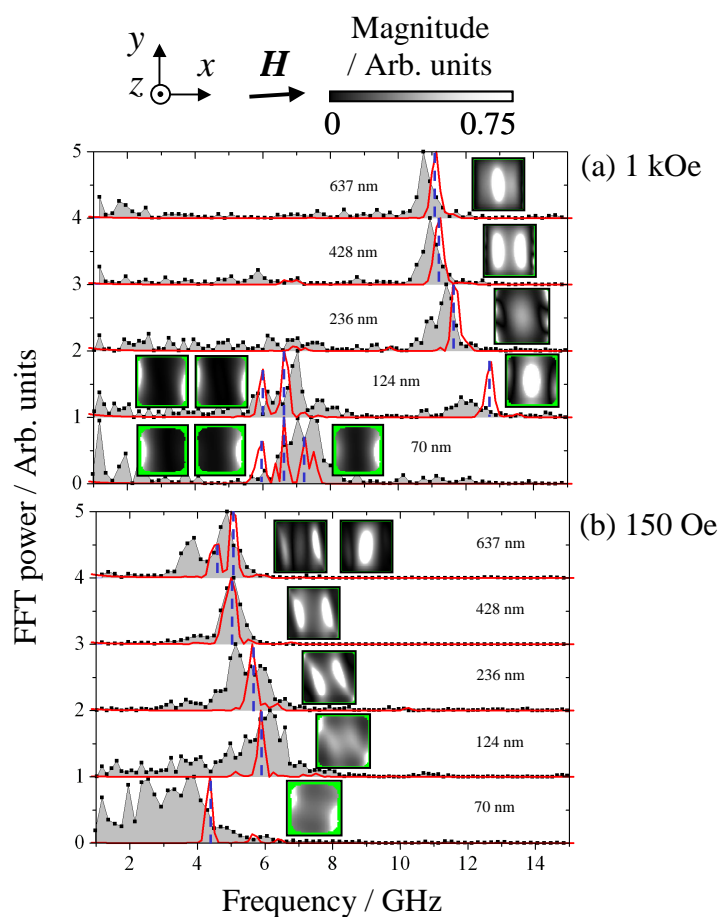


Figure 6.4.2 The dependence of the mode frequency upon the element size is shown for bias field values of 1 kOe (a) and 150 Oe (b). The shaded spectra were obtained experimentally, while simulated spectra are shown with a solid curve. For each element size, the spatial distribution of the fast Fourier transform magnitude of the modes in the simulated spectra are shown in the inset Fourier images. At a bias field of 1 kOe, a significant change in the experimental and simulated spectra is seen as the element size is reduced below 236 nm. The Fourier images reveal that the changes are due to a change in the mode character from a mode that occupies the majority of the volume of the element, to a mode that is localised near to the edges of the elements perpendicular to the bias field. The differences in the spectra at 1 kOe and 150 Oe reveal that the change in mode character has a strong field dependence.

As in Reference 11, the simulated images of Fourier magnitude reveal that modes from the higher frequency branch occupy the majority of the element volume (“centre modes”), while the modes of the lower frequency branch are localised near the edges of the element that are perpendicular to the direction of the bias field (“edge modes”). All modes are non-uniform throughout the elements due to the localised nature of the modes, particularly for the edge modes of the lower frequency branch. Non-uniformity of the centre modes from the higher frequency branch occurs in the direction of the bias field, as was previously observed in Reference 12. In Reference 12 a backward-volume type mode was introduced, since the effective wave vector is parallel to the magnetisation. The non-uniformity arises because the centre mode and backward volume type mode have similar frequencies and finite linewidths and therefore cannot be completely resolved. Also for the three largest elements non-uniformity exists in the direction orthogonal to the bias field at the edges of the element that are perpendicular to the bias field.

At the bias field of 150 Oe, the behaviour is remarkably different to that at 1 kOe. Again, the simulations reproduce the experimental data qualitatively, which allows us to use them to discuss the spatial character of the observed modes. The modes do not fall into the classification used in References 11 and 12 and in the previous paragraph. At 150 Oe, only the 637 nm element supports a centre mode with spectral power that is greater than all other excited modes. However, a lower frequency mode is observed with spectral power of about 50% of that of the centre mode. In the image of the lower frequency mode the regions of high amplitude appear to be tilted relative to, and detached from the element edges that lie perpendicular to the bias field. We will refer to these modes as “detached-edge modes”. When the element size is reduced to 428 nm we see that the mode with greatest spectral power has a similar spatial character to the lower frequency mode of the 637 nm element. This is again the case in the 236 nm element. Thus at 150 Oe we observe the size dependent crossover in mode spatial character between element sizes of 637 and 428 nm. Comparison of the size dependent crossover in Figure 6.4.2 at 1 kOe and 150 Oe indicates a strong bias field dependence of this general feature of the dynamical behaviour of non-ellipsoidal nanomagnets. As the element size decreases we again see an increase in the frequency of the excited modes. However, at 124 nm the spatial character of the dominant mode appears to be somewhat different to that of the modes seen in the larger elements. We interpret the modified spatial profile of the mode to be the result of the two detached edge modes (as seen in the element size of 236 nm) merging at the centre of the

element. The dominant mode frequency is observed to be reduced by about 2 GHz as the element size is reduced from 124 nm to 70 nm, which might be indicative of a transition of the static magnetisation state from an S-state to a leaf-state³². Consequently, the high amplitude regions have migrated to the edges of the element perpendicular to the bias field and slightly towards opposite diagonal corners where the effective field may be slightly reduced.

So far the modes shown in the Fourier images of Figure 6.4.2 have been classified as centre, edge, or detached-edge modes. However, it is not clear from Figure 6.4.2 how the mode character evolved as the bias field was reduced from 1 kOe to 150 Oe. In light of the clear field dependence of the mode spatial character, it is necessary to investigate and understand the evolution of the mode spatial character as the bias field is changed. Reducing the bias field for a particular element size allows one to study the effect of the evolution of the static magnetisation, total effective magnetic field, and interelement dipolar coupling. The increased non-uniformity of the magnetic ground state in individual elements and/or the increased interaction between elements within the arrays will be shown to be important contributions to the evolution of mode spatial character.

In order to understand the evolution of the spatial character, images of the ground state magnetisation have been simulated. Figure 6.4.3 shows images of the static magnetisation state of the centre element of the 3×3 model arrays, for all element sizes and bias field values. The grey scale represents M_y normalised to 838 emu/cm³, where white and black represent $+M_y$ and $-M_y$ respectively. At 1 kOe and for all element sizes the magnetisation was nearly saturated, but exhibited features of the S-state where the magnetisation near the edges of the elements perpendicular to the bias field was slightly canted towards the y -direction. Canting of the bias field 4° from the x -direction has stabilised the S-state in the centre element *and* the surrounding nearest neighbouring elements (not shown) for almost all element sizes and bias field values. At 150 Oe, all elements are seen to be in the S-state. The images reveal that a transition from a non-uniform S-state to a similar, but more uniform leaf-state occurs between element sizes of 124 and 70 nm and bias fields of 75 and 0 Oe. Furthermore, for the 3×3 array of 70 nm elements, one of the corner elements acquires the C-state (not shown) for bias fields of 770 Oe and below. Further canting of the bias field to 5° may eliminate this, however one corner element in the C-state has a minimal effect on the behaviour of the centre element so further simulations were not performed.

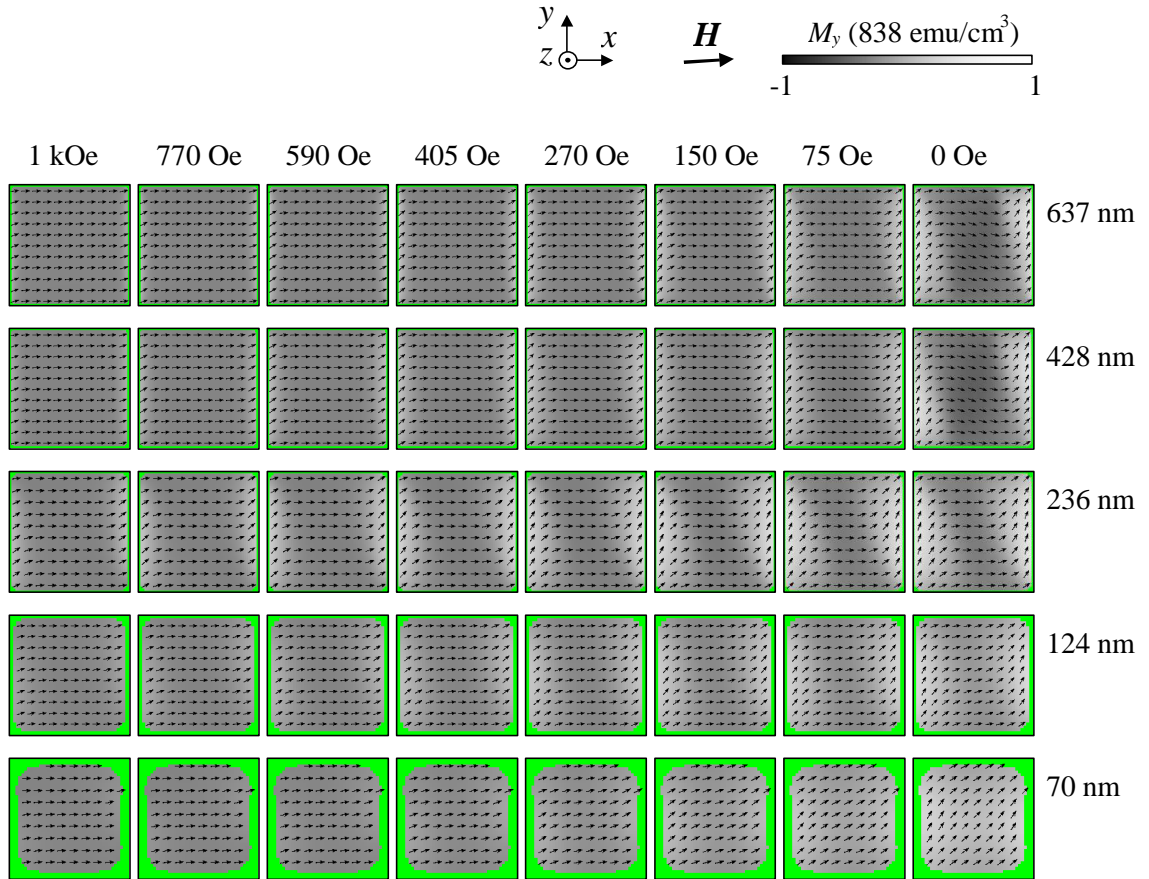


Figure 6.4.3 The simulated static magnetisation states within the centre element of 3×3 model arrays are shown. The grey scale represents M_y normalised to $M_s = 838 \text{ emu/cm}^3$, where white and black represent $+M_y$ and $-M_y$ respectively. The green background represents non-magnetic regions. The bias field was applied 4° from the x -direction in order to stabilise the S-state.

As in Reference 11, the linewidth of the experimental spectra for the array of 70 nm elements at a bias field of 1 kOe is noticeably greater than that in the larger elements. The simulations suggest that this may be due to several excited modes with frequencies between 5 and 8 GHz that may not have been resolved in the experiment. In line with this interpretation, the linewidth of the experimental spectra measured at 150 Oe is increased for all element sizes, which is echoed in the simulations by the excitation of multiple “satellite” peaks around the main spectral peak albeit with rather small spectral power. At the same time, the failure to resolve the modes experimentally should be attributed to the random nature of edge defects and rounding of element corners that give rise to inhomogeneous broadening due to variations within the array¹¹.

To verify this assumption, we performed micromagnetic simulations for nine isolated elements (not shown). Each element had different edge conditions, which

included random defects and rounding of corners. The nominal length of all nine elements was 236 nm. A bias field of 590 Oe was applied 4° from the x -direction for which the static magnetisation of all elements was found to occupy the S-state. The simulations support the interpretation of the inhomogeneous broadening, revealing that slight changes in the static state of the magnetisation due to edge defects can cause the mode frequency to vary noticeably even though the shape of the elements is only slightly varied. In some cases the edge defects were found to result in the splitting of modes. Figure 6.4.2 suggests that modes localised near to the edges in the elements of smaller sizes appear to be affected more. Two additional simulations (not shown) were performed for which defects were only included along edges of the element parallel to the bias field (case 1), and along edges of the element perpendicular to the bias field (case 2). The simulated spectra were compared to the spectrum shown in Figure 6.3.2(c) for an element with rounded corners and no defects. In all three cases the rounding of the element corners was identical. The spectra revealed that defects along the edges of the element perpendicular to the bias field (case 2) resulted in the largest variation in the mode frequencies. The variation of mode frequency seen in the spectra was most significant for the edge mode. The edge mode was found to split into two modes each of lower frequency than that of the lower frequency mode in the spectrum of Figure 6.3.2(c). The simulated spectra presented later in this chapter do not exhibit inhomogeneous broadening since the FFT spectra are calculated from the response of only the centre element of the 3×3 arrays.

Field dependence

In light of the strong dependence of the mode structure upon the exact shape of nano-elements, it is difficult to correlate the static and excited states of the magnetisation through a comparison of elements of different size and hence slightly different shape. On the other hand, the effective field and the static magnetisation state within a particular element may be varied continuously by adjusting the bias field. Since the edge profile is the same for all field values, it is advantageous to concentrate upon the field dependence of the precessional modes.

In Figures 6.4.4-8, the dependence of the precessional mode spectra upon the bias magnetic field is shown for elements sizes of 637, 428, 236, 124, and 70 nm, respectively. For the element size of 637 nm (Figure 6.4.4) the experimental and simulated spectra show a monotonic decrease of mode frequencies in the range 12 GHz

to 2 GHz as the bias field is reduced from 1 kOe to 0 Oe. The experimental and simulated spectra show evidence of lower frequency modes at bias fields of 770 Oe and below, albeit with varying spectral power. The Fourier images in the right-hand panel again show the spatial character of the simulated modes. The vertical blue dashed lines indicate the frequencies of the spectral peaks to which the Fourier images correspond. The images reveal that the mode with the largest spectral power between bias fields of 1 kOe and 150 Oe is a centre mode. At 75 Oe the two detached-edge modes possess greater spectral power than the centre mode. At 0 Oe the spectral power of the centre mode vanishes and the dominant excited modes are two detached-edge modes. At a

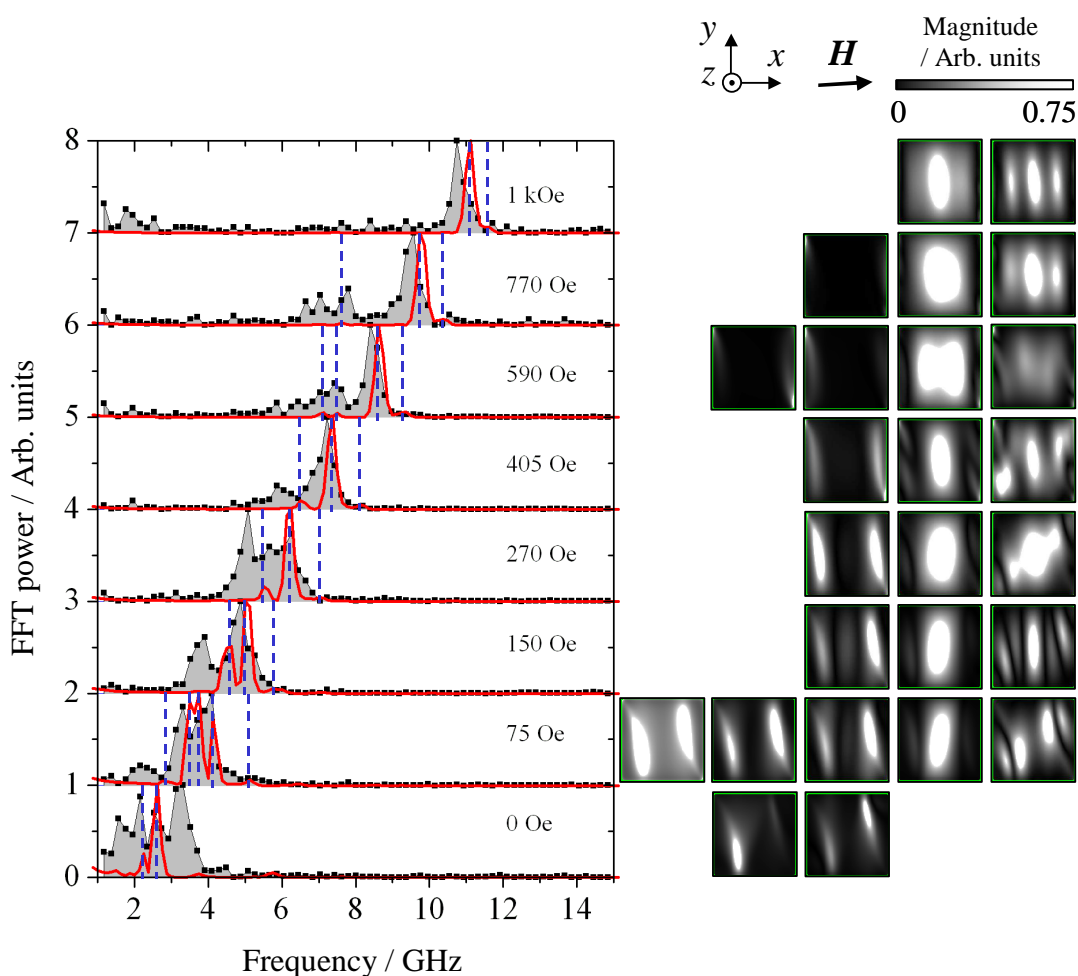


Figure 6.4.4 The dependence of the mode spectra and the spatial character of the different modes upon the bias field is shown for the 637 nm element. The shaded spectra with symbols show the experimental data, while the solid red line shows spectra obtained from micromagnetic simulations. The vertical dashed blue lines indicate the frequencies of the modes whose spatial character is shown in the Fourier images of the fast Fourier transform magnitude. The images are ordered in terms of increasing frequency .

bias field of 150 Oe, we observe a field-dependent crossover of the spatial character of the modes in the simulations. The experimental spectra do not clearly reveal the crossover, however they do reveal that more than one mode is present. It is also interesting to note that modes with backward-volume (BV) type character ($\mathbf{M} \parallel \mathbf{k}$), with a greater number of nodes and hence a greater wave number, have higher frequency than the quasi-uniform mode. The increased frequency of the BV-type modes results from the exchange field contribution to the effective field (Section 2.16) as the misalignment of neighbouring moments is increased for shorter wavelength spin waves.

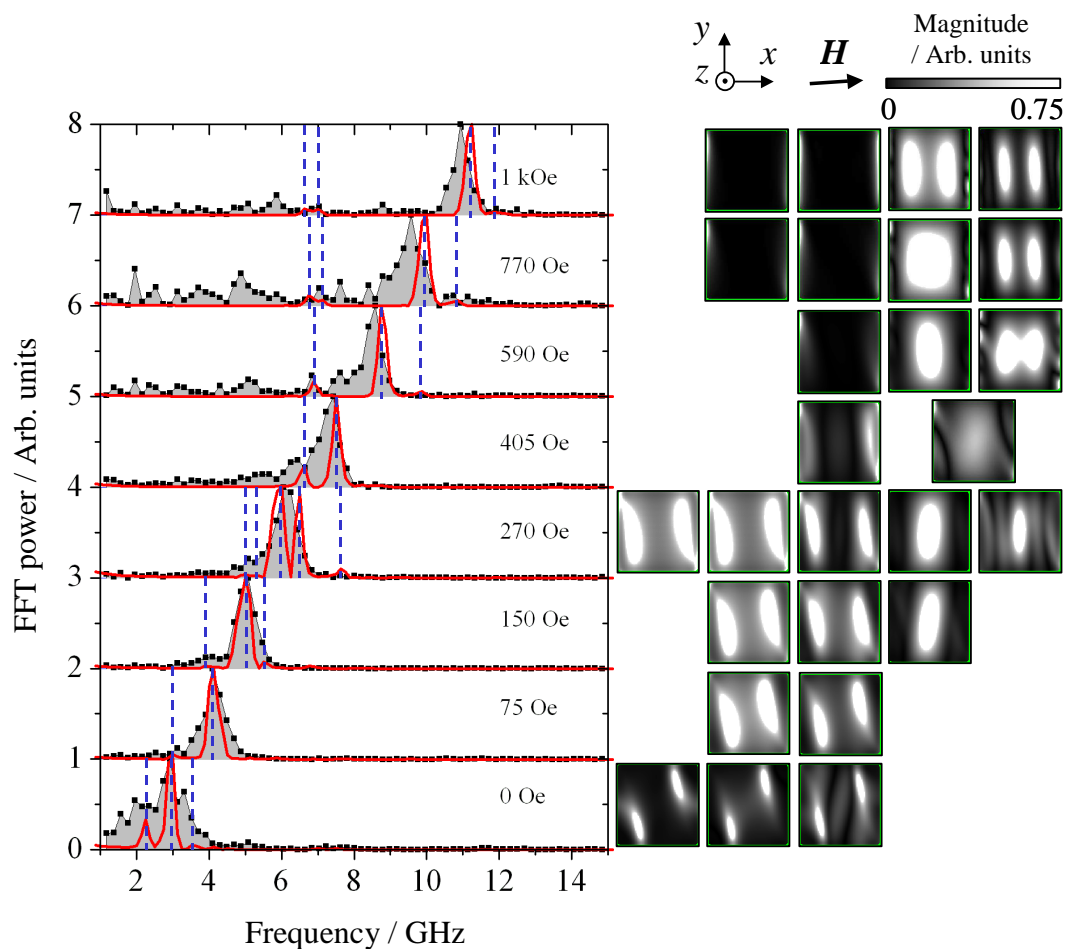


Figure 6.4.5 The dependence of the mode spectra and the spatial character of the different modes upon the bias field is shown for the 428 nm element. The shaded spectra with symbols show the experimental data, while the solid red line shows spectra obtained from micromagnetic simulations. The vertical dashed blue lines indicate the frequencies of the modes whose spatial character is shown in the Fourier images of the fast Fourier transform magnitude. The images are ordered in terms of increasing frequency .

For the element size of 428 nm (Figure 6.4.5), the field dependence of the mode character is similar to that of the 637 nm element. Again the experimental and simulated spectra show a monotonic decrease of mode frequencies in the range 12 GHz to 2 GHz as the bias field is reduced from 1 kOe to 0 Oe. At a bias field of 1 kOe, evidence of lower frequency edge modes can be seen in both the experimental and simulated spectra. Also, interference between the high-frequency BV-type mode and the centre mode leads to a Fourier image that is non-uniform at the centre of the element with two anti-nodes. This composite centre mode continues to have the largest spectral power until the bias field is reduced to 270 Oe, where a detached-edge mode becomes the mode with largest spectral power. At 150 Oe the spectral power of the centre mode is greatly reduced and the detached-edge modes dominate the dynamical response as the bias field is reduced further. From the simulations we see that the field dependent crossover of mode spatial character has taken place at a higher bias field value of 270 Oe.

For the element size of 236 nm (Figure 6.4.6), a crossover from a centre mode to a detached-edge mode occurs between bias fields of 770 and 590 Oe. The experimental spectra show that the lower frequency edge mode has greater spectral power at 770 Oe, while the simulated spectra suggest that the edge mode becomes dominant at 590 Oe. As the bias field is reduced from 1 kOe to 590 Oe, the lower frequency edge modes do not exhibit a monotonic decrease in frequency, but instead increase in frequency by about 0.5 GHz. As for the 637 and 428 nm elements, the frequency of the centre mode of the 236 nm element exhibits a monotonic decrease as the bias field is reduced, before the mode amplitude is greatly attenuated at 270 Oe. Also, between bias field values of 1 kOe and 405 Oe the Fourier images reveal that the centre mode is non-uniform. At all bias field values the simulated spectra and Fourier images reveal a non-uniform mode between 9.6 and 10.3 GHz. Similarly for bias field values of 1 kOe to 590 Oe a non-uniform mode exists between 9.8 and 9.5 GHz. Between 1 kOe and 590 Oe at least one of the non-uniform modes has a similar frequency to the centre mode. As seen for the 637 and 428 nm elements it is not possible to completely resolve modes with similar frequencies since the spectral lines have a finite linewidth. At 590 Oe the mode with frequency of about 9.8 GHz at 770 Oe seems to merge with the centre mode spectral peak. The corresponding Fourier image reveals significant non-uniformity of the high amplitude region at the centre of the element. At 590 Oe the experimental spectral peak is very broad and is accompanied by two modes of similar frequency in the simulated spectrum. The inhomogeneous broadening is again attributed to the random nature of

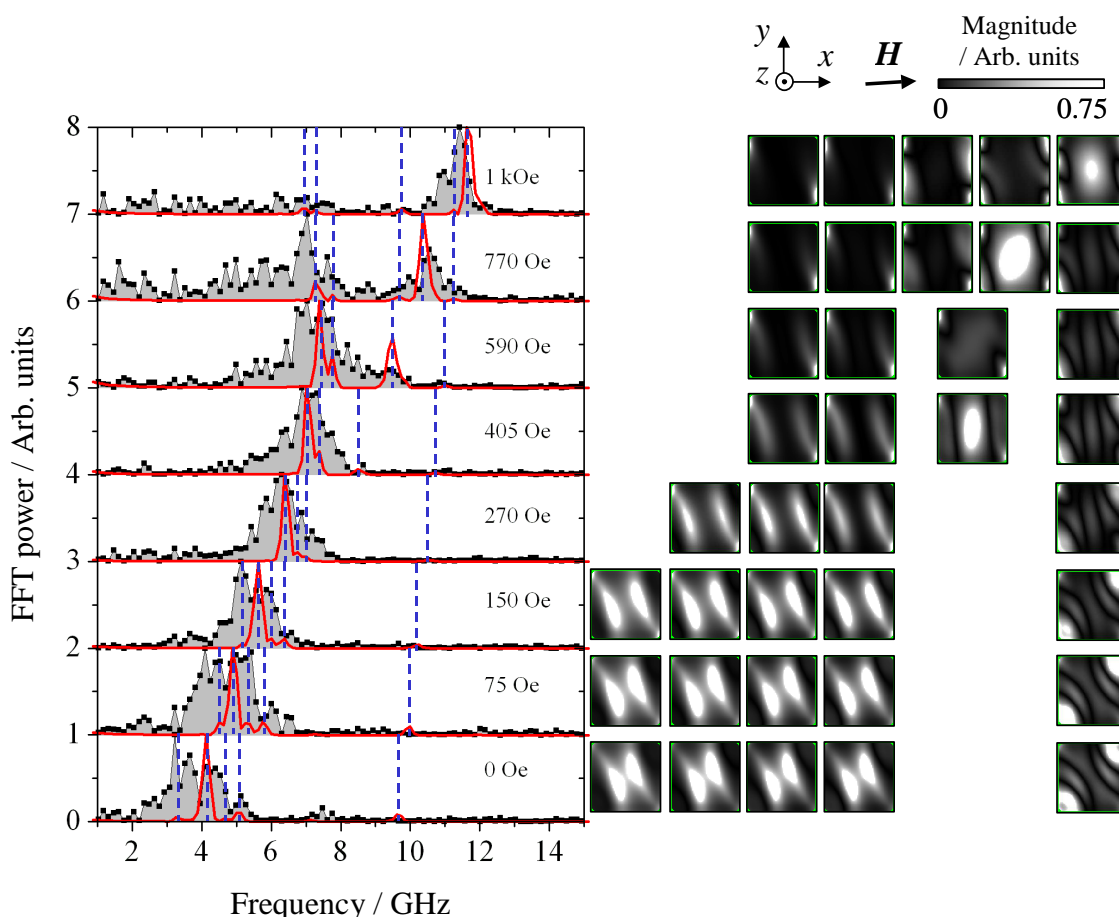


Figure 6.4.6 The dependence of the mode spectra and the spatial character of the different modes upon the bias field is shown for the 236 nm element. The shaded spectra with symbols show the experimental data, while the solid red line shows spectra obtained from micromagnetic simulations. The vertical dashed blue lines indicate the frequencies of the modes whose spatial character is shown in the Fourier images of the fast Fourier transform magnitude. The images are ordered in terms of increasing frequency .

defects and irregularities at the edges of the elements, which causes dispersion of the frequency of the excited modes near to element edges due to variations of the local effective field and pinning of the magnetisation. The Fourier images corresponding to simulated spectra for bias fields of 590 Oe and below reveal that the modes of different frequency are in fact weakly associated with the element edges. Finally, the simulated spectra reveal that for all bias field values, lower frequency modes with different frequency possess very similar, if not the same, spatial character, which is the result of collective-type excitations across the 3×3 array (discussed later).

For the element size of 124 nm (Figure 6.4.7), a crossover from a centre mode to an edge mode occurs at 1 kOe. Between bias fields of 770 and 270 Oe the lower

frequency (< 8 GHz) experimental spectra are very broad. The simulated spectra show that there are many lower frequency modes (up to 6) excited with variable frequency and spectral power. In line with the previous discussion, smaller elements will be more susceptible to frequency dispersion and inhomogeneous broadening of spectra since the effects of edge defects and irregularities are more pronounced. Furthermore, the excited modes in smaller elements seem to be mostly edge-type modes, which again are more susceptible to edge conditions. Between 1 kOe and 590 Oe there seem to be two centre modes with different frequency, which are the result of collective-type excitations (discussed later). Similarly, many of the lower frequency edge-type modes share the same spatial character, but again with different frequency. Between 270 Oe and 75 Oe the high amplitude regions of the edge-type modes have extended into the centre of the

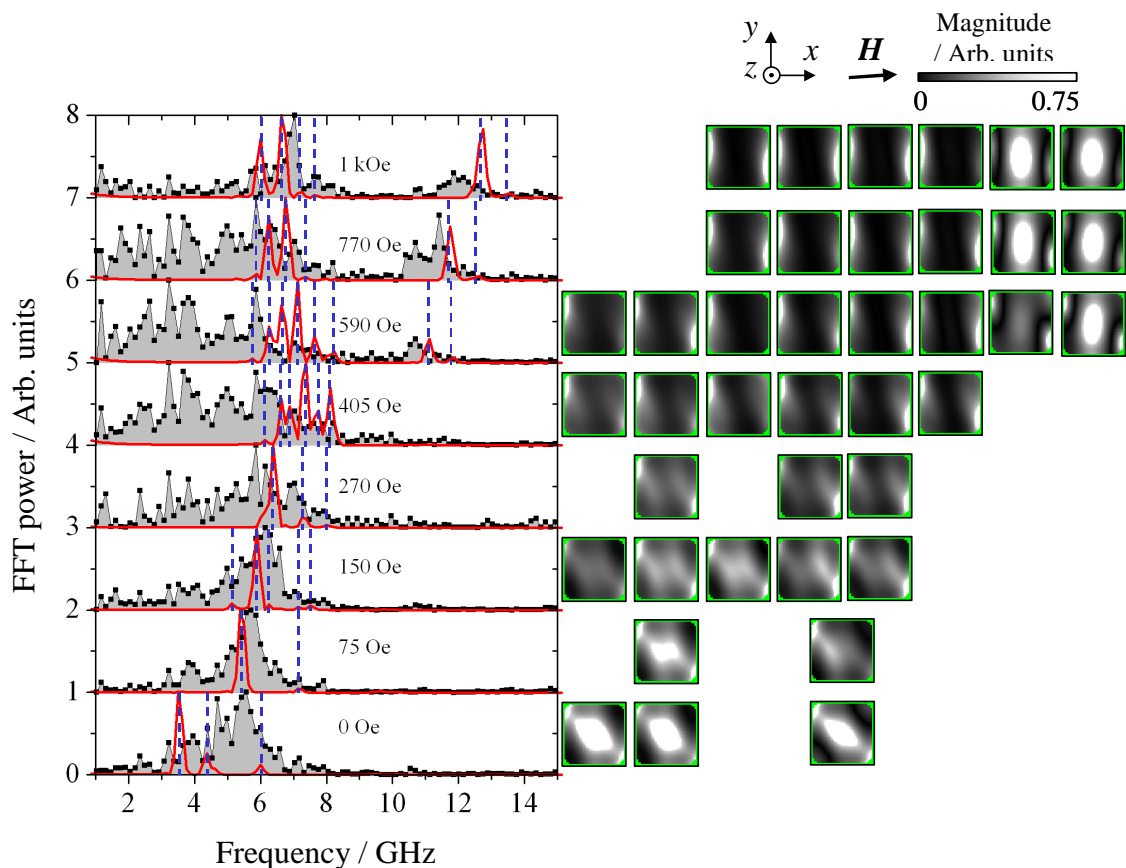


Figure 6.4.7 The dependence of the mode spectra and the spatial character of the different modes upon the bias field is shown for the 124 nm element. The shaded spectra with symbols show the experimental data, while the solid red line shows spectra obtained from micromagnetic simulations. The vertical dashed blue lines indicate the frequencies of the modes whose spatial character is shown in the Fourier images of the fast Fourier transform magnitude. The images are ordered in terms of increasing frequency .

element, while at 0 Oe the high amplitude region has become detached from the element edges. This may be interpreted as being due to a change of the static magnetisation configuration. In the simulated spectra a large change in frequency (~ 2 GHz) is seen between 75 Oe and 0 Oe which is not so apparent in the experimental spectra. Indeed simulated images of the static magnetisation (Figure 6.4.3) and the effective field (shown and discussed later) reveal a transition from an S-state to a leaf-state.

For the element size of 70 nm (Figure 6.4.8), a crossover of mode character is not observed when the bias field is reduced. The crossover may be revealed in micromagnetic simulations performed at a bias field value above 1 kOe. The experi-

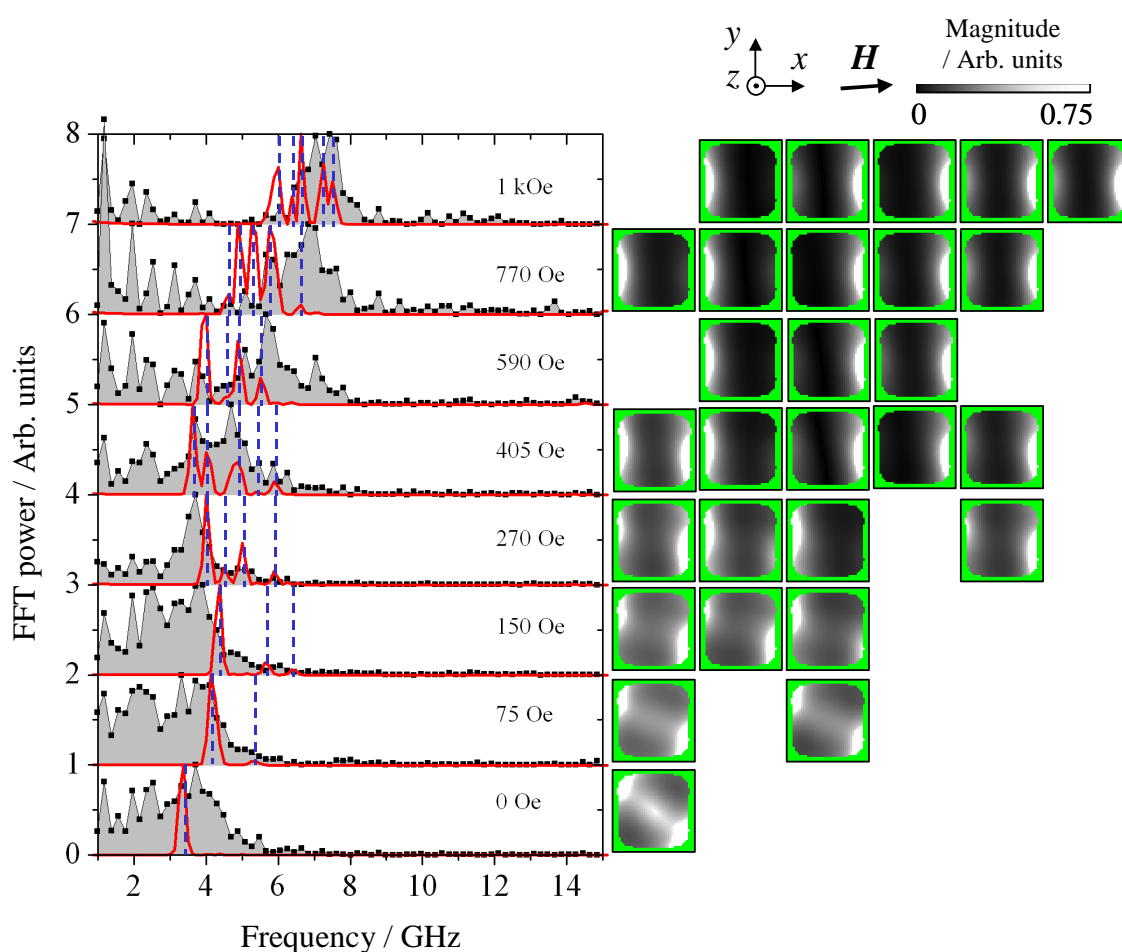


Figure 6.4.8 The dependence of the mode spectra and the spatial character of the different modes upon the bias field is shown for the 70 nm element. The shaded spectra with symbols show the experimental data, while the solid red line shows spectra obtained from micromagnetic simulations. The vertical dashed blue lines indicate the frequencies of the modes whose spatial character is shown in the Fourier images of the fast Fourier transform magnitude. The images are ordered in terms of increasing frequency.

mental and simulated spectra show that only lower frequency (< 8 GHz) modes are excited for bias fields of 1 kOe and below. That is, the higher frequency branch of the centre mode is not observed in either the experimental spectra or simulated spectra.

The corresponding Fourier images reveal that all modes excited between 1 kOe and 150 Oe are edge-type modes. Again there is significant inhomogeneous broadening of the experimental spectra, which is supported by the presence of many modes with slightly different frequency in the simulated spectra. As seen for the 124 nm element, the high amplitude regions of the 70 nm element have extended into the centre of the element between 75 Oe and 0 Oe. Again the simulated static magnetisation and effective field reveal a transition from an S-state to a leaf-state between these bias field values.

Results of micromagnetic simulations on 3×3 arrays shown in Figure 6.4.9 have revealed that the frequencies of edge-type modes are dependent upon the static state of the magnetisation of the centre element, *and* the surrounding nearest neighbour elements. In Figure 6.4.9(a) the experimental spectra for the 236 nm element array at a bias field of 770 Oe is shown. In Figure 6.4.9(b) and (d), the simulated spectra correspond to the response of the centre element for which the ground state of the array at 770 Oe is shown in Figure 6.3.1(a) and (b) respectively. The spectrum in Figure 6.4.9(c) corresponds to a similar ground state to that shown for 770 Oe in Figure 6.3.1(b), but instead the centre element occupies the C-state. In the latter case the ground state was obtained by relaxing the magnetisation from the state shown in Figure 6.3.1(a) at 1 kOe, rather than relaxing from uniform saturation as in the case of Figure 6.3.1(a) at 770 Oe. Schematic illustrations of the ground state magnetisation of the array are shown in Figure 6.4.9(inset) for each case.

Near edges of the element perpendicular to the bias field, the canting of the magnetisation away from the direction of the bias field is different for the S- and C-states, Figure 6.3.1. For different static states the effective field near to the element edge, and the interelement interactions are different. Therefore, the frequency of modes excited in the edge regions can be different. The simulated spectra in Figure 6.4.9(b) and (c) reveal splitting, a decrease in spectral power, and a small increase in frequency of the edge-type modes when the ground state of the centre element is changed from an

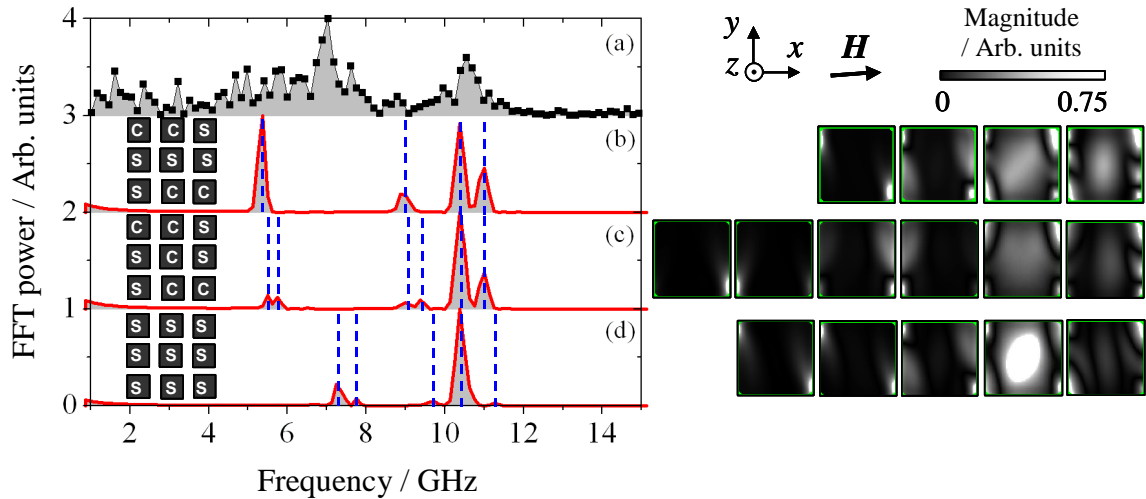


Figure 6.4.9 The experimental spectra for the 236 nm element array at a bias field of 770 Oe are shown in (a). In (b) and (d) the simulated spectra correspond to the centre element response in 3×3 arrays where the ground state in each case was that shown for 770 Oe in Figure 6.3.1(a) and (b) respectively. In (b) the ground state was similar to that in (b) except that the centre element occupied the C-state. Schematic illustrations (inset) show the ground state magnetisation of the array for each case. The vertical dashed blue lines indicate the modes corresponding to the Fourier images.

S- to a C-state. At the same time, the higher frequency modes, including the centre mode at 10.4 GHz, are affected less. This is expected since the different edge conditions of the C- and S-state will mostly affect the frequency of the edge-type modes. The Fourier images corresponding to Figure 6.4.9(b) and (c) reveal slight changes in the spatial character of the dynamic magnetisation when the static state of the centre element is changed.

Comparison of the simulated spectra in Figure 6.4.9(b) and (d) reveal the changes in the spectra due to interelement interactions when the static states of the nearest neighbour elements are changed. In both cases at 770 Oe, the centre element occupies the S-state. For the spectra shown in Figure 6.4.9(b) the nearest neighbour elements occupy C- and S-states (Figure 6.3.1(a)), while for the spectra shown in Figure 6.4.9(d), all neighbouring elements occupy the S-state (Figure 6.3.1(b)). Again splitting of the edge-type mode is observed along with a significant increase in frequency of ~ 2 GHz, which matches the frequency of the edge mode in the experimental spectra in Figure 6.4.9(a). In contrast to the spectra in Figure 6.4.9(b) and (c), the spectral power

of the highest frequency mode at 11.25 GHz is significantly reduced, which indicates that it too may be sensitive to interelement interactions.

It is clear from Figure 6.4.9 that the ground state of *all* elements in the array is important since the magnetostatic interactions between elements can modify the spectra. This is particularly important when the magnetisation is non-uniform. Here the magnetisation is non-uniform along the edges perpendicular to the bias field, in regions where the edge-type modes are excited and where magnetostatic interactions with nearest neighbours are greatest. By comparing the experimental spectra with the simulated spectra, it is possible to obtain insight into the ground state of the elements within the array. For example, the spectrum in Figure 6.4.9(b) is from an array with mixed C- and S-states. The frequency of the edge-type mode is found to be about 2 GHz below that in the experimental spectra. The spectra in Figure 6.4.9(d), where all elements were in the S-state, reproduce the frequency of the edge-type mode very well, although the spectral power is somewhat different. The simulated spectra in Figure 6.4.9 demonstrate how sensitive the edge mode frequency is to the ground state of both the centre element, and the entire array. The agreement between the spectra in Figures 6.4.9(a) and (d) allow us to infer that in our measurements the majority of elements are in the S-state. For all element sizes and all bias field values, both methods of preparing the ground state, described in Section 6.3, were used. The best agreement between the experimental and simulated spectra was obtained when all elements of the 3×3 array were in the S-state. Figure 6.4.9 illustrates how different results may be obtained with the two methods. Such quantitative analysis of the experimental spectra allows the ground state to be inferred, providing information that cannot be easily obtained from hysteresis loop measurements.

It is clear from the images in Figure 6.4.3 that the static state of the magnetisation becomes increasingly non-uniform as the bias field is decreased. In Figure 6.4.10 images of the total effective field (H_{eff}) corresponding to the magnetisation configurations in Figure 6.4.3 are shown. The effective field includes contributions from the applied, demagnetising, anisotropy, and exchange fields. The greyscale represents the magnitude of the effective field normalised to the bias field, except at remanence where the field was normalised to 75 Oe. The images clearly show that a reduction of either the element size or the bias field can result in a non-uniform effective field. At 1 kOe, the effective field is nearly uniform at the centre of all elements (light grey). For the 637 and 428 nm elements, regions of small internal field exist in narrow regions along the edges perpendicular to the applied field (black). As

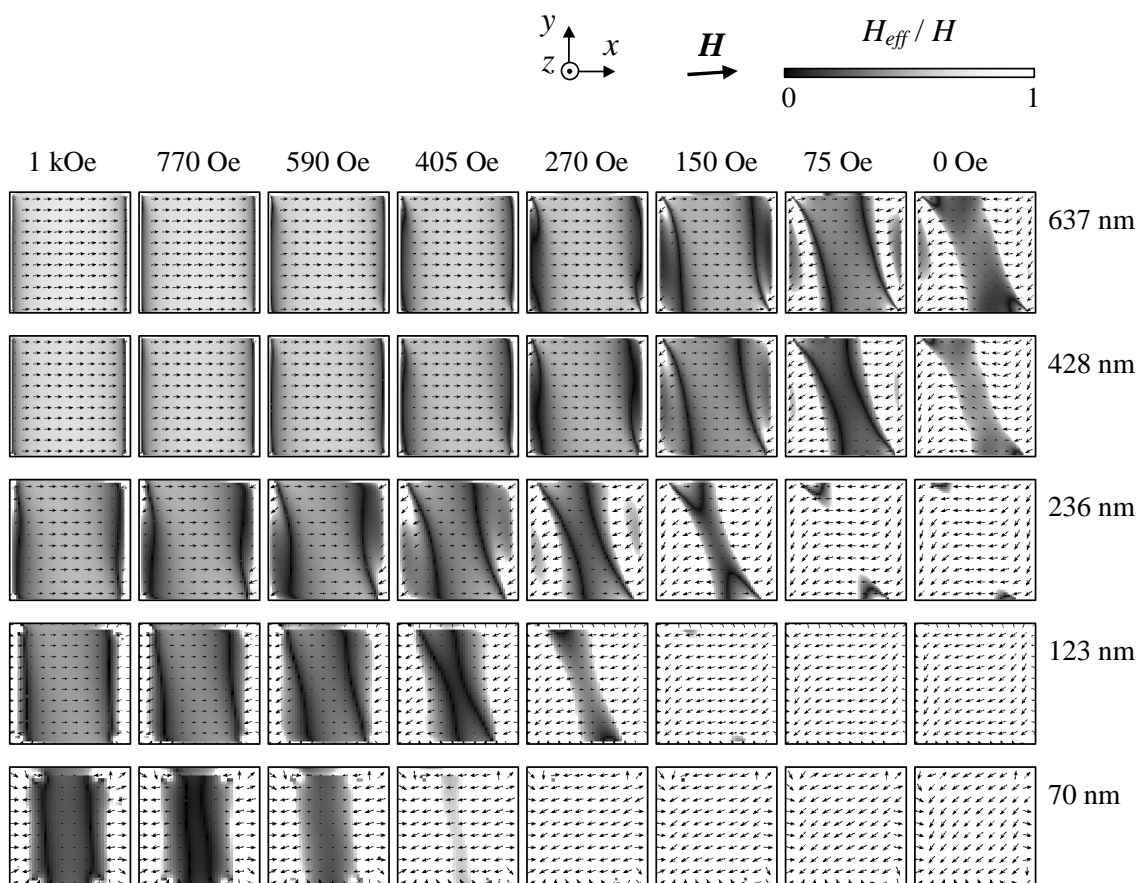


Figure 6.4.10 Images of the simulated total effective field within the centre element of the 3×3 model arrays are shown. The effective field includes contributions from the applied, demagnetising, anisotropy, and exchange fields. The greyscale represents the magnitude of the effective field normalised to the bias field, except at remanence where the field was normalised to 75 Oe. At large bias fields, narrow regions of small internal field exist in the larger elements along the edges that are perpendicular to the bias field (black). As the element size and/or bias field are reduced, the regions of small internal field move towards the centre of the elements so that the effective field becomes non-uniform. In the smallest elements at low bias fields, the effective field becomes completely opposite to the static magnetisation (Figure 6.4.3).

the element size is reduced from 236 to 70 nm the regions of small internal field move towards the centre of the element and remain perpendicular to the bias field. Similarly, when the bias field is reduced from 1 kOe the regions of small internal field within the 637 and 428 nm elements begin to move towards the centre of the element at 405 Oe. However, at bias field values of 405 Oe and below the effective field becomes non-uniform in both x - and y -directions. At 75 Oe regions of negative internal field can clearly be seen from the direction of the arrows. A similar evolution of the effective

field is seen for the 236 and 123 nm elements as the bias field is reduced, however it seems that regions of small internal field are observed at bias field values of 1 kOe and greater. At a bias field value (element size) of 0 Oe (637 and 428 nm), 150 Oe (236 nm), 270 Oe (123 nm), and 590 Oe (70 nm), the effective field becomes negative throughout the majority of the element. The most significant contribution to the effective field is then the demagnetising field and the regions of small internal field (black) are expelled from the element near the edges parallel to the bias field.

In Figure 6.4.11 cross-sections of the effective field images (shown in Figure 6.4.10) for a bias field of 1 kOe are shown for each element size. The sections were taken parallel to the x -direction and through the centre of the elements. The sections reveal that for all element sizes regions of negative effective field exist along the edges of the element perpendicular to the bias field. For the 637 nm element the negative effective field occupies very narrow regions with width Δx less than 1% of the total element length. In contrast, in the 70 nm element, the width of the regions is 27% of the total element length.

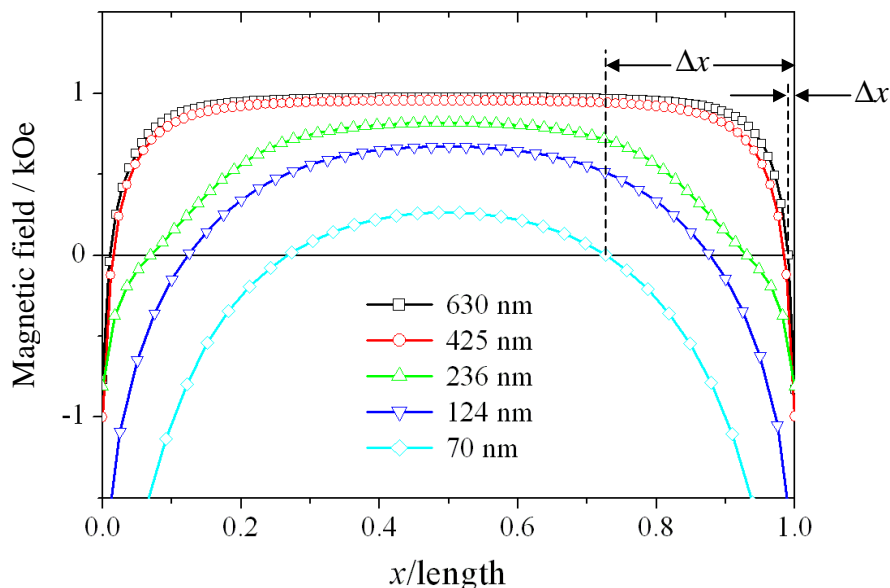


Figure 6.4.11 Cross-sections of the simulated total effective field within the centre element of the 3×3 model arrays at a bias field of 1 kOe. The sections show the x -component of the effective field. Regions of negative effective field exist for all element sizes. The width of the regions, labeled as Δx , is found to occupy a larger proportion of the total element length as the element size is reduced.

For the 637, 236, and 70 nm elements respectively, Figures 6.4.12-14 show cross-sections of (a) the effective field images (shown in Figure 6.4.10), and (b) the Fourier images of the dominant edge and centre modes, where both appear, (shown in Figures 6.4.4, 6, and 8) for four different bias field values. Generally there are three regions of interest in the cross-section of the effective field, i) a region of zero or negative effective field adjacent to the edges of the element perpendicular to the bias field (edge region), ii) a region of positive effective field at the centre of the element (centre region), iii) a region that connects the first two regions where the gradient of the effective field is large (gradient region).

For the 637 nm element, Figure 6.4.12(a) reveals that there is a small increase in the width Δx of the edge regions of about 2% of the element length as the bias field is reduced from 1 kOe to 270 Oe. At the same time, the magnitude of the effective field in the edge regions decreases from about -750 Oe to -250 Oe. At 75 Oe it can be seen that the width of the edge regions has increased significantly to about 28% of the element length, and a well in the negative effective field has formed. Within these edge regions at 75 Oe, the magnitude of the negative effective field is larger than the positive effective field in the centre region. As the bias field is reduced from 1 kOe to 75 Oe the effective field in the centre region remains approximately equal to the bias field. Furthermore, the width of the gradient regions increases at the expense of that of the centre region.

In Figure 6.4.12(b) two types of modes are seen from the cross-section of the Fourier images; i) a mode with large FFT magnitude at the centre of the element (open black squares), ii) a mode with large FFT magnitude near the edges of the element perpendicular to the bias field (open red circles). It would be incorrect to characterise these modes in terms of strict localisation at the centre, edge or gradient regions. For example, for a mode to be centre (or edge) localised one would expect the FFT magnitude to be equal to zero at the edges (or centre) of the element. In Figure 6.4.12(b) at 1 kOe the 11.1 GHz mode has two minima in the profile of the FFT magnitude near to the element edges. As the bias field is reduced, the minima migrate from positions near the edge of the element at 1 kOe towards the centre of the element. At 590 Oe the lower frequency mode (7.1 GHz) has two maxima in the profile of the FFT magnitude that correspond to the position of the two minima of the higher frequency (8.6 GHz) mode. As the bias field is reduced these maxima also migrate towards the centre of the element. Features in the cross-section of the FFT magnitude for both modes are correlated with those of the effective field in Figure 6.4.12(a). In

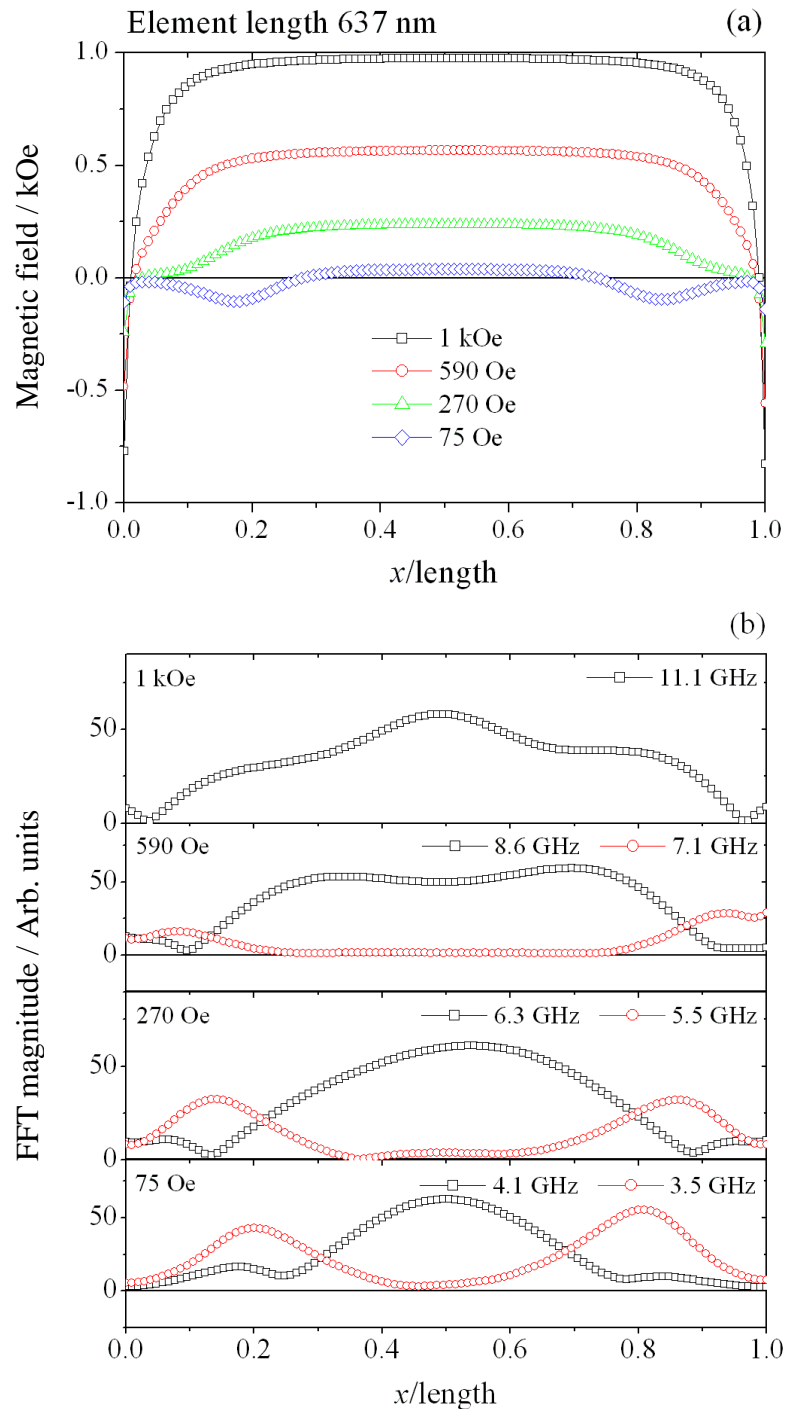


Figure 6.4.12 Cross-sections are shown of the x -component of the simulated total effective field (a) and the FFT magnitude (b) within the centre element of the 3×3 model array of 637 nm elements. The sections are shown for four different values of the bias field.

Reference 40 for a transversely magnetised microscale stripe, a gradient region near to the stripe edge was identified as the region of localisation for low frequency modes with edge-type spatial character. The edge region (zero field and non-uniform magnetisation) was assumed to reflect spin-waves propagating from the centre of the

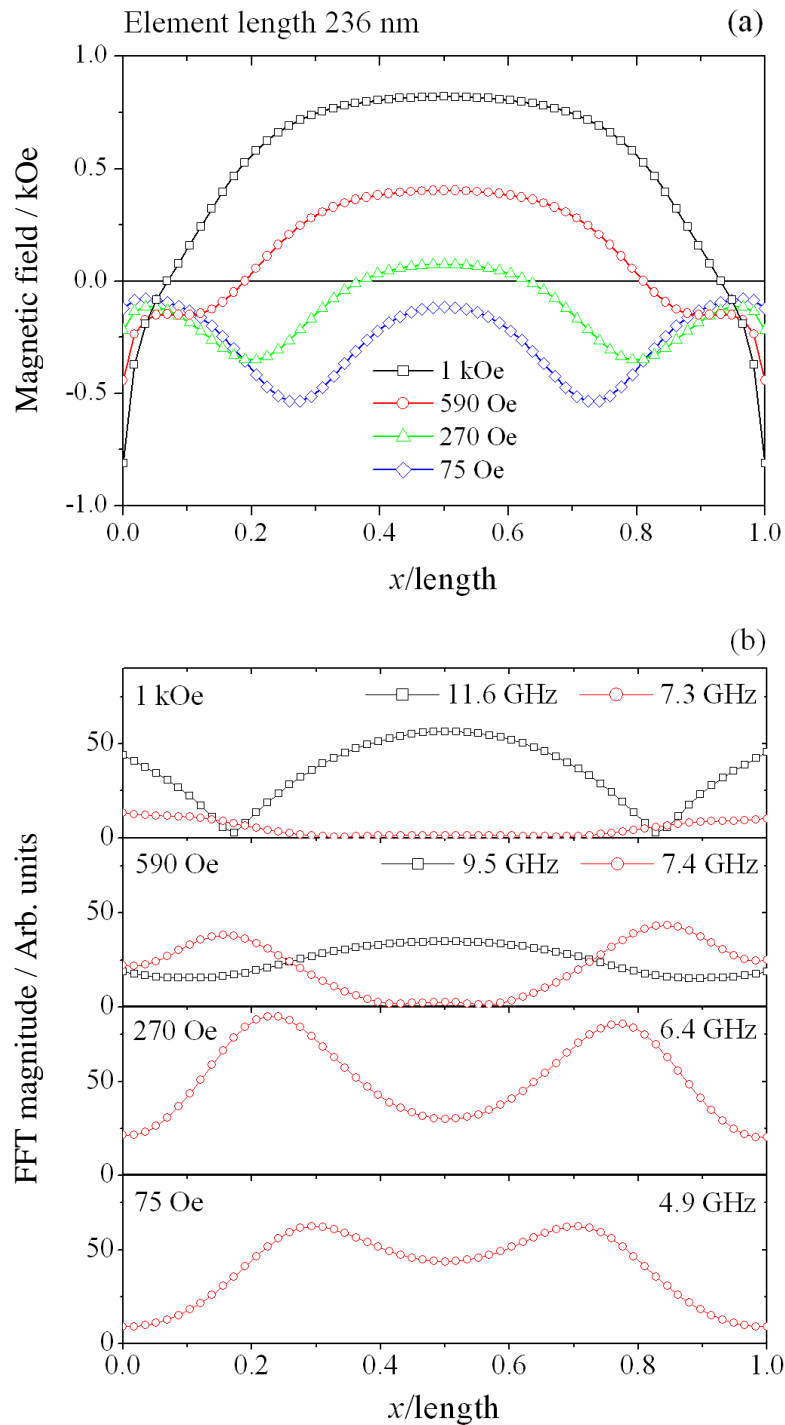


Figure 6.4.13 Cross-sections are shown of the x -component of the simulated total effective field (a) and the FFT magnitude (b) within the centre element of the 3×3 model array of 236 nm elements. The sections are shown for four different values of the bias field.

stripe towards these regions. Furthermore, a second turning point in the effective field was identified, above which only modes with an imaginary effective wavevector could exist. The region between these two boundaries was identified as the region of localisation of the lowest frequency mode. Here, in smaller sub-micron non-ellipsoidal

elements the lower frequency modes have large FFT magnitude in the gradient regions, but are not localised there. The FFT magnitude extends across regions of positive and negative internal field, as seen in Figure 6.4.12(b) at 590 Oe. The region of large FFT magnitude associated with the higher frequency mode decreases in width as the bias field is decreased. At the same time, the FFT magnitude of the lower frequency mode increases near the edge of the elements and moves towards the centre of the element. However, while the effective field is positive in the centre region, the FFT amplitude of the lower frequency mode in that region remains small.

For the 236 nm element at 590 Oe, the effective field (Figure 6.4.13(a)) in the centre region is positive and the FFT magnitude (Figure 6.4.13(b)) of the lower frequency mode is small. However, at 75 Oe, the effective field is negative across the whole section of the element. The regions of high FFT magnitude of the lower frequency mode that were near the element edges now also extend across the whole element. It is clear from Figure 6.4.13(a) that the effective field within the centre region of the element is no longer similar to the bias field. Instead, the demagnetising field contributes significantly to the effective field.

For the 70 nm element, the effective field (Figure 6.4.14(a)) is only positive in the centre region when the bias field is 1 kOe, and is significantly less than the bias field value. As discussed earlier, modes from the higher frequency branch that were found to occupy the centre region of larger elements (Figures 6.4.4-7) were not observed in the simulation of 70 nm elements at 1 kOe (Figure 6.4.8). Instead, at 1 kOe the modes excited within the 70 nm element have large FFT magnitude in the edge regions (Figure 6.4.14(b)) where the effective field is large (~ 3 kOe) and negative. In the centre region where the effective field is positive, the FFT magnitude of the modes is small. Between the bias field values of 590 and 75 Oe the large demagnetising field results in a negative effective field across the whole section of the element. Figure 6.4.8 reveals a number of different non-uniform modes that tend to have maximum magnitude at the edges of the element. Figure 6.4.14(b) reveals that the FFT magnitude of these modes is non zero throughout the element, with regions of large FFT magnitude correlated with regions of large negative internal field. Finally, at 75 Oe, Figures 6.4.3, 6.4.10, and 6.4.14(a) reveal that the 70 nm element no longer occupies the S-state, but instead occupies the leaf-state. In this case the negative effective field and the FFT magnitude are almost constant across the whole section of the element.

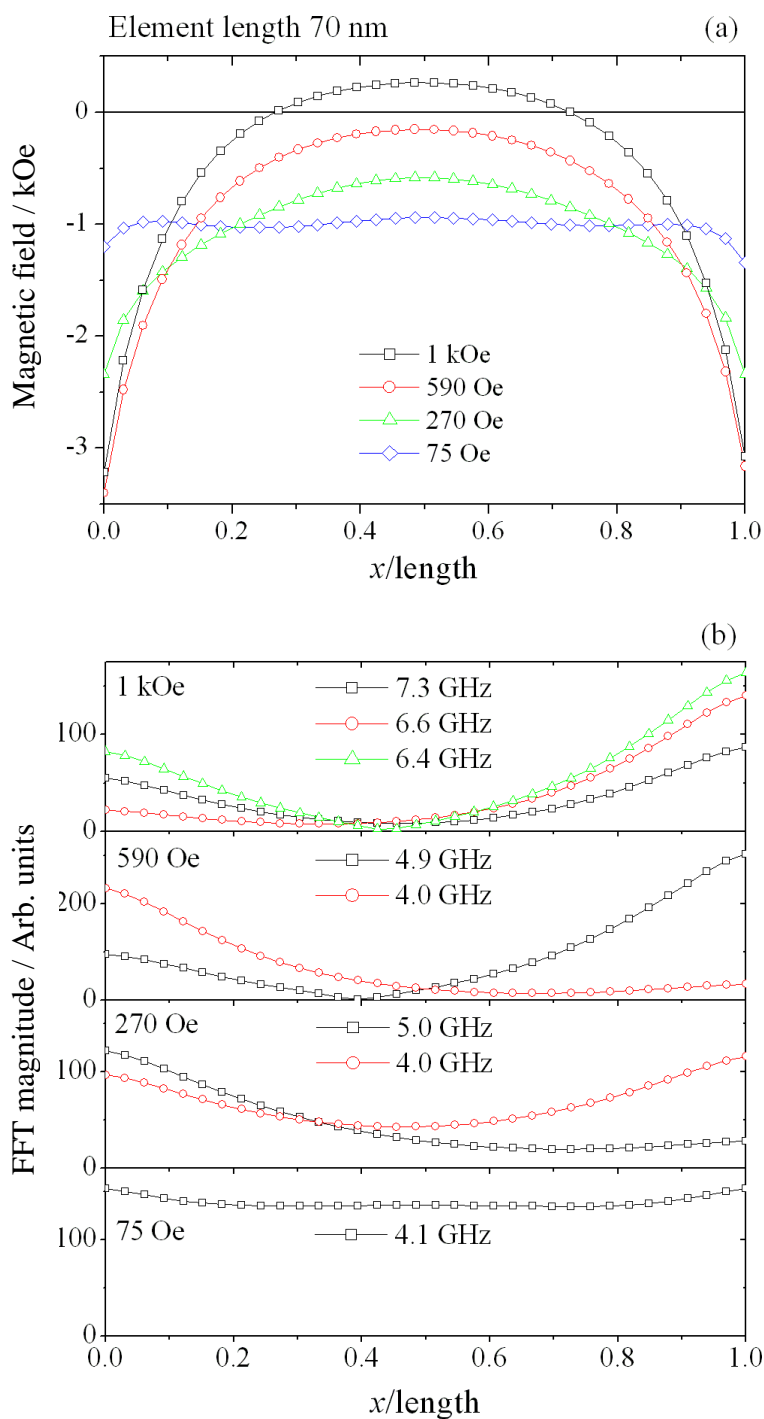


Figure 6.4.14 Cross-sections are shown of the x -component of the simulated total effective field (a) and the FFT magnitude (b) within the centre element of the 3×3 model array of 70 nm elements. The sections are shown for four different values of the bias field.

It is clear from Figure 6.4.13(b) that the crossover observed in the experimental and simulated spectra in Figure 6.4.6 is the result of a change in the spatial character of the excited modes that is mediated by the changes in the effective field throughout the element as the bias field is decreased. In a similar manner the change in the effective

field that occurs as the element size is reduced (Figure 6.4.11) can be used to explain the size dependent crossover of the spatial character of the mode seen in Figure 6.4.2. However, since the modes have non-zero FFT magnitude throughout, the crossover cannot be simply described as a crossover from a centre- to an edge-localised mode character.

6.5 Collective modes within arrays

In Reference 87 the effect of inter-element interactions upon high frequency normal modes was modelled in 3×3 square arrays of circular permalloy dots of thickness 50 nm, diameter 200 nm and interdot separation ranging from 50 to 800 nm. For an interelement separation greater than about 200 nm the high frequency response was found to be successfully modelled by that of an individual element. For interelement separations less than 200 nm, the magnetostatic interaction was found to significantly modify the mode character in the dots. Here, the interelement separation is less than 200 nm for all element sizes, and the separation is not varied. However, by varying the bias field the magnetostatic interaction between elements can be changed and investigated.

So far in this chapter the experimental spectra have been interpreted by comparing them with the corresponding simulated spectra for the centre element of 3×3 model arrays and then calculating the Fourier images of the spatial character for particular modes. For all element sizes, particularly for the lower frequency modes (< 8 GHz) the spatial character of modes excited in the centre element are similar if not the same as other excited modes for a particular element size and bias field. This has been interpreted as evidence for collective modes within the 3×3 array. The simulated Fourier images of the centre element reveal that the spatial character of the FFT magnitude *and* phase were similar for modes with different frequency. However, in these cases the spatial character of amplitude and phase across the 3×3 array were found to be different.

In Figure 6.5.1(a), the FFT magnitude and phase are shown for two modes with frequencies of 6.75 and 7.0 GHz excited in the centre element of a 3×3 array of 236 nm elements. While there is a finite phase difference between the two modes, the variation of the phase within each image is similar. In Figure 6.5.1(b) the FFT magnitude is shown for all elements in the 3×3 array. While the spatial character of the two modes are similar in the centre element, the character of the modes across the array are very

different demonstrating that collective modes are excited within the array. The excitation of collective modes with similar frequencies may contribute to linewidth broadening of the experimental spectra in Figures 6.4.4-8. The Fourier images in Figures 6.4.4-8 reveal that below the crossover field there are often several modes at a particular bias field with similar spatial character. Indeed, as the bias field is reduced the static magnetisation state becomes increasingly non-uniform and the magnetostatic interaction between elements increases³⁹. Therefore, below the crossover field a larger splitting of the frequencies of the collective modes is expected. This is supported by the increased linewidth observed experimentally at lower bias field values.

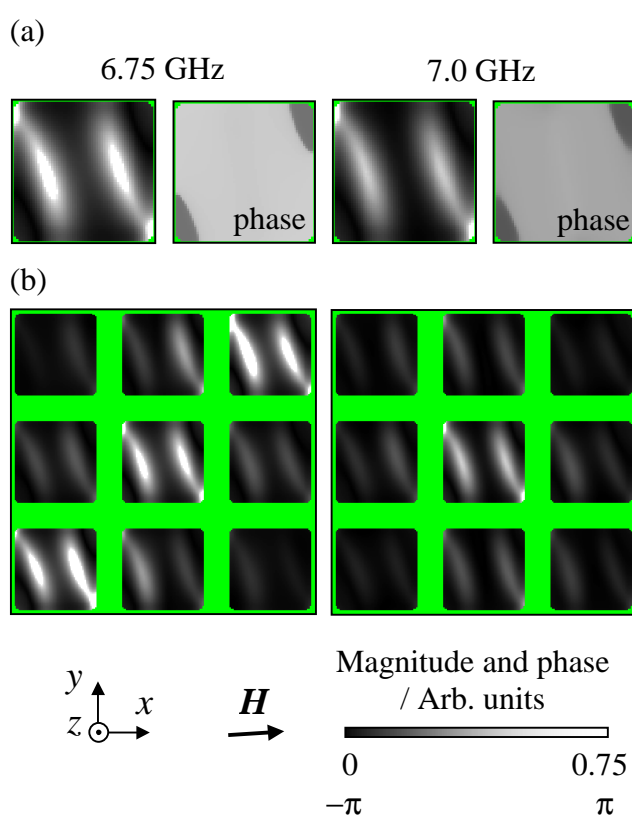


Figure 6.5.1 Simulated Fourier images of FFT magnitude and phase are shown in (a) for two modes with frequencies of 6.75 and 7.0 GHz excited in the centre element of a 3×3 array of 236 nm elements at a bias field of 270 Oe. In (b) the FFT magnitude is shown for all elements in the 3×3 array.

6.6 Summary

TRSKM measurements upon arrays of square ferromagnetic nano-elements of different size and for a range of bias fields have been performed. The experimental results were compared to micromagnetic simulations of model arrays in order to understand non-uniform precessional dynamics within the elements. Experimentally, two branches of excited modes were observed to co-exist above a particular bias field. Below the so called crossover field, the higher frequency branch was observed to vanish.

Micromagnetic simulations and Fourier imaging revealed the spatial character of the two mode branches. The modes of the higher frequency branch were found to have high FFT amplitude at the centre of the element in regions of positive effective field, while modes of the lower frequency branch were found to have high FFT amplitude near the edges of the element perpendicular to the bias field. Cross-sections of the simulated images of the effective field and FFT magnitude revealed that the crossover between the higher and lower frequency branches was mediated by the complicated evolution of the total effective field within the element. Below the crossover field the increase in the width of the edge region of negative effective field, at the expense of the centre region of positive effective field, allowed the edge-type mode to extend over the entire element. The simulations revealed that the majority of the modes were de-localised with non-zero FFT magnitude throughout the element. Therefore, the spin-wave well model introduced in Reference 40 for micron sized non-ellipsoidal elements could not be used here to characterise the excited modes as strictly centre- or edge-localised modes. The de-localised nature of the excited modes seems to be an intrinsic property of square nano-elements. However, the mode spatial character was found to be correlated with features of the effective field and the static magnetisation state.

The simulations revealed that the frequency of modes from the lower frequency branch were very sensitive to the static magnetisation state of all the elements within the model array. Therefore, by matching the simulated spectra to the experimental spectra insight into the ground state of the elements studied here was gained. Since, below the crossover field the static magnetisation state was shown to be non-uniform, increased magnetostatic interaction is expected between the elements within the array. The simulated spectra revealed that many modes may be excited that have similar spatial character within the centre element. However, inspection of the entire array revealed the existence of collective modes, where the FFT amplitude in the elements surrounding

the centre element was considerably different for two such modes. The excitation of collective modes with similar spatial character in the centre element but different frequency may account for the increased linewidth observed in the experimental spectra below the crossover field.

Finally, the results presented in this chapter may be useful for the development of a thorough analytical theory of non-uniform modes within magnetic nano-elements with non-uniform static magnetisation and total effective field. Detailed knowledge of the mode character of square nano-elements and their static magnetisation state is also essential for data storage applications in the finite field regime.

“Symmetry is what we see at a glance”. – Blaise Pascal (1623-1662)

Chapter 7

Dynamic configurational anisotropy in nanomagnets

7.1 Introduction

In this chapter I will present the results of experiments on nano-elements with similar composition to those studied in Chapter 6, but with thickness of ~ 2.5 nm. In Reference 11 the experimentally observed modes of the same, thinner, nano-elements were found to fall upon two branches, with a crossover from the high- to low-frequency regime as the element size was reduced to less than 220 nm. However, the signal-to-noise ratio of the experiment was insufficient for the coexistence of modes from each branch in the 220 nm element to be clearly observed. My contribution to the work presented in this chapter was the construction of the time-resolved scanning Kerr microscope with an enhanced signal-to-noise ratio so that two modes were clearly resolved. The improvements to the experiments have already been described in Section 3.7 of this thesis. The time-resolved data for this chapter was acquired by myself and Dr Volodymyr Kruglyak^{*}, while the analysis of the data and the interpretation of the results was carried out by Dr Volodymyr Kruglyak.

As described in Section 2.9, the internal magnetic field in elongated or flattened ferromagnetic elements is different when the external magnetic field is applied along the long and short axes. This effect is referred to as the shape anisotropy. Generally, the

^{*} School of Physics, University of Exeter, Stocker Road, Exeter, EX4 4QL

shape anisotropy is determined by the aspect ratio of the element and is not determined by the uniformity of its magnetic configuration. In particular, the shape anisotropy exists in ellipsoidal magnetic elements in which the internal magnetic field and hence the magnetisation are uniform. However, a simple calculation shows that the internal magnetic field in the centre of a square magnetic element does not depend upon the direction of the external magnetic field applied in the plane of the element.

In magnetic nano-elements with a non-ellipsoidal shape, small deviations of the static magnetisation from the uniformly magnetised state result in a strong anisotropy with a symmetry that, to a first approximation, corresponds to that of the shape of the nano-element^{71,102-104}. Schabes and Bertram¹⁰² identified this so-called configurational anisotropy from a numerical study of the dependence of the magnetic hysteresis loop upon the direction of the magnetic field applied to ferromagnetic nano-cubes. Cowburn *et al.*^{71,104} studied experimentally the dependence of the total free energy of and the average total effective magnetic field in thin nano-elements upon the direction of a bias magnetic field of constant magnitude. They showed that the effective magnetic field due to the configurational anisotropy could have a magnitude of a few hundred Oersteds in the centre of a magnetic nano-element and so could easily dominate its static magnetic properties.

The manifestations of the configurational anisotropy in the magnetisation dynamics of magnetic elements were discussed further in a series of recent publications by different groups. Chérif *et al.* observed a difference between spin wave frequencies within the Brillouin light scattering (BLS) spectra measured with the bias magnetic field applied parallel to the edge and to the diagonal of rectangular elements^{105,106}. The effect of the configurational anisotropy upon the ferromagnetic resonance mode was studied by Zhai *et al.*¹⁰⁷ and more recently by Pardavi-Horvath *et al.*¹⁰⁸. The spatial character of the anisotropic magnetisation dynamics in micrometer sized square magnetic elements was directly studied by time-resolved scanning Kerr microscopy by Barman *et al.*^{63,92,109,110}. In addition to the fourfold variation of the frequency of the uniform precessional mode, they found that the spatial character of magnetostatic modes of finite wave number depends sensitively upon the direction of the bias magnetic field, and the dephasing of the modes leads to an anisotropic apparent damping of the precessional signal.

In contrast to the isolated element anisotropy discussed above, which can be referred to as an intrinsic configurational anisotropy, the effective magnetic field inside an element within an array can also contain an anisotropic contribution due to the stray

field from the neighbouring elements^{72,111-114}. This anisotropy is mediated by the magnetically unsaturated regions situated near the edges of the elements⁷², and can be referred to as an extrinsic configurational anisotropy.

The anisotropic variation of the high frequency magnetisation dynamics observed in References 63, 72, 92, and 105-114 could be explained by an anisotropic modification of the static effective magnetic field in the magnetic element either due to the configuration of the static magnetisation or due to the static stray field from the neighbors. However, Cowburn *et al.*¹⁰⁴ found that the static configurational anisotropy essentially vanishes in squares of thickness equal to or smaller than 3 nm and of size equal to or smaller than 200 nm. In this chapter the angular variation of the precessional mode frequencies of a square magnetic nano-element of similar size and thickness will be presented. The variation of frequency with bias field orientation is governed in this regime by the variation of both the static and dynamic magnetisation configuration and the associated dynamic effective magnetic field. There is therefore a dynamic configurational anisotropy. The anisotropy is intrinsic and originates from the anisotropy of the magneto-dipole interaction, which has also been known to govern the dispersion of magnetostatic modes in uniformly magnetised magnetic slabs³⁸ (Section 2.15) and in magnetic stripes with non-uniform magnetisation¹¹⁵ (Section 2.17). The angular variation of the magnetisation dynamics in elements of different size, *e.g.*, those in References 11 and 85, will in general be governed by a competition of dynamic and static configurational anisotropies.

7.2 Sample and experimental details

The sample (wafer reference number A77) was fabricated by Dr Jeffrey Childress* and Dr Jordan Katine*. The array was square, with length $\sim 4 \mu\text{m}$, and consisted of elements of length(separation) 220 (95) nm. The array was formed from a Ta(50 Å)/Al₂O₃(10 Å)/Co₈₀Fe₂₀(10 Å)/Ni₈₈Fe₁₂(27 Å)/Ta(100 Å) film sputtered onto a Si wafer and patterned by electron beam lithography and ion milling. The Al layer was oxidised in O₂ at 500 mTorr for 15 minutes. Uniaxial anisotropy was induced in the sheet material by field annealing prior to the post-deposition array fabrication. As described

* Hitachi Global Storage technologies, San Jose Research Center, 3403 Yerba Buena Road, San Jose, California 95135

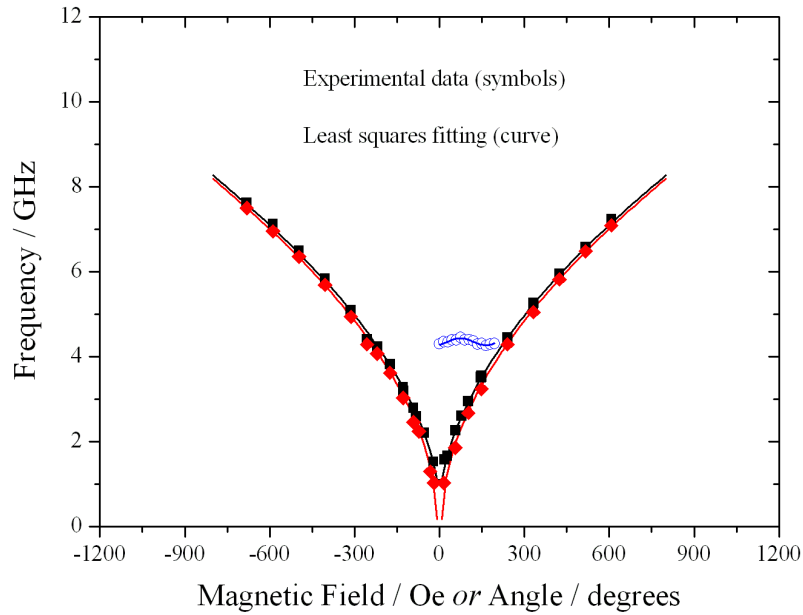


Figure 7.2.1 The dependence of the uniform mode frequency on the bias field magnitude (red and black symbols and curves), and on the bias field orientation (blue symbols and curve) for a $6 \mu\text{m}$ square element. Black squares and red diamonds show the experimental frequencies when the bias field was applied along the easy and hard axes respectively. Blue open circles show experimental frequencies as a function of the bias field orientation when the bias field magnitude was 270 Oe. The corresponding curves are least squares fits to the macrospin model in the quasi alignment approximation.

in Section 6.2, a coplanar stripline (CPS) was fabricated around the array so that pump-probe measurements could be performed. A microscope objective of numerical aperture 0.65 ($\times 40$) was used and the out-of-plane component of the dynamic magnetisation was detected by measuring the polar Kerr rotation, as described in Section 3.5. The amplitude of the measured Kerr rotation was typically a few tens of microdegrees. The magnetic parameters of the sample studied in this chapter are given in Reference 85. The volume-weighted magnetisation of the bilayer was 930 emu/cm^3 , where the saturation magnetisations of the $\text{Co}_{80}\text{Ni}_{20}$ and $\text{Ni}_{88}\text{Fe}_{12}$ were given in Section 6.2. Figure 7.2.1 shows the frequency of the uniform mode excitation in a $6 \mu\text{m}$ square element as a function of the bias field value, and bias field orientation. The uniaxial ($9450 \pm 677 \text{ erg/cm}^3$) and surface ($-0.491 \pm 0.018 \text{ erg/cm}^2$) anisotropy parameters of the patterned material were extracted by fitting the frequency versus bias field data to a macrospin model in the quasi-alignment approximation. The value of the g -factor was

assumed be 2.1. The easy axis was found to be canted by about 10° from the direction of the striplines. The material parameters deduced here were used in the micromagnetic simulations. The validity of the assumption of quasi-alignment was verified by performing dynamical macrospin simulations in which the ground state or static orientation of the magnetisation was determined using the steepest descent method.

The size of an individual element within the array was smaller than the spatial resolution of the experiment. Therefore, numerical simulations were performed with the Object Oriented Micromagnetic Framework⁴¹ (OOMMF). The numerical methods described in Section 6.3 were used to reproduce the observed variations in the mode frequencies. Once the agreement between the experimental and the simulated spectra was established, the spatial distributions of the out-of-plane component of the dynamic magnetisation could be mapped, and the associated effective fields¹² calculated.

7.3 Experimental and numerical results

The measured time-resolved (TR) Kerr signals and their fast Fourier transform (FFT) spectra are presented in Figures 7.3.1 and 7.3.2 for different values and orientations of the bias magnetic field. In Figure 7.3.1, when the field is applied parallel to an element edge, the FFT spectrum contains two modes. In Reference 11, the higher and the lower frequency modes were found to be associated with the central area of the element (“centre mode”) and the element edges perpendicular to the field direction (“edge mode”), respectively. The edge mode FFT peaks are noticeably broader than those of the centre mode, which was interpreted in Reference 11 in terms of the increased influence of the edge roughness. For the field applied parallel to a diagonal of the element, the FFT spectrum contains only one mode at a frequency that is similar to but slightly smaller than that of the centre mode observed when the field was applied parallel to an edge.

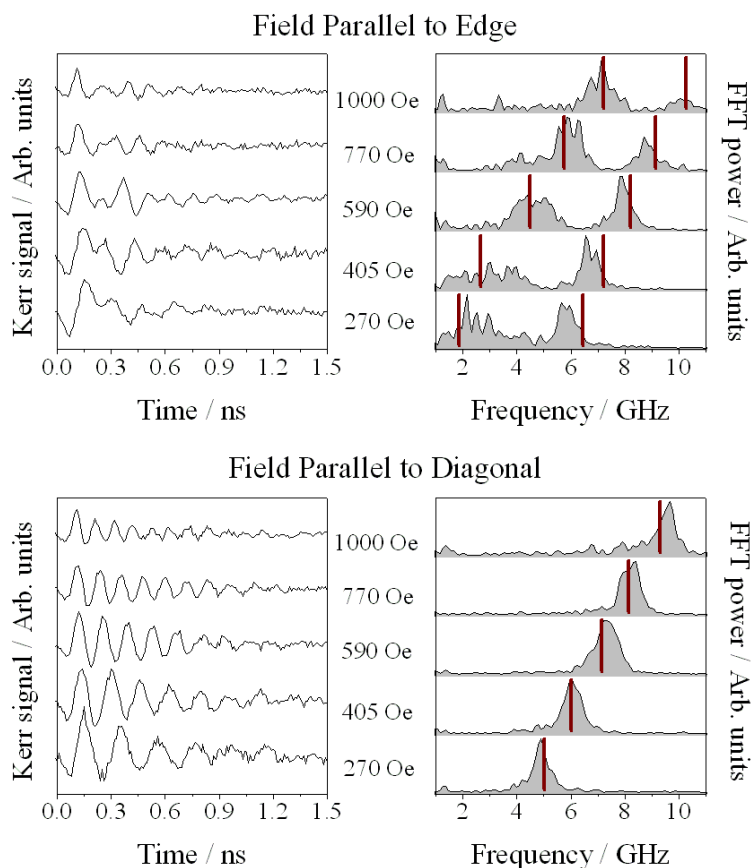


Figure 7.3.1 TR Kerr signals (left panels) and their FFT spectra (right panels) obtained for different values of the bias magnetic field are shown for the field applied parallel to the edge (upper panels) and diagonal (lower panels) of the element. In each panel, curves from top to bottom correspond to bias field values of 1000, 770, 590, 405, and 270 Oe, respectively. The vertical dashes show the frequencies of the modes obtained from the micromagnetic simulations.

In order to elucidate how the transition between the “two mode” and “single mode” regimes occurs, measurements were performed as a bias field of fixed value (589 Oe) was rotated through 360° in steps of 15° . The results are shown in Figure 7.3.2. In the FFT spectra obtained with the field aligned 15° from the element edges, a strong peak was observed at a frequency somewhere in between those of the edge and centre modes observed with the field parallel to an edge. A smaller less distinct peak was also sometimes observed at a frequency higher than that of the centre mode observed with the field parallel to an edge. In the FFT spectra obtained for field directions 15° from an element diagonal, a single peak was observed at a frequency similar to that of the mode observed with the field parallel to a diagonal.

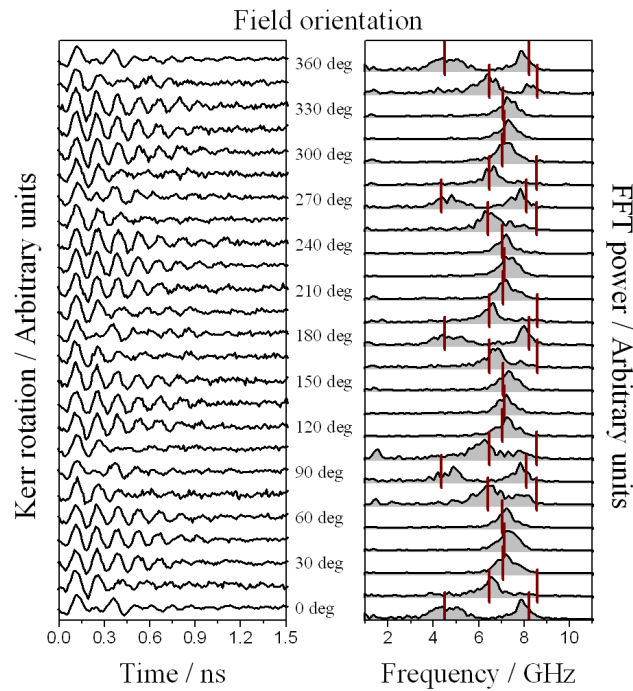


Figure 7.3.2 TR Kerr signals (left panel) and their FFT spectra (right panel) obtained for different orientations of the bias magnetic field are shown for the field value of 590 Oe. For $0^\circ/360^\circ$, 90° , 180° and 270° the field lies parallel to an edge of the element. The vertical dashes show the frequencies of the modes obtained from the micromagnetic simulations.

Focused, vector hysteresis loops were acquired from the array using the vector bridge detector as described in Chapter 4. Figure 7.3.3 shows M_{\parallel} hysteresis loops obtained for four orientations of the applied field. In Figure 7.3.3(a) and (c) the field was applied parallel the edges of the element along 0° and 90° respectively, while in Figure 7.3.3(b) and (d) the field was applied along the element diagonals along 45° and 135° respectively. Figure 7.3.3 shows that the coercive H_c and saturation fields H_s are similar to within ± 5 Oe for all directions of the applied field. Small variations of these field values may be attributed to the shape or configurational anisotropy of the element within the array. On the other hand, the loops exhibit noise and drift (observed as the opening of the loop for $H > H_s$), which can also lead to the variation of H_c and H_s . Importantly, Figure 7.3.3 reveals that $H_s \approx 30$ Oe so that at a bias field value of 590 Oe the magnetisation was saturated. Furthermore, the loops confirm that the static configurational anisotropy is small.

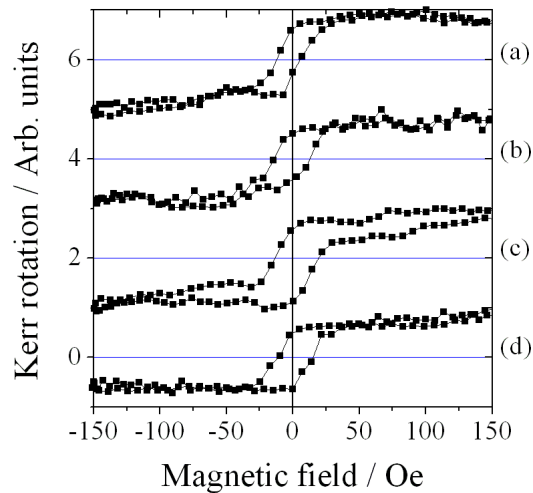


Figure 7.3.3 Focused, vector hysteresis loops are shown for the case when the magnetic field was applied parallel to the edges of the element along (a) 0° and (c) 90° , and along the element diagonals along (b) 45° and (d) 135° .

In order to understand the observed behaviour, we simulated the magnetisation dynamics within both an isolated element and a model array of 3×3 identical elements so that the centre element of the array had the same neighbourhood as in the experiment. The simulations were performed with the material parameter values determined experimentally in Reference 85 and used in the simulations of Reference 11. In order to avoid numerical artefacts due to the presence of sharp edges^{116,117}, the shape of the element was derived from a scanning electron microscope image of the array. The static state at each bias field value and orientation was prepared by allowing the magnetisation to relax from a uniform state. These static states were then used as the initial configuration in two kinds of dynamical simulation. In the first, the sample was excited by an out-of-plane pulsed field¹¹. In the second, a small harmonic out-of-plane field was applied with frequency corresponding to one of the modes identified from the response to the pulsed excitation^{12,112}.

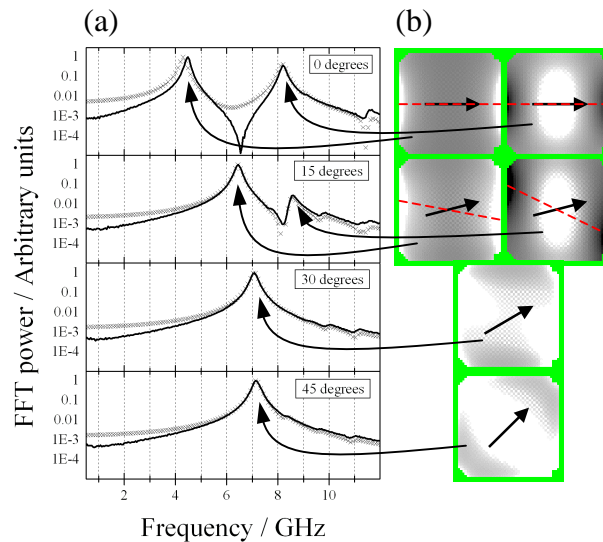


Figure 7.3.4 Simulated FFT spectra of the out-of-plane component of the average dynamic magnetisation of the centre element in a 3×3 array (solid line) and of an isolated element (symbols) in response to a pulsed magnetic field are shown in (a) for four different orientations of a bias field of 589 Oe. The dynamic configurations of the magnetisation within an isolated element subject to a harmonic magnetic field at a frequency corresponding to the FFT peak marked by the arrow are shown in the images in (b). White and black correspond to the positive and negative values of the dynamic out-of-plane component of magnetisation, respectively. The arrows and the dashed lines in the images represent the directions of the bias field and of the effective wave vector, respectively.

As indicated in Figure 7.3.1 and 7.3.2, the simulations for the model array with a pulsed magnetic field reproduced well the experimentally observed variation of the mode frequencies with the value and orientation of the bias magnetic field. Figure 7.3.4(a) compares the FFT spectra calculated from the out-of-plane component of the dynamic magnetisation in response to the pulsed field excitation. The response was averaged over the volume of the isolated element, and of the same element situated in the centre of a 3×3 model array. The two simulations were in excellent agreement for all bias field orientations, except for a tiny difference of the edge mode frequency. Therefore we can neglect effects associated with the extrinsic configurational anisotropy in the present discussion. The images of the dynamic magnetisation within the individual element in response to the harmonic excitation are shown in Figure 7.3.4(b) as the bias field is rotated between the directions parallel to the edge and to the diagonal of the element.

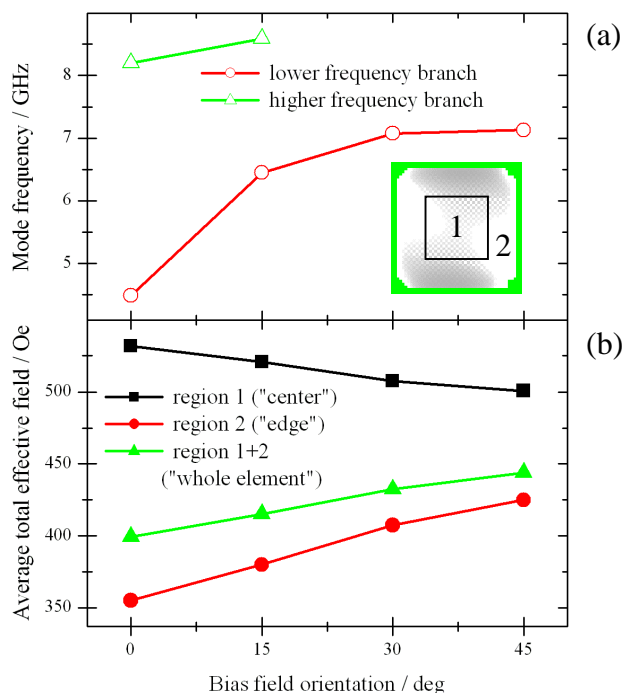


Figure 7.3.5 The dependence of the calculated mode frequencies (a) and of the total effective field averaged over different regions of the sample (b) upon the orientation of the bias magnetic field is shown. The inset shows the centre (1) and edge (2) regions of the sample over which the averaging was performed.

The mode frequencies calculated from the simulations for the isolated element are plotted in Figure 7.3.5(a) for different orientations of the bias magnetic field, while Figure 7.3.5(b) shows the corresponding values of the *static* effective field averaged over the centre and edge regions of the element, as well as the entire element. As expected from Reference 103, because of the large aspect (size-to-thickness) ratio, the variation of the static effective field with the applied field angle due to the static configurational anisotropy (< 70 Oe) is too small, on its own, to explain the observed variation of the mode frequencies (> 2.5 GHz). Indeed, one can estimate from Figure 7.3.1 that such a frequency change requires a field change of about 250 Oe. In additional simulations, the magnitude of the applied field for the different orientations was slightly adjusted (by less than 16 Oe) so that the value of the average static effective field was the same in each case. This resulted in a modification of the mode frequencies by less than 0.1 GHz. Therefore, we conclude that the observed effects must be due to dynamic rather than static configurational anisotropy.

7.4 Discussion

If the Hamiltonian describing a magnetic element is time invariant, the energy of small perturbations to the ground state (magnons) is conserved in the absence of the magnetic damping. The spin wave mode frequencies f then represent “good” quantum numbers, and can be obtained by solving the following eigenvalue problem, derived from the linearised Landau-Lifshitz equation¹¹⁸,

$$i2\pi f \mathbf{m}_f(\mathbf{r}) = -\gamma[\mathbf{m}_f(\mathbf{r}) \times \mathbf{H}_{eff}(\mathbf{H}, \mathbf{M}(\mathbf{H}, \mathbf{r}))] - \gamma[\mathbf{M}(\mathbf{H}, \mathbf{r}) \times \mathbf{h}_{eff}(\mathbf{m}_f(\mathbf{r}))], \quad (7.4.1)$$

where \mathbf{M} and \mathbf{H}_{eff} are the static magnetisation and static total effective field, γ is the gyromagnetic ratio, and \mathbf{r} is the spatial coordinate. The angular variation of \mathbf{H}_{eff} is responsible for the static configurational anisotropy. The dynamic effective field \mathbf{h}_{eff} is related to the dynamic magnetisation \mathbf{m}_f for a particular mode by a linear integro-differential operator¹¹⁵, and is responsible for the dynamic configurational anisotropy.

The translational invariance of the system is broken in both in-plane directions due to the non-uniform static effective field and magnetisation^{11,12}. Hence, it is impossible to ascribe a constant wave vector (momentum) to a particular mode. Moreover, a coordinate dependent wave vector, such as that introduced in Reference 115 for a long stripe, is inappropriate here because it is impossible to assign a direction to the wave vector. However, in order to gain some insight into the mechanisms that underlie the observed variations in frequency, it is useful to make comparison with the dispersion of dipolar-exchange spin waves excited within a continuous ultrathin film *i.e.* in a system with translational invariance for which the in-plane wave vector is well defined. Neglecting any in-plane anisotropy, the frequency of the spin wave modes depends upon the angle φ between the in-plane wave vector ($|\mathbf{k}| = k = 2\pi/\lambda$) and the static magnetisation as¹¹⁹

$$2\pi f(\varphi) = \gamma \sqrt{\left(H + \frac{2A}{M_s} k^2 + 2\pi M_s k d \sin^2 \varphi \right) \left(H + \frac{2A}{M_s} k^2 + 4\pi M_s \left(1 - \frac{kd}{2} \right) \right)}, \quad (7.4.2)$$

where A is the exchange constant and M_s is the saturation magnetisation. Let us now introduce an effective “wave vector direction” as shown in Figure 7.3.4. This direction appears to lie parallel to the field when the field is applied along the edge of the element, but seems to be strongly rotated from the direction of the field when the field is

applied at 15° from the edge. Equation 7.4.2 shows that the dynamic dipolar interaction influences the frequency through both the magnitude of the wave vector (in the terms containing kd) and its direction φ with respect to the static magnetisation, while the exchange interaction influences the frequency only through the magnitude of the wave vector. Using the parameter values stated previously, Equation 7.4.2 can easily account for the observed frequency variation if φ and k are allowed to vary by about 15° and 10% respectively as the orientation of the applied field is varied.

The arguments presented in the previous paragraph allow us to explain qualitatively the dynamic configurational anisotropy in terms of the dispersion of dipolar-exchange spin waves. A more rigorous analysis requires Equation 7.4.1 to be solved in terms of a more appropriate set of eigenfunctions^{8,115}. The solution should also take into account the transition of the mode character from “edge” to “centre” observed in Figure 7.3.4 as the orientation of the bias field is changed. As the modes span different areas of the element, they also “see” different static effective magnetic fields and hence different contributions from the static configurational anisotropy, as indicated in Figure 7.3.5. However, the frequency of the lowest mode changes only slightly at the mode crossover from the edge to centre character observed at the field orientations of 30° and 45° . This suggests that, in the present case, changes in the effective wave vector drive the variation in frequency of the lowest lying mode as the orientation of the static field is changed. Although the regions over which the static field is averaged in Figure 7.3.5 provide only a crude approximation of the regions of confinement of the edge and centre modes, they give a good qualitative account of the small variation of the static effective field. A rigorous analytical theory of the observed phenomena is however beyond the scope of this experimental chapter.

7.5 Summary

In summary, the resonant modes of a square shaped magnetic nano-element have been studied experimentally and numerically. Both the number of modes and their frequencies were observed to vary as the orientation of the external magnetic field was rotated in the plane of the element. It was shown that the observed variation cannot be explained by either the effect of the extrinsic configurational anisotropy or the static intrinsic configurational anisotropy. Instead the variation of the dynamic effective field is due to a dynamic intrinsic configurational anisotropy. This new anisotropy can dominate the ultrafast magnetisation dynamics of ultrathin nanomagnets for which the static intrinsic configurational anisotropy is of minor importance.

“If your result needs a statistician then you should design a better experiment”.

– Ernest Rutherford (1871-1937)

Chapter 8

Recent experimental developments for future work

8.1 Introduction

The magnetisation dynamics of the samples presented in this thesis were measured using the time-resolved scanning Kerr microscope (TRSKM) described in Chapter 3. In Section 3.7 the limitations of the TRSKM were discussed in addition to the action taken to extend the limits of the experiment. As a result of the action taken, previously undetected phenomena could be observed and investigated, *e.g.* the dynamic configurational anisotropy in an array of CoFe/NiFe nanomagnets (Chapter 7). However, an adequate signal-to-noise ratio was only obtained for a sufficiently long integration time of the lock-in amplifiers. Furthermore, while arrays of nanomagnets exhibit interesting magnetic phenomena, *e.g.* collective excitations, such phenomena make the magnetic behaviour of an individual nanomagnet difficult to isolate. Primarily, the magnetisation dynamics of nanomagnets were measured within arrays to enhance the signal-to-noise ratio. The construction of an experiment with sufficient sensitivity and stability for measurements upon a single nanomagnet is a difficult task. The combination of limitations that led to long data acquisition times and low sample throughput were the motivation for the redesign of the experimental set-up of the TRSKM. In this chapter I will describe the experimental developments for future work. I will also present some preliminary results obtained using the new experimental set-up.

Where possible, the improvements will be illustrated by comparing the new results to those obtained using the experimental set-up described in Chapter 3.

8.2 Recent developments

During the final year of my PhD research project I rebuilt the TRSKM in order to increase the functionality, mechanical stability and productivity of the experiment. Construction of a microwave probe station has allowed impulse generators with pulse widths down to 70 ps and microwave synthesisers with frequencies up to 50 GHz to be used to excite various samples, and is expected to facilitate ultrafast switching of nanomagnets. Construction of a new vector bridge detector with enhanced bandwidth has facilitated vector-resolved measurements of the precessional magnetisation dynamics in addition to the *in-situ* measurement of hysteresis loops from sub-micron sized samples. The changeover time for realignment between different types of experiments performed on the probe station is now less than an hour, while for the previous experimental set-up mounting a sample and connecting the pulse field device often required days. The microscope was redesigned and built with a vertical probe beam path for increased mechanical stability, which is essential for the measurement of individual nanomagnets. The modifications give much faster data acquisition rates, without compromising the data quality. For example, measurements that used to require half an hour now require little more than five minutes.

8.3 Experimental set-up

The new experimental set-up of the TRSKM is shown in Figure 8.3.1. The Tsunami output beam is not split into pump and probe beams, but instead is used as a magneto-optical probe only. The beam is passed along an optical time delay with a range of 8 ns prior to entering the scanning Kerr microscope. The set-up of the scanning Kerr microscope is very similar to that described in Chapter 3. The beam is expanded by a factor of ten using a beam expander (Thorlabs BE10X-B) with anti-reflection coating suitable for a range of wavelengths from 650 to 1050 nm. The BE10X-B is favoured over the expansion optics used in the previous set-up since the optical components are contained within a more compact assembly. In the new

scanning Kerr microscope set-up, the piezoelectric (flexure) stage is used to scan the microscope objective lens instead of the sample. The effect of scanning the objective lens on the magneto-optical measurements has been tested and will be discussed later.

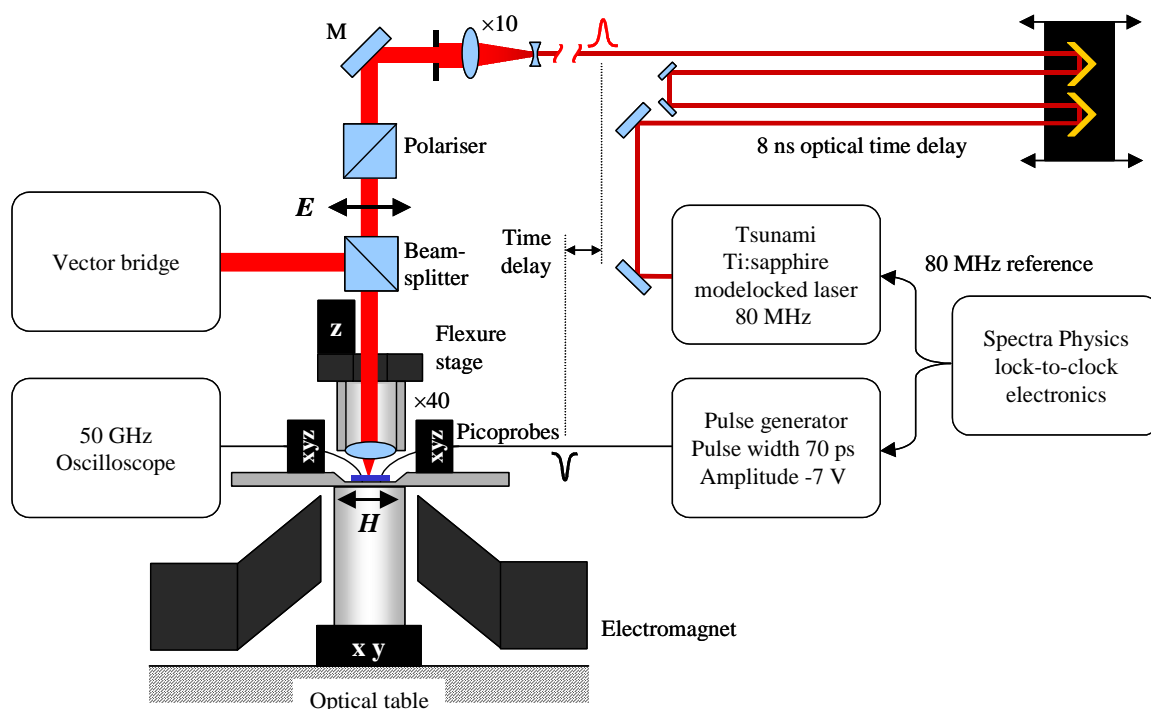


Figure 8.3.1 A schematic of the set-up of the TRSKM and microwave probe station used in pulsed magnetic field experiments.

The design of the probe station began with the electromagnet. The electromagnet was designed by Professor Rob Hicken* and built by Mr Russell Edge*. Detailed plans of the probe station assembly were drawn by Mr Russell Edge and are shown in Figures A3.1 to A3.3 of Appendix 3. The design of the electromagnet was specific to the vertical alignment of the microscope. The pole pieces have a separation of 5 cm to accommodate the sample stage and allow for coarse positioning of the sample stage below the focused laser spot. The pole pieces are raised above the level of the coils so that the sample is at the same level as the top edge of the pole pieces, as shown in Detail B, Figure A3.2. The maximum constant magnetic field at the sample position is ~ 1.8 kOe. The coils can be water cooled. The water flows between the coil windings and the yolk, and then flows around the outside of the windings. The water

* School of Physics, University of Exeter, Stocker Road, Exeter, EX4 4QL

cooling is necessary to prevent thermal expansion of the sample stage and microscope, both of which result in mechanical drift. The electromagnet is mounted on a tapered roller bearing so that the magnetic field can be applied along any in-plane direction of the sample.

Mechanical vibration

The sample stage main support (item no. 9, Figure A3.1) is mounted on two linear stages for coarse xy -positioning of the sample stage beneath the laser spot. The stages have non-influencing locks that are used to prevent mechanical drift and vibration. To prevent mechanical vibration of the sample stage, four supports with spring-loaded roller-balls in contact with the optical table were fitted to the sample stage and braced to the adapter block (item no. 8, Figure A3.1). The spring-loaded roller-balls act to reduce the amplitude of vibrations, while allowing the sample stage to be positioned as required. The supports were built by Mr Kevyn White*.

Before and after the supports were attached, the amplitude of the vibrations was estimated by scanning the focused laser spot across the edge of a $6\ \mu\text{m}$ square CoFe/NiFe element using the flexure stage. The vibration along the x - and y -direction was investigated by scanning the spot across orthogonal edges of the square. In Figure 8.3.2 oscilloscope traces of the reflectivity signal are shown as the focused laser spot was placed at different positions Δx parallel to the x -direction for the case when the sample stage was (a) unsupported and (b) supported. The difference in the reflectivity signal when the whole spot was initially on the substrate and then on the sample was $\sim 1\ \text{V}$. When the spot was positioned directly over the edge of the square an oscillatory signal was observed in the reflectivity signal as a result of the mechanical vibration. Before and after the supports were attached, the frequency of vibration was $\sim 32\ \text{Hz}$ and $\sim 44\ \text{Hz}$ respectively. The peak-to-peak amplitude of the signal was found to be less than $1\ \text{V}$. Therefore, the peak-to-peak amplitude of the vibration was less than the diameter of the focused laser spot. The schematic in Figure 8.3.2(c) can be used to approximately estimate the peak-to-peak amplitude of the vibration δx . In Figure 8.3.2(a) the position of the focused spot was moved through $3.5\ \mu\text{m}$, and the oscillatory signals correspond to a peak-to-peak amplitude of vibration of $3.5 - 0.8 = 2.7\ \mu\text{m}$, assuming that the full-width at half-maximum spot diameter is $800\ \text{nm}$

* School of Physics, University of Exeter, Stocker Road, Exeter, EX4 4QL

(Figure 8.3.2(c)). The spot diameter was estimated from an image of a 3×3 array of 637 nm square elements (Figure 4.2.5(g)) obtained using the same $\times 40$ microscope objective lens, Figure 3.5.1(inset). In Figure 8.3.2(b) the spot has moved through $1.0 \mu\text{m}$, and the signals corresponds to a peak-to-peak amplitude of vibration of ~ 200 nm. Similar data for the y -direction revealed that the amplitude of vibration was reduced from $2.7 \mu\text{m}$ to ~ 400 nm. The amplitude of vibration was reduced along both axes, however further control of the mechanical vibration is required in order to perform experiments upon individual nanomagnets.

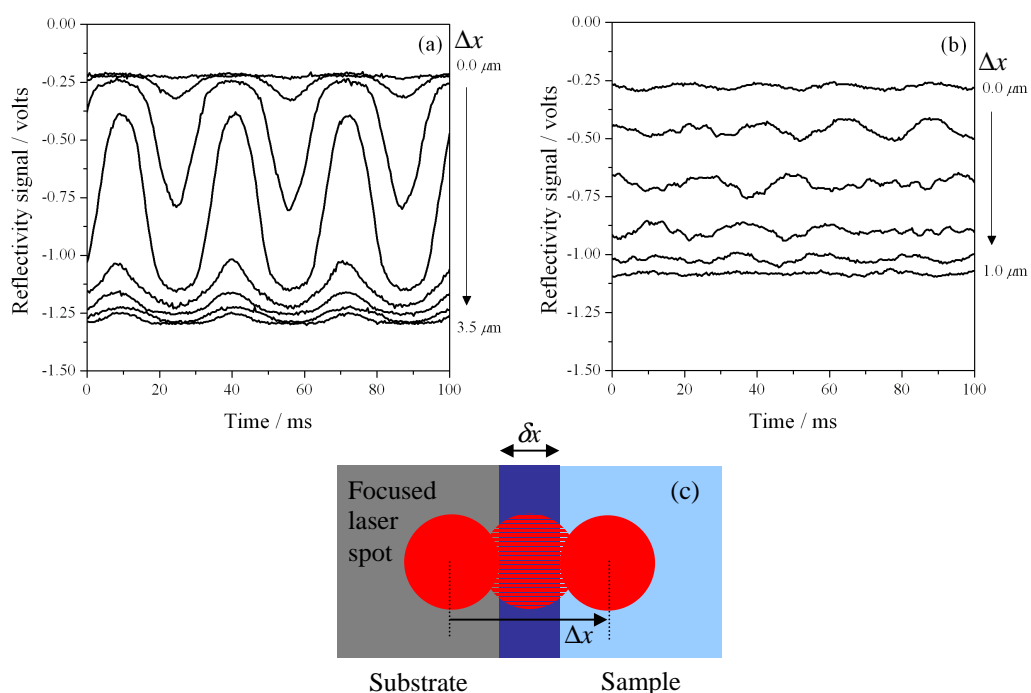


Figure 8.3.2 Oscilloscope traces of the reflectivity signal are shown as the focused laser spot was placed at different positions Δx relative to the edge of a $6 \mu\text{m}$ square element. Traces in (a) were obtained when the sample stage was unsupported. The traces in (b) show the reduction of the amplitude of vibrations by attaching supports to the sample stage. The peak-to-peak amplitude of the vibration δx may be estimated from the focused laser spot diameter (c).

The flexure stage was another source of mechanical vibration. The microscope column, microscope objective lens, and a linear stage for coarse focusing are mounted on the flexure stage. Detailed plans of the piezoelectric microscope mount are also shown in Appendix 3, Figure A3.3. The mass of the assembly is 2.1 kg. The electronics for the flexure stage include servomechanisms (or feedback loops) that

control the position of each axis of the flexure stage by monitoring capacitive position sensor outputs. A notch filter on the Servo-Control Submodule¹²⁰ was used to remove the oscillation of the stage at the first resonance frequency of the mechanics. The microscope mount and flexure stage were sent to the manufacturer so that the control electronics could be calibrated for that particular load. The flexure stage can also resonate if the servo-control loop gain is too high. Furthermore, the operating environment of the flexure stage can influence the loop gain. Therefore, the loop gain was tuned by myself in Exeter with the stage in its operating environment and the microscope mount attached. The procedure to tune the loop gain is outlined in Reference 120 and will be briefly described here. A gallery of the procedure is shown in Appendix 4.

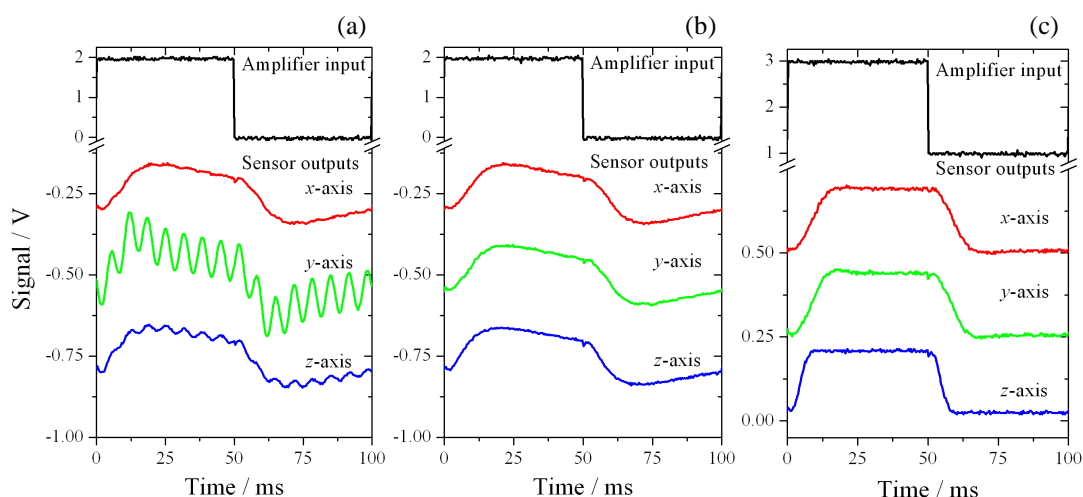


Figure 8.3.3 Oscilloscope traces of the capacitive position sensor outputs in response to an oscillatory input signal. In (a) the servo-control loops gain for the y-axis is too high and the axis is unstable. In (b) the loops gain for the y-axis has been reduced and the loops gain is too low and the response of each axis is too slow. In (c) the loop gain for each axis has been tuned so that the response of each axis is optimum.

The loop gain for each axis of the flexure stage was tuned by monitoring the output signal of the corresponding capacitive position sensor as the axis responded to an oscillatory input signal. The input signal was a square waveform of peak-to-peak amplitude of 2 V, dc offset of 1 V, and frequency of 10 Hz. The signal was applied to each axis in turn using the control input sockets (BNC) on the front panel of the Amplifier Module¹²¹. Three dc offset potentiometers on the front panel were used to set

each axis to midrange, *i.e.* $x = y = 50 \mu\text{m}$, $z = 10 \mu\text{m}$. The capacitive sensor outputs were monitored using an oscilloscope probe to measure the voltage signals of each pin of the sensor monitor socket (LEMO) on the front panel of the Position Servo-Control Module¹²². The socket shield was used as ground. In order to gain access to the Servo-Control Submodule an extension board (see Appendix 4, Figure A4.1) was used so that the loop gain could be changed and the sensor monitor output measured in real time. To change the loop gain of each axis, potentiometer P402 of the corresponding Servo Control Submodule was adjusted. Potentiometer P402 was located using Section 3.2.1 of Reference 120. The adjustment for the y-axis is shown in Figure A4.9.

Oscilloscope traces of the sensor monitor outputs are shown in Figure 8.3.3 for all three axes of the stage (a) before tuning, (b) after tuning of the loop gain of the y-axis, and (c) after optimising the loop gain of all three axes. In Figure 8.3.3(a) the traces reveal that the loop gain of the x- and z-axes was set too low, the axes were slow to respond to the input signal and the settle time was too long. In contrast the loop gain of the y-axis was set too high so that the axis would overshoot, become unstable, and oscillate at a frequency of ~ 150 Hz. Furthermore, the ringing had an effect on the response of the x- and z-axes for which ringing of the sensor monitor output was observed, albeit with smaller amplitude. In Figure 8.3.3(b) the y-axis potentiometer P402 was adjusted by a single anticlockwise turn. The loop gain of all three axes was then set too low, however the y-axis was stable and the ringing in the x- and z-axes had vanished. In Figure 8.3.3(c) the response of each axis was optimised by adjusting corresponding potentiometer P402 accordingly. When the loop gain was optimised, the rise time of the sensor monitor output was relatively fast, with little overshoot.

Scanning the microscope objective lens

As already mentioned, the microscope objective lens is mounted on the flexure stage. The diameter of the beam falling upon the rear aperture of the microscope is larger than the aperture diameter. Therefore, the rear aperture of the objective lens is completely illuminated when the objective lens is scanned through maximum range of the flexure stage. Reflectivity and magnetic images are obtained by scanning the focused laser spot across the sample by scanning the objective lens. However, the reflected, re-collimated beam is translated with respect to the optical axis of the microscope. As a result the beam position on the photodiodes within the bridge detector is changed slightly when microscope objective is scanned. A change in beam position

only affects the vector bridge detector, in which the difference of halves of quadrant photodiodes are used to recover information of the in-plane components of the magnetisation (Chapter 4). If the position of the beam changes with respect to the centre of a quadrant photodiode, the difference of halves will change. In Figure 8.3.4 two $70 \times 70 \mu\text{m}^2$ scans over a continuous film of Co(50 nm) show (a) contrast in the x -direction and (b) contrast in the y -direction. The contrast is the result of the beam moving on the quadrant photodiodes as the microscope objective is scanned. The change in contrast in the x -direction was 0.74 V, while the change in contrast in the y -direction was 0.43 V. The contrast is not magnetic. For example, the hysteresis loop height measured from the same film was 3 mV. Furthermore, the background contrast shown in Figure 8.3.4 does not prevent the measurement of hysteresis loops using the vector bridge detector. Instead the measured hysteresis loops are superimposed upon a

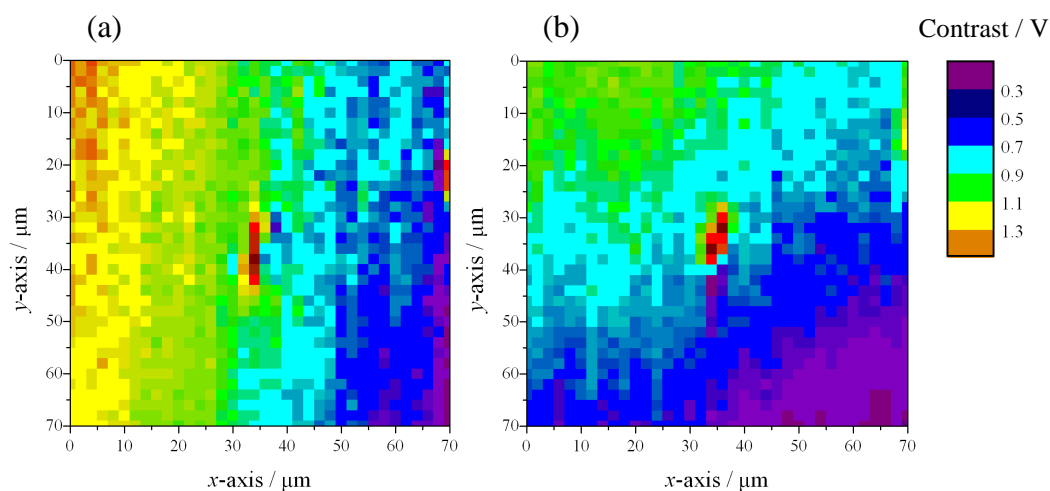


Figure 8.3.4 The contrast measured using the in-plane channels of the vector bridge detector as the microscope objective lens is scanned over a continuous film of Co(50 nm). In (a) and (b) the contrast was measured using the in-plane channel sensitive to contrast in the x - and y -direction respectively.

dc offset that corresponds to the contrast in Figure 8.3.4. Hysteresis loops were measured at positions corresponding to the limits of the flexure stage. The hysteresis loop height was 3 mV in all cases, only the dc offset varied as the position of the objective lens was changed. Finally, it should be noted that the new experimental set-up is designed to investigate microscale elements and arrays of nanomagnets, with the

ultimate aim to investigate individual nanomagnets. Therefore, for example, image scans are typically over $6 \times 6 \mu\text{m}^2$ for a $4 \times 4 \mu\text{m}^2$ array and so the change in contrast as the microscope objective is scanned is reduced.

The pulsed magnetic field device

In Section 3.6 the optically triggered pulsed magnetic field device was described. The limitations of the pulsed magnetic field were discussed with particular attention to the temporal profile of the current pulse generated by the device. Impedance matching throughout the device is essential in order to prevent reflections of the current pulse. For example, reflections of the current pulse can lead to coherent suppression of the magnetisation dynamics⁶⁶. Reflections were always present in the temporal profile of the current pulse, and action had to be taken in order to optimise the current pulse profile, as described in Section 3.6.

To prevent reflections of the current pulse, the impedance of the pulsed field device and the connecting circuitry needs to be matched. The coplanar stripline (CPS) used to deliver the pulsed field to the sample was redesigned for a characteristic impedance of 50Ω . The CPS was designed and fabricated by Dr Volodymyr Kruglyak* and is shown in Figure 8.3.5(a). To prevent reflections of the current pulse within the CPS, the structure is completely straight *c.f.* Figure 3.6.5. The calculated profile of the in-plane and out-of-plane components of the pulsed magnetic field are shown in Figure 8.3.5(b). The peak current was assumed to be 60 mA ($= 3 \text{ V}/50 \Omega$) where the peak voltage was estimated from Figure 8.3.6 (discussed below). The separation between the tracks of the CPS is $30 \mu\text{m}$, so that over the region of the largest samples, *e.g.* $10 \mu\text{m}$ element, the out-of-plane pulsed magnetic field is uniform. At the centre of the CPS the calculated value of the out-of-plane component of the pulsed magnetic field is 2 Oe and was found to vary by less than 1% within $\pm 5 \mu\text{m}$ of the centre of the CPS.

The current pulse was generated by a pulse generator (Picosecond Pulse Labs 3600). The pulse generator and the Tsunami were synchronised using an 80 MHz reference signal generated by the Tsunami's lock-to-clock electronics (Spectra Physics Model 3930), Figure 8.3.1. In the previous experimental set-up, the time delay between pump and probe pulses was adjusted by adding or subtracting a few centimetres of optical path length of the pump beam using mirrors M_8 and M_9 (Figure 3.6.2) so that

* School of Physics, University of Exeter, Stocker Road, Exeter, EX4 4QL

zero time delay was observed near the beginning of the scan. The same principle applies in the new experimental set-up, however instead of changing the optical path length, the length of the cables to the CPS were adjusted. Furthermore, the range of optical time delay of the probe beam is 8 ns, while the magnetisation precession is typically observed over 2 ns. Therefore, it was relatively straight forward to find the time-resolved signal in the available range of time delay since the sample was excited every 12.5 ns at a repetition rate of 80 MHz.

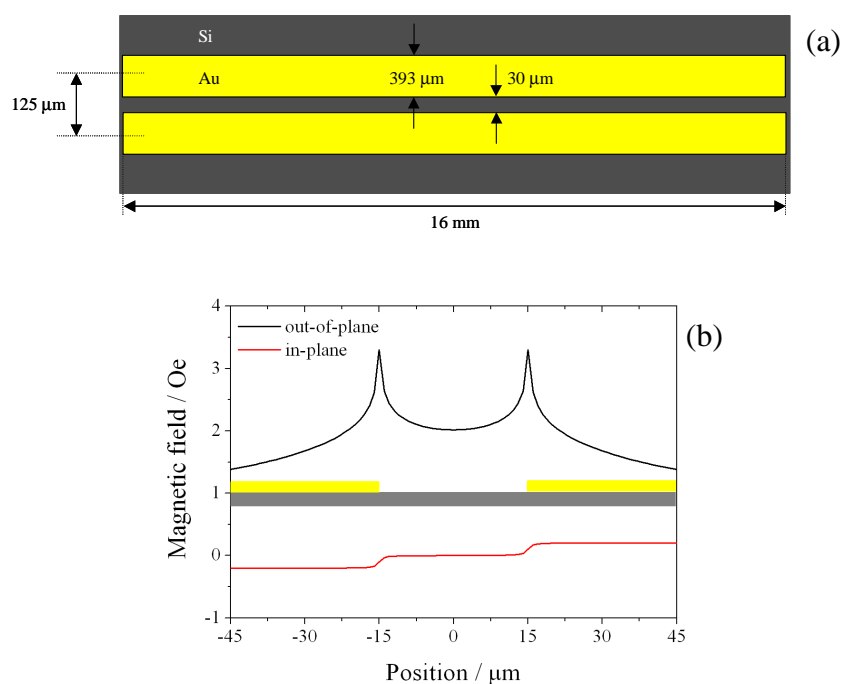


Figure 8.3.5 A schematic of the coplanar stripline is shown in (a). In (b) the calculated profile of the in-plane and out-of-plane components of the pulsed magnetic field is shown.

The current pulse was delivered to the CPS using impedance matched microwave probes (GGB Industries Picoprobe 40A-DS). Detailed drawings of the Picoprobes are available from Reference 123 and are shown in Appendix 3, Figure A3.4. The Picoprobes have a characteristic impedance of 50Ω , a frequency range of dc to 40 GHz, and are available in three configurations, (i) ground-signal, (ii) signal-ground, and (iii) ground-signal-ground, Figure A3.4. Two probes, one of each configuration (i) and (ii), are used to supply a current pulse to a CPS structure. The first probe delivers the pulse at one end of the CPS. The second probe allows the current pulse to propagate out of the CPS without being reflected at the end of the tracks.

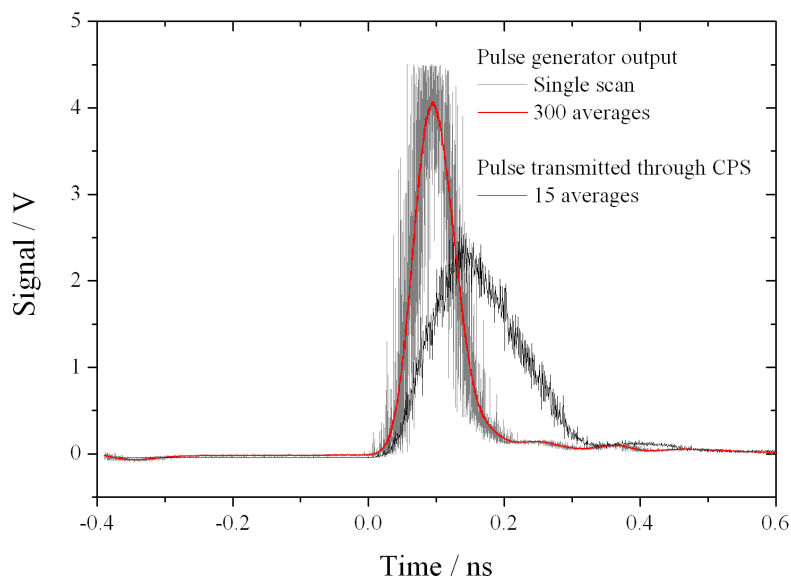


Figure 8.3.6 Traces of the current pulse profile acquired using a 50 GHz sampling oscilloscope. A single scan and an average of 300 scans are shown for the pulse generator output. An average of 15 scan of the pulse transmitted through the CPS reveals dispersion and attenuation of the pulse.

Similarly two probes of configuration (iii) can be used to supply a current pulse to a coplanar waveguide⁶⁵ (CPW) structure. The second probe is connected to a $50\ \Omega$ input terminal of a 50 GHz sampling oscilloscope (Agilent Infinium DCA-J) so that the current pulse is absorbed. Since the pulsed field device and circuitry is impedance matched at $50\ \Omega$, there are no reflections of the current pulse. In Figure 8.3.6, oscilloscope traces of a single pulse and an average of 300 pulses generated by the pulse generator are shown. The measured average of 15 pulses transmitted through the CPS structure reveals dispersion and attenuation of the pulse. The peak voltage used in the calculation of the pulsed field profile (Figure 8.3.5(b)) was taken to be the average of the peak of the pulse generator output, and the peak of the pulse transmitted through the CPS, Figure 8.3.6.

A “gate input” socket on the front panel of the pulse generator allowed the output of the pulse generator to be modulated. A signal generator (Stanford Research Systems DS340 15 MHz) was used to generate a TTL signal of frequency ~ 1 -2 kHz. At the same time, the signal generator was used to supply a reference signal of the same frequency to the lock-in amplifiers for phase sensitive detection. The modulation of the pulse generator output is equivalent to the mechanical chopping of the pump laser beam described in Section 3.6.

The enhanced signal-to-noise ratio

The signal-to-noise ratio of the new experimental set-up was significantly enhanced as a result of the improvements described above. Figure 8.3.7 shows typical time-resolved scans obtained from a disc with a diameter of $6\ \mu\text{m}$ using the probe station (a), and from a square of length $6\ \mu\text{m}$ using the previous experimental set-up.

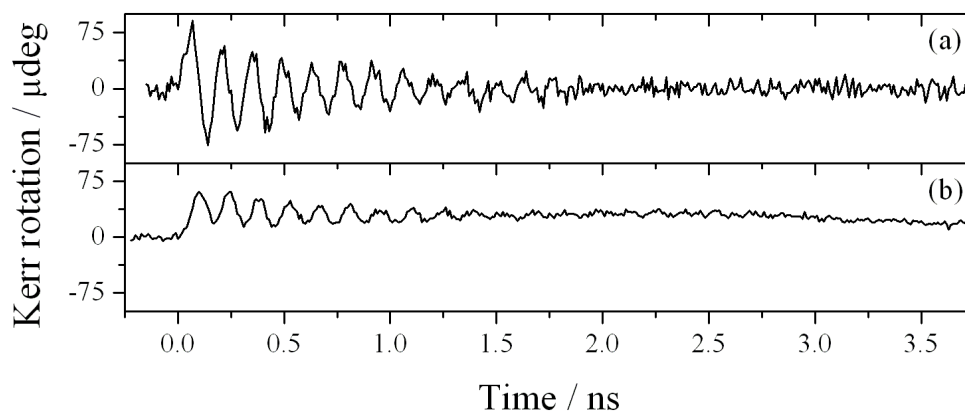


Figure 8.3.7 Time-resolved signals obtained using the probe station (a) and the previous experimental set-up (b). The sample used in (a) was a $6\ \mu\text{m}$ disc patterned from a CoFe/NiFe(2.5 nm) bilayer. The sample used in (b) was a $6\ \mu\text{m}$ square patterned on the same wafer.

The elements were patterned on the same wafer as the arrays of nanomagnets studied in Chapter 7. The bias field was $\sim 590\ \text{Oe}$ and the polar-Kerr rotation was measured using the bridge detector described in Section 3.5. In Figure 8.3.7(a) the polar-Kerr signal oscillates around zero, while in Figure 8.3.7(b) the oscillatory signal is superimposed on the transient background of the pulsed magnetic field (Section 3.6). The transient background is absent in Figure 8.3.7(a) because the duration of the current pulse is short (Figure 8.3.6) so that the effective field lies in the plane of the sample after the current pulse has passed. The peak-to-peak amplitude of the oscillatory polar-Kerr signal measured using the probe station and the previous set-up was found to be $168\ \mu\text{deg}$ and $43\ \mu\text{deg}$, respectively. The signal-to-noise ratio of the scans appear to be similar. However, to acquire the scan in Figure 8.3.7(b), an integration time (τ_c) of 1 s was required for an adequate signal-to-noise ratio. For the scan in Figure 8.3.7(a) an integration time of 200 ms was used. The acquisition time for each data point was $4 \times \tau_c$

seconds. The total acquisition time for the 400 data point scans in Figure 8.3.7(a) and (b) was about 7 and 27 minutes respectively. Therefore, the construction of the probe station and the experimental improvements have led to an increase in experimental productivity of about a factor of four for this particular sample.

8.4 Antireflective coatings

For other samples, the data acquisition time was still too long. For example, time-resolved measurements were performed on a disc with diameter of $6\mu\text{m}$ patterned from a magnetic tunnel valve stack with composition Si/SiO₂(substrate)/Ta(50 Å)/PtMn(250 Å)/Co₈₀Fe₂₀(80 Å)/Al₂O₃(7 Å)/Co₈₀Fe₂₀(10 Å)/Ni₈₈Fe₁₂(27 Å)/Ta(100 Å). The sample was fabricated by Dr Jeffrey Childress* and Dr Jordan Katine*. The Al₂O₃ layer was achieved by oxidising an Al layer in O₂ at 500 mTorr for 15 minutes. The sample has a similar composition to that of a magnetic tunnel valve used in hard-disk read-head sensors⁷. The CoFe(8 nm) layer was pinned by the exchange bias field generated by the interface atomic moments of the PtMn antiferromagnetic layer (Section 2.9). The CoFe/ NiFe(2.5 nm) free layer had the same composition and thickness as the sample used in Chapter 7. As already discussed, the time-resolved scan acquired from the free layer sample (Figure 8.3.7(a)) was found to have an enhanced signal-to-noise ratio. However, the peak-to-peak amplitude of time-resolved scans obtained from the tunnel valve element was $22\ \mu\text{deg}$, less than one-seventh of the amplitude observed in scans acquired from the free layer element. Exchange coupling between the pinned and free layer across the Al₂O₃ barrier may act to pin the free layer and hence reduce the precession amplitude. In order to achieve an adequate signal-noise-ratio, an integration time of 5 s was required. The data acquisition time per data point was 20 s. Therefore, time-resolved scans were acquired over 1 ns, corresponding to an acquisition time of about 34 minutes for a 100 data point scan. However, the time over which the time-resolved scan is measured is related to the frequency resolution of the corresponding Fourier spectrum. For higher frequency resolution, longer scans are required, which are only feasible if the Kerr signal is enhanced so that the data acquisition time is reduced.

* Hitachi Global Storage Technologies, San Jose Research Center, 3403 Yerba Buena Road, San Jose, California 95135

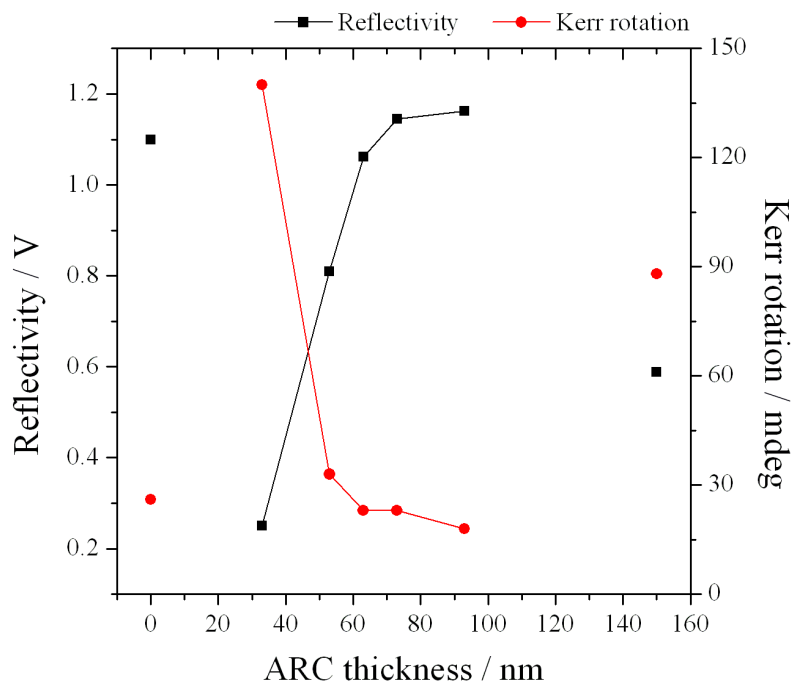


Figure 8.4.1 The reflectivity signal and the Kerr rotation as a function of ZnS thickness.

A dielectric antireflective coating (ARC) deposited onto a ferromagnetic film can be used to enhance the Kerr effect. The enhancement is a result of constructive multiple reflection from the ferromagnetic film when the refractive index and the thickness of the ARC are chosen correctly^{124,125}. To enhance the Kerr effect, most of the incident light must be coupled to the ferromagnetic film by matching the refractive indices of the film and the ARC¹²⁶. The complex refractive index of the sample was estimated to be $2.29 + i4.04$ by calculating the volume weighted average of the refractive index of the constituent layers. The sample used was a continuous film tunnel valve stack (coupon reference number SA0521B) that was co-deposited with the patterned film. The values for the complex refractive index of the constituent materials at a photon energy of 1.6 eV were obtained from Reference 127. The dielectric material ZnS was found to have a similar refractive index (2.31) to the real part of the sample refractive index. An online ARC thickness calculator¹²⁸ was used to estimate the optimum ZnS thickness, for which the reflectivity was minimised. The optimum thickness was calculated to be 63 nm. Six ZnS ARC(t) strips of width of ~ 1 mm were thermally evaporated through a shadow mask onto the coupon by Mr David Jarvis* for

* School of Physics, University of Exeter, Stocker Road, Exeter, EX4 4QL

$t = 33, 53, 63, 73, 93, 150$ nm. Vector hysteresis loops were obtained from each strip. Figure 8.4.1 shows the reflectivity signal and the Kerr rotation (loop height) as a function of ZnS thickness. Experimentally, it was found that the optimum ZnS thickness was 33 nm. The Kerr rotation was found to increase from 18 mdeg for an ZnS thickness of 93 nm, to 140 mdeg for a thickness of 33 nm. As expected the reflectivity showed the opposite trend, decreasing from 1.16 V, to 0.25 V over the same range of ZnS thickness.

A ZnS(33 nm) film was deposited on top of the 6 μm diameter disc composed of the same tunnel valve stack as the coupon (SA0521B). The sample (wafer reference number A79) was fabricated by Dr Jeffrey Childress* and Dr Jordan Katine* using dc magnetron sputtering, e-beam lithography, and ion milling. Both vector hysteresis loops and time-resolved scans revealed an enhanced Kerr signal. Figure 8.4.2(a) shows vector hysteresis loops acquired from the 6 μm tunnel valve element when the field was applied parallel and perpendicular(inset) to the exchange bias direction. The vector loops acquired when the field was parallel to the exchange bias direction reveal that the exchange bias field acting on the pinned layer is about 270 Oe. The loops acquired from the sample with a ZnS ARC are shown with black squares, while the loops from the “as-deposited” stack are shown with red circles. The loops show that the longitudinal-Kerr signal is enhanced by a factor of three. Figure 8.4.2(b) shows time-resolved scans obtained from the 6 μm tunnel valve disc at remanence following saturation of the sample in a bias field of 1 kOe applied in the exchange bias field direction. The same magnetic field history was applied to the sample before each time-resolved scan to ensure that the magnetisation of the pinned layer is parallel to that of the free layer. In Figure 8.4.2(c) Fourier spectra corresponding to the time-resolved scans in Figure 8.4.2(b) are shown. The similarity of the frequency of each scan suggests that the ground state of the free and pinned layers was the same for each measurement, as expected from the vector hysteresis loops. Thus, the difference in amplitude is the result of enhancement of the Kerr effect and not a result of different interlayer interaction for different ground states of the pinned layer. The time-resolved scans show a factor of four enhancement of the polar-Kerr signal from 22 μdeg to 91 μdeg . The signal-to-noise of the time-resolved scans appears to be similar. However, the enhanced Kerr signal was acquired using a 1 s integration time, corresponding to a 200 point scan acquisition time of about 14 minutes. As described at

* Hitachi Global Storage Technologies, San Jose Research Center, 3403 Yerba Buena Road, San Jose, California 95135

the end of the previous section, the acquisition time of a 100 point scan from the “as-deposited” stack was about 34 minutes. Furthermore, the scan from the “as-deposited” stack is an average of two scans, while the scan from the sample with ZnS ARC is a single scan. Since the data acquisition time was reduced, longer time-resolved scans were acquired. The time-resolved scans and Fourier spectra in Figures 8.4.2(b) and (c) also show how increasing the length of the time-resolved scan increases the resolution of the spectra.

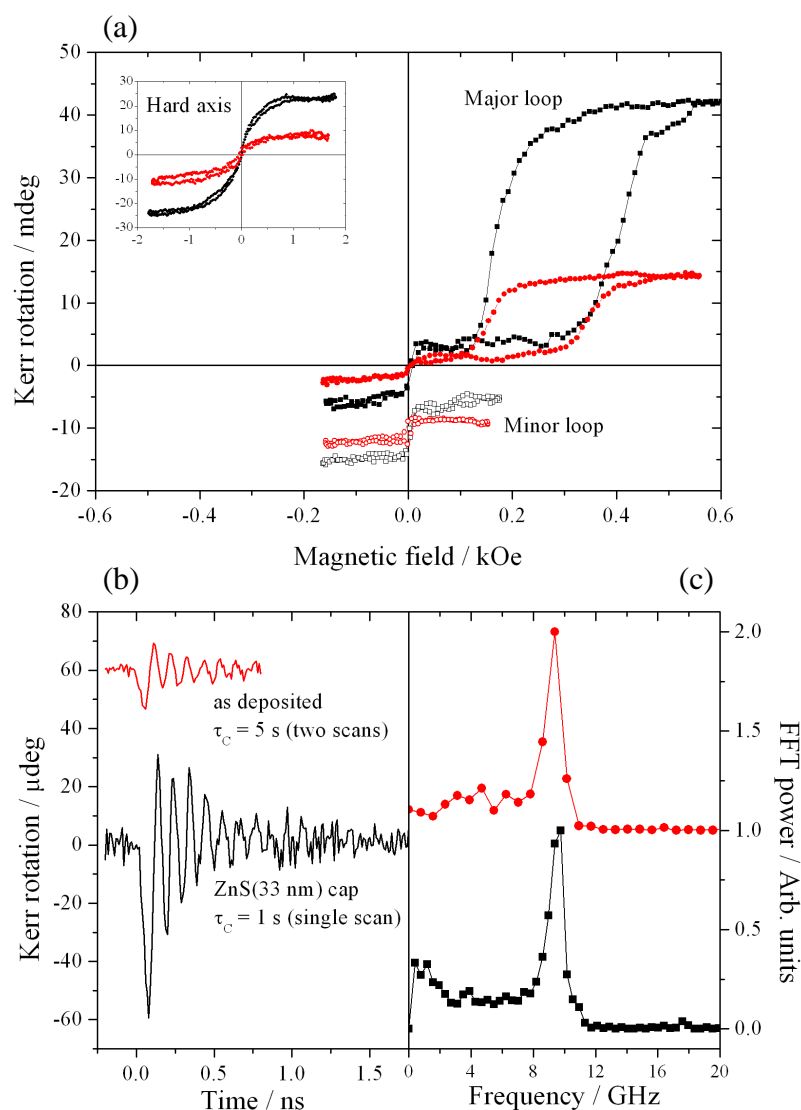


Figure 8.4.2 Vector hysteresis loops (a) and time-resolved scans (b) acquired from a $6 \mu\text{m}$ diameter disc patterned from a PtMn(25 nm)/CoFe(8 nm)/Al₂O₃(0.7 nm)/[CoFe/NiFe](2.5 nm) tunnel-valve stack with (black lines and symbols) and without (red lines and symbols) a ZnS(33 nm) antireflective coating deposited on top of the sample. The fast Fourier transform spectra shown in (c) correspond to the time-resolved scans shown in (b).

8.5 Vector- and time-resolved scanning Kerr microscopy

The Mk II vector bridge

Attempts to acquire time-resolved scans using the vector bridge detector described in Chapter 4 were unsuccessful. During the final year of my PhD research project I designed and built a second vector bridge detector (Mk II vector bridge). The main features of the Mk II vector bridge are the enhanced mechanical stability, increased bandwidth, and external alignment and nulling controls. The mechanics of the Mk II vector bridge were built by Mr Kevyn White*. The design of the electronics was based on that of the vector bridge described in Chapter 4. The electronic circuit for the Mk II vector bridge is shown in Appendix 5, Figure A5.1. I received useful advice from Dr Charles Williams*, Mr Tom Addison* and Mr Chris Forrest* on how to increase the detector bandwidth while maintaining the detector gain, and how to avoid electrical noise. Initially, each operational amplifier (op-amp) had the same values of capacitance and resistance as the op-amps in the previous vector bridge (Mk I vector bridge). The bandwidth was tested electronically using a 15 MHz signal generator and a 500 MHz oscilloscope and was found to be ~ 2 kHz. At frequencies higher than the bandwidth of an op-amp the gain begins to fall off at steady rate of 6 dB/octave¹²⁹. Attempts to use the Mk I vector bridge to measure time-resolved scans were unsuccessful because the detector was being used to detect a modulated (~ 2 kHz) Kerr signal at the limit of the electronic bandwidth. In the Mk II vector bridge the bandwidth was increased by reducing the feedback capacitance of the op-amps.

The bandwidth of the Mk II vector bridge was measured by modulating the polarisation of the Tsunami output beam using an electro-optic modulator (Con-Optics 350-80) similar to that described in Section 3.6. The modulator was controlled using driver electronics (Con-Optics 302) to apply dc and ac voltages to the birefringent crystal within the modulator assembly. A dc bias voltage was used to change the polarisation of incident linearly polarised light to circularly polarised light, while an ac signal was applied to the crystal to alternate the degree of ellipticity of the transmitted light. Finally, a quarter waveplate was used to change the alternating ellipticity into an alternating rotation of linearly polarised light. The frequency of the polarisation modulation was then varied while the “magnetic” outputs of the Mk II vector bridge were monitored using a 500 MHz oscilloscope. The bandwidth of the detector was

* School of Physics, University of Exeter, Stocker Road, Exeter, EX4 4QL

found to be ~ 32 kHz. The increased bandwidth may facilitate the further reduction in the data acquisition time of time-resolved scans by allowing the use of higher, *e.g.* 10 kHz, modulation frequencies.

As described in Section 4.3 for the Mk I vector bridge, it was necessary to ensure that the outputs of the Mk II vector bridge were proportional to the Kerr rotation. It should be noted that the response of the in-plane signals must be measured while half of the beam is blocked (Section 4.2 and 4.3), while the whole beam may be used to measure the response of the out-of-plane signal. Figure 8.5.1 shows the output of one of

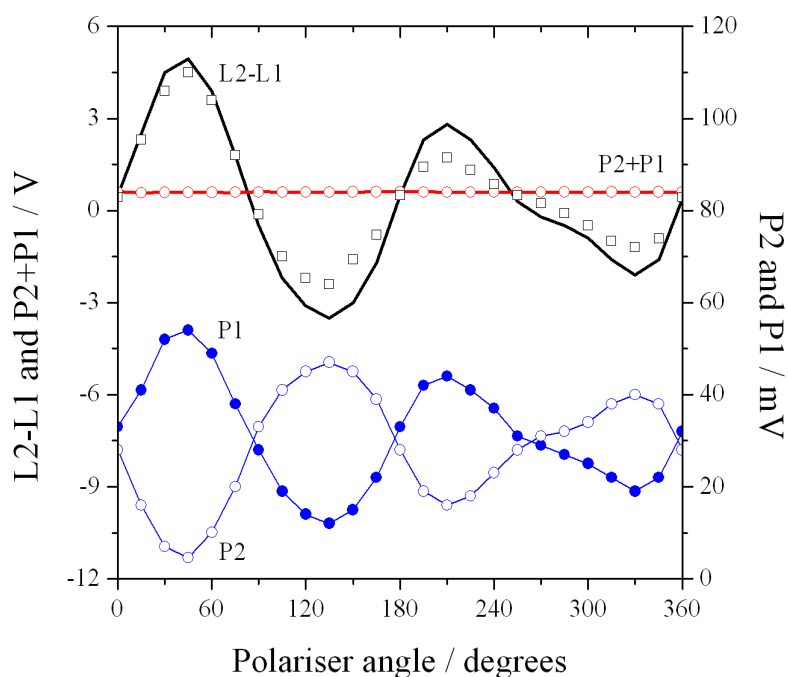


Figure 8.5.1 The Mk II vector bridge output L2-L1, used to detect in-plane component of the magnetisation vector, is shown as a function of polariser angle. The reflectivity signal P2+P1 and intensity signals P1 and P2 of quad-detectors 1 and 2 are also shown. For L2-L1 and P2+P1 the symbols are measured, while the lines are calculated from the measured outputs P2 and P1.

the in-plane signals (labelled L2-L1) as the polariser is rotated through 360° . The reflectivity output is also shown (labelled P2+P1) as well as the intensity signal of each quad-detector (labelled P1 and P2). For L2-L1 and P2-P1, the symbols are measured values, while the lines are calculated from the measured P2 and P1 outputs. The nominal gain of the L2-L1 op-amp is 100. However, the discrepancy between the

measured and calculated values of L2-L1 suggest that the gain may be slightly lower than expected. From Figure 8.5.1 it can be seen that the output signal L2-L1 is linear in the region about a polariser angle of 176° . Since the Kerr rotation is typically small (~ 10 mdeg), L2-L1 can be assumed to be linearly proportional to the in-plane component of the magnetisation. Similar results for the second in-plane signal (T2-T1) and the out-of-plane signal (P2-P1) are shown in Appendix 5, Figure A5.2 and A5.3.

Vector hysteresis loops

In Figure 8.5.2(a) vector hysteresis loops acquired using the Mk II vector bridge are shown for a $10\ \mu\text{m}$ square element patterned from a CoFe/NiFe(13.6 nm) film previously studied in Chapters 4 and 6. The loops were acquired by Mr Marco Delchini* under my supervision during his summer research placement in Exeter. The field was applied along the hard axis of the material and the loops show the component of magnetisation parallel M_{\parallel} and perpendicular M_{\perp} to the applied field. Comparing the vector loops on Figure 8.5.2(a) with those in Figure 4.3.3(c) and 4.3.3(d) reveals that the quality of the hysteresis loop data has been maintained. Furthermore, Figure 8.5.2(b) shows easy axis M_{\parallel} vector loops acquired from the arrays of square

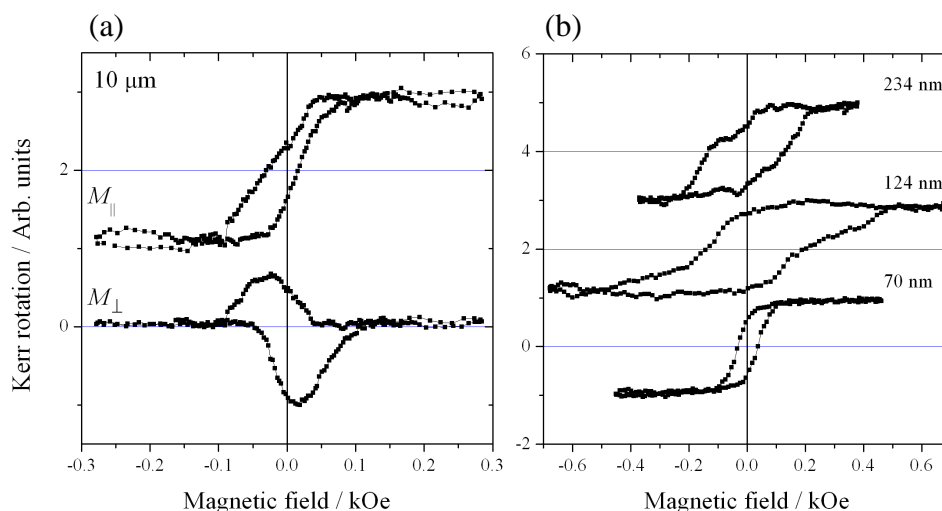


Figure 8.5.2 Vector hysteresis loops acquired using the Mk II vector bridge are shown for (a) a $10\ \mu\text{m}$ square and (b) arrays of square nanomagnets of size 234, 124, and 70 nm.

* L'Ecole Nationale Supérieure de Physique de Grenoble (ENSPG), Minatec - Bât. INPG, 3 parvis Louis Néel, BP 257 - 38016 Grenoble Cedex 1, France

nanomagnets using the Mk II vector bridge. The loops were acquired from the three smallest nanomagnets with length(separation) 234(77), 124(30) and 70(37) nm shown in Figures 4.2.5(c), (d), and (e) respectively. The loops obtained from the arrays of 234 nm and 124 nm element are very similar to those shown in Figure 4.3.4(a), demonstrating again that the quality of data has been maintained. Previous attempts to measure vector loops from the array of 70 nm elements were unsuccessful. However, Figure 4.2.5(e) shows a good hysteresis loop acquired from the array of 70 nm elements using the Mk II vector bridge. As the element size is reduced from 124 nm to 70 nm, the coercive field decreases from ~ 165 Oe to ~ 35 Oe.

Vector- and time-resolved images

Finally, the Mk II vector bridge was successfully used to acquire time-resolved images of magnetisation dynamics in a $40 \times 40 \mu\text{m}^2$ element patterned from a film of $(\text{Fe}_{90}\text{Co}_{10})_{78}\text{B}_{12}\text{Si}_{10}$ with thickness of 160 nm. The sample was fabricated by Dr Michael Frommberger*. The time-resolved experiments were performed by Dr Andreas Neudert** and Dr Volodymyr Kruglyak**. The experimental set-up in Figure 8.3.1 was used to acquire a time-resolved scan in response to an pulsed magnetic

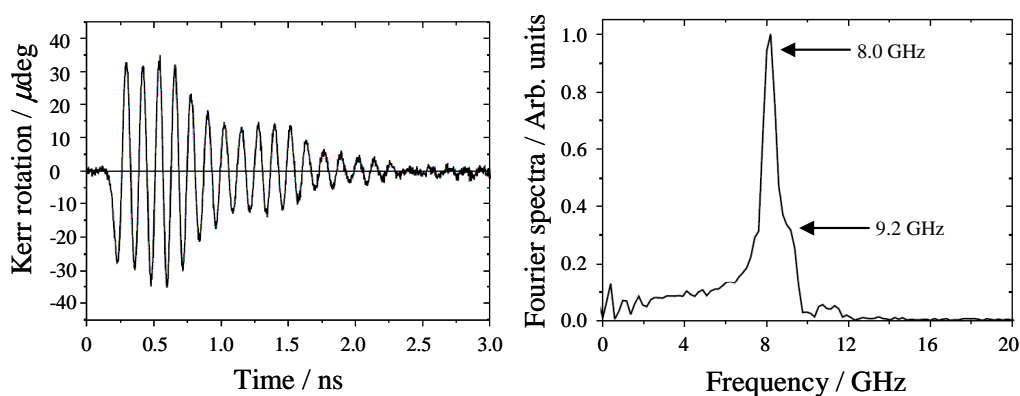


Figure 8.5.3 A time-resolved scan and the corresponding Fourier spectrum acquired from a $40 \mu\text{m}$ square patterned from a film of $(\text{Fe}_{90}\text{Co}_{10})_{78}\text{B}_{12}\text{Si}_{10}$ with thickness of 160 nm. At a bias field of 500 Oe modes with frequency of 8.0 and 9.2 GHz were observed.

* Center of Advanced European Studies And Research (CAESAR), Smart Materials Group, 53175 Bonn, Germany

** School of Physics, University of Exeter, Stocker Road, Exeter, EX4 4QL

field delivered using a CPW device. A bias field of 500 Oe was applied parallel to the central conductor of the CPW structure. The resulting oscillatory Kerr signal was recorded using the bridge detector described in Section 3.5. Figure 8.5.3 shows the time-resolved scan and the corresponding Fourier spectrum. The time-resolved scan shows clear beating suggesting that two modes with similar frequency were excited. The main peak seen in the Fourier spectrum at 8.0 GHz and its shoulder at 9.2 GHz confirm that at least two modes are excited. The method of excitation used in the experimental set-up in Figure 8.3.1 was modified by Dr Andreas Neudert and Dr Volodymyr Kruglyak so that harmonic field excitation could be used to hold a particular mode at resonance. Figure 8.5.4 shows the modified set-up. The laser is phase locked to the microwave signal generator (Rohde and Schwarz SMA-100A 1-22 GHz) using a signal generator/clock (Rohde and Schwarz SMA-100A 9 kHz-3 GHz) with 10 and 80 MHz reference signal outputs. To excite a particular mode, *e.g.* at 8.0 GHz, a harmonic field is delivered to the sample by passing an 8.0 GHz microwave signal along the CPW. The optical time delay of the phase locked probe pulse is set so that each pulse reaches the sample at the same point on each cycle of the magnetisation precession *e.g.* an anti-node.

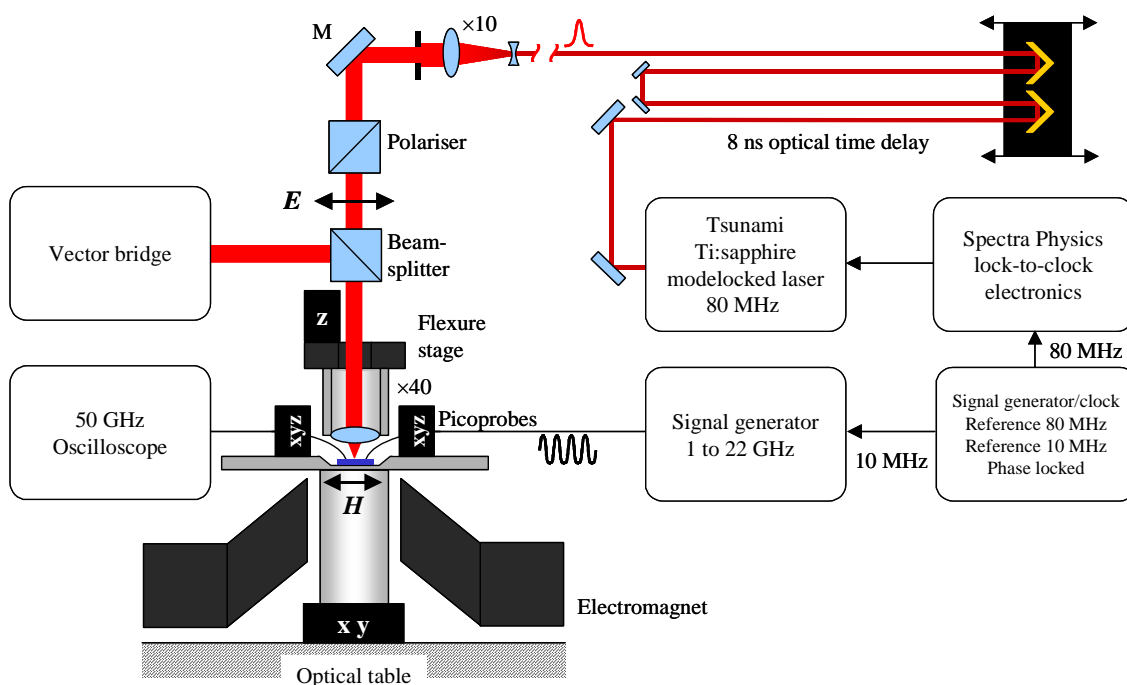


Figure 8.5.4 A schematic of the set-up of the TRSKM and microwave probe station used in harmonic magnetic field experiments.

By scanning the focused laser spot across the sample and measuring the Kerr rotation for each pixel, an image of the dynamic magnetisation for a particular mode can be obtained. The vector bridge was successfully used to acquire images corresponding to the in-plane and out-of-plane component of magnetisation for the 8.0 GHz mode, while only the out-of-plane component was imaged for the 9.2 GHz mode. Figure 8.5.5 shows the vector-resolved images of the dynamic magnetisation for the two modes. Such vector-resolved images of the dynamic magnetisation in microscale elements acquired using a harmonic field excitation have not previously been reported. In Figure 8.5.5(a) time-resolved scans of the polar- and longitudinal-Kerr signals are shown for the out-of-plane M_z and in-plane M_{\perp} component of the sample magnetisation. The longitudinal-Kerr image is referred to as “transverse” since it is the in-plane component of magnetisation perpendicular to the applied field that is sensed. M_{\perp} is *not* sensed using the transverse-Kerr effect. The change in the in-plane component of the magnetisation parallel to the bias field M_{\parallel} is very small and is not shown. The images in Figure 8.5.5(a) correspond to the data points at 0 ps and 27 ps on the time-resolved scans. The polar and transverse images show that when the out-of-plane component is small the in-plane component is large and *vice-versa*. In Figure 8.5.5(b) the two images of the higher frequency mode correspond to opposite anti-nodes of the harmonic field. The lower frequency mode is more uniform throughout the element, while the centre and edge regions of the higher frequency mode precess out of phase (opposite contrast).

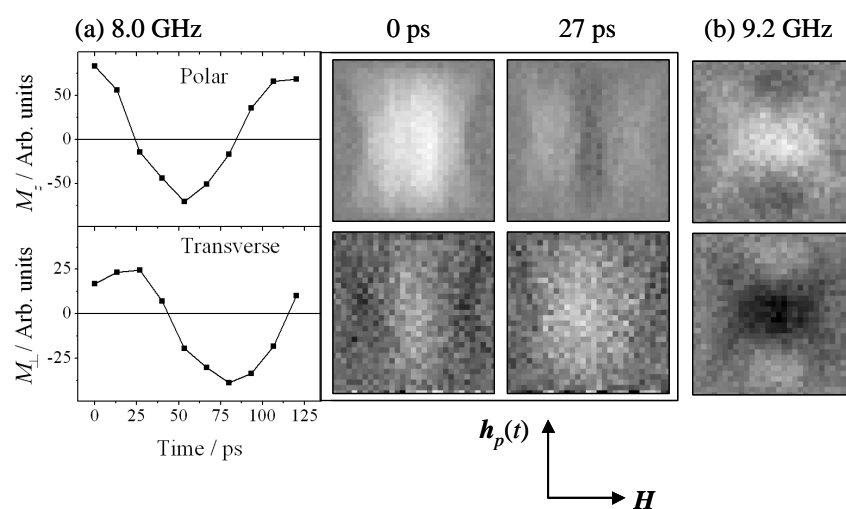


Figure 8.5.5 Vector- and time-resolved scans and images of the dynamic magnetisation are shown for two modes with frequency 8.0 GHz (a) and 9.2 GHz (b). The inset shows the orientation of the bias \mathbf{H} and harmonic magnetic fields $\mathbf{h}_p(t)$.

8.6 Summary

In this chapter details of the improvements made to the TRSKM and the development of the microwave probe station were presented. Evidence that an enhanced signal-to-noise ratio was achieved as a result of the development was also presented. The aim was to perform vector- and time-resolved Kerr measurements on an individual nanomagnet. While such a measurement has not yet been achieved, the efforts described in Chapter 8 will continue with the aim to enhance the mechanical stability and the magneto-optical Kerr signal further. The development of the microwave probe station will facilitate the controlled precessional switching of nanomagnets, while the improvements to the vector bridge detector will allow the trajectory of the switching to be measured.

“What we call the beginning is often the end. And to make an end is to make a beginning. The end is where we start from”. – T.S. Eliot (1888-1965)

Chapter 9

Summary

In this thesis the results of magneto-optical experiments have been presented. The experiments have been performed on micro-arrays of square nanomagnets in order to characterise the static and time-dependent behaviour of the nanomagnets. The time-dependent behaviour was investigated in time-resolved scanning Kerr microscopy (TRSKM) experiments. In these so-called pump-probe experiments, magnetisation dynamics were induced by applying a pulsed magnetic field (pump), and detected using the magneto-optical polar Kerr effect (probe). The longitudinal Kerr effect was utilised in the scanning Kerr microscope in order to measure the in-plane components of the static magnetisation. The static and time-dependent behaviour of the magnetisation was found to become more complicated as the size of the nanomagnets was reduced. In particular, vector hysteresis loops revealed changes in the coercive field, while interpretation of fast Fourier transform (FFT) spectra of time-resolved signals using micromagnetic simulations revealed that the magnetisation dynamics became increasingly non-uniform as the element size was reduced. The high frequency magnetisation dynamics of nanomagnets are expected to underpin the future operation of hard-disk read-head sensors. However, the reduction in the element size has been shown in this thesis to lead to the excitation of spin wave modes with a complicated spatial character that have similar frequency to that of future read-head sensors. Such non-uniform excitations may lead to reduced signal-to-noise in read-head sensors as their operation frequency is pushed into the microwave regime.

In Chapter 4 hysteresis loops of the vector magnetisation have been obtained from continuous sheet material, individual microscale square elements, and $4\ \mu\text{m}$ arrays of nanoscale square elements using a scanning Kerr microscope of sub-micrometer spatial resolution equipped with a vector bridge detector. The measurements on sheet material have demonstrated that two orthogonal in-plane components of the vector magnetisation are sensed, and that the corresponding hysteresis loops can be measured simultaneously. A comparison of experimental loops obtained from different element sizes has revealed an increase in the coercive field as the element size was reduced in addition to a greater similarity between the easy and hard axis loop shape. However, loops for two arrays of 637 nm elements with different element separation have revealed that the coercive and switching fields are sensitive to inter-element dipolar interactions. Micromagnetic simulations of hysteresis loops and magnetisation configurations within a single 236 nm element have revealed that the magnetisation switches via a series of non-uniform single domain states. When the magnetic field was applied along different edges of the element, the simulated magnetisation configurations revealed that the incoherent switching mechanisms were similar, which lead to a similar hysteresis loop shape for each field direction. Since the simulations were performed for single nanoscale elements, the trends in coercive field seen for the experimental loops obtained from arrays of nanoscale elements could not be fully interpreted. Indeed the acquisition of the hysteresis loop is often a prerequisite for understanding the high frequency response of micro- and nanoscale magnetic elements. This work demonstrates that a scanning Kerr microscope equipped with a vector bridge detector is a powerful tool for the characterisation of nanomagnet arrays of very small area.

In Chapter 5 it was demonstrated that a hybrid Au/indium tin oxide (ITO) coplanar stripline (CPS) allows magnetisation dynamics to be studied in a sample fabricated on an opaque substrate, following excitation by either an in-plane or an out-of-plane pulsed magnetic field. It was shown that a phase shift exists in the time-resolved Kerr signals obtained at different positions across the ITO window. Macrospin simulations confirmed the variation of the pulsed field between the out-of-plane and in-plane configurations. While the hybrid Au/ITO CPS device was not used in experiments presented in subsequent chapters, the work presented in Chapter 5 demonstrates that the device can be used to apply a pulsed magnetic field of any orientation to any sample fabricated on any separate substrate.

In Chapter 6 the results of TRSKM measurements upon arrays of square nanomagnets of different size and for a range of bias fields were presented. The

experimental results were compared to micromagnetic simulations of model arrays in order to understand non-uniform precessional dynamics within the elements. Experimentally, two branches of excited modes were observed to co-exist above a particular bias field. Below the so called crossover field, the higher frequency branch was observed to vanish. Micromagnetic simulations and FFT imaging revealed the spatial character of the two mode branches. The modes of the higher frequency branch were found to have high FFT amplitude at the centre of the element in regions of positive effective field, while modes of the lower frequency branch were found to have high FFT amplitude near the edges of the element perpendicular to the bias field. Cross-sections of the simulated images of the effective field and FFT magnitude revealed that the crossover between the higher and lower frequency branches was mediated by the complicated evolution of the total effective field within the element. Below the crossover field the increase in the width of the edge region, of negative effective field, at the expense of the centre region, of positive effective field, allowed the edge-type mode to extend over the entire element. The simulations revealed that the majority of the modes were de-localised with non-zero FFT magnitude throughout the element. Therefore, the spin-wave well model introduced in Reference 34 for micron sized non-ellipsoidal elements could not be used here to characterise the excited modes as strictly centre- or edge-localised modes. The de-localised nature of the excited modes seems to be an intrinsic property of sub-micrometer and nanoscale non-ellipsoidal elements. However, the mode spatial character was found to be correlated with features of the effective field and the static magnetisation state. The simulations revealed that the frequency of modes from the lower frequency branch were very sensitive to the static state magnetisation of all the elements within the model array. Therefore, by matching the simulated spectra to the experimental spectra we are able to infer that the elements studied here occupy the S-state. Since, below the crossover field the static magnetisation state was shown to be non-uniform, increased magnetostatic interaction is expected between the elements within the array. The simulated spectra revealed that many modes may be excited that have similar spatial character within the centre element. However, inspection of the entire array revealed the existence of collective modes, where the FFT amplitude in the elements surrounding the centre element was considerably different for two such modes. The excitation of collective modes with similar spatial character in the centre element but different frequency may account for the increased linewidth observed in the experimental spectra below the crossover field.

In Chapter 7 experimental and numerical results of resonant modes of a square nanomagnet were presented. Both the number of modes and their frequencies were observed to vary as the orientation of the external magnetic field was rotated in the plane of the element. It was shown that the observed variation cannot be explained by either the effect of the extrinsic configurational anisotropy or the static intrinsic configurational anisotropy. Instead the variation of the dynamic effective field is due to a dynamic intrinsic configurational anisotropy. This new anisotropy can dominate the ultrafast magnetisation dynamics of ultrathin nanomagnets for which the static intrinsic configurational anisotropy is of minor importance.

In Chapter 8 details of the improvements made to the TRSKM and the development of the microwave probe station were presented. It was shown that an enhanced signal-to-noise ratio was achieved as a result of the advances in the experimental set-up. The aim was to perform vector- and time-resolved Kerr measurements on an individual nanomagnet. At this time, such a measurement has not been achieved. Therefore the efforts described in Chapter 8 to enhance the mechanical stability and the magneto-optical Kerr signal will continue. The development of the microwave probe station will facilitate the controlled precessional switching of nanomagnets, while the improvements to the vector bridge detector will allow the trajectory of the switching to be measured.

Appendix 1

Calculation of the vector bridge longitudinal Kerr signal for the component of magnetisation perpendicular to the applied field

In Figure 4.2.4 for the two rays shown, the Kerr rotation Φ_K is proportional to M_{\perp} , but is equal and opposite in opposite halves of the beam. The intensity of the electric field that falls upon the opposite halves Q_1+Q_2 and Q_3+Q_4 of quadrant-photodiode 1 is

$$I_{Q_1+Q_2} \propto \cos^2\left(\frac{\pi}{4} + \Phi_K\right) \quad (\text{A1.1})$$

and

$$I_{Q_3+Q_4} \propto \cos^2\left(\frac{\pi}{4} - \Phi_K\right), \quad (\text{A1.2})$$

where Q_i ($i = 1,2,3,4$) are the quadrant labels according to the specifications supplied by the manufacturer. Similarly, the intensity that falls upon opposite halves of quadrant-photodiode 2 is

$$I_{Q_1+Q_2} \propto \cos^2\left(\frac{\pi}{4} - \Phi_K\right), \quad (\text{A1.3})$$

and

$$I_{Q_3+Q_4} \propto \cos^2\left(\frac{\pi}{4} + \Phi_K\right). \quad (\text{A1.4})$$

Using a trigonometric identity for $\cos(\alpha \pm \beta)$ Equation A1.1 may be written as

$$I_{Q_1+Q_2} \propto \left[\cos\left(\frac{\pi}{4}\right) \cdot \cos(\Phi_K) + \sin\left(\frac{\pi}{4}\right) \cdot \sin(\Phi_K) \right]^2, \quad (\text{A1.5})$$

where Φ_K is typically small so that Equation A1.5 may be written as

$$I_{Q_1+Q_2} \propto \left[\frac{1}{\sqrt{2}} + \frac{1}{\sqrt{2}} \cdot \Phi_K \right]^2. \quad (\text{A1.6})$$

Expanding the square and neglecting second order terms in Φ_K gives

$$I_{Q_1+Q_2} \propto \frac{1+2\Phi_K}{2}. \quad (\text{A1.7})$$

Similarly for Equation A1.2, we obtain

$$I_{Q_3+Q_4} \propto \frac{1-2\Phi_K}{2}. \quad (\text{A1.8})$$

Table 4.2.1 shows that the quad-detector signal output at Pad 3 is proportional to the difference signal $(V_1+V_2)-(V_3+V_4)$. For quad-detector 1 (QD1), such an operation yields

$$[(V_1+V_2)-(V_3+V_4)]_{\text{QD1}} \propto \frac{1+2\Phi_K}{2} - \frac{1-2\Phi_K}{2} = 2\Phi_K, \quad (\text{A1.9})$$

where Φ_K is proportional to M_\perp . A similar analysis of quad-detector 2 yields

$$-[(V_1+V_2)-(V_3+V_4)]_{\text{QD2}} \propto -\left(\frac{1-2\Phi_K}{2} - \frac{1+2\Phi_K}{2} \right) = 2\Phi_K, \quad (\text{A1.10})$$

where the additional negative sign in Equation A1.10 accounts for the inversion of quadrant-photodiode 2 with respect to quadrant photodiode 1. Therefore, the Kerr signals in Equation A1.9 and A1.10 have the same sign.

In the case of detecting M_\perp (as shown in Figure 4.2.4) a summing amplifier was used to perform the following operation

$$(\text{Pad 3})_{\text{QD2}} + (\text{Pad 3})_{\text{QD1}} \propto 4\Phi_K. \quad (\text{A1.11})$$

where the output signal is a factor of two larger than the individual output signals from Pad 3 of quad-detectors 1 and 2.

Appendix 2

Time-resolved signals acquired from arrays of nanomagnets

The figures presented in this appendix show time-resolved signals that correspond to the fast Fourier transform spectra presented in Chapter 6.

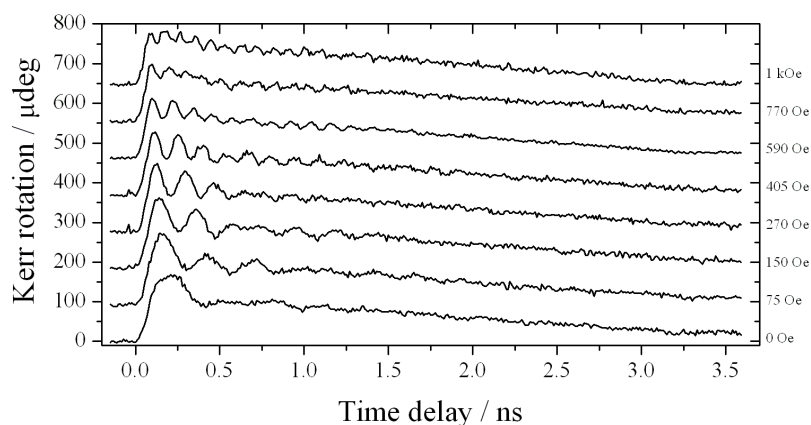


Figure A2.1 Raw time-resolved signals obtained from an array of 637 nm square elements of CoFe/NiFe(13.6 nm) are shown for different bias field values.

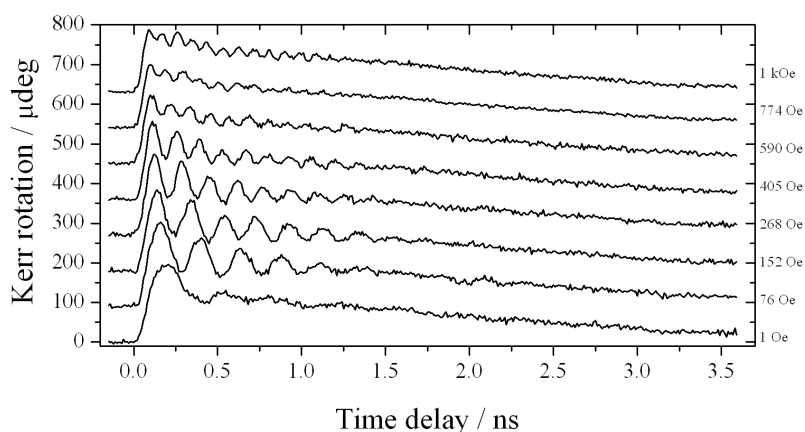


Figure A2.2 Raw time-resolved signals obtained from an array of 428 nm square elements of CoFe/NiFe(13.6 nm) are shown for different bias field values.

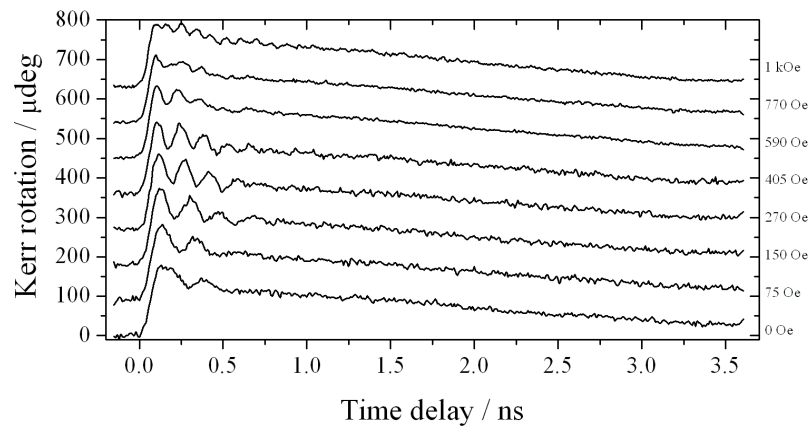


Figure A2.3 Raw time-resolved signals obtained from an array of 236 nm square elements of CoFe/NiFe(13.6 nm) are shown for different bias field values.

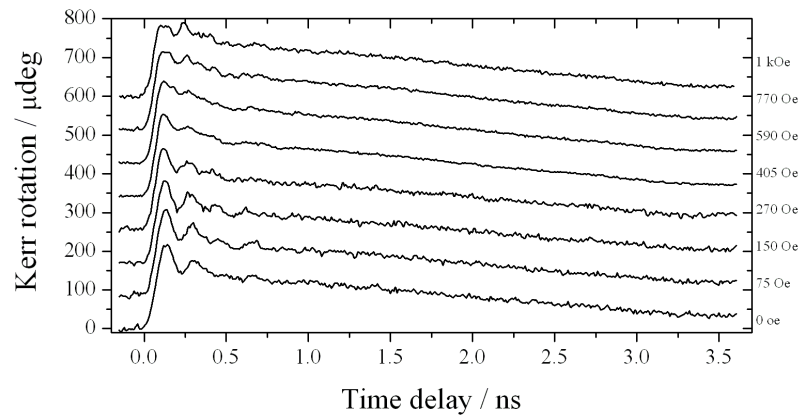


Figure A2.4 Raw time-resolved signals obtained from an array of 124 nm square elements of CoFe/NiFe(13.6 nm) are shown for different bias field values.

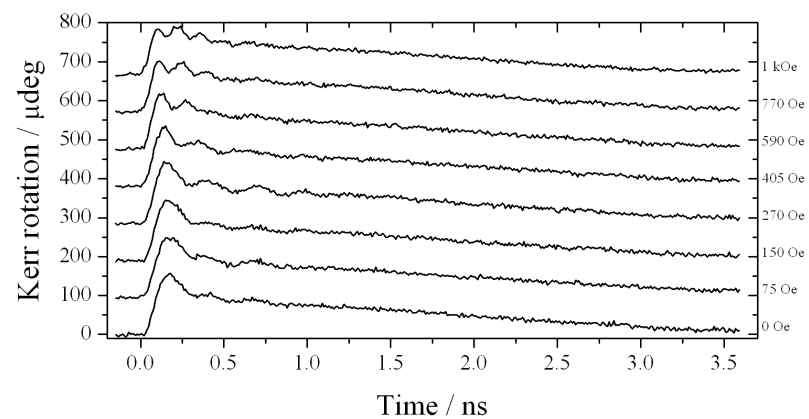


Figure A2.5 Raw time-resolved signals obtained from an array of 70 nm square elements of CoFe/NiFe(13.6 nm) are shown for different bias field values.

Appendix 3

The probe station assembly

The figures presented in this appendix show detailed drawings of the components of the probe station assembly described in Chapter 8.

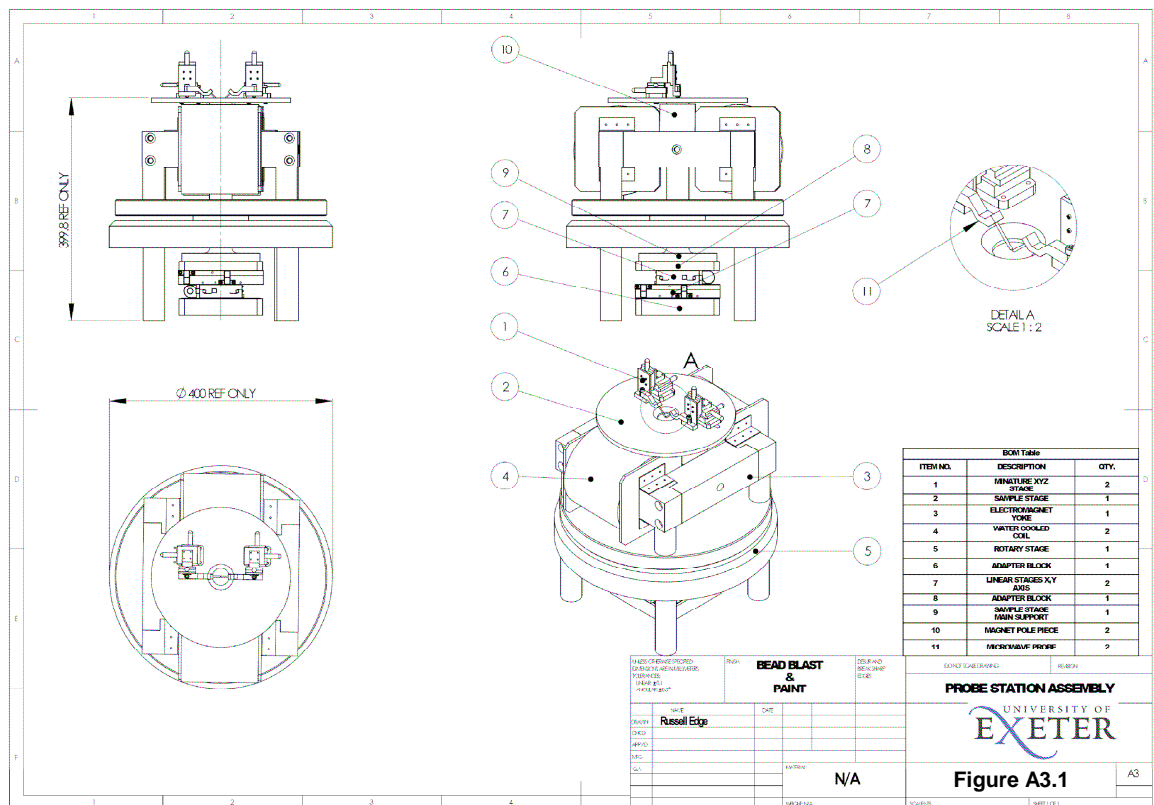
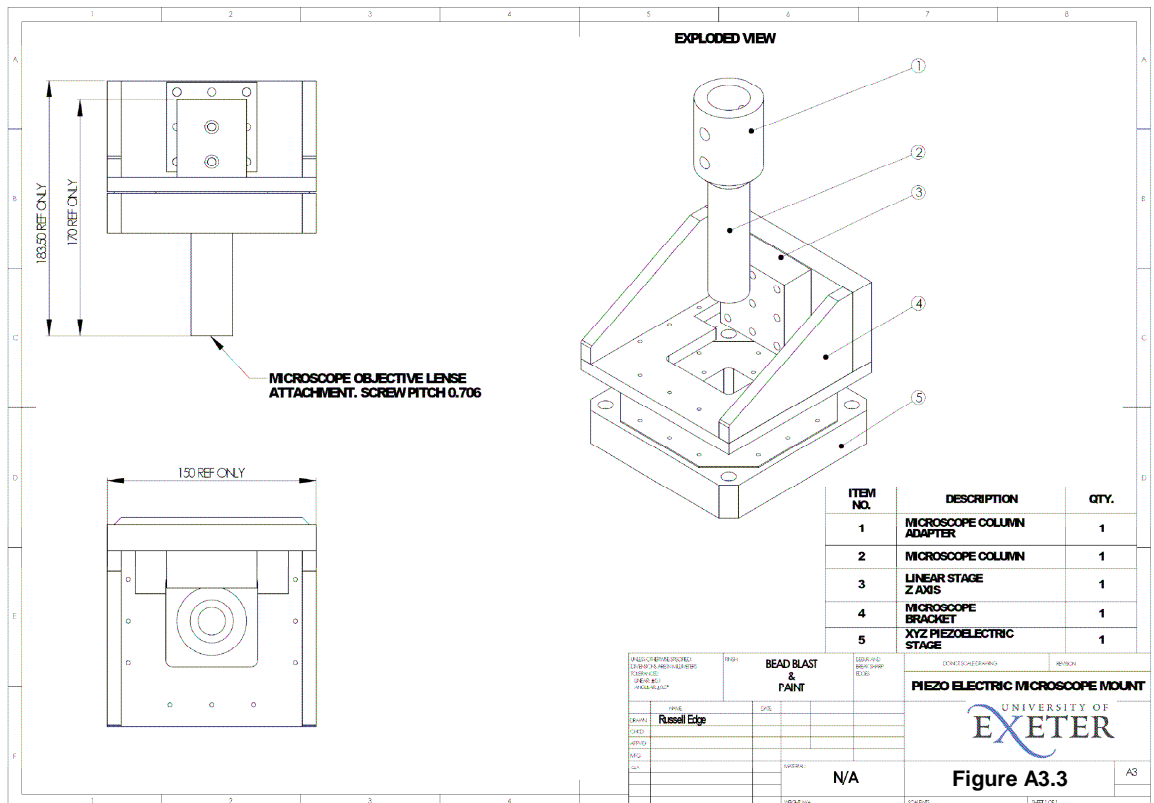
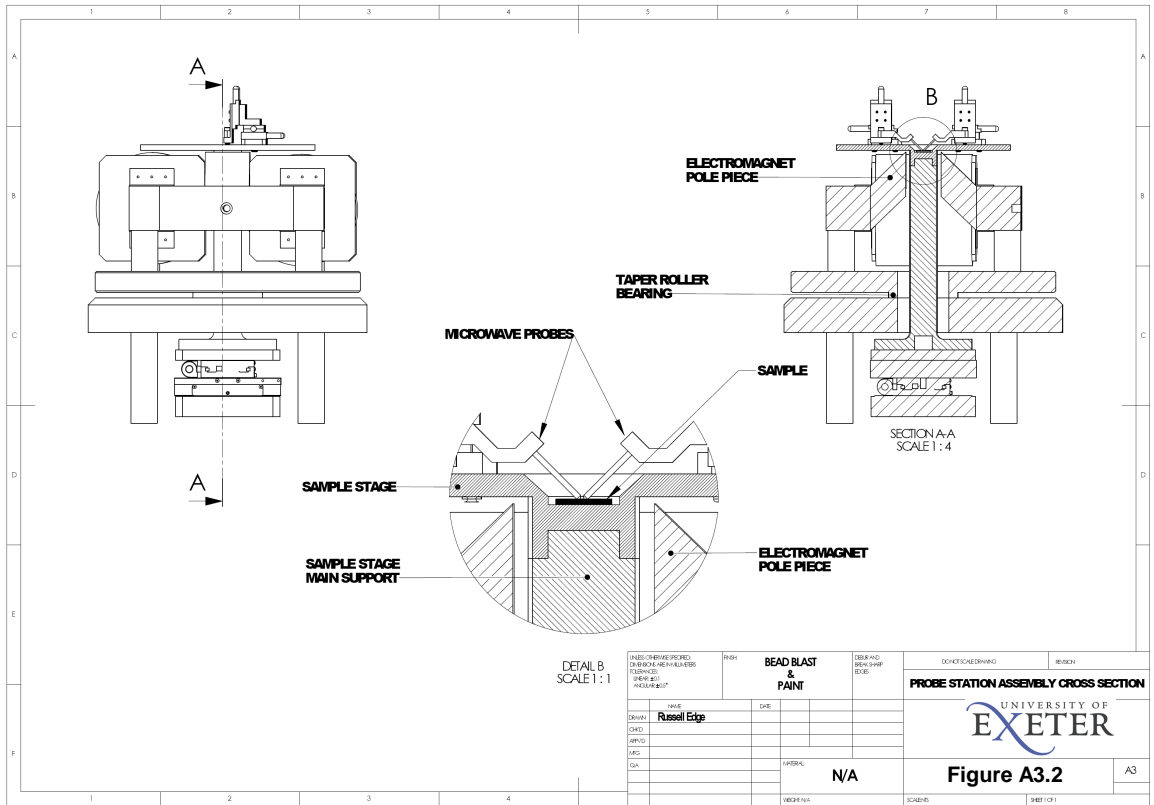


Figure A3.1



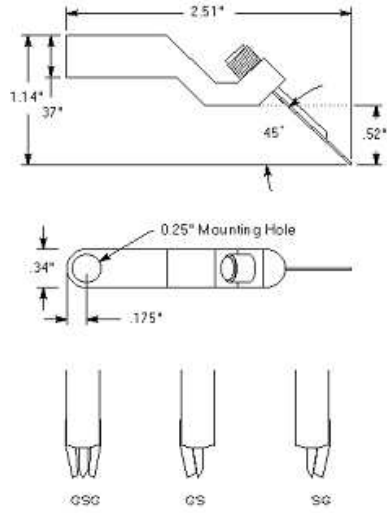


Figure A3.4 The GGB Industries Picoprobes 40A-DS are shown. Detail of the ground-signal-ground (GSG), ground-signal (GS), and signal-ground (SG) tips are shown. This figure was taken from Reference 123.

Appendix 4

Tuning the servomechanism loop gain

This series of photographs show the procedure for tuning the capacitive position sensor servomechanism loop gain for the piezoelectric stage.

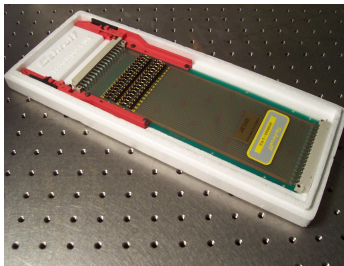


Figure A4.1
Extension board (loaned from
Lambda Photometrics)

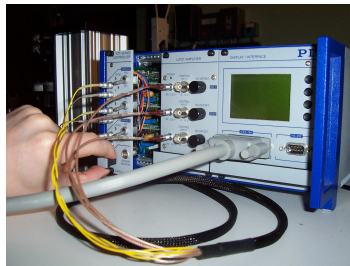


Figure A4.2
Switch off device and remove
Position Servo-Control Module

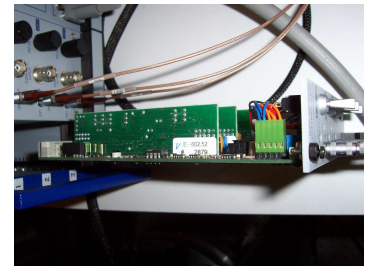


Figure A4.3
The Servo-Control Submodule
(E-802.52)

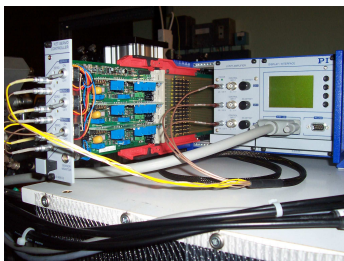


Figure A4.4
Insert extension board and attach
Position Servo-Control Module

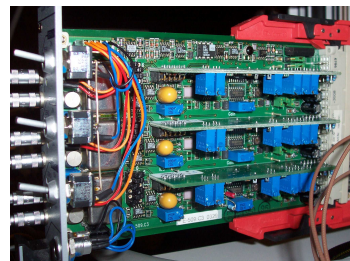


Figure A4.5
Device can now be switched on

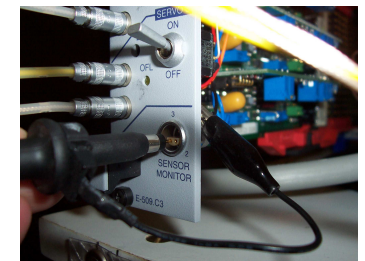


Figure A4.6
Monitor sensor outputs

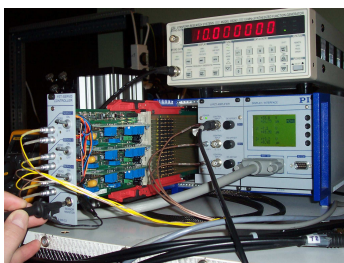


Figure A4.7
Apply square wave form to the
control input sockets of the
Amplifier Module

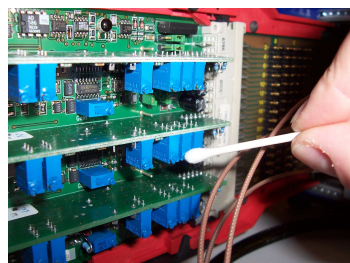


Figure A4.8
Remove seal on loop gain
potentiometer P402 using
isopropanol

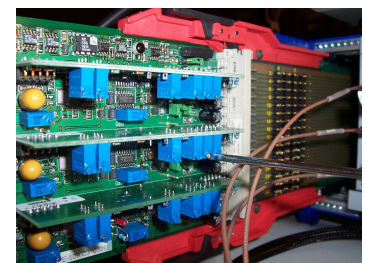


Figure A4.9
Adjust P402 while monitoring
the sensor outputs until loop gain
is tuned

Appendix 5

The Mk II vector bridge

The figures presented in this appendix show the electronic circuit diagram and output signals of the Mk II vector bridge detector. Following the discussion and calculation of the longitudinal Kerr signals in Section 4.2 and Appendix 1, the in-plane signals $L2-L1$ and $T2+T1$ are calculated using a difference and summing amplifiers respectively, Figure A5.1. In the Mk II vector bridge the option for a signal gain of 10^2 or 10^4 is available. In the Mk I vector bridge the gain of the in-plane signals was fixed at 10^4 . Furthermore, the Mk II vector bridge offers offset potentiometers that allow any offset of the output signals of the quad-detectors to be removed *in-situ* prior to performing experiments. Removing any dc offset allows the dynamic range of data acquisition software to be reduced, which increases the resolution of the data acquisition card. OP27 low noise, precision operational amplifiers were used as they have low dc offset and thermal drift¹³⁰.

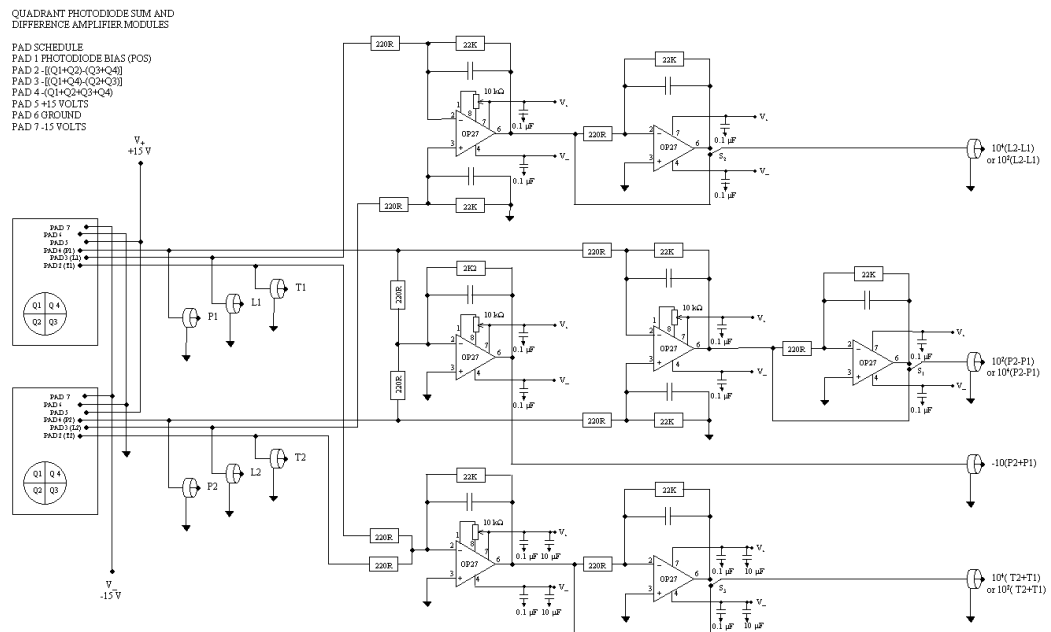


Figure A5.1 The electronic circuit for the Mk II vector bridge is shown.

Figure A5.2 reveals that the in-plane signal $T2+T1$ is linear in the region about a polariser angle of 176° , which confirms that a summing amplifier was required to recover the signal.

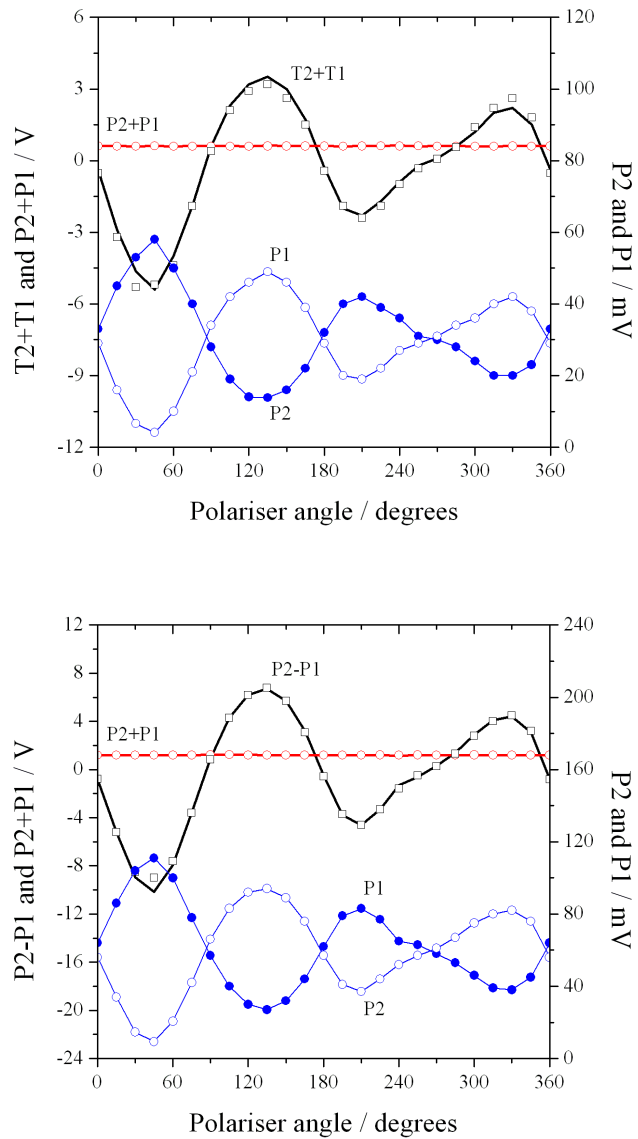


Figure A5.2 The Mk II vector bridge output $T2+T1$ and $P2-P1$, used respectively to detect the second in-plane component and the out-of-plane component of the vector magnetisation, is shown as a function of polariser angle. The reflectivity signal $P2+P1$ and intensity signals $P1$ and $P2$ of quad-detectors 1 and 2 are also shown. For $T2+T1$, $P2-P1$, and $P2+P1$ symbols are measured, while the lines are calculated from the measured outputs $P2$ and $P1$.

Bibliography

- ¹ M.R. Freeman and J.F. Smyth, *J. Appl. Phys.* **79**, 5898 (1996).
- ² P.M.W. French, *Rep. Progr. Phys.* **58**, 169 (1995).
- ³ E. Beaurepaire, J.-C. Merle, A. Daunois, and J.-Y. Bigot, *Phys. Rev. Lett.* **76**, 4250 (1996).
- ⁴ M. van Kampen, C. Jozsa, J. T. Kohlhepp, P. LeClair, L. Lagae, W.J.M. de Jonge, and B. Koopmans, *Phys. Rev. Lett.* **88**, 227201 (2002).
- ⁵ R.J. Hicken, *Phil. Trans. R. Soc.* **A361**, 2827 (2003).
- ⁶ S. Tamaru, J.A. Bain, R.J.M. van de Veerdonk, T.M. Crawford, M. Covington, and M.H. Kryder, *Phys. Rev. B* **70**, 104416 (2004).
- ⁷ J.R. Childress and R.E. Fontana Jr, *C. R. Physique* **6**, 997 (2005).
- ⁸ C. Bayer, J. Jorzick, S.O. Demokritov, A.N. Slavin, K.Y. Guslienko, D.V. Berkov, N.L. Gorn, M.P. Kostylev, and B. Hillebrands, *Top. Appl. Phys.* **101**, 57 (2006).
- ⁹ W.K. Hiebert, G.E. Ballentine, and M.R. Freeman, *Phys. Rev. B* **65**, 140404(R) (2002).
- ¹⁰ Th. Gerrits, H.A.M. van den Berg, J. Hohlfeld, L. Bär & Th. Rasing, *Nature* **418**, 509 (2002).
- ¹¹ V.V. Kruglyak, A. Barman, R. J. Hicken, J. R. Childress, and J. A. Katine, *Phys. Rev. B* **71**, 220409(R) (2005).
- ¹² V.V. Kruglyak, P.S. Keatley, R.J. Hicken, J.R. Childress, and J.A. Katine, *J. Appl. Phys.* **99**, 08F306 (2006).
- ¹³ A.H. Morrish, *The Physical Principles of Magnetism*, John Wiley & Sons (1965).
- ¹⁴ P. Curie, *Ann. chim. et phys.* (7) **5**, 289 (1895).
- ¹⁵ P. Weiss, *J. Phys.* **6**, 667 (1907).
- ¹⁶ W. Heisenberg, *Z. Physik* **49**, 619 (1928).
- ¹⁷ C. Kittel, *Introduction to Solid State Physics*, 7th ed., John Wiley & Sons (1996).
- ¹⁸ J.C. Slater, *Phys. Rev.* **35**, 509 (1930), **36**, 57 (1930).
- ¹⁹ E.C. Stoner, *Proc. Roy. Soc. (London)* **A-165**, 372 (1938), **A-169**, 339 (1939), *Phil. Mag.* **25**, 899 (1938).
- ²⁰ S.V. Vonsovsky, *J. Phys. (USSR)* **10**, 468 (1946); S.V. Vonsovsky and E.A. Turov, *J. Exptl. Theoret. Phys. (USSR)* **24**, 419 (1953).
- ²¹ C. Zener, *Phys. Rev.* **81**, 440 (1951), **83**, 299 (1951); C. Zener and R.R. Heikes, *Revs. Mod. Phys.* **25**, 191 (1953).
- ²² A. Aharoni, *Introduction to the Theory of Ferromagnetism*, Oxford University Press (2000).
- ²³ V. Baltz, J. Sort, S. Landis, B. Rodmacq, and B. Dieny, *Phys. Rev. Lett.* **94**, 117201 (2005).
- ²⁴ K.J. Kirk, *Contemporary Physics* **41**, 61 (2000).

-
- ²⁵ J.G. Gay and R. Richter, *Ultrathin Magnetic Structures I*, eds. J.A.C. Bland and B. Heinrich, Springer-Verlag (1994).
- ²⁶ C. Kittel, *Rev. Mod. Phys.* **21**, 541 (1949).
- ²⁷ V.V. Kruglyak, PhD Thesis, *Femtosecond optical pump-probe investigations of ultrafast electron and spin dynamics in metals*, University of Exeter (2004).
- ²⁸ H. Stoll, A. Puzic, B. van Waeyenberge, P. Fischer, J. Raabe, M. Buess, T. Haug, R Höllinger, C. Back, D. Weiss, and G. Denbeaux, *Appl. Phys. Lett.* **84**, 3328 (2004).
- ²⁹ M. Buess, J. Raabe, K. Perzlmaier, C. H. Back, and C. Quitmann, *Phys. Rev. B* **74**, 100404 (2006).
- ³⁰ A. Hubert and R. Schäfer, *Magnetic Domains: the Analysis of Magnetic Microstructures*, Springer-Verlag (1998).
- ³¹ C. Kittel, *Phys. Rev.* **70**, 965 (1946).
- ³² O. Fruchart, A. Thiaville, *C. R. Physique* **6**, 921 (2006).
- ³³ E.C. Stoner and E.P. Wohlfarth, *Phil. Trans. Roy. Soc.* **A240**, 597 (1948).
- ³⁴ L. Landau, and E. Lifshitz, *Phys. Z. Sowjetunion* **8**, 153 (1935).
- ³⁵ T.L. Gilbert, *Phys. Rev.* **100**, 1243 (1955).
- ³⁶ C. Kittel, *Phys. Rev.* **73**, 155 (1948).
- ³⁷ L.R. Walker, *Phys. Rev.* **105**, 390 (1957).
- ³⁸ R.W. Damon and J.R. Eshbach, *J. Phys. Chem. Solids* **19**, 308 (1961).
- ³⁹ S.O. Demokritov, B. Hillebrands, and A.N. Slavin, *Phys. Rep.* **348**, 442 (2001).
- ⁴⁰ J. Jorzick, S.O. Demokritov, B. Hillebrands, M. Bailleul, C. Fermon, K.Y. Guslienko, A.N. Slavin, D.V. Berkov, and N.L. Gorn, *Phys. Rev. Lett.* **88**, 047204 (2002).
- ⁴¹ M. J. Donahue and D. G. Porter, OOMMF User's Guide, Version 1.0, NISTIR 6376, National Institute of Standards and Technology, Gaithersburg, MD, Sept 1999; <http://math.nist.gov/oommf>.
- ⁴² M. Faraday, *Trans. Roy. Soc. (London)* **5**, 592 (1846).
- ⁴³ A. Kundt, *Phil. Mag. (5)*, **18**, 308 (1884).
- ⁴⁴ J. Kerr, *Phil. Mag.* **3**, 339 (1877), **5**, 161 (1878).
- ⁴⁵ Z.Q. Qui and S.D. Bader, *Nonlinear Optics in Metals*, ed. K.H. Bennemann, Oxford University Press (1998).
- ⁴⁶ H.J. Zeiger and G.W. Pratt, *Magnetic Interactions in Solids*, Oxford University Press (1973).
- ⁴⁷ M. van Kampen, PhD Thesis, *Ultrafast Spin Dynamics in Ferromagnetic Metals*, Technische Universiteit Eindhoven (2003).
- ⁴⁸ P.N. Argyres, *Phys. Rev.* **97**, 334 (1955).
- ⁴⁹ H.R. Hulme, *Proc. Roy. Soc.* **A135**, 237 (1932).
- ⁵⁰ S.D. Bader and J.L. Erskine, *Ultrathin Magnetic Structures I*, eds. J.A.C. Bland and B. Heinrich, Springer-Verlag (1994).

-
- 51 L.D. Landau and E.M. Lifshitz, *The Classical Theory of Fields*, 4th ed., trans. M. Hamermesh, Elsevier Butterworth Hienemann, Amsterdam (1980).
- 52 H.S. Bennett and E.A. Stern, *Phys. Rev.* **137**, A448 (1965).
- 53 G. Metzger, P. Pluinage, R. Tourget, *Ann. Phys.* **10**, 5 (1965).
- 54 J. Wu, J.R. Moore and R.J. Hicken, *J. Magn. Magn. Mater.* **222**, 189 (2000).
- 55 R. Vollmer, *Nonlinear Optics in Metals*, ed. K.H. Bennemann, Oxford University Press (1998)
- 56 G.S. Krinchik, V.A. Artem'ev, *Sov. Phys. JETP* **26**, 1080 (1968).
- 57 A.B. Marchant, *Optical Recording: A Technical Review*, Addison-Wesley (1990).
- 58 J. Wu, PhD Thesis, *Optical Pump-Probe Studies of Spin Dynamics in Ferromagnetic Materials*, University of Exeter (2001).
- 59 F.L. Pedrotti and L.S. Pedrotti, *Introduction to Optics*, Prentice Hall (1996).
- 60 W.K. Hiebert, PhD Thesis, *Experimental Micromagnetic Dynamics: Ultrafast Magnetization Reversal Using Time Resolved Scanning Kerr Effect Microscopy*, University of Alberta (2001).
- 61 Spectra-Physics Tsunami Mode-Locked Ti:sapphire Laser, *User Manual*, Part Number 0000-232A (1995).
- 62 J. Wu, N.D. Hughes, J.R. Moore, and R.J. Hicken *J. Magn. Magn. Mater.* **241**,96 (2002).
- 63 A. Barman, V.V. Kruglyak, R.J. Hicken, J.M. Rowe, A. Kundrotaite, J. Scott, and M. Rahman, *Phys. Rev. B* **69**, 174426 (2004).
- 64 A. Barman, V.V. Kruglyak, R.J. Hicken, A. Kundrotaite and M. Rahman *IEE Proc. Sci. Meas. Technol.* **150**, 260 (2003).
- 65 K.C. Gupta, R. Garg, I.J. Bahl, *Microstrip Lines and Slotlines*, Artech House (1979).
- 66 A. Barman, V.V. Kruglyak, R.J. Hicken, J. Scott, and M. Rahman, *J. Appl. Phys.* **97**, 10A710 (2005).
- 67 J.A.Ewing, *Phil. Trans.*, **176**, 523 (1885).
- 68 J.F. Smyth, S. Schultz, D. Kern, H. Schmid, and Dennis Yee, *J. Appl. Phys.* **63**, 4237 (1988).
- 69 J.F. Smyth, S. Schultz, D.R. Fredkin, D.P. Kern, S.A. Rishton, H. Schmid, M. Cali, and T.R. Koehler, *J. Appl. Phys.* **69**, 5262 (1991).
- 70 M.E. Schabes and H. N. Bertram, *J. Appl. Phys.* **64**, 1347 (1998).
- 71 R.P. Cowburn, A.O. Adeyeye, and M.E. Welland, *Phys. Rev. Lett.* **81**, 5414 (1998).
- 72 C. Mathieu, C. Hartmann, M. Bauer, O. Buettner, S. Riedling, B. Roos, S.O. Demokritov, B. Hillebrands, B. Bartenlian, C. Chappert, D. Decanini, F. Rousseaux, E. Cambril, A. Müller, B. Hoffmann, and U. Hartmann, *Appl. Phys. Lett.* **70**, 2912 (1997).
- 73 S.M. Weekes, F.Y. Ogrin, P.S. Keatley, *J. Appl. Phys.* **99**, 08B102 (2006).
- 74 W.W. Clegg, N.A.E. Heyes, E.W. Hill, and C.D. Wright, *J. Magn. Magn. Mater.* **95**, 49 (1991).

-
- ⁷⁵ T. Thomson, G. Hu, and B.D. Terris, Phys. Rev. Lett. **96**, 257204 (2006).
- ⁷⁶ M. Belov, Z. Liu, R.D. Sydora, and M.R. Freeman, Phys. Rev. B **69**, 094414 (2004).
- ⁷⁷ B.C. Choi, G.E. Ballentine, M. Belov, and M.R. Freeman, Phys. Rev. B **64**, 144418 (2001).
- ⁷⁸ T.J. Silva, C.S. Lee, T.M. Crawford, and C.T. Rogers, J. Appl. Phys. **85**, 7849 (1999).
- ⁷⁹ A. Barman, V.V. Kruglyak, R.J. Hicken, C.H. Marrows, M. Ali, A.T. Hindmarch, and B.J. Hickey, Appl. Phys. Lett. **81**, 1468 (2002).
- ⁸⁰ O’Handley, *Modern Magnetic Materials: Principles and Applications*, John Wiley & Sons (2000).
- ⁸¹ P.H. Bryant, J.F. Smyth, S. Schultz, and D.R. Fredkin, Phys. Rev. B, **47**, 11255 (1993).
- ⁸² J.P. Park, P. Eames, D.M. Engebretson, J. Berezovsky, and P.A. Crowell, Phys. Rev. Lett. **89**, 277201 (2002).
- ⁸³ S.M. Chérif, Y. Roussigné, C. Dugautier, and P. Moch, J. Magn. Magn. Mater. **242-245**, 591 (2002).
- ⁸⁴ G. Gubbiotti, M. Conti, G. Carlotti, P. Candeloro, E. Di Fabrizio, K.Y. Guslienko, A. Andre, C. Bayer, and A.N. Slavin, J. Phys.: Condens. Matter. **16**, 7709 (2004).
- ⁸⁵ V.V. Kruglyak, A. Barman, R. J. Hicken, J. R. Childress, and J. A. Katine, J. Appl. Phys. **97**, 10A706 (2005).
- ⁸⁶ M. Bailleul, R. Höllinger, and C. Fermon, Phys. Rev. B **73**, 104424 (2006).
- ⁸⁷ G. Gubbiotti, M. Madami, S. Tacchi, G. Carlotti, and T. Okuno, J. Appl. Phys. **99**, 08C701 (2006).
- ⁸⁸ A. Barman, S.Q. Wang, J.D. Maas, A.R. Hawkins, S. Kwon, A. Liddle, J. Bokor, and H. Schmidt, Nano Lett. **6**, 2939 (2006).
- ⁸⁹ V.V. Kruglyak, P.S. Keatley, R.J. Hicken, J.R. Childress, and J.A. Katine, Phys. Rev. B **75**, 024407 (2007).
- ⁹⁰ F. Giesen, J. Podbielski, B. Botters, and D. Gründler, Phys. Rev. B **75**, 184428 (2007).
- ⁹¹ M.R. Freeman, W.K. Hiebert, and A. Stankiewicz, J. Appl. Phys. **83**, 6217 (1998).
- ⁹² A. Barman, V.V. Kruglyak, R.J. Hicken, A. Kundrotaite, and M. Rahman, Appl. Phys. Lett. **82**, 3065 (2003).
- ⁹³ M. Buess, R. Höllinger, T. Haug, K. Perzmaier, U. Krey, D. Pescia, M.R. Scheinfein, D. Weiss, and C.H. Back, Phys. Rev. Lett. **93**, 77207 (2004).
- ⁹⁴ C.H. Back, D. Pescia, and M. Buess, in “Spin dynamics in confined structures III” [Top. Appl. Phys. **101**, 137 (2006)], and references therein.
- ⁹⁵ B.C. Choi, J. Rudge, M.R. Freeman, Y.K. Hong, Q.F. Xiao, IEEE Trans. Magn. **43**, 2 (2007).
- ⁹⁶ For example, see the list of works citing M. Donahue and D.G. Porter, OOMMF User’s guide, Version 1.0, Interagency Report NISTIR 6376, NIST, Gaithersburg, MD, 1999 at http://math.nist.gov/oommf/oommf_cites.html.

-
- ⁹⁷ J.I. Martín, J. Nogués, K. Liu, J.L. Vicent, and I.K. Schuller, *J. Magn. Magn. Mater.* **256**, 449 (2003), and references therein.
- ⁹⁸ L. Giovannini, F. Montoncello, and F. Nizzoli, *Phys. Rev. B* **75**, 024416 (2007).
- ⁹⁹ P.S. Keatley, V.V. Kruglyak, R.J. Hicken, J.R. Childress, and J.A. Katine, *J. Magn. Magn. Mater.* **306**, 298 (2006).
- ¹⁰⁰ P.S. Keatley, V.V. Kruglyak, A. Barman, S. Ladak, R.J. Hicken, J. Scott, and M. Rahman, *J. Appl. Phys.* **97**, 10R304 (2005).
- ¹⁰¹ M.R. Freeman, R.R. Ruf, and R.J. Gambino, *IEEE Trans. Magn.* **27**, 4840 (1991).
- ¹⁰² M.E. Schabes and H.N. Bertram, *J. Appl. Phys.* **64**, 1347 (1988).
- ¹⁰³ R.P. Cowburn and M.E. Welland, *Phys. Rev. B* **58**, 9217 (1998).
- ¹⁰⁴ R.P. Cowburn, D.K. Koltsov, A.O. Adeyeye, and M.E. Welland, *Europhys. Lett.* **48**, 221 (1999).
- ¹⁰⁵ S.M. Chérif, C. Dugautier, J.-F. Hennequin, and P. Moch, *J. Magn. Magn. Mater.* **175**, 228 (1997).
- ¹⁰⁶ S.M. Chérif, Y. Rousigné, C. Dugautier, and P. Moch, *J. Magn. Magn. Mater.* **242-245**, 591 (2002).
- ¹⁰⁷ Y. Zhai, J. Shi, X.Y. Zhang, L. Shi, Y.X. Xu, H.B. Haung, Z.H. Lu, and H.R. Zhai, *J. Phys.: Cond. Matter* **14**, 7865 (2002).
- ¹⁰⁸ M. Pardavi-Horvath, C.A. Ross, and R.D. McMichael, *IEEE Trans. Magn.* **41**, 3601 (2005).
- ¹⁰⁹ A. Barman, V.V. Kruglyak, R.J. Hicken, A. Kundrotaite, and M. Rahman, *J. Magn. Magn. Mater.* **272-276**, 2121 (2004).
- ¹¹⁰ A. Barman, V.V. Kruglyak, R.J. Hicken, J. Scott, A. Kundrotaite, and M. Rahman, *J. Appl. Phys.* **95**, 6998 (2004).
- ¹¹¹ B. Hillebrands, C. Mathieu, C. Hartmann, M. Bauer, O. Büttner, S. Riedling, B. Roos, S.O. Demokritov, B. Bartenlian, C. Chappert, D. Decanini, F. Rousseaux, E. Cambri, A. Müller, B. Hoffmann, and U. Hartmann, *J. Magn. Magn. Mater.* **175**, 10 (1997).
- ¹¹² S. Jung, B. Watkins, L. DeLong, J.B. Ketterson, and V. Chandrasekhar, *Phys. Rev. B* **66**, 132401 (2002).
- ¹¹³ G.N. Kakazei, P.E. Wigen, K.Y. Guslienko, R.W. Chantrell, N.A. Lesnik, V. Metlushko, H. Shima, K. Fukamichi, Y. Otani, and V. Novosad, *J. Appl. Phys.* **93**, 8418 (2003).
- ¹¹⁴ G.N. Kakazei, P.E. Wigen, K.Y. Guslienko, V. Novosad, A.N. Slavin, V.O. Golub, N.A. Lesnik, and Y. Otani, *Appl. Phys. Lett.* **85**, 443 (2004).
- ¹¹⁵ C. Bayer, J.P. Park, H. Wang, M. Yan, C.E. Campbell, and P.A. Crowell, *Phys. Rev. B* **69**, 134401 (2004).
- ¹¹⁶ A. Aharoni, *J. Appl. Phys.* **83**, 3432 (1998).
- ¹¹⁷ A. Aharoni, *Physica B* **306**, 1 (2001).
- ¹¹⁸ A.G. Gurevich and G.A. Melkov, *Magnetization oscillations and waves*, CRC Press, (1996).

-
- ¹¹⁹ J.F. Cochran, J. Rudd, W.B. Muir, B. Heinrich, and Z. Celinski, *Phys. Rev. B* **42**, 508 (1990).
- ¹²⁰ Physik Instrumente PZ 113E, *E-802 Servo-Controller Submodule User Manual*, Release 1.4.0 (2004).
- ¹²¹ Physik Instrumente PZ 62E, *E-500 Series PZT Control Electronics User Manual*, Release 2.13.1 (2004).
- ¹²² Physik Instrumente PZ 77E, *E-509 Position Servo-Control Module User Manual*, Release 2.7.0 (2005).
- ¹²³ <http://www.picoprobe.com/40a.html>
- ¹²⁴ S. Wang, A. Barman, H. Schmidt, J.D. Maas, A.R. Hawkins, S. Kwon, B. Harteneck, S. Cabrini, and J. Bokor, *Appl. Phys. Lett.* **90**, 252504 (2007).
- ¹²⁵ P. Lissberger, *J. Opt. Sci. Am.* **51**, 957 (1961).
- ¹²⁶ P.R. Cantwell, U.J. Gibson, D.A. Allwood, H.A.M. Macleod, *J. Appl. Phys.* **100**, 093910 (2006).
- ¹²⁷ *Handbook of Chemistry and Physics*, 75th ed., CRC Press (1994).
- ¹²⁸ <http://www.ee.byu.edu/photonics/ARcoatings.phtml>
- ¹²⁹ N. Storey, *Electronics: A Systems Approach*, 2nd ed., Addison Wesley (1998).
- ¹³⁰ Analogue Devices, *Low Noise, Precision Operational Amplifier OP27*, Data Sheet Revision F (2006).